RECOVERY OF GEOCHEMICAL PROCESSES IN KOMATIITES USING LINEAR
ALGEBRAIC METHODS

by

LUKE HILCHIE

B.Sc., Dalhousie University, 2009
M.Sc., Dalhousie University, 2011

A THESIS SUBMITTED IN PARTIAL FULFILLMENT OF
THE REQUIREMENTS FOR THE DEGREE OF

DOCTOR OF PHILOSOPHY

in

THE FACULTY OF GRADUATE AND POSTDOCTORAL STUDIES

(Geological Sciences)

THE UNIVERSITY OF BRITISH COLUMBIA

(Vancouver)

December, 2017

Abstract

The metasomatic reactions responsible for the mineralogical and chemical alteration of komatiites have not been fully identified. The geochemical effects of these reactions inhibit recovery of the nature and extent of magmatic processes recorded by komatiite rocks. Metasomatism is a challenge in lithogeochemical research because protolith variability and metasomatism together define high-dimensional geochemical spaces. Standard methods that require a conserved element are of limited use, as conserved elements may not be present. This work develops and applies linear algebraic techniques to test mass transfer hypotheses against whole rock compositions without assumptions of elemental behaviour. The methods enabled quantification of the stoichiometry and the relative effects of magmatic and metasomatic processes in komatiites. Such processes include magmatic differentiation, serpentinization, and breakdown of clinopyroxene to actinolite. Three main findings are: (1) geochemical and petrological evidence exists for within-flow differentiation and the possibility of lateral continuity between komatiite and komatiitic basalt flows; (2) serpentinization occurred neither by isochemical nor fully metasomatic processes in a lava flow from Pyke Hill in the Abitibi greenstone belt; and (3) small magnitudes of metasomatic reactions are sufficient to modify primary geochemical signals, such that their neglect in geochemical interpretation could lead to incorrect conclusions. Future studies could delve deeper into the possibility of lateral continuity between komatiites and komatiitic basalts, and expand determination of viable serpentinization reactions to a wider range of localities and lithologies.

Lay summary

Komatiites are magnesium-rich volcanic rocks (lavas) formed from ultra-hot magmas during the first half of Earth's history. These rocks host important precious and base metal deposits that formed after eruption and during cooling. However, these rocks seldom preserve their original minerals because of chemical reactions with low-temperature fluids after eruption. Chemical changes that occur during these transformations make recovery of ore-forming processes difficult. The main reaction – serpentinization – is common problem in magnesium-rich rocks in general, and has implications for a broad range of geological processes. This work presents new mathematical techniques for test for and quantify the extent and nature of these chemical changes. The methods use the chemical compositions of the rocks to estimate the relative effects of processes that occurred in the molten state and chemical reactions that occurred after solidification, during fluid infiltration. Serpentinization removed a significant amount of iron from the rocks, and other reactions changed the abundances of calcium, sodium, and potassium. Although significant, the changes are small compared to magmatic processes. Yet, these small changes obscure primary information about the magmatic processes and could compromise ore deposit modeling if neglected.

Preface

This document is my original, previously unpublished work. Geochemical data used herein derive from prior studies (LaHaye and Arndt, 1996; LaHaye et al., 1995; Shimizu et al., 2005; Shore 1997; Smith et al., 1980). My supervisor, Dr. Kelly Russell, directed me towards linear algebraic methods and provided invaluable direction and education in this regard. He also provided Matlab code to compute whole rock Mg-Fe equilibria, updated from his previous work (Russell and Snyder, 1997). My supervisory committee (Drs. Kelly Russell, James Scoates, Maya Kopylova, and Lucy Porritt) helped to narrow down the scope of this project to its present form. Dr. James Scoates' advice on the introductory and concluding chapters significantly improved their quality and accessibility.

Table of contents

List of tables

List of figures

List of abbreviations and symbols

Italics indicate symbols and subscript/superscript identifiers in equations.

A	– An_{70}
Act	– Actinolite
Adr	– Andradite
Amph	– Amphibole
aq	– Aqueous
Aug	– Augite
Brc	– Brucite
Cc	– Calcite
Chl	– Chlorite
Cpx	– Clinopyroxene
Cr-Sp	– Chromian spinel
dif	– Difference
F	– Fo_{90}
GCM	– Geochemical matrix
Gnt	– Garnet
h	– Number of hypotheses (columns) in *H*
H	– Hypothesis matrix
H-Gnt	– Hydrogarnet
i	– A specific entity in a group of entities; e.g., the ith column in a matrix, the ith oxide in a rock composition
I	– Identity matrix and its modifications (as indicated)
j	– Number of oxides
m	– Number of rows in GCM.
M	– Melt
Mg#	– Magnesium number (100 Mg / [Mg + Fe])
MI	– Metasomatic index
Mt	– Magnetite

n	– Number of columns in *GCM*
N	– Number of moles
NNO	– Nickel-nickel oxide
Ol	– Olivine
PER	– Pearce element ratio
PGE	– Platinum group element
Pl	– Plagioclase
proj	– Projected
r	– Rank
R	– Synthetic rock sample
RA	– Synthetic rock sample from Suite A
rec	– Reconstructed from projection
rp	– Extent of reaction progress
rxn	– Reaction
Sp	– Spinel
Srp	– Serpentine
SVD	– Singular value decomposition
t	– Transpose
T	– Temperature
Tr	– Transformation matrix, or transformed
Trm	– Tremolite
Ttn	– Titanite (sphene)
u	– Orthonormal matrix containing the first *r* columns of *U*; the rock composition space
U	– Orthonormal matrix containing the column and left null spaces of *GCM*
wt	– Weight
X	– Mole fraction
Δ	– Change or difference
θ	– Angle of separation
Σ	– Sum

Glossary

Alteration Mineralogical transformations attending hydrothermal metamorphism.

Closure The constant sum (unity, 100%) of concentrations in a bulk composition resulting from their intensive (size or amount-independent) nature.

Differentiation Chemical diversification of rocks deriving from a parental composition of restricted variability.

Fractionation Evolution of liquid composition by way of crystallization.

Hydration Chemical reaction yielding addition of water to a bulk composition.

Isochemical Of chemical reactions involving no net bulk compositional change other than addition of H_2O and/or CO_2.

Komatiite Ultramafic lavas derived from parental liquids with >18 wt. % MgO.

Komatiitic basalts Oliviniferous basalts derived from liquids with 18 to ~6 wt. % MgO.

Metasomatism Net bulk compositional changes attending metamorphism.

Serpentinization Chemical reactions forming serpentine group minerals, usually at the expense of olivine and other magnesian silicates.

Sorting Physical separation of crystals from their conjugate liquid.

Acknowledgements

CHAPTER 1: Introduction

1.1. Komatiites

Komatiites are ultramafic volcanic rocks deriving from liquids that erupted predominantly in the Archean (Arndt et al., 2008). They occur within cratonic greenstone belts on every continent (Figure 1.1). Their extreme eruption temperatures (~1500-1650 °C; Green, 1975; Arndt, 1976; Arndt et al., 2008) point to a hotter mantle in first half of Earth's history, and thus imply cooling over geological time (Green, 1975; Nisbet et al., 1993; Grove and Parman, 2004; Arndt et al., 2008; Berry et al., 2008; Condie et al., 2016). The compositions and isotopic characteristics of komatiites reflect the chemical nature and geological history of their source regions in the mantle (Takahashi and Scarfe, 1985; Scarfe and Takahashi, 1986; Nisbet et al., 1987; Sun, 1987; Gruau et al., 1990; Herzberg, 1992; Lesher and Arndt, 1995; Blichert-Toft and Arndt, 1999; Parman, 2004; Parman and Grove, 2004; Sobolev et al., 2016; Sossi et al., 2016). As hosts to Ni, Cu, and platinum group element (PGE) deposits (e.g., Lesher et al., 1984; Lesher, 1989; Barnes et al., 2004; Barnes et al., 2007; Arndt et al., 2008; Fiorentini et al., 2010), these rocks also bear economic significance. Considerable scientific interest followed recognition of komatiites as ultramafic lavas (Viljoen and Viljoen, 1969a; Viljoen and Viljoen, 1969b; Pyke et al., 1973), giving rise to a substantial body of literature dealing with conditions of formation (e.g., Green et al., 1975; Takahashi and Scarfe, 1985; Scarfe and Takahashi, 1986; Herzberg, 1992; Zhang and Herzberg, 1994; Herzberg and Zhang, 1996; Arndt et al., 1998; Herzberg and O'Hara, 1998; Walter, 1998; Parman, 2004; Sobolev et al., 2016; Sossi et al., 2016), volcanology (e.g., Arndt, 1982; Huppert et al., 1984; Lesher et al., 1984; Huppert and Sparks, 1985; Lesher, 1989; Dann, 2000; Dann, 2001; Houlé et al., 2009; Houlé et al., 2011), conditions of emplacement (e.g., Green, 1975; Canil, 1997; Parman et al., 1997; Kamenetsky et al., 2010), and hydrothermal alteration (e.g., Hynes, 1980; Beswick, 1983; Lowe and Byerly, 1986; Duchač and Hanor, 1987; Hanor and Duchač, 1990; Tourpin et al., 1991; LaHaye et al., 1995; LaHaye and Arndt, 1996; Lazar et al., 2012).

The geochemical processes that produced and differentiated komatiites and their parental liquids reflect conditions in and on the Archean Earth, from the depths of the upper mantle through to the surface. Perhaps the most sparsely studied part of this
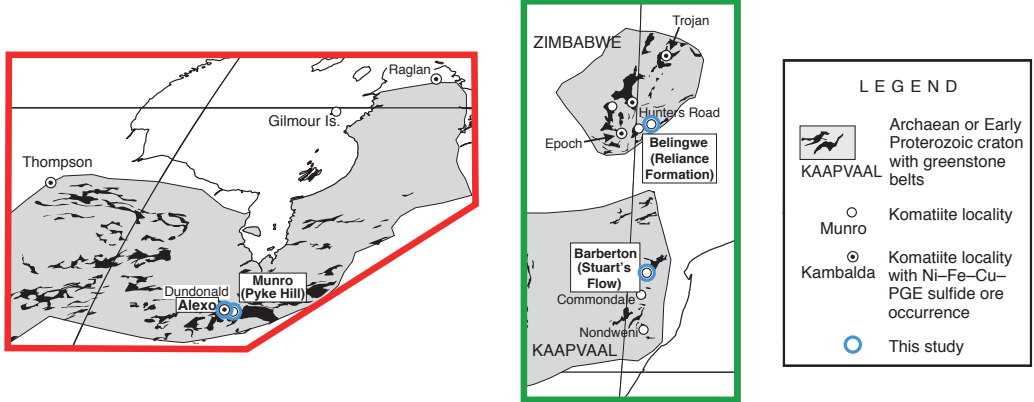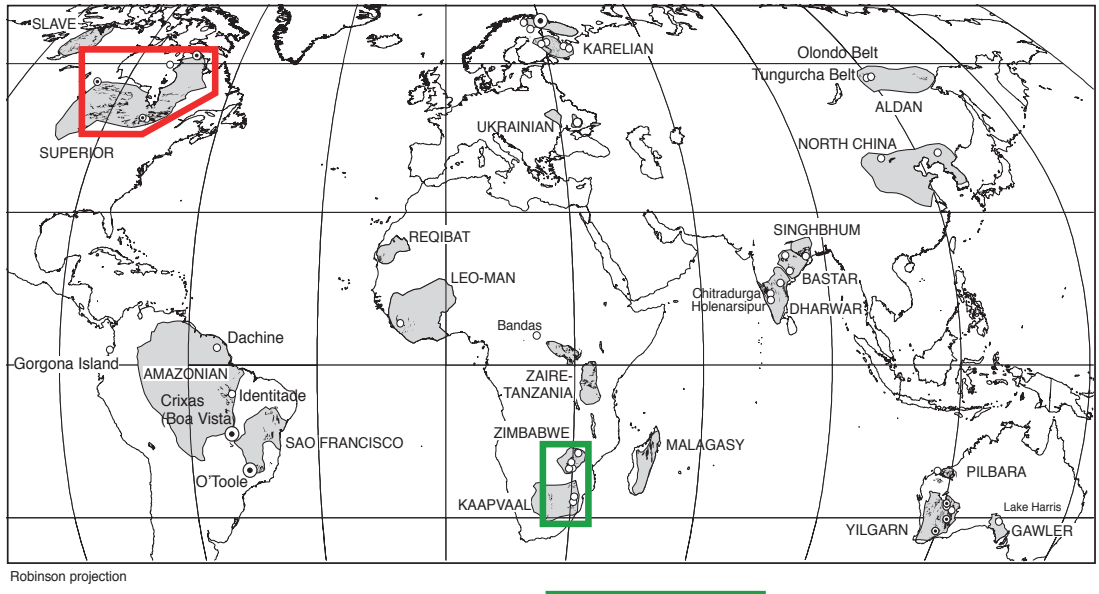
Figure 1.1. Global distribution of komatiites, modified after Arndt et al. (2008). Insets magnify the regions surrounding the lavas in this study.

geochemical history is their serpentinization (LaHaye et al., 1995; LaHaye and Arndt, 1996; Shore, 1997; Kyser et al., 1999; Lazar et al., 2012), which principally expresses as replacement of olivine. Recognition that serpentinization was perhaps crucial to atmospheric chemistry (Lazar et al., 2012) and the development and success of early life (Sleep et al., 2004; Sleep et al., 2011; McCollom and Seewald, 2013; Holm et al., 2015) makes komatiite alteration a prime target for exploring these significant proposals. The objectives of my research are to establish methods that enable stringent tests of geochemical hypotheses at any stage in the formation or modification of rock suites, and to specifically apply these to problems of magmatic differentiation and metasomatism of komatiites. This research serves as a blueprint to extraction of viable chemical processes, including serpentinization reactions, in these primordial rocks. The methods described herein are further applicable to any problem of chemical differentiation in geology.

1.1.1. Geochemical diversification of komatiites

Komatiite magmas form from high (~50%) to low (< 10%) degrees of partial melting of mantle peridotites at ~1-2 GPa to $\geq$7 GPa, respectively (e.g., Green, 1975; Takahashi, 1986; Zhang and Herzberg, 1994; Herzberg and Zhang, 1996; Walter, 1998; Arndt et al., 2008) Higher pressures of partial melting result in greater retention of Al in the source owing to increasing modal garnet in the residuum, thereby giving rise to high Ti/Al and Ca/Al komatiites (e.g., Barberton komatiites; Figure 1.1). Relatively low pressure equivalents (e.g., Abitibi komatiites, Belingwe komatiites; Figure 1.1) bear correspondingly low Ti/Al and Ca/Al. True komatiite lavas, deriving from liquids with >18 wt.% MgO (by definition), cannot have differentiated significantly during ascent, as rapid sorting of liquidus olivine precludes such elevated MgO contents (Arndt et al., 2008). However, komatiites commonly occur in close association with komatiitic basalts (<18 wt.% MgO), some of which may derive from the same parental komatiite magma (Arndt et al., 1977; Arndt and Nesbitt, 1984; Shimizu et al., 2005; Arndt et al., 2008).

The main differentiation process in komatiite magmas is olivine sorting (Barnes et al., 1983; Beswick, 1983; Arndt, 1986; Canil, 1987; LaHaye and Arndt, 1996; Arndt et al., 2008), as olivine is the lone liquidus phase over a wide temperature interval (Arndt, 1976; Arndt et al., 2008). The most conspicuous physical expression of this phenomenon

is the common occurrence of thick dunitic cumulate zones beneath the spinifex texture-dominated upper portions of komatiite lavas (e.g., Viljoen and Viljoen, 1969a; Viljoen and Viljoen, 1969b; Pyke et al., 1973; Arndt et al., 2008). Accumulation may have occurred within ponded, stagnant lavas and/or within propagating flows (Figure 1.2 A; Arndt et al., 2008). The latter process must have occurred where the thickness of cumulates is greater than what could derive from the overlying spinifex rocks (Figure 1.2 B; Lesher, 1989; Arndt et al., 2008). Such syn-propagation differentiation may produce refractory, ultramafic vent-proximal rocks that grade to increasingly evolved rocks downstream (Figure 1.2 A, B; Lesher, 1989; Arndt et al., 2008). If komatiite and komatiitic basalt can be laterally continuous in this way, their co-occurrence in greenstone belts may be the expression of surficial differentiation in the absence of deep-seated magma chambers. Such a scenario would have implications for the distribution of heat in the Archean crust associated with komatiite and komatiitic basalt magmatism, bearing consequences for crustal anatexis and the formation continental crust.

Occurrence of thick (hundreds of metres) cumulates in some lavas requires continuous passage of large volumes of liquid and necessitates some degree of downstream differentiation (e.g., Barnes et al., 1988; Arndt et al., 2008). These occurrences likely correspond to channelized flow pathways near the vent (Figure 1.2 A, B; Arndt et al., 2008). This continuous transport of hot magma enabled thermal erosion (i.e., assimilation) of the underlying substrate (Figure 1.2 B), particularly where the solidus temperatures were low and the surface area was high (Huppert and Sparks, 1985; LaHaye et al., 2001; Arndt et al., 2008; Houlé et al., 2011; Sobolev et al., 2016). Assimilation of appropriate substrates (e.g., sulphidic sediments) enabled formation of magmatic sulphide deposits in some localities (e.g., Alexo; LaHaye et al., 2001; Arndt et al., 2008; Houlé et al., 2011; Sobolev et al., 2016).

Infiltration of fluids following emplacement caused alteration of all komatiite lavas (Figure 1.2 C, D; Smith et al., 1980; Beswick, 1983; LaHaye et al., 1995; LaHaye and Arndt, 1996; Kyser et al., 1999). The least altered exposures on Gorgona Island, Colombia, and in the Reliance Formation (Figure 1.1), Belingwe greenstone belt, Zimbabwe, both feature minor serpentinization of olivine (Echeverría, 1980; Nisbet et al., 1987; Renner et al., 1994; Arndt et al., 2008). Generally, olivine shows virtually
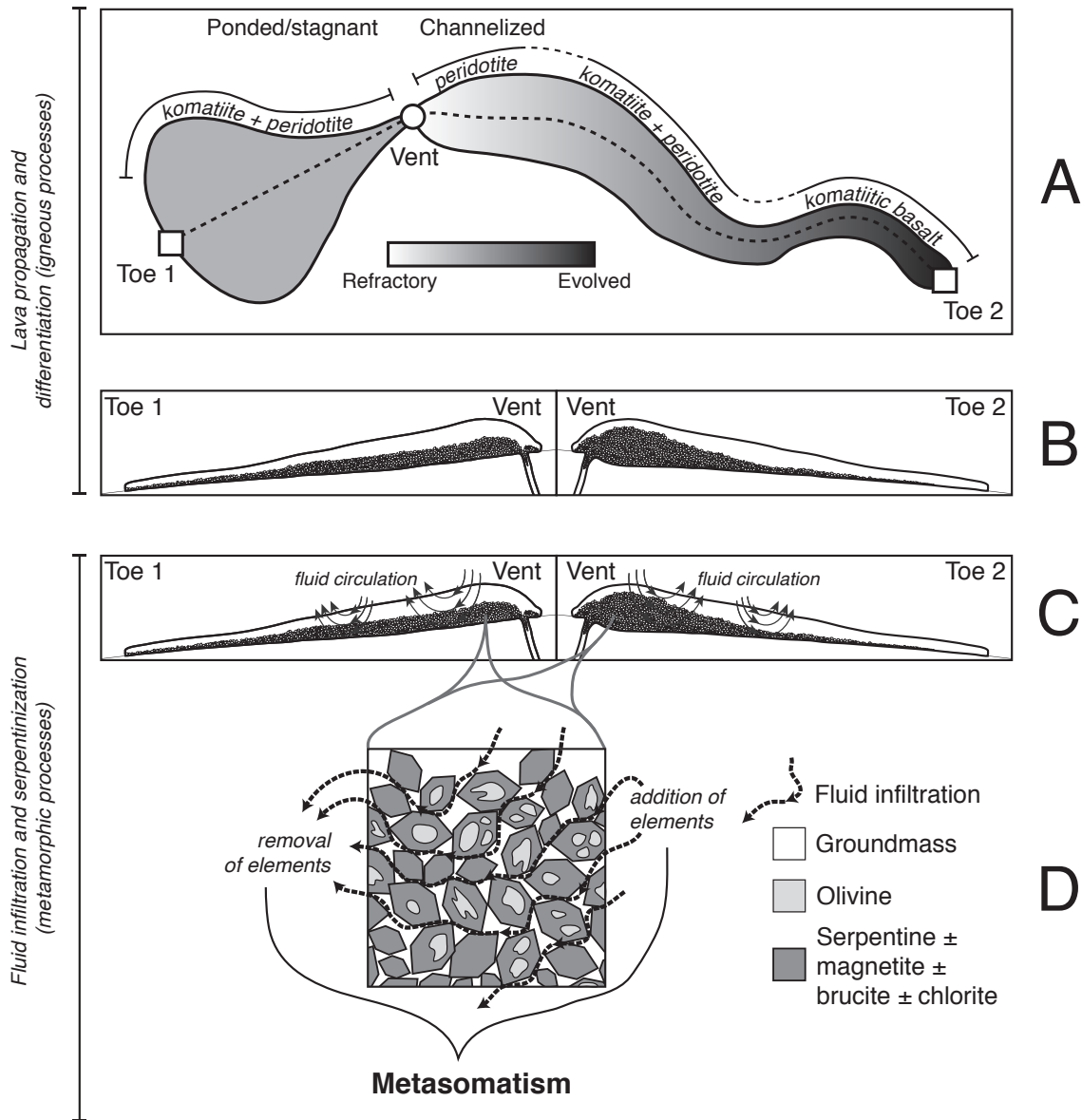
Figure 1.2. Geochemical differentiation processes in komatiites. (**A**) Single-pulse, ponded lava flows may exhibit uniform bulk composition (through a given vertical section), whereas multiple-pulse channelized flows may show compositional and lithological gradations from the vent (refractory) to the toe (evolved). (**B**) Comparison of longitudinal sections through a ponded (left) and a channelized (right) flow. The relative thickness of cumulates varies little through the ponded flow, whereas the channelized flow features progressive thinning of cumulates downstream. Passage of multiple magma injections may enable thermal erosion (i.e., basal assimilation) of the substrate, particularly at the hottest locations proximal to the vent. (**C**) Circulation of fluids following emplacement affects either type of flow, resulting in hydrothermal alteration (panel D) of the rocks, which predominantly expresses as serpentinization of olivine. (**D**) Serpentinization attending fluid infiltration may involve addition or removal of elements to the protolith (i.e., hydrothermal alteration is likely metasomatic).

5

complete replacement (Arndt et al., 2008), and extensively serpentinized rocks are regarded as weakly altered (Arndt et al. 2008) relative to their pervasively carbonated (Hynes, 1980; Tourpin et al., 1991) or silicified counterparts (Duchač and Hanor, 1987; Hanor and Duchač, 1990).

Mobilization of elements during alteration (i.e., metasomatism; Figure 1.2 D) expresses differently across komatiite localities (Hynes, 1980; Beswick, 1983; Duchač and Hanor, 1987; Hanor and Duchač, 1990; Tourpin et al., 1991; LaHaye et al., 1995; LaHaye and Arndt, 1996; Arndt et al., 2008). The major elements most susceptible to metasomatism include Ca, Na, and K, although reports of Si, Mg, Fe, and Ti mobility exist (summarized by Arndt et al., 2008). However, the methods to evaluate element mobility rely heavily on the pretense of a simple magmatic differentiation history (Section 1.1.2) and typical behaviour of elements (Section 1.1.2 and Chapter 2). The resulting interpretations are commonly equivocal, and questions remain about which elements were mobile and whether they experienced enrichment or depletion. Without more definitive approaches to characterizing metasomatic effects, recovery of the responsible reactions, quantitative magnitude, and their relationships with mineralogical modifications is unattainable.

1.1.2. Methods to evaluate metasomatism in komatiites and their limitations

The two principal approaches to assess metasomatism in komatiites rely on the assumption that olivine fractionation was the sole important magmatic differentiation process (Arndt et al., 2008). Accordingly, many workers use trends on variation diagrams (i.e., oxide-oxide plots; Harker, 1909) with MgO concentration on the x-axis and other components on y to test for geochemical diversity being the result of olivine fractionation alone (e.g., Barnes et al., 1983; LaHaye et al., 1995; LaHaye and Arndt, 1996; Arndt et al., 2008; Sossi et al., 2016). Figure 1.3 A schematically illustrates this approach, wherein all magmatic variability should plot along a single line connecting the composition of fractionating olivine and the parental liquid; deviations must result from action of other processes, such as metasomatism or assimilation. Similarly, other workers exploit molar element ratio diagrams (i.e., Pearce element ratio diagrams), which reflect the stoichiometry of chemical processes (Pearce, 1968; Russell and Nicholls, 1988), to test
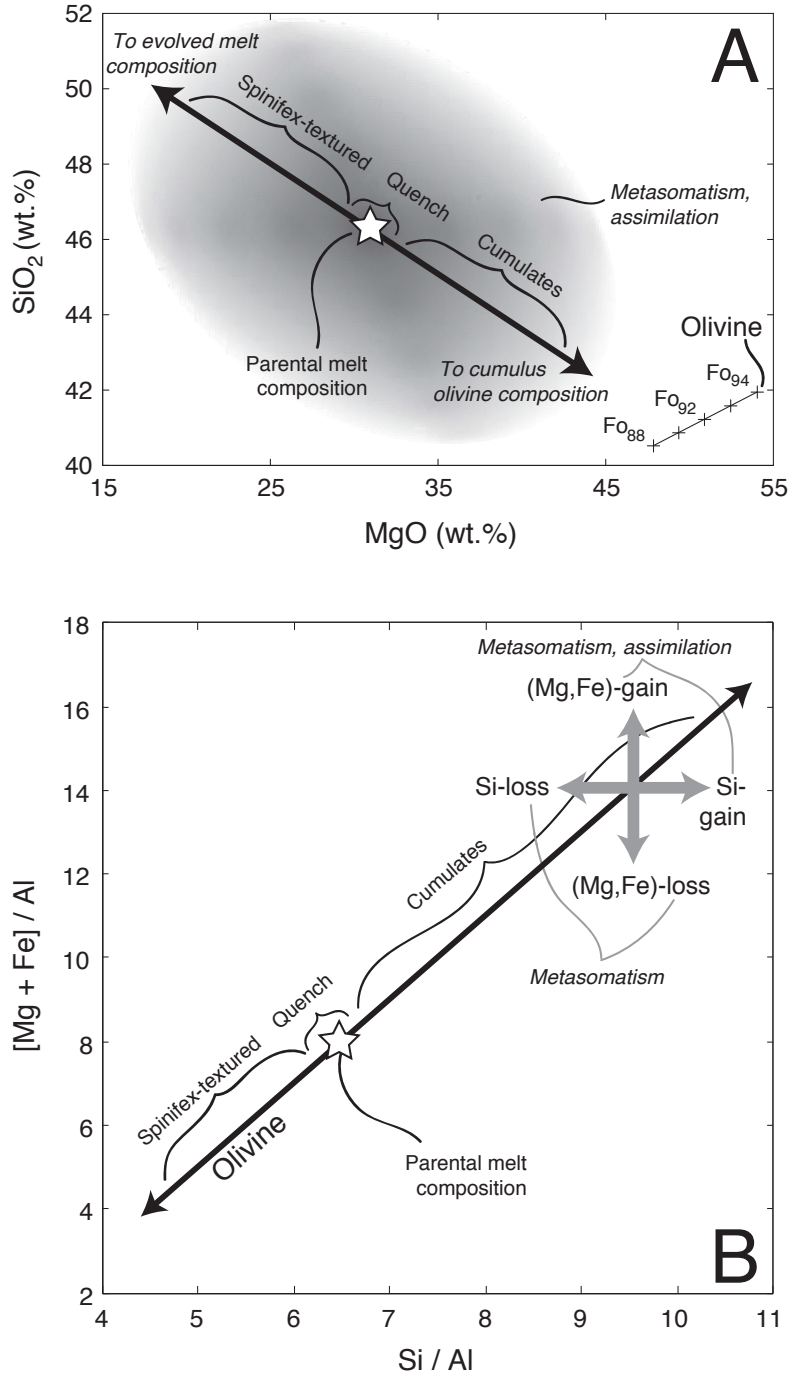
Figure 1.3. Schematic illustrations showing the principal methods to identify metasomatism in komatiites. (**A**) Variation diagrams of MgO versus other components show linear mixing trends connecting the parental melt composition to the composition of fractionating olivine. Deviations from linearity result from other processes (e.g., metasomatism or assimilation), although whether a given component increased or decreased is unclear. (**B**) Pearce element ratio (PER) diagrams recover the stoichiometry of geochemical processes, thus pristine komatiites should define olivine stoichiometry. Deviations represent other processes, such as metasomatism (elemental losses or gains) or assimilation (elemental gains only).

for consistency with olivine fractionation (e.g., Barnes et al., 1983; Beswick, 1983; Barnes, 1985; Canil, 1987; Walter, 1998). Deviations from olivine control must arise from other processes, such as metasomatism or assimilation (Figure 1.3 B). Both of these methods can reliably identify deviations from olivine-control, but are subject to limitations that become more important as the degree of geochemical complexity increases. Moreover, determining the nature (e.g., metasomatic reaction or assimilation) of the causative processes remains elusive.

Rock compositions suffer from closure, the phenomenon whereby changes in concentrations of components occur regardless of whether they were involved in extensive processes active in the sampled system (Chayes, 1962). In geology, this constant sum nature of compositions imposes increases or decreases in concentrations of elements regardless of whether they were mobile (Chayes, 1962), thereby rendering interpretations of variation diagrams equivocal. So reliable identification of mobile elements and the direction of their movement (gain or loss) is difficult, if possible, using these diagrams. The PER approach is more robust, but requires assumption or knowledge of a conserved element (Pearce, 1968; Russell and Nicholls, 1988; Stanley, 1993). Knowledge or sound assumption of element conservation verges on unattainable as the extent of alteration and geological complexity increases; action of every new independent process upon a geochemical system adds another dimension of complexity to its constituent rocks. Thus, studies of alteration want for approaches that robustly test geochemical hypotheses and quantify their effects without assumptions about the behaviour of elements. Such advances would improve assessment of the extent and nature of metasomatism and strengthen interpretations of igneous processes in komatiites.

1.2. Serpentinization

The problem of alteration in komatiites (Figure 1.2 C, D) is an example of the broader phenomenon of serpentinization (Hostetler et al., 1966; Thayer, 1966; Moody, 1976; Wicks and Whittaker, 1977; O'Hanley, 1996; Evans et al., 2013). This replacement, principally of olivine and pyroxenes, is common among mafic rocks and pervasive among ultramafic rocks, a group spanning chondrites, peridotites, pyroxenites, kimberlites, and komatiites. Just as metasomatic serpentinization reactions must figure

into interpretation of komatiite rock compositions (Barnes et al., 1983; Canil, 1987; LaHaye et al., 1995; LaHaye and Arndt, 1996; Walter, 1998; Arndt et al., 2008), the same is true for all of the above lithologies (Hostetler et al., 1966; Thayer, 1966; Coleman and Keith, 1971; Moody, 1976; Komor et al., 1985; O'Hanley, 1992; Shervais et al., 2005; Stripp et al., 2006; Sparks et al., 2009; Brooker et al., 2011; Velbel, 2014). As serpentinization reactions are only softly constrained despite a large body of research on the process (e.g., Hostetler et al., 1966; Thayer, 1966; Moody, 1976, Komor et al. 1985, O'Hanley 1992, Shervais et al. 2005, Frost et al. 2013), accounting for its geochemical effects (e.g., Brooker et al., 2011) remains an uncertain endeavor.

This more general problem of serpentinization is significant by virtue of the rocks it acted upon, as they include Earth's parental materials (Carlson et al., 2014), primordial ultra-hot lavas (Viljoen and Viljoen, 1969a,b; Pyke et al.,1973; Arndt et al. 2008) Earth's mantle rocks including oceanic lithosphere (Coleman, 1971; Nixon, 1987), metal (including the PGEs) and diamond ores (Mitchell, 1986; Lesher, 1989), and the deepest magmatic and xenolithic rock samples of Earth's interior (Mitchell, 1986). Moreover, modern serpentinization generates molecular H_2 by reducing H^+ and oxidizing Fe^{2+}, providing a source of chemical energy that sustains chemotrophic organisms and their ecosystems at hydrothermal seafloor vents (e.g., McCollum and Seewalk, 2013). The hypothesis that such processes were instrumental in cultivation of the earliest life on Earth and perhaps on extraterrestrial bodies drives a fertile area of research (e.g., Sleep et al., 2004; Sleep et al., 2011; McCollum and Seewald, 2013; Holm et al., 2015). Interpretation of these rocks thus contributes to our collective view of major processes including plate tectonics (Coleman, 1971; Escartín et al., 2001; Herzberg, 2004; Hirth and Guillot, 2013), magma genesis (Green, 1975; Dalton and Presnall, 1998; Walter, 1998; Gudfinnsson and Presnall, 2005), planet formation (Carlson et al., 2014), and perhaps the origins of life on Earth and elsewhere (Sleep et al., 2004; Sleep et al., 2011; McCollom and Seewald, 2013; Holm et al., 2015). Geochemical effects of serpentinization may therefore influence views of some of the defining geological processes on Earth. Moreover, serpentinites themselves contribute to element exchange between the hydrosphere, crust, and mantle, and production of magmas at volcanic arcs (Hattori and Guillot, 2003; Hattori and Guillot, 2007; Deschamps et al., 2013; Guillot and

Hattori, 2013). Development of methods to better delineate and quantify serpentinization reactions in komatiites is also relevant to serpentinization generally and could lead to later breakthroughs in the study of any of the associated rocks and their formative processes.

1.3. Metasomatism

Serpentinization is one portion of the larger category of processes of metasomatism (Figure 1.2 D) and alteration (e.g., Schwartz, 1939; Hemley and Jones, 1964; Gresens, 1967; Grant, 1986; Putnis and Austrheim, 2010). Alteration encompasses essentially all chemical interactions between hydrothermal (or carbonic) fluids and the solid Earth; those that produce a net change in bulk composition (apart from volatiles) are metasomatic. Metasomatism is critical to the formation of diverse array of mineral deposits, including porphyry copper (Gustafson and Hunt, 1975; Carten, 1986; Dilles and Einaudi, 1992; Sillitoe, 2010), skarn (Kerrick, 1977; Taylor and O'Neil, 1977; Einaudi and Burt, 1982; Meinert, 1992; Sillitoe, 2010), epithermal and hydrothermal gold (Heald et al., 1987; Sillitoe, 2010; Zhu et al., 2011), emerald (Groat et al., 2008), gem corundum (Rakotondrazafy et al., 2008), diamond (Shirey et al., 2013), and others.

Just as metasomatism clouds attempts to glean geochemical process from komatiite bulk rock compositions, the more complex metasomatism associated with many mineral deposits makes determination of their formative processes particularly challenging. Nevertheless, element ratio-based approaches (both Pearce and other) have successfully identified chemical anomalies surrounding ore bodies (Urqueta et al., 2009), and recovered geochemical patterns matching observed mineralogy of metasomatized rocks (Polito et al., 2007; Urqueta et al., 2009). However, PER analysis requires knowledge of conserved elements to test hypotheses, and general element ratios are better suited to semi-quantitative comparison of rock compositions to alteration assemblage stoichiometry, rather than strict hypothesis testing. Thus, a method that tests geochemical hypotheses without knowledge of element behaviour would take lithogeochemistry a step further in characterization of metasomatism in mineral deposits and other settings. Such an advance could aid in quantification of metasomatism and establishment of its

significance to modification of primary geochemistry and ore mineralization over a range of magnitudes.

1.4. Structure and contributions of this thesis

This thesis develops a new approach to testing mass transfer hypotheses using whole rock geochemical data, and applies this approach to magmatic differentiation and metasomatism of komatiite lavas.

Chapter 2 probes the positive and negative attributes of three conventional methods used to portray and interpret geochemical data: (i) variation diagrams (Harker, 1909), (ii) PER diagrams (Pearce, 1968; Russell and Nicholls, 1988), and (iii) isocon analysis (Gresens, 1967; Grant, 1986; Grant, 2005; Guo et al., 2009). My analysis demonstrates the strengths and weaknesses of each technique and provides the motivation for developing a more universal and robust method based on linear algebraic techniques, which appears in Chapter 3. Algorithms to aid in implementation of these methods appear in the Appendix, Section A2.

In Chapter 4, I applied these methods to test primary melt compositions (Shimizu et al., 2001; Sobolev et al., 2016; Sossi et al., 2016) and the composition of fractionating olivine in komatiite lavas. Results of those tests enabled thermodynamic modeling of Mg-Fe equilibria (Roeder and Emslie, 1970; Russell and Snyder, 1997; Sossi and O'Neill, 2016) that provided estimates of the evolved melt composition and the amount of excess olivine in vertical sections through a flow. This research found geochemical and petrological support for the hypothesis that lateral, within-flow differentiation of komatiitic liquid could produce komatiitic basalt downstream (Lesher, 1989). I also quantified deviation from magmatic variability to define a Metasomatic Index for komatiite lavas.

Application of this metric, PER analysis, and geometric hypothesis testing to the Abitibi Flow C (Shore, 1997) enabled identification of mobile elements and discovery of viable metasomatic reactions (Chapter 5). A geochemical model comprising the magmatic and metasomatic sources of variability recovers rock compositions, with the exception of alkalis, whose variability remains only partly explained. Reaction of clinopyroxene to form actinolite accounts for most metasomatic modification of Ca

abundances. Formation of serpentine and chlorite after olivine and groundmass can explain metasomatic Fe mobility, and entirely accounts for disruptions to whole rock Mg-Fe equilibria, which substantially affect cumulates despite the small overall magnitude of metasomatism. Serpentinization of this komatiite occurred neither by constant volume (Thayer, 1966) nor isochemical reactions (Hostetler et al., 1966; O'Hanley, 1992).

This thesis demonstrates that whole rock compositions and linear algebraic methods can together test for any mass transfer process operating at the hand sample scale. Further applications to komatiites would expand tests of the lateral differentiation hypothesis (Lesher, 1989), testing whether derivation of komatiitic basalt occurs predominantly within magma chambers at depth (Shimizu et al., 2005) or within lavas at the surface. Expansion to ultramafic rocks generally would yield key constraints on serpentinization reactions through geologic time and across lithologies, with implications for Archean microbial niches (Sleep et al., 2004; Sleep et al., 2011; McCollom and Seewald, 2013; Holm et al., 2015) and the compositional evolution of the atmosphere (Lazar et al., 2012). The methods in this thesis have virtually limitless applications in the field of geology and its many sub-disciplines.

CHAPTER 2: A review of methods to analyze mass transfer using whole rock compositions

2.1. Introduction

Untangling the chemical diversity in geological systems is essential to recovering processes that form and affect the solid Earth, whether by partial melting, hydrothermal metamorphism, weathering, physical sorting, and beyond (Figure 2.1). Compositions of geological samples (e.g., rocks) are intensive properties (i.e., independent of the size of the system), whereas those processes that produce chemical diversity operate by transfer of finite amounts of material (i.e., they are extensive). This disconnection between the nature of the processes and the observable properties complicates robust interpretation of process using rock compositions (cf. Chayes, 1962; Gresens, 1967; Pearce, 1968; Grant, 1986; Pearce, 1987; Rollinson and Roberts, 1987; Nicholls, 1988; Russell and Nicholls, 1988; Russell and Stanley, 1990a; Stanley, 1993; Nicholls and Gordon, 1994).

The problem is that a rock composition is a suite of concentrations of components per unit mass. Thus, any removal or addition of a component to or from a portion of a system modifies the concentrations of all components therein, including those conserved in the geochemical process. The term for this effect is closure (Chayes, 1962). Common practice in studies of whole rock compositions is to visualize the raw data (e.g., as variation diagrams of wt. % oxides), which portray concentrations that reflect both geological process and closure. More sophisticated methods rely upon stipulation of a conserved element (Pearce, 1968; Grant, 1986; Russell and Nicholls, 1988; Guo et al., 2009), and still involve two-dimensional representations of data.

Here I introduce and demonstrate, by way of synthetic datasets built from known processes, three different methods (variation diagrams, molar element ratios, and isocon analysis) of using whole rock compositions to help develop and test mass transfer hypotheses. The purpose is to show the strengths and weaknesses of the different methods, and identify outstanding problems that warrant solution.

2.2. The synthetic datasets

I computed several suites of synthetic whole rock compositions whose chemical diversity arises from stipulated geological processes. The datasets include two groups: the igneous
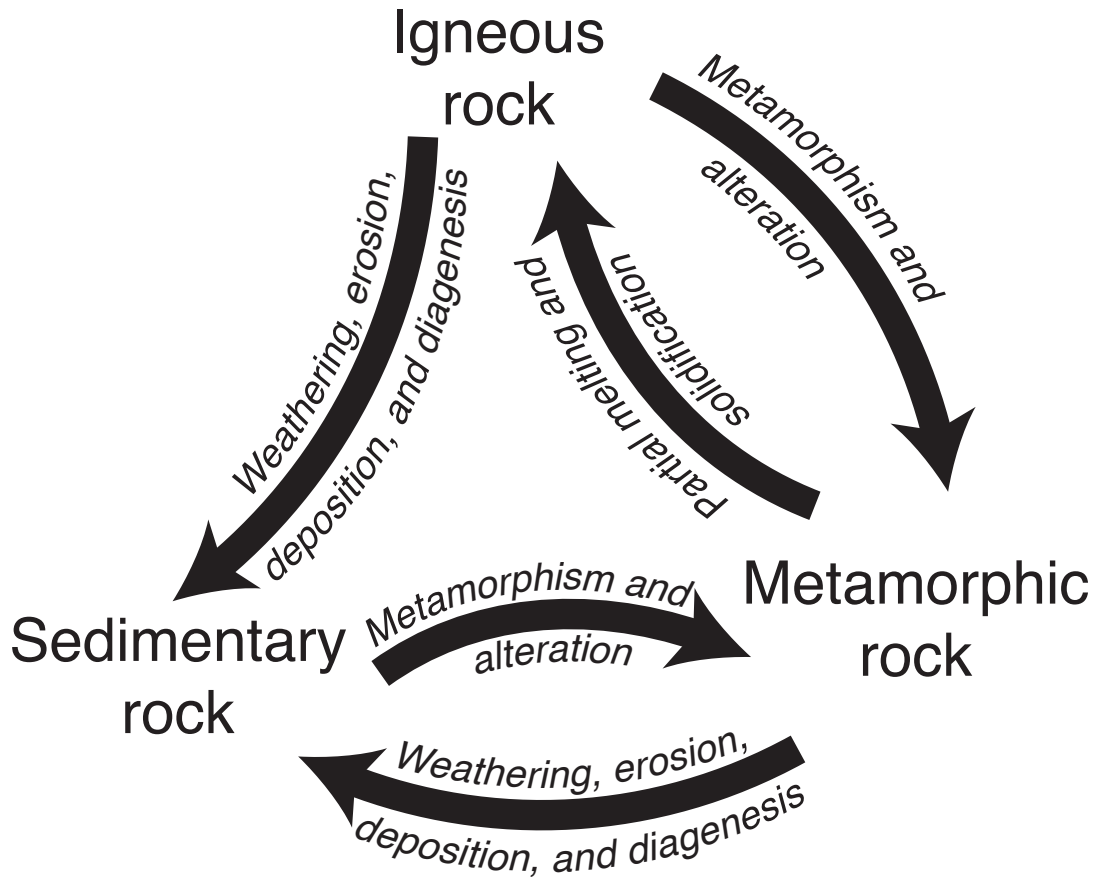
Figure 2.1. Geological processes active in the rock cycle commonly produce geochemical diversity in rock suites. Recovering these processes is a central aspect of geological study.

suites and the altered suites.

2.2.1. The igneous suites

The igneous suites involve fractionation-accumulation of olivine (Fo$_{90}$) with or without plagioclase (An$_{70}$) from two initial melts (Melt 1 and Melt 2; Table 2.1). I chose arbitrary whole numbers for the oxide concentrations in Melt 1. Melt 2 is a basaltic composition. The purpose of having two different melt compositions is to compare the geochemical trends produced by the action of otherwise identical processes upon different initial bulk compositions.

Igneous suites A and B represent 100 moles of melt (Melt 1 and Melt 2, respectively) that accumulated and fractionated olivine (Fo$_{90}$) at regular increments of two moles, from -10 to 28 moles (tables 2.2 and 2.3). Suites C and D are modified versions of A and B (respectively), to which I added or removed random amounts of plagioclase (An$_{70}$) spanning 25 moles (from -17.56 to 4.26 moles; tables 2.4 and 2.5). The purpose of choosing random amounts of An$_{70}$ was to ensure complete independence (i.e., decoupling) of the processes of accumulation/fractionation of Fo$_{90}$ and An$_{70}$, although such complete decoupling is geologically unlikely. The amounts of plagioclase are the same for both suites C and D.

In computing and reporting the synthetic data (i.e., tables 2.1 to 2.9), I chose molar proportions to eliminate the distorting effects of varying molar masses of the different oxides. I chose to round values to the second decimal place to mimic typical reporting of whole rock major and minor oxide concentrations and to ensure consistency in all calculations. Compositions of all phases are in Table 2.1 as mole percent of oxides.

The equations describing the computation of the igneous datasets are

$$N_R^i = X_{i,M}*N_M + X_{i,F}*N_F + X_{i,A}*N_A \ , \tag{2.1}$$

and

$$X_R = \frac{N_R^i}{\Sigma_1^j N_R^i} \ , \tag{2.2}$$

where N_{phase} denotes the number of moles of a phase, $X_{i,phase}$ denotes the mole fraction of oxide i in a phase, j is the number of oxides, and R is the synthetic sample in question. The phase abbreviations are M = melt, F = Fo$_{90}$, and A = An$_{70}$. The final molar oxide

Table 2.1. Compositions of phases in synthetic datasets (mol. %).

	Melt 1	Melt 2	Fo$_{90}$	An$_{70}$
SiO$_2$	45.00	50.95	33.33	57.50
TiO$_2$	1.00	1.91	0.00	0.00
Al$_2$O$_3$	8.00	16.30	0.00	21.25
FeO	13.00	9.34	6.67	0.00
MnO	2.00	0.20	0.00	0.00
MgO	10.00	6.97	60.00	0.00
CaO	9.00	9.81	0.00	17.50
Na$_2$O	3.00	3.02	0.00	3.75
K$_2$O	4.00	1.14	0.00	0.00
P$_2$O$_5$	5.00	0.36	0.00	0.00
H$_2$O	0.00	0.00	0.00	0.00
Total	100.00	100.00	100.00	100.00

Table 2.2. Compositions of samples in synthetic Suite A (mol. %).

	A1	A2	A3	A4	A5	A6	A7	A8	A9	A10	A11	A12	A13	A14	A15	A16	A17	A18	A19	A20
SiO_2	46.30	46.01	45.74	45.49	45.24	45.00	44.77	44.55	44.34	44.14	43.94	43.75	43.57	43.39	43.22	43.06	42.90	42.74	42.59	42.45
TiO_2	1.11	1.09	1.06	1.04	1.02	1.00	0.98	0.96	0.94	0.93	0.91	0.89	0.88	0.86	0.85	0.83	0.82	0.81	0.79	0.78
Al_2O_3	8.89	8.70	8.51	8.33	8.16	8.00	7.84	7.69	7.55	7.41	7.27	7.14	7.02	6.90	6.78	6.67	6.56	6.45	6.35	6.25
FeO	13.70	13.55	13.40	13.26	13.13	13.00	12.88	12.76	12.64	12.53	12.42	12.32	12.22	12.13	12.03	11.94	11.86	11.77	11.69	11.61
MnO	2.22	2.17	2.13	2.08	2.04	2.00	1.96	1.92	1.89	1.85	1.82	1.79	1.75	1.72	1.69	1.67	1.64	1.61	1.59	1.56
MgO	4.44	5.65	6.81	7.92	8.98	10.00	10.98	11.92	12.83	13.70	14.55	15.36	16.14	16.90	17.63	18.33	19.02	19.68	20.32	20.94
CaO	10.00	9.78	9.57	9.38	9.18	9.00	8.82	8.65	8.49	8.33	8.18	8.04	7.89	7.76	7.63	7.50	7.38	7.26	7.14	7.03
Na_2O	3.33	3.26	3.19	3.13	3.06	3.00	2.94	2.88	2.83	2.78	2.73	2.68	2.63	2.59	2.54	2.50	2.46	2.42	2.38	2.34
K_2O	4.44	4.35	4.26	4.17	4.08	4.00	3.92	3.85	3.77	3.70	3.64	3.57	3.51	3.45	3.39	3.33	3.28	3.23	3.17	3.13
P_2O_5	5.56	5.43	5.32	5.21	5.10	5.00	4.90	4.81	4.72	4.63	4.55	4.46	4.39	4.31	4.24	4.17	4.10	4.03	3.97	3.91
H_2O	0.00	0.00	0.00	0.00	0.00	0.00	0.00	0.00	0.00	0.00	0.00	0.00	0.00	0.00	0.00	0.00	0.00	0.00	0.00	0.00
Total	100.00	100.00	100.00	100.00	100.00	100.00	100.00	100.00	100.00	100.00	100.00	100.00	100.00	100.00	100.00	100.00	100.00	100.00	100.00	100.00
Moles of Melt1	100.00	100.00	100.00	100.00	100.00	100.00	100.00	100.00	100.00	100.00	100.00	100.00	100.00	100.00	100.00	100.00	100.00	100.00	100.00	100.00
Moles of Fo_{90}	-10.00	-8.00	-6.00	-4.00	-2.00	0.00	2.00	4.00	6.00	8.00	10.00	12.00	14.00	16.00	18.00	20.00	22.00	24.00	26.00	28.00

Table 2.3. Compositions of samples in synthetic Suite B (mol. %).

	B1	B2	B3	B4	B5	B6	B7	B8	B9	B10	B11	B12	B13	B14	B15	B16	B17	B18	B19	B20
SiO_2	52.90	52.48	52.07	51.68	51.31	50.95	50.60	50.27	49.95	49.64	49.34	49.06	48.78	48.52	48.26	48.01	47.77	47.54	47.31	47.09
TiO_2	2.12	2.07	2.03	1.99	1.95	1.91	1.87	1.83	1.80	1.77	1.73	1.70	1.67	1.64	1.62	1.59	1.56	1.54	1.51	1.49
Al_2O_3	18.11	17.72	17.34	16.98	16.63	16.30	15.98	15.68	15.38	15.09	14.82	14.56	14.30	14.05	13.82	13.59	13.36	13.15	12.94	12.74
FeO	9.64	9.58	9.51	9.46	9.40	9.34	9.29	9.24	9.19	9.15	9.10	9.06	9.02	8.97	8.94	8.90	8.86	8.83	8.79	8.76
MnO	0.23	0.22	0.22	0.21	0.21	0.20	0.20	0.20	0.19	0.19	0.19	0.18	0.18	0.18	0.17	0.17	0.17	0.16	0.16	0.16
MgO	1.08	2.36	3.59	4.76	5.89	6.97	8.01	9.01	9.98	10.90	11.79	12.65	13.49	14.29	15.06	15.81	16.54	17.24	17.92	18.57
CaO	10.90	10.66	10.43	10.22	10.01	9.81	9.62	9.43	9.25	9.08	8.92	8.76	8.60	8.46	8.31	8.17	8.04	7.91	7.78	7.66
Na_2O	3.35	3.28	3.21	3.14	3.08	3.02	2.96	2.90	2.85	2.79	2.74	2.69	2.65	2.60	2.56	2.51	2.47	2.43	2.40	2.36
K_2O	1.27	1.24	1.21	1.19	1.17	1.14	1.12	1.10	1.08	1.06	1.04	1.02	1.00	0.98	0.97	0.95	0.94	0.92	0.91	0.89
P_2O_5	0.40	0.39	0.38	0.37	0.36	0.36	0.35	0.34	0.34	0.33	0.32	0.32	0.31	0.31	0.30	0.30	0.29	0.29	0.28	0.28
H_2O	0.00	0.00	0.00	0.00	0.00	0.00	0.00	0.00	0.00	0.00	0.00	0.00	0.00	0.00	0.00	0.00	0.00	0.00	0.00	0.00
Total	100.00	100.00	100.00	100.00	100.00	100.00	100.00	100.00	100.00	100.00	100.00	100.00	100.00	100.00	100.00	100.00	100.00	100.00	100.00	100.00
Moles of Melt2	100.00	100.00	100.00	100.00	100.00	100.00	100.00	100.00	100.00	100.00	100.00	100.00	100.00	100.00	100.00	100.00	100.00	100.00	100.00	100.00
Moles of Fo_{90}	-10.00	-8.00	-6.00	-4.00	-2.00	0.00	2.00	4.00	6.00	8.00	10.00	12.00	14.00	16.00	18.00	20.00	22.00	24.00	26.00	28.00

Table 2.4. Compositions of samples in synthetic Suite C (mol. %).

	C1	C2	C3	C4	C5	C6	C7	C8	C9	C10	C11	C12	C13	C14	C15	C16	C17	C18	C19	C20
SiO_2	46.34	46.34	43.18	45.83	44.69	42.34	42.91	43.71	44.81	44.63	41.62	44.25	44.03	42.36	43.22	40.76	41.67	43.08	42.57	42.90
TiO_2	1.11	1.06	1.30	1.01	1.07	1.21	1.12	1.02	0.91	0.89	1.06	0.86	0.85	0.92	0.85	0.97	0.89	0.79	0.79	0.76
Al_2O_3	8.94	9.05	5.73	8.70	7.58	5.18	5.88	6.81	8.04	7.92	4.88	7.66	7.49	5.85	6.78	4.35	5.32	6.79	6.33	6.70
FeO	13.65	13.17	16.33	12.88	13.72	15.77	14.76	13.58	12.19	12.07	14.55	11.87	11.82	13.01	12.03	13.84	12.85	11.51	11.71	11.26
MnO	2.21	2.11	2.59	2.02	2.13	2.43	2.25	2.05	1.82	1.78	2.13	1.72	1.70	1.85	1.69	1.93	1.78	1.58	1.59	1.52
MgO	4.43	5.49	8.29	7.69	9.38	12.13	12.59	12.70	12.37	13.20	17.03	14.79	15.60	18.13	17.63	21.25	20.61	19.23	20.35	20.30
CaO	10.03	10.00	7.85	9.61	8.81	7.19	7.55	8.08	8.81	8.67	6.59	8.38	8.21	7.05	7.63	5.91	6.53	7.49	7.13	7.35
Na_2O	3.34	3.27	3.07	3.14	3.03	2.84	2.82	2.83	2.86	2.81	2.55	2.72	2.67	2.50	2.54	2.30	2.35	2.45	2.38	2.39
K_2O	4.43	4.23	5.18	4.05	4.26	4.85	4.50	4.10	3.64	3.57	4.26	3.44	3.39	3.70	3.39	3.86	3.55	3.15	3.18	3.03
P_2O_5	5.53	5.28	6.48	5.06	5.33	6.07	5.62	5.12	4.55	4.46	5.32	4.30	4.24	4.62	4.24	4.83	4.44	3.94	3.97	3.79
H_2O	0.00	0.00	0.00	0.00	0.00	0.00	0.00	0.00	0.00	0.00	0.00	0.00	0.00	0.00	0.00	0.00	0.00	0.00	0.00	0.00
Total	100.00	100.00	100.00	100.00	100.00	100.00	100.00	100.00	100.00	100.00	100.00	100.00	100.00	100.00	100.00	100.00	100.00	100.00	100.00	100.00
Moles of Melt1	100.00	100.00	100.00	100.00	100.00	100.00	100.00	100.00	100.00	100.00	100.00	100.00	100.00	100.00	100.00	100.00	100.00	100.00	100.00	100.00
Moles of Fo $_{90}$	-10.00	-8.00	-6.00	-4.00	-2.00	0.00	2.00	4.00	6.00	8.00	10.00	12.00	14.00	16.00	18.00	20.00	22.00	24.00	26.00	28.00
Moles of An $_{70}$	0.37	2.64	-16.83	2.83	-4.19	-17.56	-13.04	-6.33	3.94	4.12	-16.06	4.26	3.93	-7.87	0.01	-16.45	-9.46	2.89	-0.19	3.99

Table 2.5. Compositions of samples in synthetic Suite D (mol. %).

	D1	D2	D3	D4	D5	D6	D7	D8	D9	D10	D11	D12	D13	D14	D15	D16	D17	D18	D19	D20
SiO_2	52.92	52.62	50.89	51.85	51.03	49.55	49.59	49.80	50.22	49.93	47.95	49.37	49.07	47.86	48.26	46.50	46.95	47.76	47.30	47.41
TiO_2	2.11	2.01	2.47	1.93	2.03	2.31	2.14	1.95	1.73	1.70	2.03	1.64	1.62	1.76	1.62	1.84	1.69	1.50	1.52	1.44
Al_2O_3	18.13	17.82	16.49	17.10	16.43	15.25	15.21	15.31	15.59	15.32	13.72	14.80	14.53	13.53	13.82	12.37	12.70	13.33	12.93	12.99
FeO	9.60	9.31	11.59	9.18	9.82	11.33	10.65	9.84	8.86	8.81	10.66	8.72	8.71	9.63	8.94	10.31	9.61	8.62	8.81	8.49
MnO	0.23	0.22	0.26	0.21	0.22	0.25	0.23	0.21	0.19	0.18	0.22	0.18	0.17	0.19	0.17	0.20	0.18	0.16	0.16	0.15
MgO	1.08	2.30	4.37	4.63	6.15	8.46	9.19	9.60	9.62	10.50	13.81	12.19	13.04	15.33	15.06	18.32	17.93	16.84	17.94	18.01
CaO	10.92	10.85	8.89	10.43	9.67	8.17	8.46	8.91	9.55	9.39	7.45	9.08	8.90	7.80	8.31	6.69	7.24	8.13	7.77	7.96
Na_2O	3.35	3.29	3.09	3.16	3.05	2.86	2.84	2.85	2.88	2.83	2.57	2.73	2.68	2.52	2.56	2.32	2.37	2.46	2.39	2.40
K_2O	1.26	1.21	1.48	1.16	1.22	1.39	1.28	1.17	1.04	1.02	1.22	0.98	0.97	1.06	0.97	1.10	1.01	0.90	0.91	0.87
P_2O_5	0.39	0.38	0.46	0.36	0.38	0.43	0.40	0.37	0.32	0.32	0.38	0.31	0.30	0.33	0.30	0.34	0.32	0.28	0.28	0.27
H_2O	0.00	0.00	0.00	0.00	0.00	0.00	0.00	0.00	0.00	0.00	0.00	0.00	0.00	0.00	0.00	0.00	0.00	0.00	0.00	0.00
Total	100.00	100.00	100.00	100.00	100.00	100.00	100.00	100.00	100.00	100.00	100.00	100.00	100.00	100.00	100.00	100.00	100.00	100.00	100.00	100.00
Moles of Melt2	100.00	100.00	100.00	100.00	100.00	100.00	100.00	100.00	100.00	100.00	100.00	100.00	100.00	100.00	100.00	100.00	100.00	100.00	100.00	100.00
Moles of Fo $_{90}$	-10.00	-8.00	-6.00	-4.00	-2.00	0.00	2.00	4.00	6.00	8.00	10.00	12.00	14.00	16.00	18.00	20.00	22.00	24.00	26.00	28.00
Moles of An $_{70}$	0.37	2.64	-16.83	2.83	-4.19	-17.56	-13.04	-6.33	3.94	4.12	-16.06	4.26	3.93	-7.87	0.01	-16.45	-9.46	2.89	-0.19	3.99

Table 2.6. Compositional vectors (moles per unit Fo90) corresponding to the serpentinization processes in suites A', A", and A'".
Values represent changes attending reaction of one unit of Fo90, as represented in Table 2.1.

	Suite A'	*Suite A"*	*Suite A'"*
	Isochemical	**SiO$_2$-gain**	**Isovolumetric**
SiO$_2$	0.00	11.11	-6.47
TiO$_2$	0.00	0.00	0.00
Al$_2$O$_3$	0.00	0.00	0.00
FeO	0.00	0.00	-2.64
MnO	0.00	0.00	0.00
MgO	0.00	0.00	-23.73
CaO	0.00	0.00	0.00
Na$_2$O	0.00	0.00	0.00
K$_2$O	0.00	0.00	0.00
P$_2$O$_5$	0.00	0.00	0.00
H$_2$O	50.00	44.44	26.87
Total	50.00	55.56	-5.97

Table 2.7. Compositions of samples in synthetic Suite A' (mol. %).

	A'1	A'2	A'3	A'4	A'5	A'6	A'7	A'8	A'9	A'10	A'11	A'12	A'13	A'14	A'15	A'16	A'17	A'18	A'19	A'20
SiO_2	46.30	46.01	45.74	45.49	45.24	45.00	44.49	44.52	44.25	43.62	42.90	42.27	42.50	41.07	40.98	39.84	40.94	41.44	42.13	39.79
TiO_2	1.11	1.09	1.06	1.04	1.02	1.00	0.97	0.96	0.94	0.92	0.89	0.86	0.86	0.82	0.80	0.77	0.78	0.78	0.79	0.73
Al_2O_3	8.89	8.70	8.51	8.33	8.16	8.00	7.79	7.69	7.53	7.32	7.10	6.90	6.85	6.53	6.43	6.17	6.26	6.25	6.28	5.86
FeO	13.70	13.55	13.40	13.26	13.13	13.00	12.80	12.75	12.62	12.38	12.13	11.90	11.92	11.48	11.41	11.05	11.32	11.42	11.57	10.89
MnO	2.22	2.17	2.13	2.08	2.04	2.00	1.95	1.92	1.88	1.83	1.78	1.73	1.71	1.63	1.61	1.54	1.56	1.56	1.57	1.46
MgO	4.44	5.65	6.81	7.92	8.98	10.00	10.91	11.92	12.81	13.54	14.20	14.84	15.75	15.99	16.71	16.96	18.15	19.08	20.10	19.63
CaO	10.00	9.78	9.57	9.38	9.18	9.00	8.77	8.65	8.47	8.24	7.99	7.76	7.70	7.34	7.23	6.94	7.04	7.04	7.07	6.59
Na_2O	3.33	3.26	3.19	3.13	3.06	3.00	2.92	2.88	2.82	2.75	2.66	2.59	2.57	2.45	2.41	2.31	2.35	2.35	2.36	2.20
K_2O	4.44	4.35	4.26	4.17	4.08	4.00	3.90	3.84	3.77	3.66	3.55	3.45	3.42	3.26	3.21	3.08	3.13	3.13	3.14	2.93
P_2O_5	5.56	5.43	5.32	5.21	5.10	5.00	4.87	4.80	4.71	4.58	4.44	4.31	4.28	4.08	4.02	3.86	3.91	3.91	3.93	3.66
H_2O	0.00	0.00	0.00	0.00	0.00	0.00	0.62	0.06	0.19	1.17	2.36	3.39	2.44	5.35	5.19	7.47	4.57	3.05	1.08	6.26
Total	100.00	100.00	100.00	100.00	100.00	100.00	100.00	100.00	100.00	100.00	100.00	100.00	100.00	100.00	100.00	100.00	100.00	100.00	100.00	100.00
Moles of Fo_{90}	0.00	0.00	0.00	0.00	0.00	0.00	2.00	4.00	6.00	8.00	10.00	12.00	14.00	16.00	18.00	20.00	22.00	24.00	26.00	28.00
Extent of reaction (%)	NA	NA	NA	NA	NA	NA	63.85	3.36	6.88	31.96	53.09	65.44	40.76	82.00	71.84	96.86	53.13	32.51	10.56	61.10

Table 2.8. Compositions of samples in synthetic Suite A" (mol. %).

	A"1	A"2	A"3	A"4	A"5	A"6	A"7	A"8	A"9	A"10	A"11	A"12	A"13	A"14	A"15	A"16	A"17	A"18	A"19	A"20
SiO_2	46.30	46.01	45.74	45.49	45.24	45.00	44.60	44.53	44.29	43.82	43.31	42.86	42.93	42.01	41.89	41.16	41.74	41.97	42.32	40.90
TiO_2	1.11	1.09	1.06	1.04	1.02	1.00	0.97	0.96	0.94	0.91	0.89	0.86	0.85	0.81	0.80	0.76	0.78	0.78	0.78	0.73
Al_2O_3	8.89	8.70	8.51	8.33	8.16	8.00	7.79	7.69	7.53	7.31	7.08	6.88	6.83	6.49	6.39	6.12	6.23	6.23	6.27	5.82
FeO	13.70	13.55	13.40	13.26	13.13	13.00	12.79	12.75	12.61	12.37	12.10	11.86	11.89	11.41	11.34	10.96	11.26	11.38	11.55	10.81
MnO	2.22	2.17	2.13	2.08	2.04	2.00	1.95	1.92	1.88	1.83	1.77	1.72	1.71	1.62	1.60	1.53	1.56	1.56	1.57	1.45
MgO	4.44	5.65	6.81	7.92	8.98	10.00	10.90	11.91	12.80	13.53	14.17	14.78	15.70	15.90	16.62	16.82	18.06	19.01	20.07	19.49
CaO	10.00	9.78	9.57	9.38	9.18	9.00	8.76	8.65	8.47	8.23	7.97	7.73	7.68	7.30	7.19	6.88	7.00	7.01	7.06	6.55
Na_2O	3.33	3.26	3.19	3.13	3.06	3.00	2.92	2.88	2.82	2.74	2.66	2.58	2.56	2.43	2.40	2.29	2.33	2.34	2.35	2.18
K_2O	4.44	4.35	4.26	4.17	4.08	4.00	3.89	3.84	3.77	3.66	3.54	3.44	3.41	3.24	3.20	3.06	3.11	3.12	3.14	2.91
P_2O_5	5.56	5.43	5.32	5.21	5.10	5.00	4.87	4.80	4.71	4.57	4.43	4.30	4.27	4.06	3.99	3.82	3.89	3.90	3.92	3.64
H_2O	0.00	0.00	0.00	0.00	0.00	0.00	0.55	0.06	0.17	1.04	2.09	3.00	2.16	4.73	4.59	6.58	4.04	2.70	0.96	5.53
Total	100.00	100.00	100.00	100.00	100.00	100.00	100.00	100.00	100.00	100.00	100.00	100.00	100.00	100.00	100.00	100.00	100.00	100.00	100.00	100.00
Moles of Fo_{90}	0.00	0.00	0.00	0.00	0.00	0.00	2.00	4.00	6.00	8.00	10.00	12.00	14.00	16.00	18.00	20.00	22.00	24.00	26.00	28.00
Extent of reaction (%)	NA	NA	NA	NA	NA	NA	63.85	3.36	6.88	31.96	53.09	65.44	40.76	82.00	71.84	96.86	53.13	32.51	10.56	61.10

Table 2.9. Compositions of samples in synthetic Suite A''' (mol. %).

	A'''1	A'''2	A'''3	A'''4	A'''5	A'''6	A'''7	A'''8	A'''9	A'''10	A'''11	A'''12	A'''13	A'''14	A'''15	A'''16	A'''17	A'''18	A'''19	A'''20
SiO_2	46.30	46.01	45.74	45.49	45.24	45.00	44.72	44.55	44.32	44.04	43.75	43.48	43.37	42.95	42.79	42.42	42.52	42.49	42.51	41.92
TiO_2	1.11	1.09	1.06	1.04	1.02	1.00	0.98	0.96	0.94	0.93	0.91	0.90	0.88	0.87	0.85	0.84	0.82	0.81	0.79	0.79
Al_2O_3	8.89	8.70	8.51	8.33	8.16	8.00	7.85	7.69	7.55	7.42	7.29	7.17	7.04	6.94	6.82	6.73	6.60	6.48	6.36	6.30
FeO	13.70	13.55	13.40	13.26	13.13	13.00	12.85	12.75	12.63	12.49	12.33	12.19	12.13	11.91	11.82	11.63	11.67	11.65	11.65	11.35
MnO	2.22	2.17	2.13	2.08	2.04	2.00	1.96	1.92	1.89	1.85	1.82	1.79	1.76	1.74	1.71	1.68	1.65	1.62	1.59	1.58
MgO	4.44	5.65	6.81	7.92	8.98	10.00	10.69	11.89	12.74	13.16	13.44	13.75	15.00	14.31	15.13	14.64	16.84	18.25	19.83	17.91
CaO	10.00	9.78	9.57	9.38	9.18	9.00	8.83	8.65	8.49	8.35	8.21	8.07	7.92	7.81	7.68	7.57	7.42	7.29	7.15	7.09
Na_2O	3.33	3.26	3.19	3.13	3.06	3.00	2.94	2.88	2.83	2.78	2.74	2.69	2.64	2.60	2.56	2.52	2.47	2.43	2.38	2.36
K_2O	4.44	4.35	4.26	4.17	4.08	4.00	3.92	3.85	3.77	3.71	3.65	3.59	3.52	3.47	3.41	3.37	3.30	3.24	3.18	3.15
P_2O_5	5.56	5.43	5.32	5.21	5.10	5.00	4.91	4.81	4.72	4.64	4.56	4.48	4.40	4.34	4.27	4.21	4.12	4.05	3.97	3.94
H_2O	0.00	0.00	0.00	0.00	0.00	0.00	0.34	0.03	0.10	0.64	1.30	1.89	1.35	3.06	2.96	4.38	2.59	1.70	0.59	3.62
Total	100.00	100.00	100.00	100.00	100.00	100.00	100.00	100.00	100.00	100.00	100.00	100.00	100.00	100.00	100.00	100.00	100.00	100.00	100.00	100.00
Moles of Fo_{90}	0.00	0.00	0.00	0.00	0.00	0.00	2.00	4.00	6.00	8.00	10.00	12.00	14.00	16.00	18.00	20.00	22.00	24.00	26.00	28.00
Extent of reaction (%)	NA	NA	NA	NA	NA	NA	63.85	3.36	6.88	31.96	53.09	65.44	40.76	82.00	71.84	96.86	53.13	32.51	10.56	61.10

concentrations in tables 2.2-2.5 are molar proportions (X_R) in percent form. Equation 2.1 represents the contribution of each phase to the moles of a given oxide, whereas Equation 2.2 takes the resulting molar amounts and converts them to fractions; this equation takes the data from extensive form to intensive form (i.e., induces closure).

2.2.2. The altered suites

The altered suites represent three different serpentinization reactions acting upon the synthetic rocks of Suite A. In all cases, the only phase that alters is Fo_{90}. For those synthetic rocks that represent liquids formed by *removal* of olivine, I treated these rocks as having no olivine to serpentinize and therefore they remain unaltered.

The three serpentinization processes in the synthetic suites are: (1) *isochemical* hydration (Equation 2.3; Hostetler et al., 1966; O'Hanley, 1992; O'Hanley, 1996; Shervais et al., 2005; Frost et al., 2013), whereby the rock neither gains nor loses any component other than H_2O; (2) serpentinization by *silica addition* (Equation 2.4), whereby the rock gains H_2O and SiO_2; and (3) *isovolumetric* serpentinization (Equation 2.5; Hostetler et al., 1966; Thayer, 1966; O'Hanley, 1992; Stripp et al., 2006), whereby the rock maintains constant volume, gains H_2O, and loses SiO_2, MgO, and FeO, per the thermodynamic calculations of Turner and Verhoogen (1960; as cited by Hostetler et al., 1966) for the Mg end-members. Each of these reactions is a simplification of natural serpentinization, which might involve losses of MgO and FeO, at fixed SiO_2 to achieve the stoichiometry of serpentine. Moreover, serpentinization involves formation of magnetite by oxidation of Fe^{2+}, which I do not consider here. The purpose of restricting the alteration suites to the above reactions is to minimize the number of synthetic suites whilst exploring the geochemical expression of distinct serpentinization reactions. Schematic reactions that correspond to these processes are:

$$2Mg_{1.8}Fe_{0.2}SiO_4 + 3H_2O \rightarrow Mg_{2.7}Fe_{0.3}Si_2O_5(OH)_4 + Mg_{0.9}Fe_{0.1}(OH)_2 \,, \qquad (2.3)$$

Olivine   **Fluid**   **Serpentine**   **Brucite**

$$3Mg_{1.8}Fe_{0.2}SiO_4 + 4H_2O + SiO_2 \rightarrow 2Mg_{2.7}Fe_{0.3}Si_2O_5(OH)_4 \,, \qquad (2.4)$$

Olivine   **Fluid**   **Aq.**   **Serpentine**

and

$$2Mg_{1.8}Fe_{0.2}SiO_4 + 1.61H_2O \rightarrow \ 0.81Mg_{2.7}Fe_{0.3}Si_2O_5(OH)_4 + 0.39SiO_2 \qquad (2.5)$$

Olivine **Fluid** **Serpentine** **Aq.**

$$+ \ 1.41MgO + 0.16FeO.$$
Aq. **Aq.**
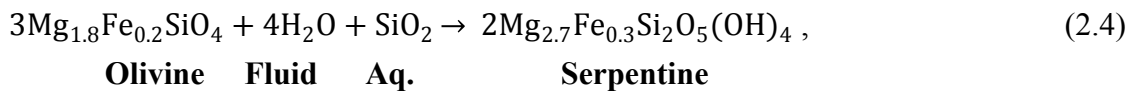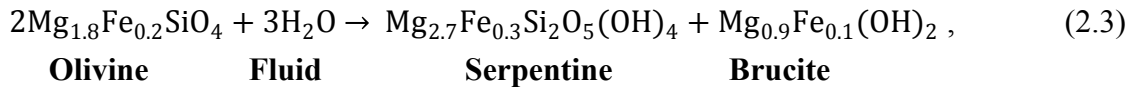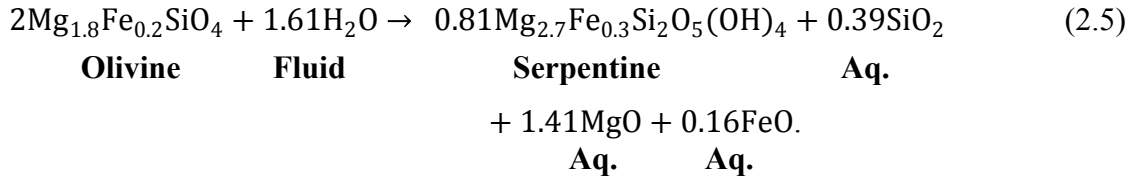
The ratios of Mg-Fe in the products and reactants are identical, because I chose the same Mg:Fe (9:1) in all reaction products containing these elements for simplicity.

The altered suites A', A'', and A''' represent equations 2.3, 2.4, and 2.5, respectively. Compositions result of the basic expression

$$N_R^i = N_{RA}^i + rp^*N_F^*\Delta N_{rxn}^i \, , \qquad (2.6)$$

where *RA* refers to the original rock from Suite A, *rp* is the extent of reaction progress (from 0 to 1, generated randomly) and ΔN_{rxn} is net transfer of the oxide resulting from reaction of one unit of Fo_{90}. The concentrations of each oxide derive from Equation 2.2. Table 2.6 gives the net transfer resulting from reaction of one hundred units of Fo_{90}, with Fo_{90} of having a mole percent basis as in Table 2.1. Tables 2.7 through 2.9 show the compositions of the altered suites.

2.3. Variation diagrams

Variation diagrams (Harker, 1909), or Harker diagrams, plot whole rock compositions as concentrations of one oxide (typically SiO_2) against one or more other oxides, here in units of mole percent.

2.3.1. The igneous suites

Figure 2.2 shows variation diagrams for each of the synthetic igneous suites. Suites A and B (Fig. 2.2 A, B), which represent sorting of olivine in a melt, both show linear relationships between SiO_2 and other oxides. All oxides except MgO positively correlate with SiO_2. Conserved oxides (all but MgO, FeO, and SiO_2 in these suites) all have positive slopes whose magnitudes correlate with the abundance of the species. Each of these trends intersects the x-axis at 33.33% SiO_2, corresponding precisely to the SiO_2 concentration in olivine. Unconserved FeO also has a positive slope, but does not share
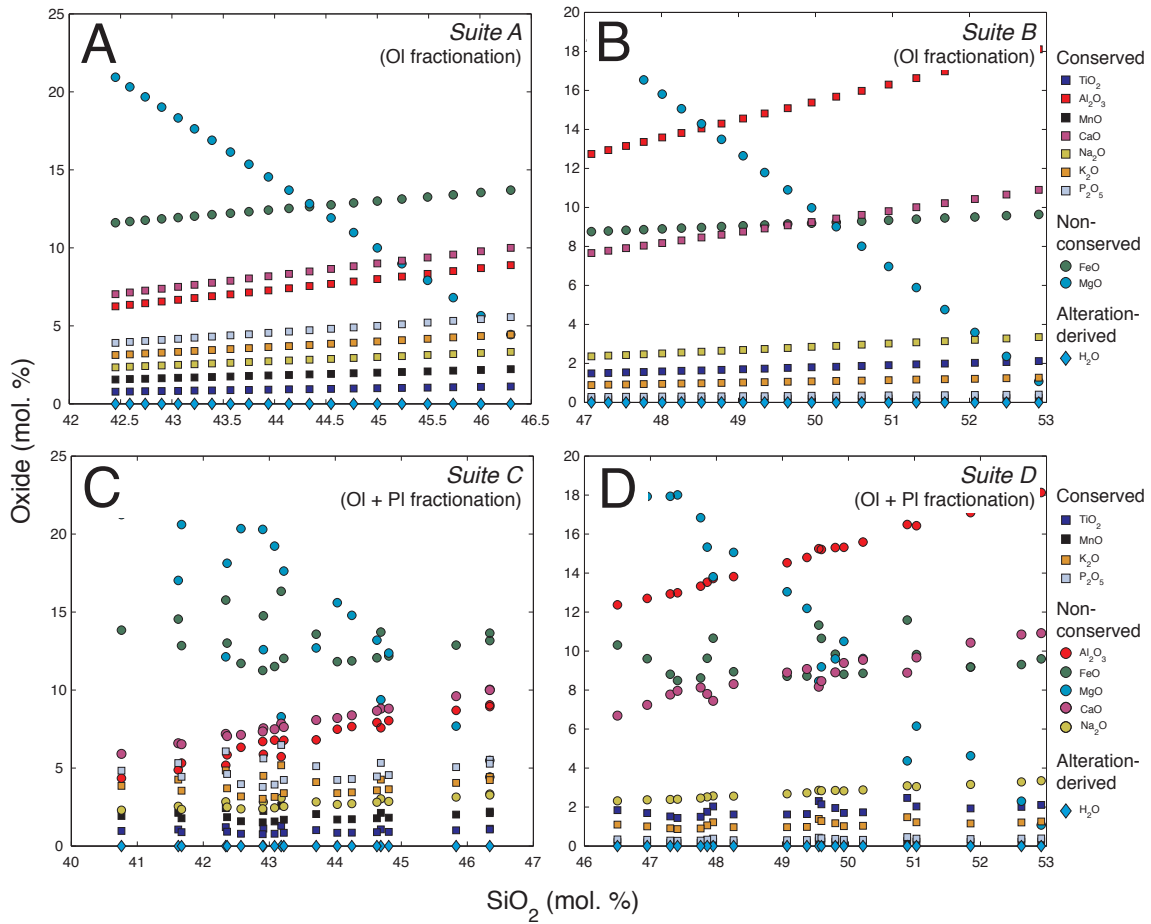
Figure 2.2. Variation (Harker) diagrams of mole % SiO$_2$ versus all other oxides in the synthetic igneous datasets A through D. Panels **A** and **B** show suites A and B, representing olivine sorting. Panels **C** and **D** show suites C and D, representing independent fractionation/accumulation of olivine and plagioclase.

24

an intercept with the conserved oxides. Unconserved MgO negatively correlates with SiO_2.

Suites C and D (Fig. 2.2 C, D), which are equivalent to A and B save for the imposition of a plagioclase sorting signal, have different trends from suites A and B. In broad terms the trends are similar, particularly in that MgO is the only oxide having a distinct inverse relationship with SiO_2. However, no oxide shows a perfect linear relationship with SiO_2. In some cases, unconserved oxides are less variable than conserved ones, whereas other unconserved oxides are more variable. Na_2O closely mimics the conserved oxides, and CaO and Al_2O_3 both show tighter linear trends than do some conserved oxides. Indeed, the apparent near-linearity of the conserved species mainly results from the scale of the y-axis relative to their small magnitudes.

Trends in suites A and B show that in a binary geochemical system, the x-intercept of conserved components on a standard variation diagram reveals the SiO_2 content of the fractionating phase. Comparison to suites C and D shows that the additional dimension of complexity obscures that relationship.

Comparison of the trends of suites A and B, and suites C and D, shows that action of the identical mass transfer processes upon different bulk compositions produces contrasting variation diagrams, including changes such as slopes (in the case of A and B) or the general patterns of the distribution of different oxides (cf. Al_2O_3, CaO, FeO, and MgO in Figure 2.2 C and D).

2.3.2. *The altered suites*

Figure 2.3 shows variation diagrams for suites A' through A'''. For each altered suite, the trends are similar to those in the parental Suite A. The main differences are that the exact linearity of the trends is absent and H_2O is present in the altered samples. In each altered suite, the most conspicuously disturbed trend is that of MgO. Where present, H_2O generally correlates negatively with SiO_2. All conserved oxides deviate from a linear relationship with SiO_2, and thus they do not define a unique x-intercept. The trend of FeO, which is not conserved, resembles the trends of the conserved elements more closely than that of MgO, despite their variation being precisely linked in both the Fo_{90} sorting and serpentinization processes.
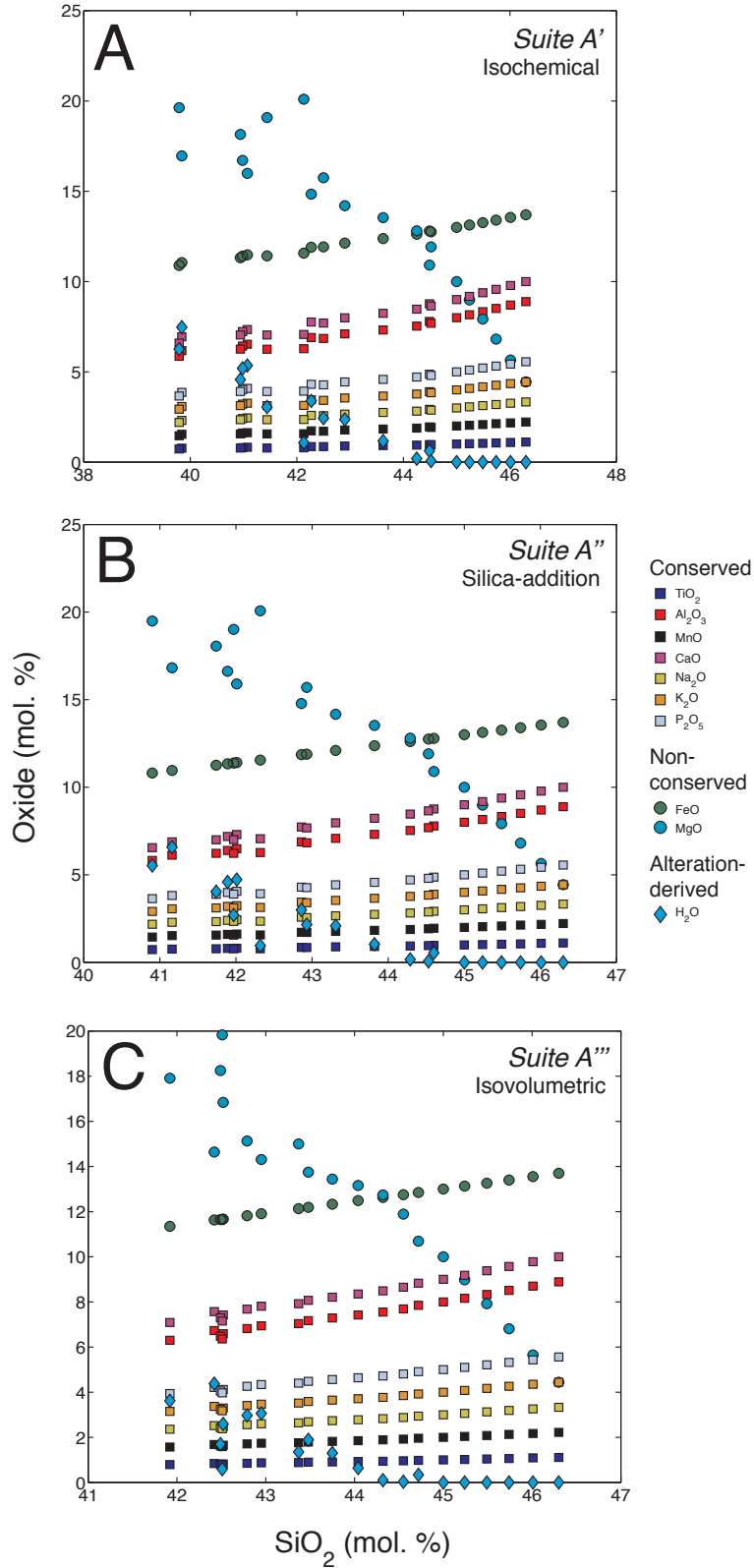
Figure 2.3. Variation (Harker) diagrams of mole % SiO_2 versus all other oxides in the altered datasets. **A** – Suite A'. **B** – Suite A''. **C** – Suite A'''.

Comparison of suites A', A'', and A''' reveals subtle differences in the abundances of each oxide, and thus some modification of the parental trends. However, the general tendencies of each oxide remain similar, and the different serpentinization reactions are not evident from inspection and comparison of the diagrams.

2.4. Molar element ratio diagrams

Molar element ratio diagrams (Pearce, 1968), also known as Pearce element ratio (PER) diagrams, are a method of recovering extensive chemical changes and testing specific mass transfer hypotheses using whole rock compositions. The premise of the method is that molar ratios of elements conserved in mass transfer processes do not change, even in intensive whole rock compositions. In contrast, the ratio of an unconserved element to a conserved one changes according to the stoichiometry of the mass transfer process and its magnitude in extensive space. Thus, the power of PER analysis is that it reveals stoichiometric controls on and true extensive relationships in geochemical datasets, and enables the design of diagrams to rigorously test for hypothetical processes of known stoichiometry (Pearce, 1987; Ernst et al., 1988; Russell and Nicholls, 1988; Russell et al., 1990; Russell and Stanley, 1990a).

As stoichiometry of geochemical processes controls the extensive movement of elements in nature, PER analysis is useful for testing not only mineral sorting processes, but also chemical reactions that produce compositional diversity. The three serpentinization reactions (reactions 2.4, 2.5, and 2.6) in the synthetic suites should modify the PER relationships in accordance with their net transfer stoichiometry.

2.4.1. The igneous suites

Figure 2.4 shows the PER equivalent of the variation diagrams in Figure 2.2. In these diagrams, changes in Si/Ti plot against the ratio of every other element to Ti, one of the known conserved elements. In each suite, every conserved element does not vary with Si. In suites A and B, Mg and Fe have positive linear slopes corresponding to Mg/Si and Fe/Si in Fo_{90}. In suites C and D, where An_{70} and Fo_{90} sorting contribute independently to the variation, the ratios of Mg, Fe, Ca, Na, and Al to Ti are each variable, whereas those of the elements absent from An_{70} and Fo_{90} are invariant. However, in suites C and D the
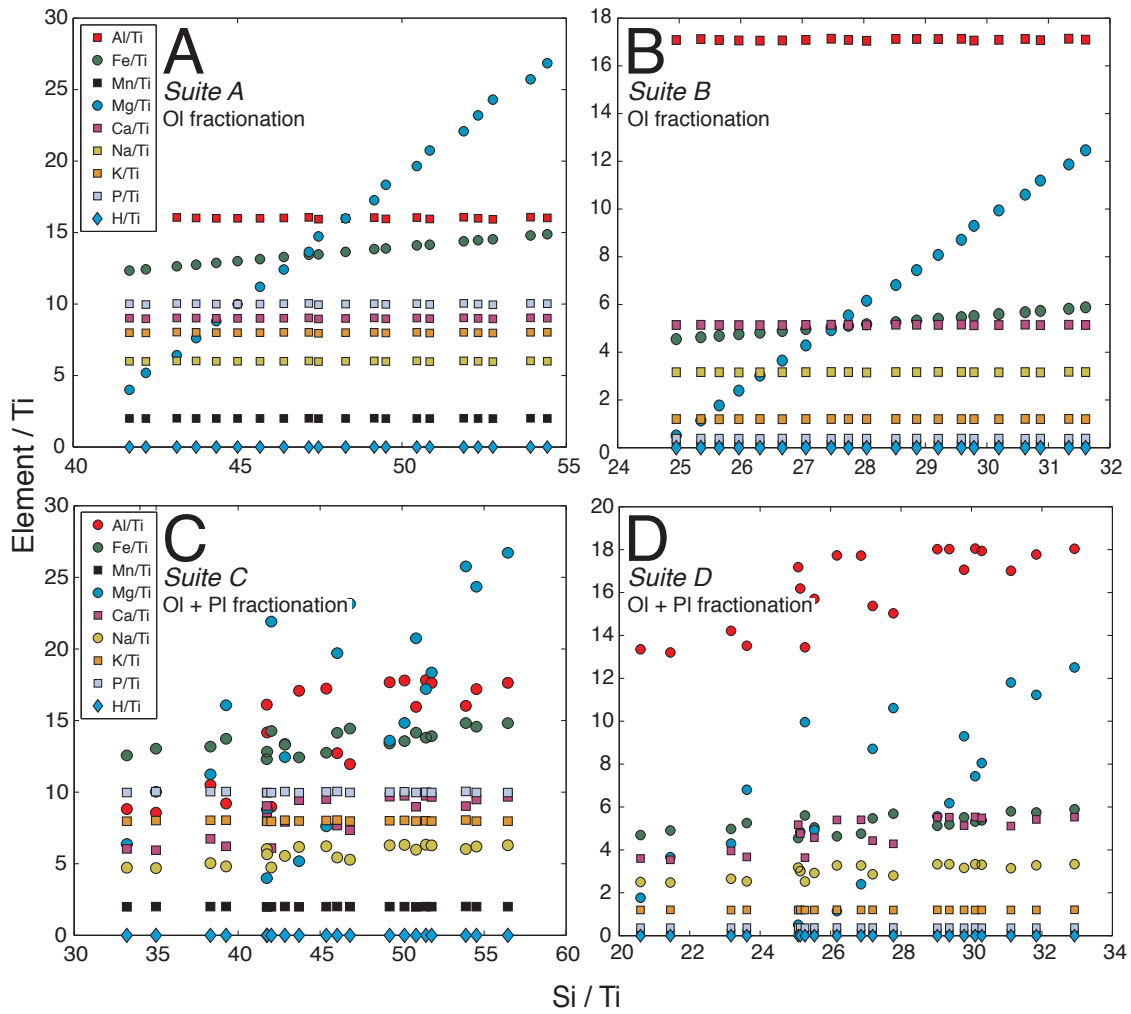
Figure 2.4. Molar (Pearce) element ratio diagrams comparing Si/Ti to [other element]/Ti in the synthetic igneous datasets. **A** – Suite A. **B** – Suite B. **C** – Suite C. **D** – Suite D.

stoichiometric relationships of the mobile species to Si are unclear, owing to the distribution of Si between three phases (melt, Fo_{90}, and An_{70}).

Figure 2.5 shows the synthetic datasets A through D plotted on two different PER diagrams. The first diagram (Fig. 2.5 A) tests for olivine sorting by plotting Si / Ti against (Mg + Fe) / Ti (Pearce, 1987; Russell and Nicholls, 1988). Suites A and B define lines with slopes of two, identical to olivine stoichiometry, and so the diagram permits olivine sorting. A suite of randomly generated data with the same range of oxide concentrations as Suite A, included to test for random correlation of ratios (Rollinson and Roberts, 1987), plots as a field in the vicinity of the Suite A data, but fails to define any obvious trend, apart from perhaps a vague covariance. Suites C and D, which represent olivine sorting *and* completely decoupled plagioclase sorting, similarly fail the test. Olivine sorting alone cannot explain the variations in Suite C or Suite D.

Figure 2.5 B shows a diagram designed to test for the action of olivine *and/or* plagioclase sorting, with both processes producing a slope of one. Each synthetic dataset plots with a slope of one except for the random data, which define a broadly co-varying cloud of points about the data from Suite A. Thus, the PER approach portrays the igneous suites as theory predicts, and robustly tests for specific stoichiometric processes.

2.4.2. The altered suites

Figure 2.6 shows the same PER diagram as Figure 2.4, but for the altered datasets. Each dataset shows positive correlations between Si/Ti and Mg/Ti, Fe/Ti, and H/Ti. The differences in the trends for the three distinct chemical reactions are minimal in this diagram.

The subtle nature of modification of the trends in Figure 2.6 might lead one to hypothesize that hydration of each dataset occurred isochemically. Pearce element ratios enable a definitive test. Assuming we have already established that olivine sorting is the only significant mass transfer process in the protolith suite, we can test the isochemical model by using the same element ratio diagram as in Figure 2.5 A. In that diagram, isochemically hydrated rocks would share the same slope as their protolith, whereas any process involving coupled hydration and mobilization of other components would deviate from it. Figure 2.7 A shows the altered suites and their protolith suite on this diagram.
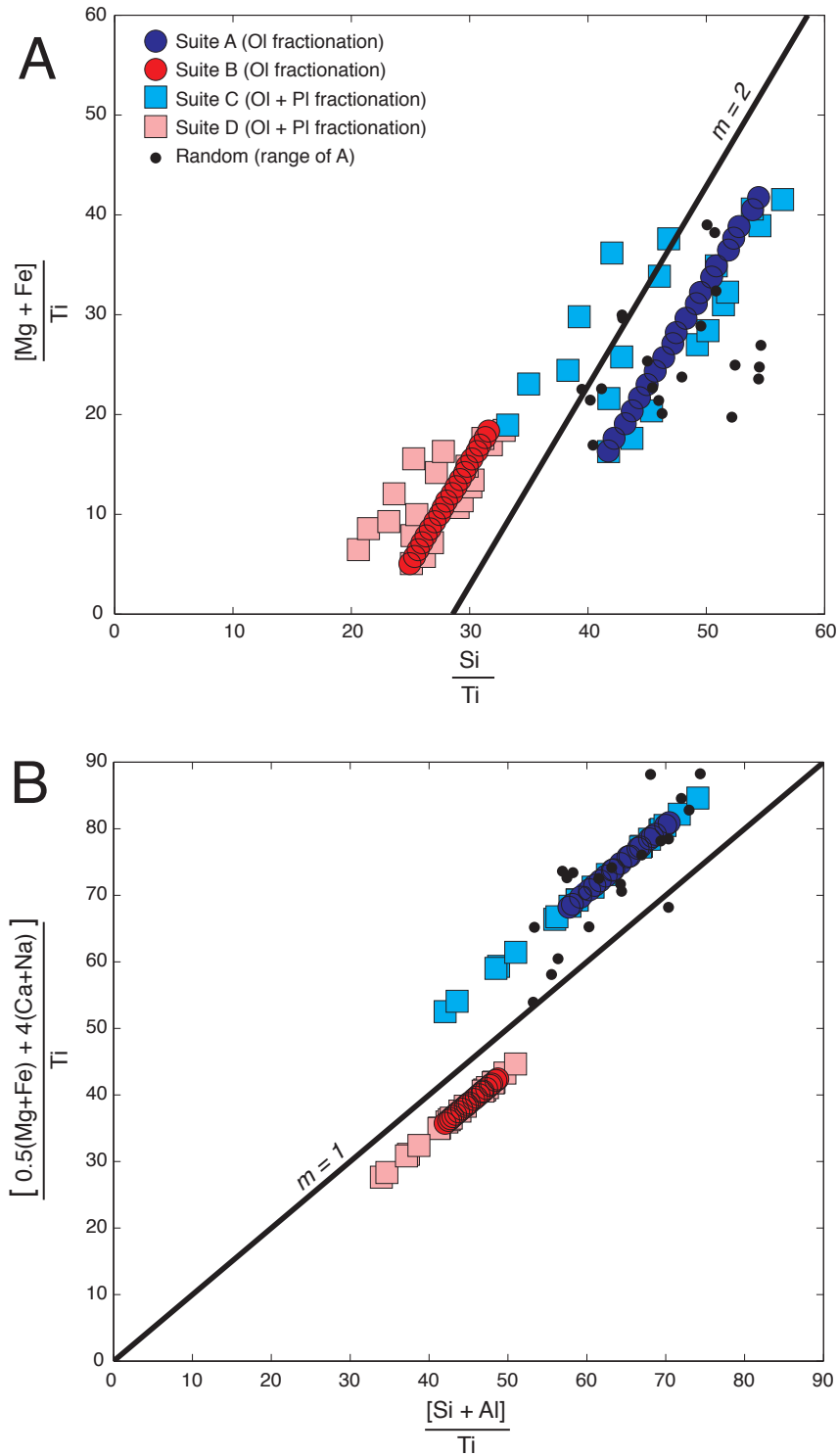
Figure 2.5. Molar (Pearce) element ratio diagrams testing for the action of crystal accumulation/fractionation processes in datasets A through D. **Panel A** shows a diagram designed to test for sole action of olivine sorting, which produces a slope of 2. **Panel B** shows a diagram that places sorting of plagioclase and/or olivine along a line with a slope of 1, testing for the action of either or both of those processes.
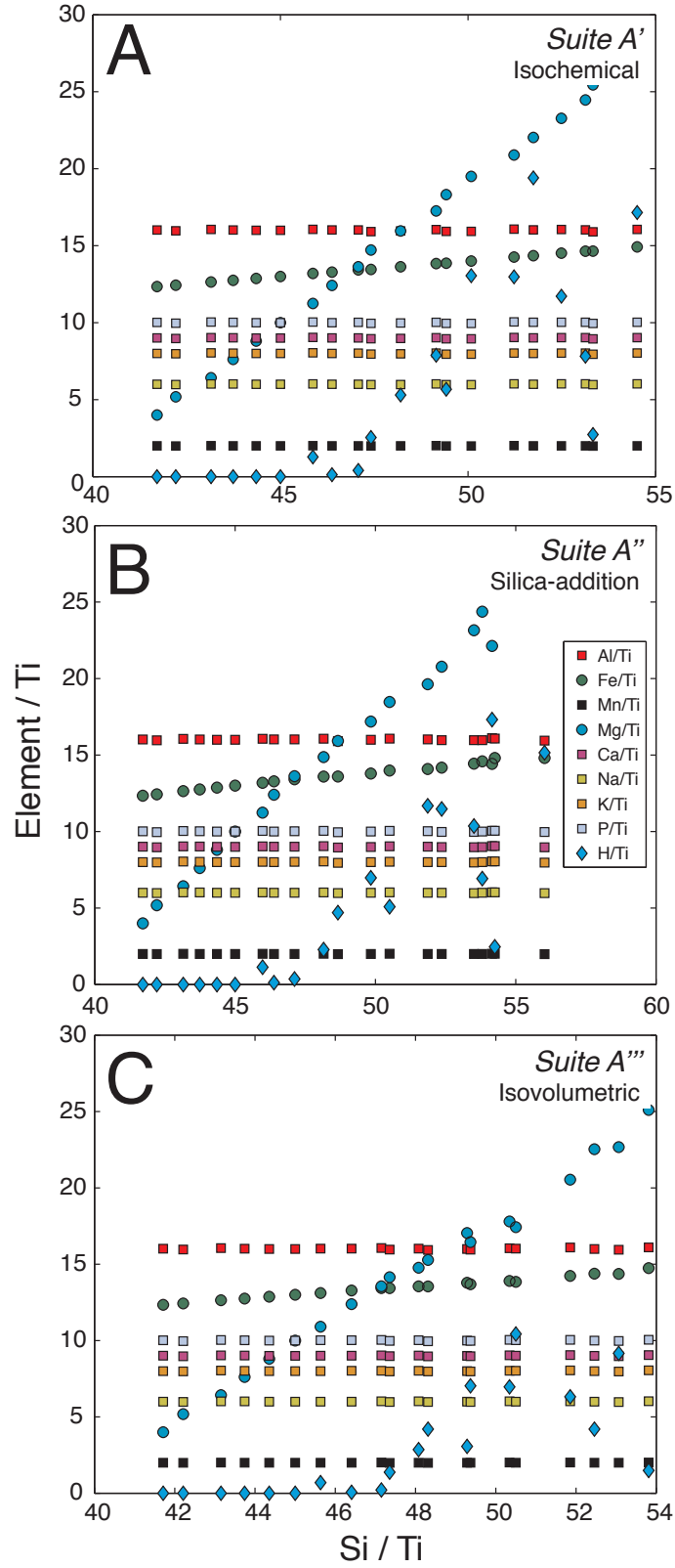
Figure 2.6. Molar (Pearce) element ratio diagrams comparing Si/Ti to [other element]/Ti in the altered datasets. **A** – Suite A'. **B** – Suite A''. **C** – Suite A'''.

31
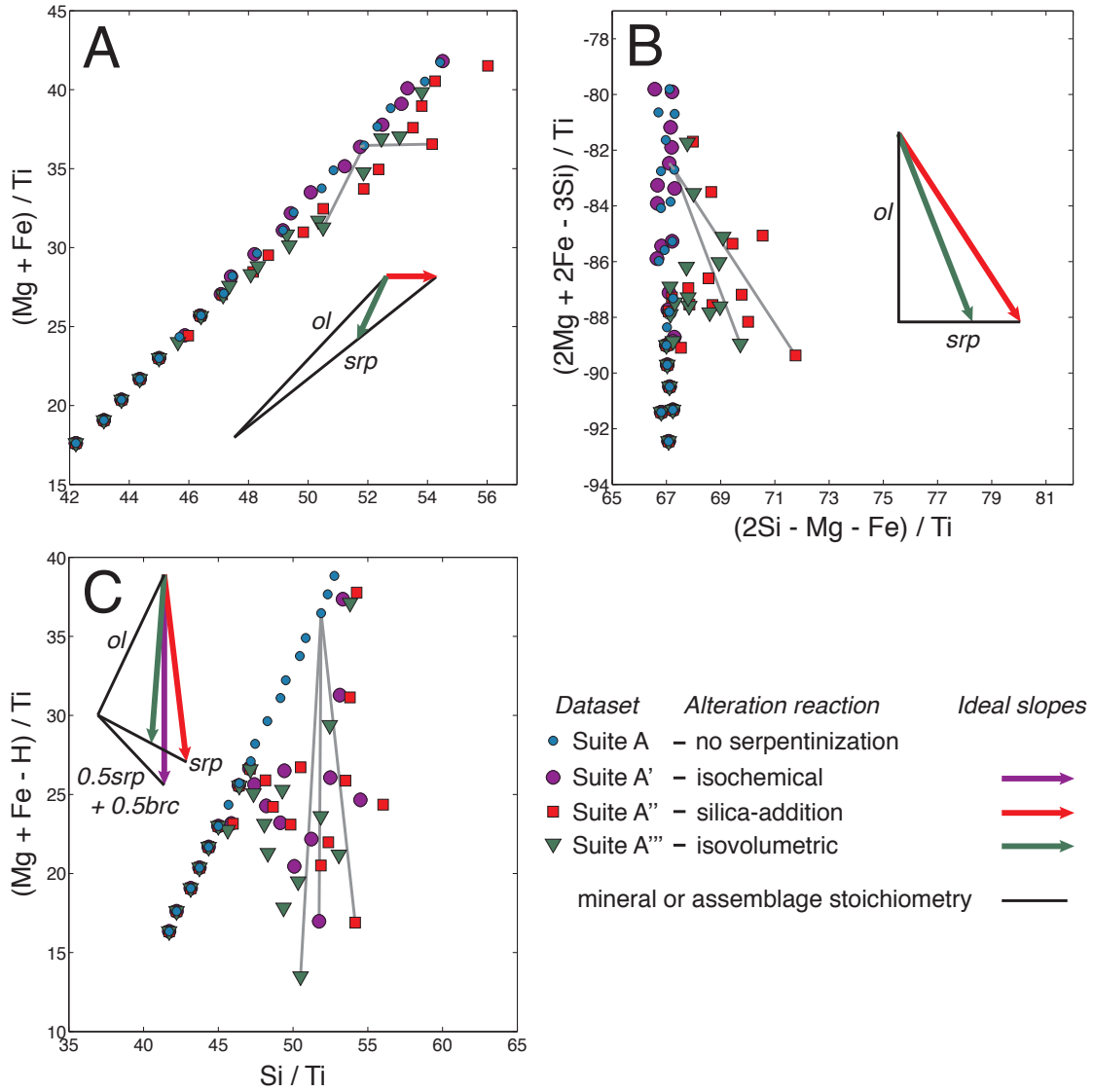
Figure 2.7. Molar (Pearce) element ratio diagrams testing for the action of different serpentinization reactions in the altered datasets A', A'', and A''', and the parental Suite A. Each panel shows the four datasets, stoichiometric trends, and tie lines connecting the most altered sample in each suite (i.e., A'16, A''16, A'''16) with their protolith (A16). **Panel A** shows the same diagram as in Figure 2.4 A, where olivine sorting produces a slope of 2. **Panel B** shows a diagram that places stoichiometric trends of olivine and serpentine at right angles to one another. **Panel C** shows a diagram that places stoichiometric trends of olivine and serpentine at right angles to one another, and distinguishes alteration by any of the reactions from the primary suite.

Suite A (protolith) and Suite A' (isochemical hydration) define the same line with a slope of two. Suites A'' and A''' deviate from that starting point, plotting in a field constrained by the trend of the protolith suite, and a serpentine-control line that extends from the location of the parental liquid. Complete reaction of the olivine-bearing samples in these suites would place all altered samples on the serpentine control line.

The diagram falsifies the hypothesis that suites A'' and A''' underwent isochemical hydration. An alternative diagram that puts the ultimate consequence of metasomatic (i.e., non-isochemical) serpentinization at a high angle to the initial trend more clearly portrays the deviations (Figure 2.7 B). Incorporation of the H in the diagram axes enables ready distinction of fresh rocks from the serpentinized (Figure 2.7 C). In each of these diagrams, the altered samples connect to their protoliths by a line whose slope is determined by the reaction (shown only for the most altered sample). However, recognition of this slope without prior knowledge of the protolith composition prevents forensic determination of the reaction.

2.5. Isocon analysis

Isocon analysis (Grant, 1986) is a method designed for comparison of altered rocks to their protoliths. The method was developed as a readily applicable alternative to Gresens' approach to metasomatism, wherein relationships between rock or mineral volume and composition constrain extents of mass and volume modification (Gresens, 1967). Grant (1986) recognized that Gresens' approach was fundamentally about mass changes. He thus developed the isocon method to enable straightforward quantitative identification of mass changes for all elements between a protolith and its altered equivalent using whole rock geochemical data, without requiring the specific gravities of the minerals and rocks in question.

If we consider a protolith and its altered equivalent rock, some elements may have been lost or gained during the alteration. Any or all of the oxide or element concentrations may vary as a consequence of the mobility of a mere subset of those components, owing to closure. However, variation of the concentrations of conserved species maintains a fixed ratio between each conserved component in the protolith and altered rock. Thus, the common principle between isocon analysis and the PER approach

is that conserved components retain their mutual relationships during mass transfer, despite modification of their concentration in the resultant rock. The isocon approach is to plot the concentrations of all oxides or elements in the altered rock against those of the protolith. The property of the constant ratios of conserved elements between the two rocks requires that they define a line extending from the origin (the *isocon,* or line of conservation). Components plotting above the line increased during alteration and those plotting below decreased, with increasing displacement from the isocon representing the magnitude of the gain or loss. The original description and prescription of the method was for comparing pairs of samples, although some works have compared larger suites in individual diagrams (examples in Grant, 2005).

A later study expanded the applicability of isocon analysis from pairs of protolith and altered samples to entire suites of whole rock compositions (Guo et al., 2009). These workers recognized that every pairing of protolith and altered sample has a different isocon, precluding sound application of the standard diagram to suites of samples. They devised an arbitrary normalization procedure wherein every component of each rock is scaled so that each sample has the same amount of a conserved component. Plotting these scaled compositions on the standard isocon diagram produces a single isocon with a slope of one that passes through the origin, for all samples. This arbitrary normalization is mathematically equivalent to calculating PERs, except that in the latter, division by the conserved component normalizes that component to one, rather than some arbitrary number. Thus, Guo et al.'s (2009) modification of the isocon merges it with PERs.

The isocon approach is applicable in the investigation of any mass transfer process, not just metasomatism or alteration. I apply it to the synthetic igneous suites and altered suites alike, and refer to the x-axis sample as the *reference rock* instead of protolith.

2.5.1. The igneous suites
In the interest of concision and clarity, the foregoing description and figure show only the data from Suite A. However, the points apply equally to each of the datasets (Figure A1, Appendix A1).

Figure 2.8 A shows the isocon diagram for samples A1 and A20, the least and most magnesian samples in the suite, respectively. All conserved oxides define a line intersecting the origin. The unconserved oxides (SiO_2, MgO, FeO) lie above the line of conservation, correctly identifying these constituents as those that define the compositional difference between samples A1 and A20. The degree to which each oxide plots away from the isocon corresponds to the relative amounts of each added to sample A20 with respect to A1, and their proportions correspond to the stoichiometry of Fo_{90}.

Figures 2.8 B and C show the same diagram (at two scales), except that they show samples A2 through A20 on the y-axis. The conserved species in these diagrams now fail to define a single isocon (Guo et al., 2009). Instead, each pair of samples defines its own unique isocon – each one being valid for comparison to sample A1 (the x-axis sample) – resulting in a fan of potential conservation defined by the uppermost and lowermost isocons. Although MgO plots well outside of this field, the other unconserved components SiO_2 and FeO are entirely within it. Thus, plotting whole suites of data on a single isocon diagram could lead to the erroneous interpretation that FeO and SiO_2 were conserved species. Plotting instead the PER equivalent to the isocon diagram, or an arbitrarily scaled one (Guo et al., 2009), remedies the multiple isocon problem and restores the true stoichiometric relationships (Figure 2.8 D). A still clearer representation of compositional change follows subtraction (negative translation) of the reference rock composition (in PER form) from each rock composition (also in PER form). Plotting these translated ratios as categories on x and magnitudes on y produces a spider diagram-like figure in which the y-axis records amounts of an element added (or removed) with respect to the reference vector, per amount of the conserved component (Figure 2.8 E).

2.5.2. The altered suites

Figure 2.9 shows isocon diagrams for the most altered sample (sample A*16) in each suite and their protolith. Each diagram correctly identifies the conserved and mobile species during reaction, although the deflections from the isocon are subtle, verging on unrecognizable for Fe and Si. The ratios of the displacements from the isocon determine the stoichiometry of the reaction and are clearest in the translated ratio diagram in Figure 2.9 D.
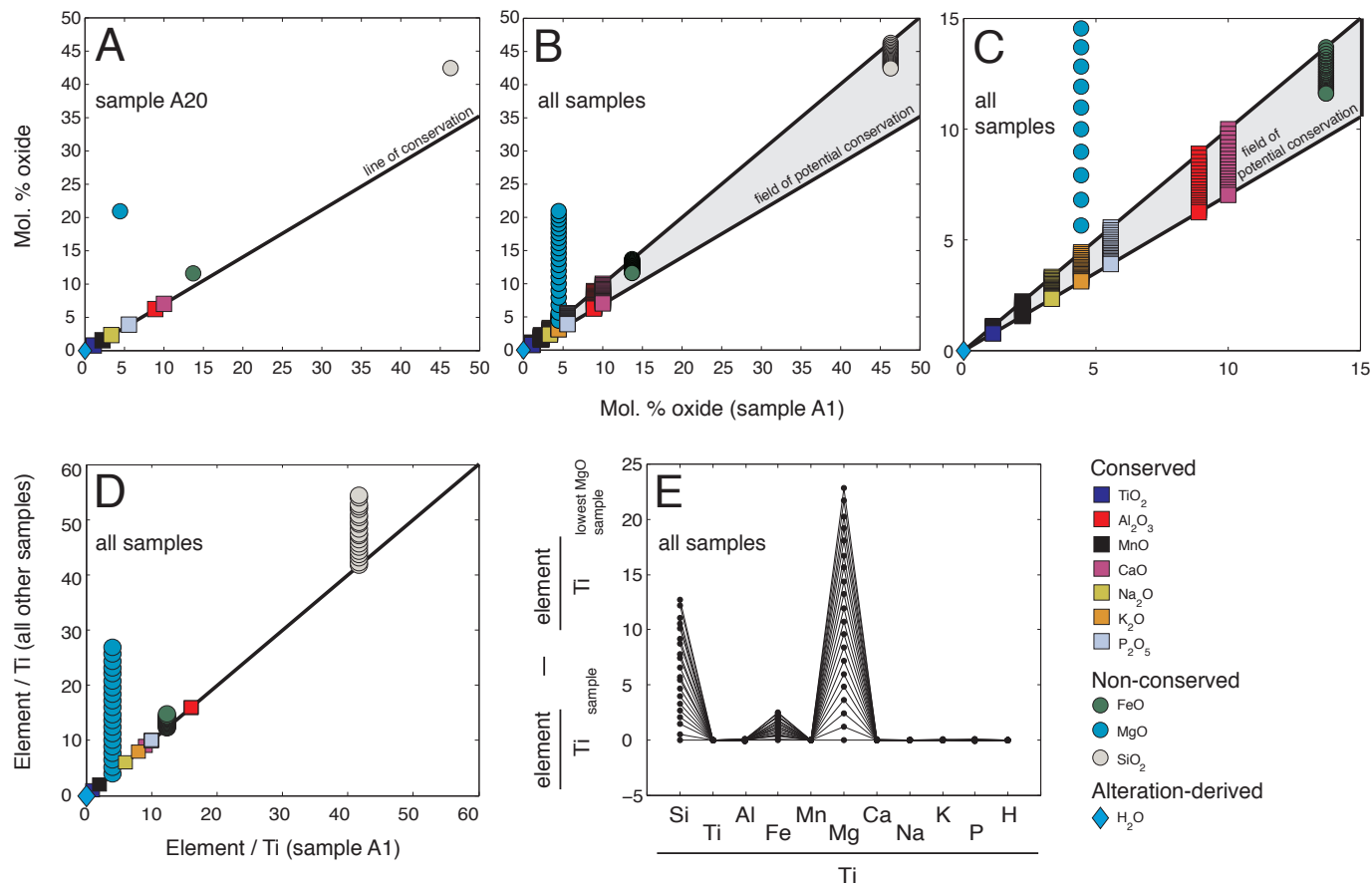
Figure 2.8. Isocon diagrams and related modifications thereof (Suite A). **Panel A** shows a diagram comparing the molar abundances of oxides in sample A1 to A20. All conserved species define a line emanating from the origin. Unconserved species each show displacement from this line of conservation. **Panels B** and **C** show the same diagram, but with samples A2 through A20 plotted against A1 (panel C shows the region near the origin). Each individual pair of samples has its own unique isocon, resulting in a field of potential conservation. **Panel D** shows the Pearce element ratio (PER) equivalent of the isocon diagram, an approach equivalent to Guo et al.'s (2009) arbitrary normalization procedure. **Panel E** shows the PERs translated by subtraction of the reference rock.
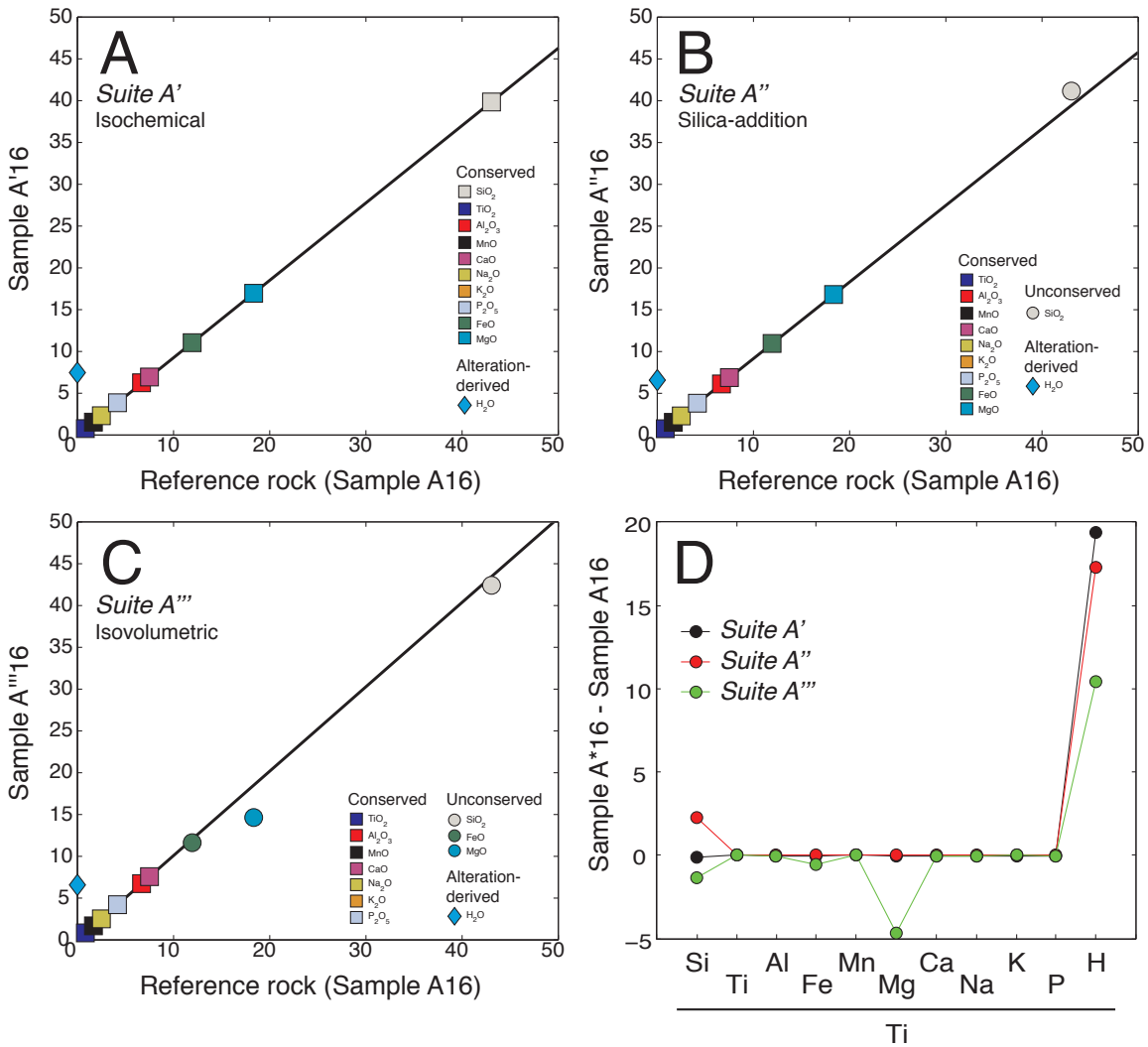
Figure 2.9. Isocon diagrams and the translated Pearce element ratio (PER) equivalent comparing the most altered sample in each suite to their protoliths. Displacements from the isocon in panels **A-C** are clearest in the translated ratios (**Panel D**). **A** – Suite A'. **B** – Suite A''. **C** – Suite A'''. **D** – Translated PERs from the three altered suites.

The isocon diagrams in Figure 2.9 constrain the stoichiometry of the reactions because the exact protolith composition each altered rock was known. In practice, were we interested in comparing a pair of natural samples from a variably altered lava (for example), the choice of reference sample is more complex because of pre-existing compositional diversity (i.e., olivine sorting). Were we to choose a reference rock from the dataset, as isocon analysis requires, the resultant diagram shows both the primary and alteration-related variability. Figure 2.10 (A-C) shows the translated ratio diagrams for the altered suites, revealing slightly differing patterns resulting from the serpentinization reactions superimposed upon a large preexisting olivine sorting signal. However, like the diagrams in Figure 2.5, the differences are subtle. Differences in the main unconserved elements are clearer in Figure 2.10 D, where the translated ratios from 2.10 A-C are plotted in the diagram testing for olivine sorting, which is identical (but translated to a new origin) to the original PER diagram (Figure 2.10 E).

2.6. Summary analysis of published methods

2.6.1. Variation diagrams

Variation diagrams are useful for portraying the compositional diversity of all samples in a suite. They are a visual complement to data tables and require no recalculation or transformation. These diagrams are therefore a sensible starting point in the assessment of datasets and the correlations therein, as well as generation of preliminary ideas as to the processes responsible for chemical diversity.

The main disadvantage to variation diagrams is that the trends they illustrate have ambiguous meaning owing to closure. Action of identical process (cf. suites A and B, C and D) upon variable initial bulk compositions can produce different trends, leaving the ready possibility of process misidentification. Finally, the variation diagrams in the altered suites resemble one another remarkably, despite their alteration occurring by different reactions. These disadvantages all result from closure. They render variation diagram-based interpretations convoluted and equivocal.

2.6.2. Molar element ratio diagrams

In contrast to variation diagrams, the PER approach circumvents the problem of closure
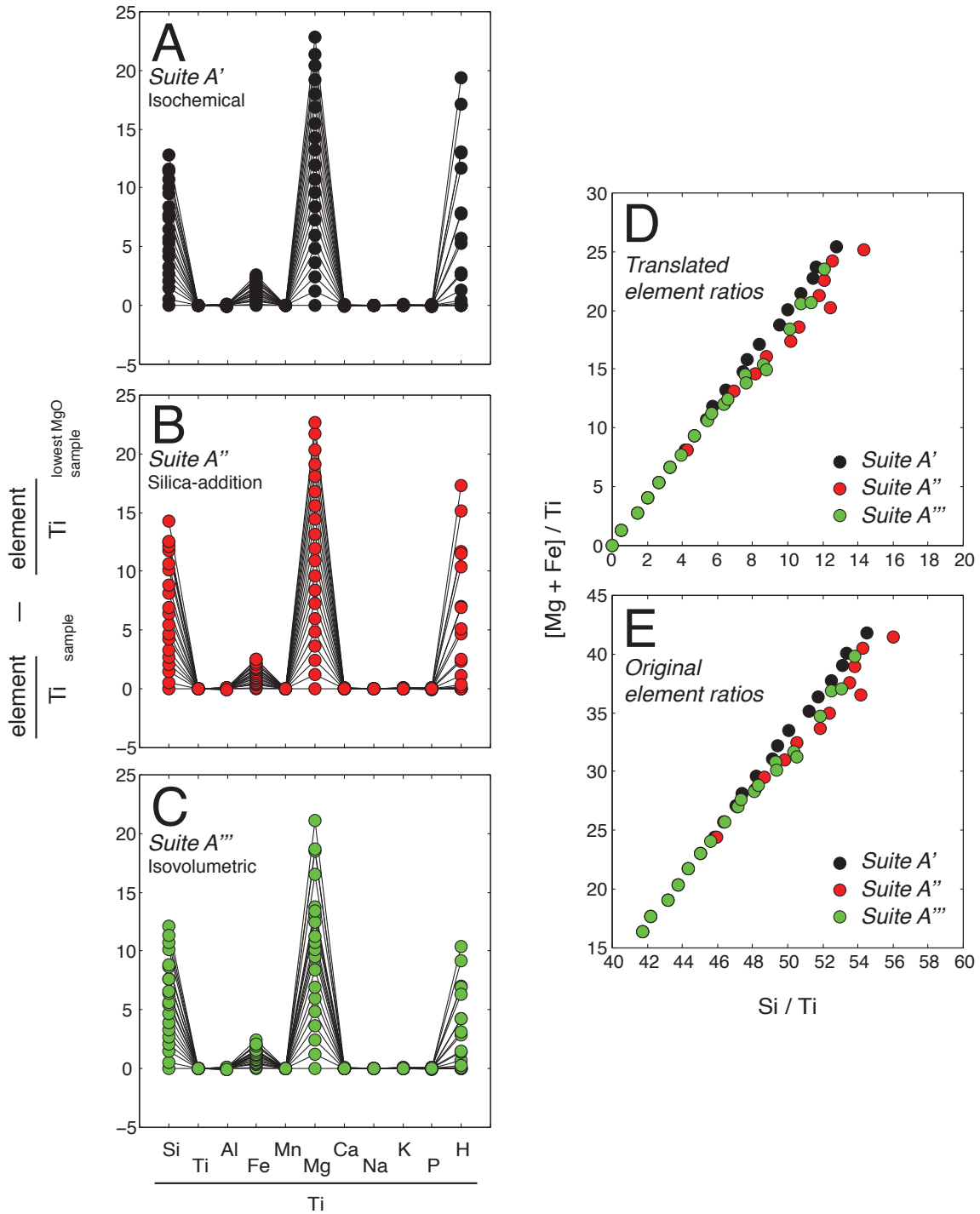
Figure 2.10. Translated Pearce element ratio (PER) diagrams showing all compositions in each altered suite (panels **A-C**) and comparison of these ratios to the original (non-translated) PERs (cf. panels **D** and **E**). **A**. Suite A'. **B**. Suite A''. **C**. Suite A'''. **D**. PER diagram testing for olivine sorting, showing translated PERs form all altered suites. **E**. Standard PER diagram testing for olivine sorting, showing all altered suites.

and portrays the stoichiometry of element mobility in extensive space. In variation diagrams, the processes (if any) that linked co-variation of two oxides were unclear. Molar ratio analysis provides a more powerful framework for exploring datasets and generating viable hypotheses than do variation diagrams. Carefully constructed PER diagrams can conclusively disprove mass transfer hypotheses.

The principal limitation of the PER approach is the requirement of knowing or assuming a conserved component in the denominator (Pearce, 1968; Russell and Nicholls, 1988; Stanley, 1993). Conservation may not exist (or be demonstrable) in natural systems, particularly where metasomatism occurs.

Finally, an additional limitation of PER analysis is the difficulty in rejecting a hypothesis in complex systems (i.e., those that underwent multiple processes). For example, the diagram testing for olivine sorting correctly rejects that process as the sole source of compositional variations in suites C and D, but it cannot determine whether olivine sorting is *one of several* permissible processes without devising new and increasingly complex diagrams (Nicholls and Gordon, 1994) that test for the action of multiple processes.

2.6.3. Isocon analysis

The best approaches to isocon analysis (Guo et al., 2009; this thesis, Section 2.5) enable comparison of the extent of non-conservation of every element or oxide in a dataset. However, those procedures highlight a fundamental sameness between PER and isocon analyses, so both methods ultimately suffer the same limiting requirement of a known conserved element. Moreover, requisite designation of a single protolith composition in isocon analysis renders distinction between primary differentiation and metasomatism difficult to recognize and quantify.

2.7. Recommendations for a new approach to quantitative analysis of geochemical processes

The ideal approach to untangle mass transfer processes would circumvent the problem of closure, not require the conservation of any component, permit analysis of all rock compositions in a dataset, and enable testing of any geochemical vector as a viable mass

transfer process. Linear algebraic approaches akin to those applied to mineral assemblages or mineral solid solutions (Greenwood, 1967; Thompson, 1982a; Thompson, 1982b; Fisher, 1989; Fisher, 1993; Russell et al., 1999) are promising methods whose potential in the analysis of whole rock compositions remains largely untapped (Gordon, 2000; Hansen et al., 2005; Gordon and Russell, 2006).

CHAPTER 3: Geometric testing of geochemical hypotheses and models

3.1. Introduction

This chapter presents a new protocol for testing geochemical hypotheses using whole rock compositions. The methods enable testing of any vector (or set of vectors) against rock compositions without any requisite knowledge or assumption about element conservation (Pearce, 1987; Russell and Nicholls, 1988; Stanley, 1993), and circumvent the issue of closure (Chayes, 1962). The approach recognizes rock compositions as vectors in high dimension spaces (Gordon and Russell, 2006). Here, I use linear algebraic techniques to determine the dimensions and identity of the rock composition space wherein permissible hypotheses lie. Any hypothesis vectors that lie outside of the rock composition space are invalid. I also present a similar approach to test whole rock datasets against geochemical models (i.e., sets of geochemical vectors). Finally, I describe methods to transform compositions (Russell et al., 1999) into proportions of their formative processes, thus enabling their forensic recovery. These methods together constitute profoundly powerful tools in the investigation of geochemical processes responsible for diversity in rock compositions.

3.2. The rock composition space

Whole rock compositions comprise m components (usually oxides). Individual compositions are thus m-component vectors emanating from the origin in m-dimensional space. A geochemical matrix (GCM) contains m rows of oxides (or elements) and n columns of rock compositions (Gordon and Russell, 2006). In this thesis, all geochemical datasets (synthetic and real) have $m < n$; that is, the matrices contain more rock compositions than oxides.

The *rock composition space* is that portion of m-dimensional space that spans all rock compositions. It is the column space (Strang, 2009) of the GCM. All rock compositions and the processes responsible for variation between them lie within this space, because rock compositions are linear combinations of the bulk composition of the geochemical system and the chemical vectors that acted upon it. The dimension of rock composition space can be any whole number from one to m. The rock composition space of GCM is analogous to the composition space (Thompson, 1982a) of a mineral

assemblage matrix, the difference being that it encompasses all linear combinations of rock compositions rather than mineral compositions.

3.3. Identifying the rock composition space and determining its rank

Fisher (1989) developed a method to determine the rank (r) of matrices of mineral compositions using the singular value decomposition (SVD). His method also retrieves a basis for the column space of the matrix. The SVD (Figure 3.1) is a deconstruction of a matrix (e.g., *GCM*) into three new matrices with special properties. These matrices are U ($m{\times}m$), S ($m{\times}n$), and V ($n{\times}n$). The matrix U is orthonormal, meaning its vectors are mutually perpendicular and have unit length, as is the matrix V. The matrix S is a diagonal matrix whose diagonals are real positive numbers (or zero) corresponding to the magnitude of the column vectors in U, in descending order.

The main property of the SVD is that

$$\underset{m\times m}{U}\ \underset{m\times n}{S}\ \underset{n\times n}{V^{t}} = \underset{m\times n}{GCM}. \tag{3.1}$$

The column vectors in U with nonzero magnitudes are an orthonormal column vector basis for *GCM*. They *define* and *represent axes* of the rock composition space of *GCM*. The rank (dimension) of *GCM* corresponds to the number of diagonal entries in S with values greater than zero (the singular values) (Fisher, 1989; Strang, 2009). The remaining columns of U are a basis for the left null space of *GCM*, which contains all the linear combinations that sum to zero; this space is analogous to the reaction space (Thompson, 1982b; Fisher, 1989; Gordon, 2000) of mineral assemblage matrices. Determining r is theoretically as straightforward as computing the SVD of *GCM*, which is trivial using computational platforms such as Matlab. However, measurement and sampling uncertainty (and rounding error) in real datasets ensure values greater than zero in every diagonal of S, thereby overestimating the rank of the *GCM* by failing to resolve the noise of uncertainty from the real geological signals in the data (Fisher, 1989).

Fisher (1989) dealt with these uncertainties by replacing the smallest value in S with zero, and reconstructing the *GCM* by Equation 3.1, giving $GCM_{r\text{-}1}$. To assess the validity of this rank-reduced matrix as a representation of *GCM* is to calculate their difference (GCM_{dif}) and compare it to uncertainties; where $|GCM_{dif}|$ is smaller than the
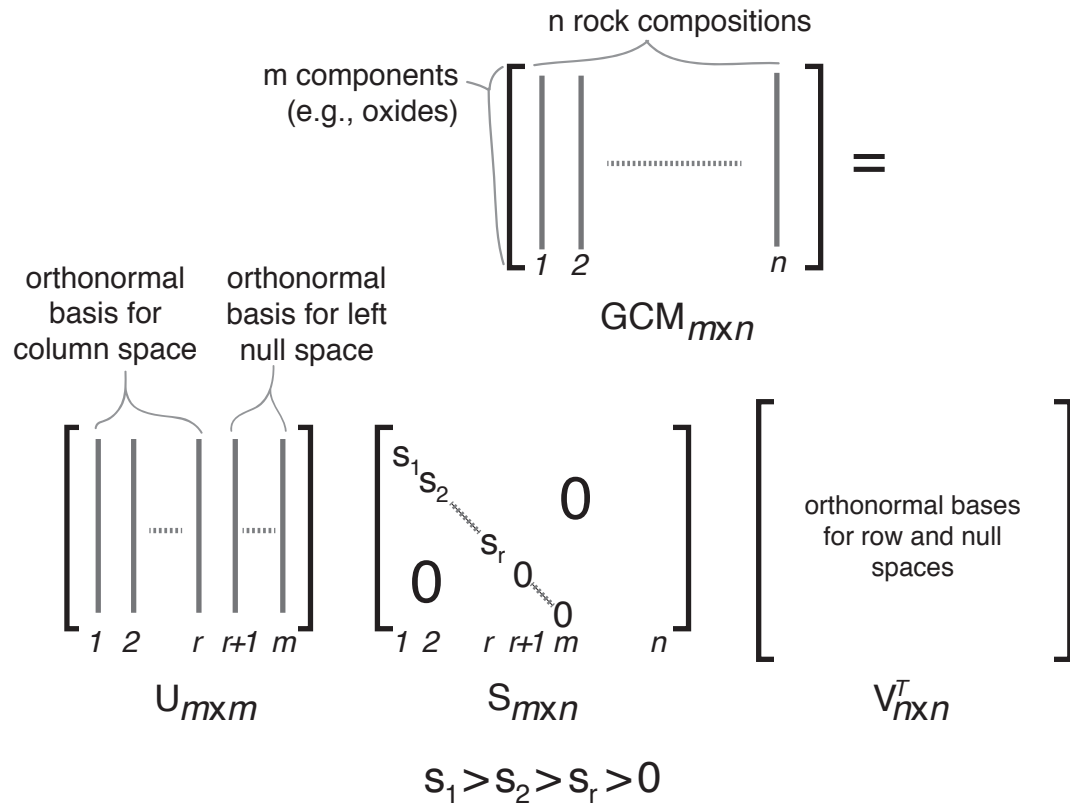
Figure 3.1. Summary of the singular value decomposition of an $m \times n$ geochemical matrix (*GCM*), wherein $m < n$. The diagonal entries (s) in S are the magnitudes of the column vectors in U, in descending order. The number of s greater than zero is the rank (r) of *GCM*. The first r columns in U define the column space of *GCM*, whereas the remaining columns are a basis for its left null space.

acceptable uncertainty limits, GCM_{r-1} is indistinguishable from GCM. Repeating the procedure until $|GCM_{dif}|$ is greater than acceptable uncertainty limits determines r, insofar as uncertainties can resolve. The number of singular values remaining in S after the final acceptable step is equal to r. This procedure, which Fisher applied to interpretation of metamorphic reactions and assemblages, is an application of the Eckart-Young Theorem for approximating a matrix by one of lower rank (Eckart and Young, 1936).

3.3.1. Examples from the synthetic datasets

Figures 3.2 and 3.3 show examples from the synthetic datasets from Chapter 2. The magnitudes of the column vectors in U for suites A-D are all greater than zero (Figure 3.2), except for the eleventh column, owing to the eleventh component (H_2O) being exactly zero in each suite. By design, the ranks of these suites are two and three in suites A and B, and C and D, respectively, indicating that the values close to zero result from rounding error (± 0.005 mol.%). Applying Fisher's method to reduce the rank to the known rank progressively increasing maximum value of each oxide in $|GCM_{dif}|$ with each step in the rank reduction process in Suite A (Figure 3.3 A). Differences fall almost entirely within this rounding error. However, the *maximum* differences of most elements fall slightly outside this range (Figure 3.3). The exact reason for this difference is unclear, but likely relates to how the orthonormal basis vectors accommodate the rounding error. In Suite A, both SiO_2 and MgO show better reproduction in the rank-reduced approximation than do other elements (Figure 3.3). These two components have the greatest variation owing to their high abundance and prominence in the olivine composition; I speculate that this prominence results in a portion of their rounding error being accommodated in the first two U basis vectors. Similarly, some of the real variation of the remaining components (arising from closure, and olivine sorting in the case of FeO) lies within the left null U basis vectors, giving rise to poorer reconstruction in the rank-reduced approximation.

Rank reduction beyond the known rank results is a sharp increase in the differences (Figure 3.3 B and C). In Suite A example, nine steps of rank reduction oversimplify the dataset well beyond the bounds of rounding error. If we accept that the maximum differences after the prior rank reduction step are close enough to expected
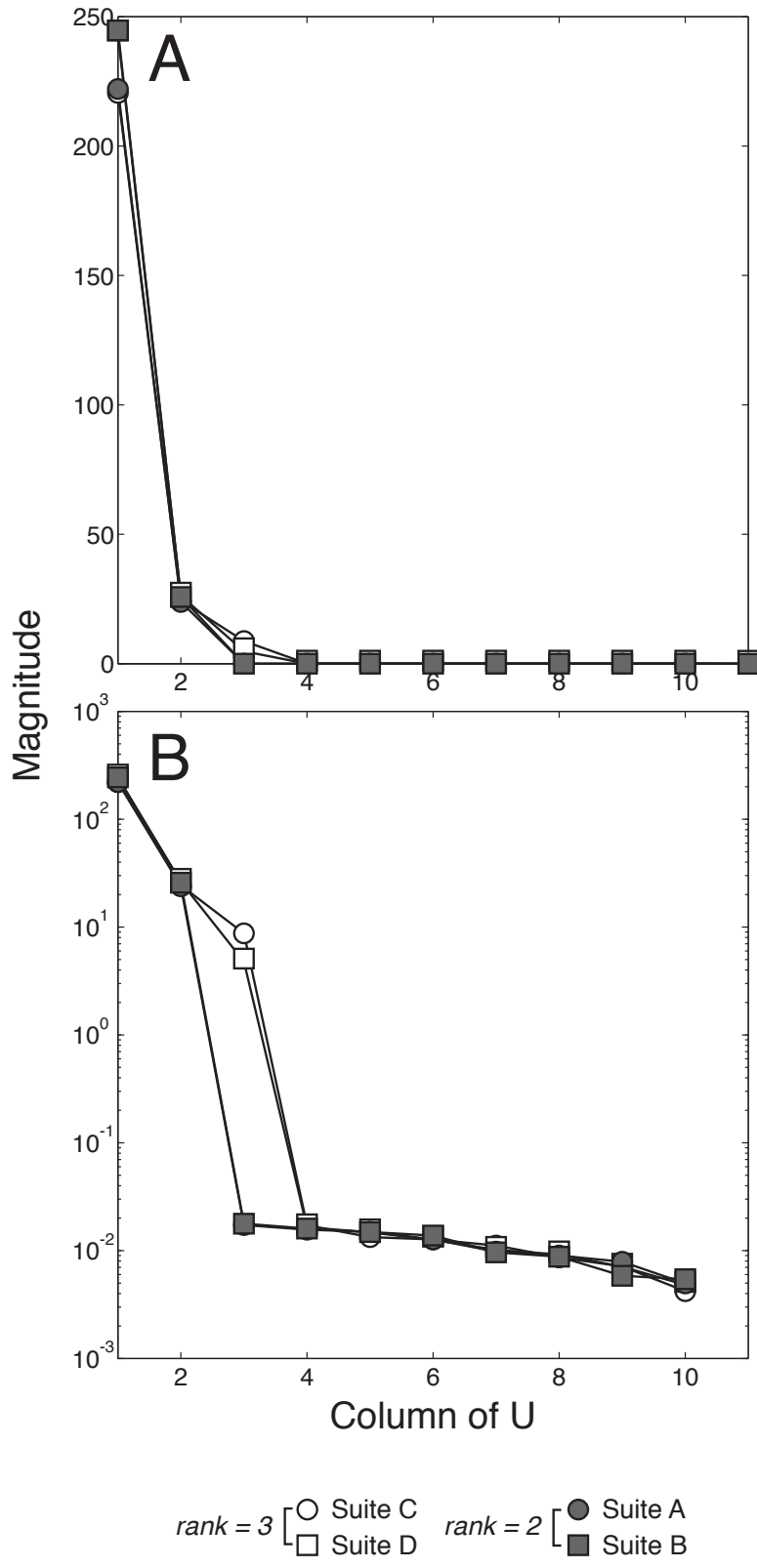
Figure 3.2. Magnitudes of column vectors in the U matrix of the singular value decomposition for synthetic suites A-D, on linear (**A**) and logarithmic scales (**B**).
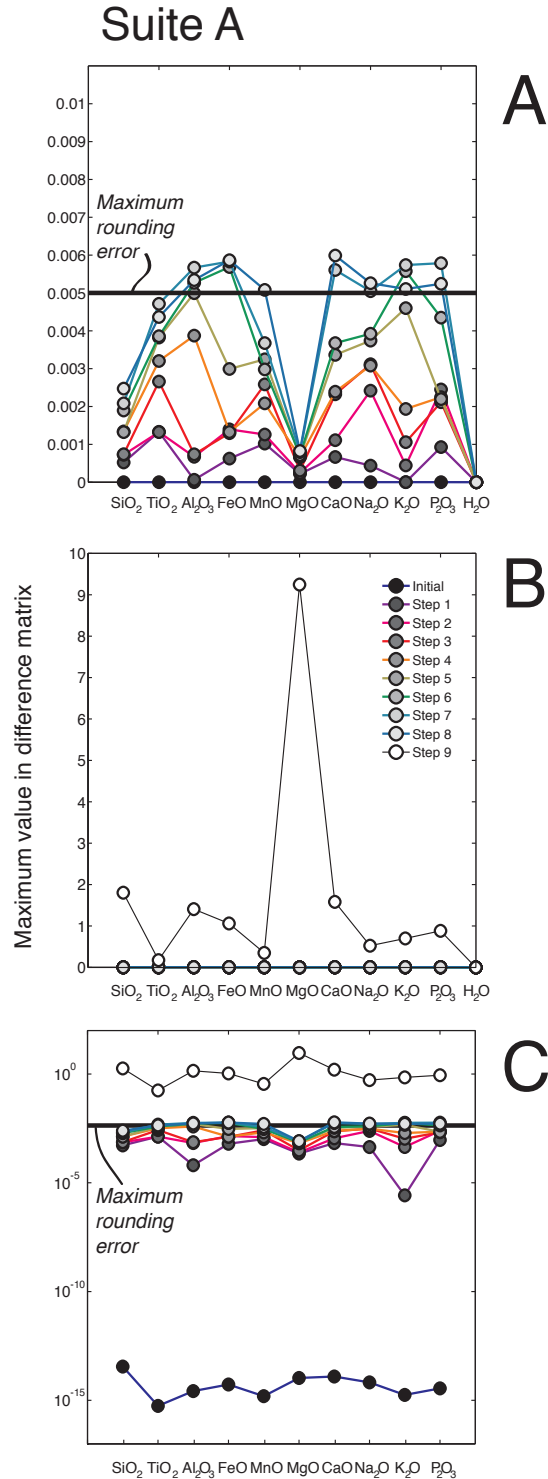
Figure 3.3. Progression in the maximum difference between the Suite A *GCM* and its low rank approximations with each step in the rank reduction process from the initial rank-ten state. **Panel A** shows progressive increases in the mismatch with each step of rank reduction; the deviations are within the maximum deviation expected from rounding error (the source of uncertainty in these synthetic compositions). Further rank reduction introduces large deviations (panels **B** and **C**) outside the bounds rounding errors allow.

error (they are up to ~0.006 mol.% instead of 0.005; Figure 3.3 A), the process correctly determines that $r = 2$. Table 3.1 shows the known rank of each synthetic dataset, the rank according to the raw SVD, and the low rank approximation by Fisher's method. In every case, the low rank approximation returns the true rank of the dataset. Fisher's application therefore enables powerful determination of rank, thereby defining the dimensionality and identity (i.e., u, the first r column vectors in U) of the rock composition space.

3.4. Geometric testing of hypotheses: The angle of separation

This section develops and describes a simple method to test whether hypothesis vectors, H, lie within the rock composition space. The method exploits the orthonormal basis (u) for the rock composition space from the SVD of the GCM. The procedure projects H onto u and then recalculates H (giving H_{rec}) from its projected coordinates in u. If the rock composition space fully contains a given vector in H, that vector is equal in H_{rec} and H. Failure of a vector in H_{rec} to equal its original composition in H indicates that the original vector lies outside the rock composition space and cannot be viable. The angle separating H from H_{rec} – the *angle of separation* – is a concise representation of this misfit, which I exploit to determine whether H vectors are viable mass transfer hypotheses. The smaller the angle of separation, the closer the vector is to the rock composition space. The procedures here test whether the GCM permits H, but does not give any information regarding its magnitude in the system. The equations for orthonormal projection are straightforward, standard linear algebraic procedures (Strang, 2009).

The rank-reduced orthonormal basis, u, defines the rock composition space, a subspace within m-dimensional space. In the case of a dataset of $r = 2$ (Figure 3.4), the first two column vectors of u define a plane within that m-dimensional space. The composition of every vector in the subspace (e.g., sample compositions, mass transfer process vectors) is a linear combination of those two vectors; all other orthonormal vectors in U have zero magnitude in GCM (Figure 3.4). In systems where $r > 2$, the same relationships apply but to r dimensions in U.

Projecting H onto u yields

$$H_{proj} = u^t \ H,$$

$$\underset{r \times h}{} \quad \underset{r \times m}{} \underset{m \times h}{}$$

(3.2)

Table 3.1. Comparison of known rank (r_{known}) of synthetic datasets, rank from raw SVD output (r_{SVD}), and rank determined by low rank approximation (r_{red}).

Suite	A	B	C	D	A'	A''	A'''
r_{known}	2	2	3	3	3	3	3
r_{SVD}	10	10	10	10	11	11	11
r_{red}	2	2	3	3	3	3	3

$$H = \begin{bmatrix} u_1 \\ u_2 \\ u_{3:m} \end{bmatrix}$$

rank = 2

rock composition space
(column space) of GCM

u_2

all permissible hypotheses (H) lie
within the rock composition space

If $u_{3:m}$ in H $\begin{array}{l} = 0 \text{ H is permissible} \\ \neq 0 \text{ H is impermissible} \end{array}$
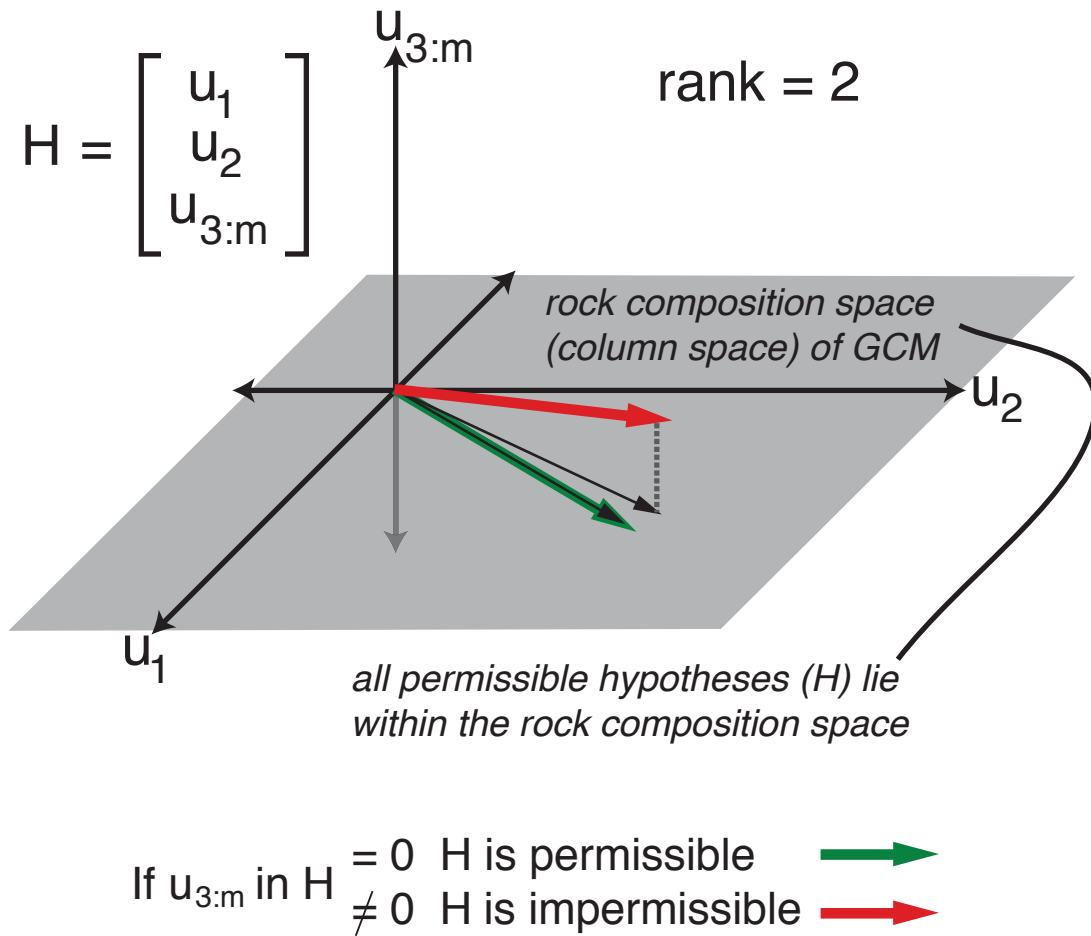
Figure 3.4. Relationship between the orthonormal basis (u_1, u_2) for the rock composition space of a rank-two geochemical matrix (*GCM*) and the permissibility of hypothesis vectors. All valid hypotheses (e.g., **green arrow**) lie within the plane defined by the column space basis vectors. Impermissible hypotheses (e.g., **red arrow**) have nonzero values in one or more of the vectors $u_{3:m}$, and thus fall outside the rock composition space. The **thin black arrows** represent the projection of the green and red hypothesis vectors onto the rock composition space.

where H_{proj} represents the hypotheses in terms of the contribution of each r column vector in u. Returning H_{proj} to the m-oxide basis gives

$$H_{rec} = u \quad H_{proj},$$
$$\phantom{H_{rec} =} m \times h \quad m \times r \quad r \times h$$
\hfill (3.3)

where H_{rec} is the hypotheses as best approximated by the column vectors in u. The angle of separation ($\theta_{H,i}$, in degrees) between the ith vector in H_{rec} and its counterpart in H measures how far out of the rock composition space the hypothesis lies:

$$\theta_{H_i} = \frac{180}{\pi} \cos^{-1} \left(\frac{H_i^t}{\sqrt{\Sigma H_i^2}} \quad \frac{H_{i_{rec}}}{\sqrt{\Sigma H_{rec,i}^2}} \right).$$
$$\phantom{\theta_{H_i} = \frac{180}{\pi} \cos^{-1} } 1 \times m m \times 1$$
\hfill (3.4)

Where $\theta_{H,i} = 0$, H_i is in the rock composition space and is a geometrically permissible hypothesis. Conversely, where $\theta_{H,i} \neq 0$, the hypothesis is outside of the rock composition space and must be rejected. The most straightforward means to define how large $\theta_{H,i}$ must be to be within uncertainty of zero is to perform Monte Carlo simulations wherein we impose random amounts of uncertainty upon one or more measured rock compositions and check the extent to which $\theta_{H,i}$ varies as a consequence. I adopted this procedure in testing both the synthetic and real datasets.

3.4.1. Examples from the synthetic datasets

Synthetic suites A-D represent the process of olivine (Fo_{90}) sorting, with (C and D) or without (A and B) plagioclase (An_{70}) sorting. Testing all compositions of these phases, using the angle of separation, reveals precisely these compositions as the sole permissible olivine and plagioclase vectors in the appropriate datasets (Figure 3.5). Thus, the method correctly rules out all other compositions of these phases as being vectors responsible for compositional variation in the datasets.

The suites A'-A''' represent different serpentinization reactions operating on the synthetic compositions of Suite A. Testing all olivine compositions again recovers Fo_{90} as the sole permissible olivine vector. The product assemblages – serpentine and brucite of Mg# = 90 (Suite A'), and serpentine of Mg# = 90 (suites A'' and A''') – also constitute permissible vectors in these datasets. Expanding to the quaternary system SiO_2-
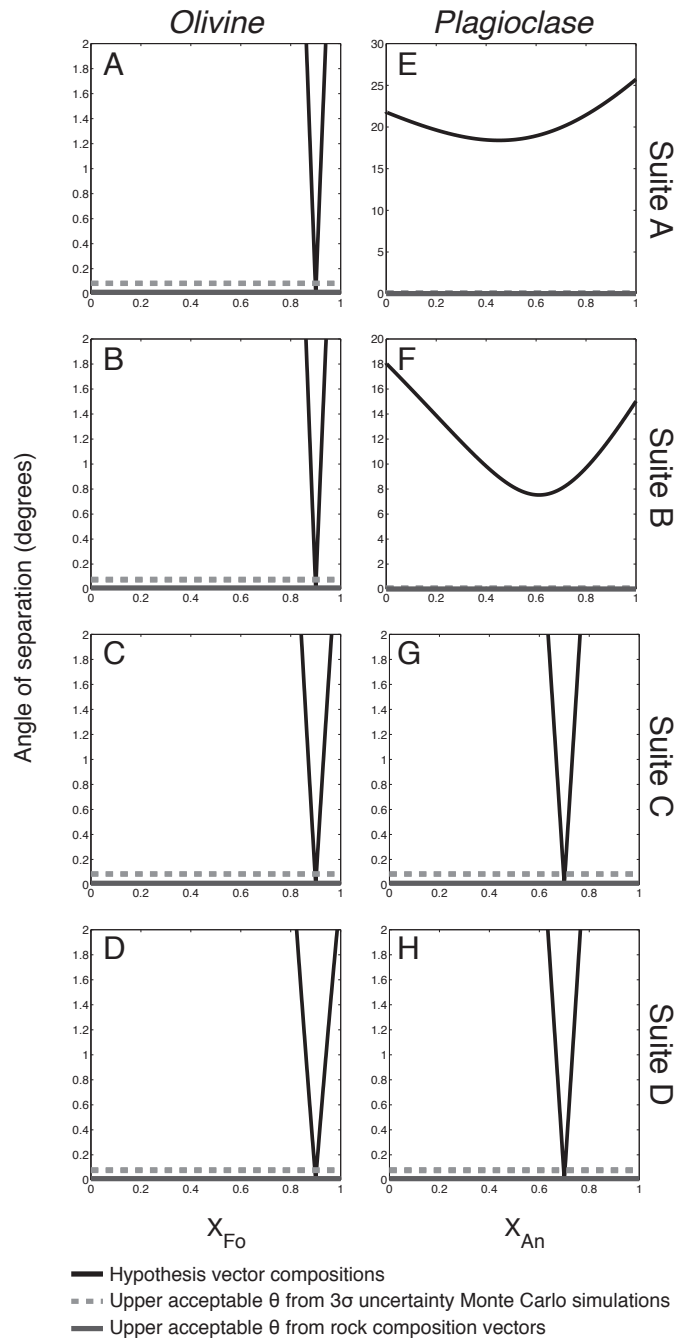
Figure 3.5. Geometric tests of all olivine (forsterite-fayalite) and plagioclase (anorthite-albite) vectors against the rock compositions of the synthetic igneous suites A-D. The test for olivine correctly identifies Fo90 as the permissible olivine vector in each suite (panels **A-D**); i.e., it has an angle of separation of essentially zero in each case. The plagioclase tests return no permissible vectors for suites A and B (panels **E** and **F**), but permit An70 in suites C and D (panels **G** and **H**), in keeping with the respective absence and presence of plagioclase signals in the design of the synthetic suites. The ***grey dashed*** and ***solid lines*** represent the maximum angles of separation from Monte Carlo simulations of uncertainty and the rock compositions themselves, respectively.

MgO-FeO-H$_2$O reveals that each of these suites permit two full dimensions of vectors therein (Figure 3.6). Within the two dimensions of possibilities lie the olivine vector, the product assemblage vector, and the net transfer reaction responsible for the serpentinization (which may lie in negative portions of SiO$_2$-MgO-FeO-H$_2$O space). Notably, despite the different net transfer reactions active in suites A'' and A''', the identical compositions of their reactants and products produce a correspondingly identical subspace of permissible vectors.

3.5. Geometric testing of models

Having tested hypothesis vectors for geometric permissibility leaves us with some number of viable hypothesis vectors (*h*). These *h* vectors together constitute a model for geochemical variation in *GCM*, *H$_{model}$*. The matrix *H$_{model}$* is a basis for the rock composition space of *GCM* if it successfully captures the compositional variation in *GCM*. I describe procedures to test the validity of *H$_{model}$* as a basis for *GCM*, and to quantify the extent to which the model matches the real data.

We begin by computing the SVD of *H$_{model}$* to get an orthonormal basis (*u$_H$*) for the column space of the model (*model space*). For simplicity, let us assume that *H$_{model}$* has the same rank as its number of columns. (If not, *H$_{model}$* contains linearly dependent columns and thus needs revision.) We take the *u$_H$* matrix from the SVD and project the data onto that basis,

$$GCM_{proj} = u_H^t \ GCM, \qquad\qquad (3.5)$$
$$\small h \times n \qquad h \times m \quad m \times n$$

then revert to the *m*-oxide descriptors:

$$GCM_{rec} = u_H \ GCM_{proj}. \qquad\qquad (3.6)$$
$$\small m \times n \qquad m \times h \quad h \times n$$

The matrix *GCM$_{rec}$* is the model approximation of *GCM*, and is identical to *GCM* if the model completely captures the variation therein. The angle of separation is again useful here to concisely quantify the extent of mismatch between the vectors in *GCM* and *GCM$_{rec}$*. Here, $\theta_{mod,i}$ corresponds to the angle between rock composition vector and model space, whereas $\theta_{H,i}$ (above) corresponds to the angle between a hypothesis vector and rock composition space. The θ_{model} for the ith rock composition is
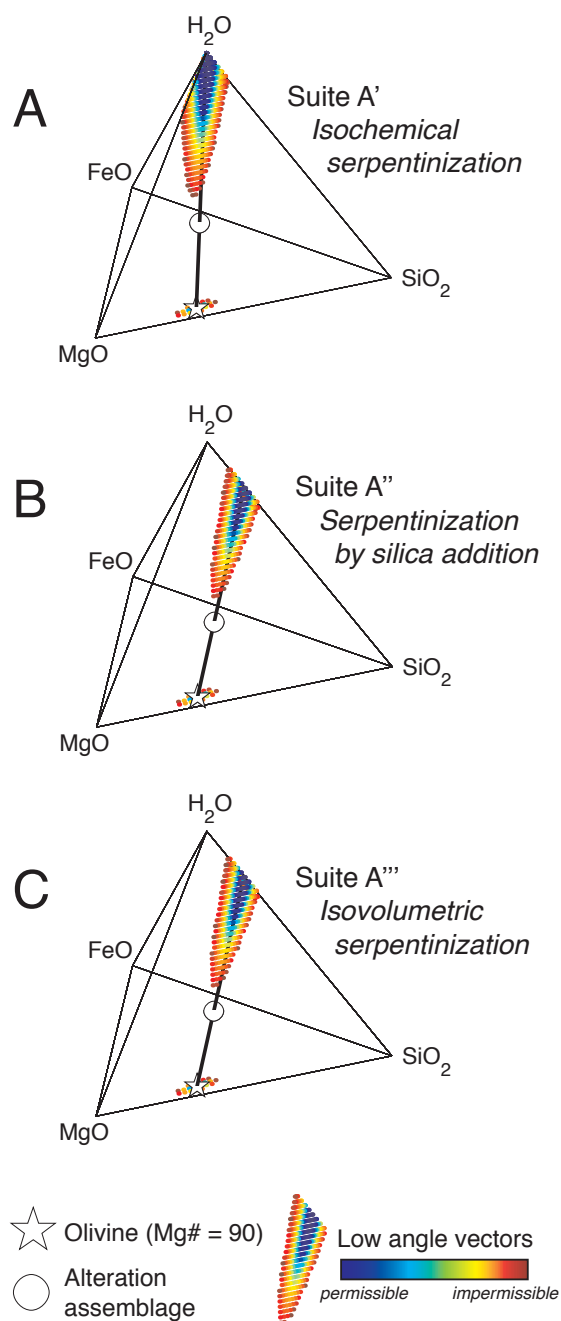
Figure 3.6. Quaternary SiO_2-MgO-FeO-H_2O diagrams showing the permissible vectors in the alteration suites A'-A'''. The plots show the low angle vectors on the surfaces of the tetrahedra for clarity. In each suite, the parental olivine (Fo90; *white stars*) and its alteration products (*white circles*) are permissible vectors, as are all linear combinations thereof, including those extending into negative space; in each suite, two dimensions of SiO_2-MgO-FeO-H_2O vectors are permissible. Suite A permits all vectors on the Fo90-H_2O join (**A**). The metasomatically serpentinized suites (A'' and A'''; **B** and **C**) permit a different two-dimensional space than Suite A. Their space is identical despite the different reactions, owing to the identical reactants and products of reaction.

$$\theta_{model,i} = \frac{180}{\pi} \cos^{-1} \left(\underbrace{\frac{GCM_i^t}{\sqrt{\sum GCM_i^2}}}_{1 \times m} \quad \underbrace{\frac{GCM_{rec,i}}{\sqrt{\sum GCM_{rec,i}^2}}}_{m \times 1} \right). \tag{3.7}$$

The further $\theta_{model,i}$ deviates from zero, the more poorly the model reconstructs the rock composition. As before, Monte Carlo simulations of uncertainty determine whether θ is within uncertainty of zero.

3.5.1. An example from the synthetic Suite C

The synthetic Suite C represents a magma in which olivine and plagioclase crystals fractionated and accumulated independently. Consider two different geochemical models for this suite to demonstrate the validity of geometric testing: one in which only olivine fractionates, and one in which olivine and plagioclase fractionate. The matrices corresponding to these models ($H_{model,Ol}$ and $H_{model,Ol+Pl}$) both comprise a reference rock composition (rock C_1) and the optimal olivine vectors (Fo_{90}; Figure 3.5 C). $H_{model,Ol+Pl}$ has an additional plagioclase vector (An_{70}; Figure 3.5 G). The rock compositions fail to plot in the olivine fractionation model space (Figure 3.7 A), with the contribution of the plagioclase vector (known because the dataset is synthetic) controlling the magnitude of the failure. The model space of the olivine and plagioclase fractionation model fully captures the compositional variation in the suite (Figure 3.7 B). The angle of separation between rock compositions and the model space is essentially zero in the olivine and plagioclase fractionation case, but is large and corresponds systematically to the absolute value of the fraction of the plagioclase vector in the sample in the case of olivine fractionation (Figure 3.8).

3.6. Quantifying the model vector contributions

At this point, one might have a model comprising geometrically (and geologically) validated vectors that explains the significant portion of compositional variability. Each of these model vectors contributes to the composition of a given rock. The following procedures transform rock compositions from an oxide basis to the model vector basis, thereby giving the contribution of each vector to each rock composition. They are the same procedures previously applied to garnet solid solutions (Russell et al., 1999).
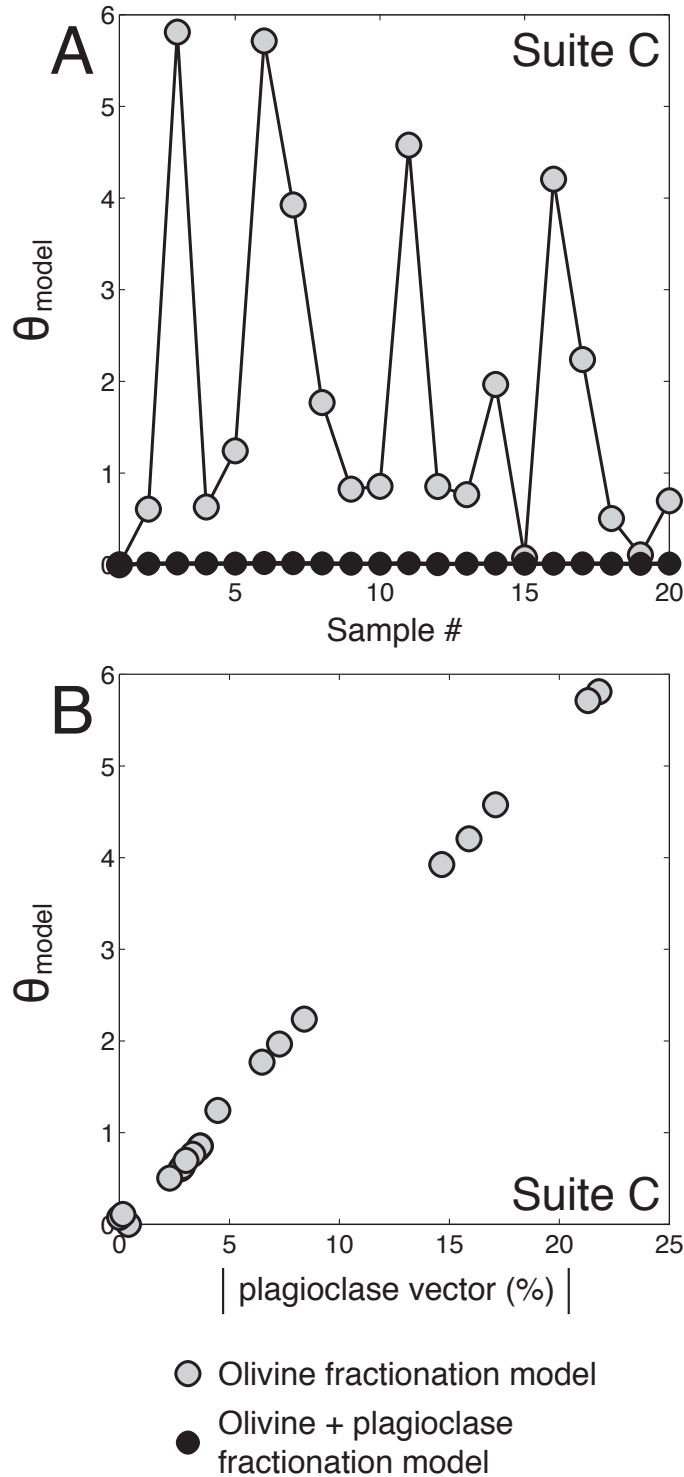
Figure 3.8. The angles of separation (θ_{model}) and their relationship to the magnitude of the plagioclase vector in each rock composition in synthetic Suite C. (**A**) θ_{model} is large in the case of the olivine fractionation model, but essentially zero in the olivine + plagioclase fractionation model. (**B**) The absolute fraction of the plagioclase vector in the rock compositions systematically controls θ_{model} in the olivine fractionation model.
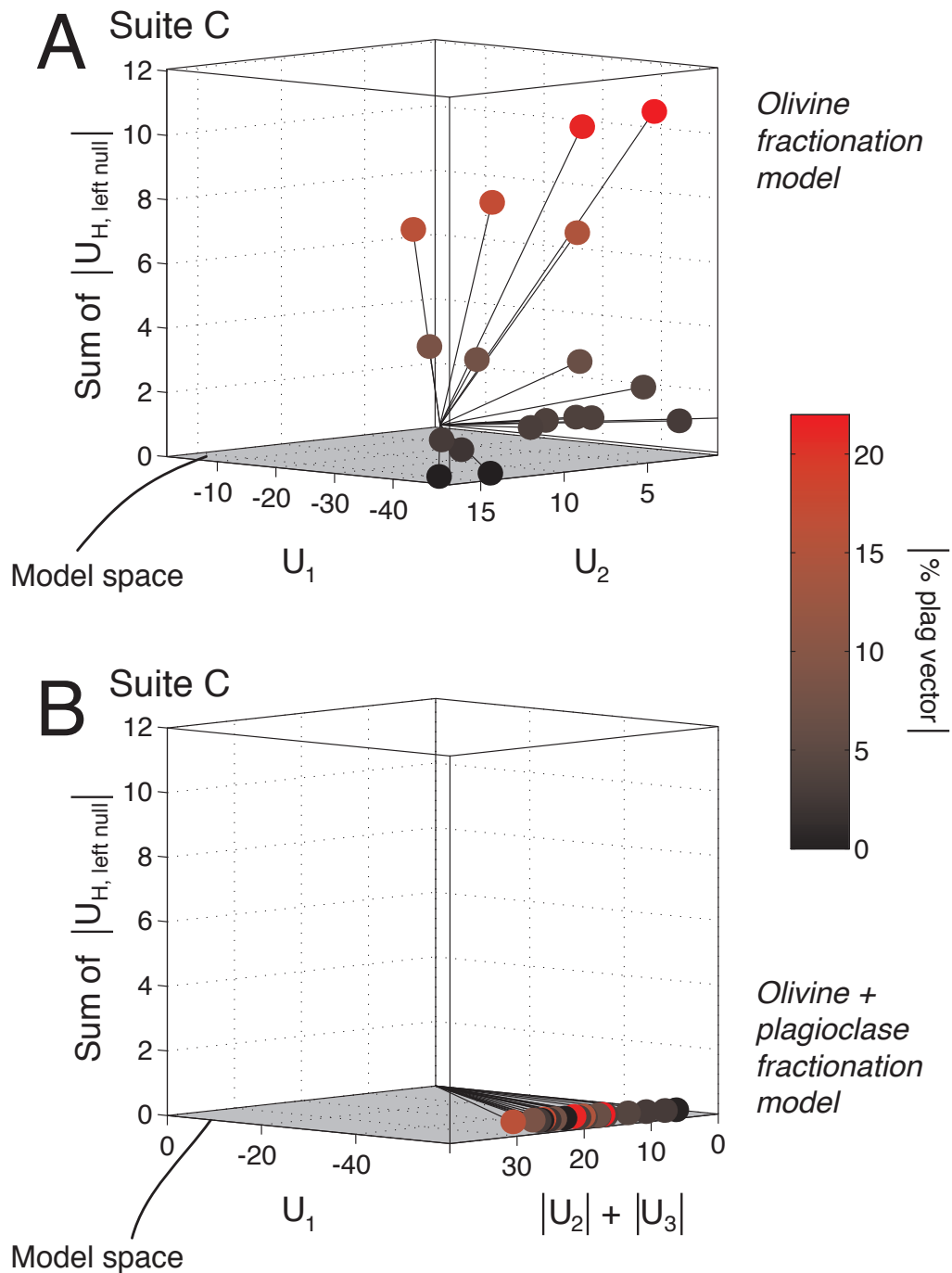
Figure 3.7. Geometric tests of two model explanations for the compositional variability in synthetic Suite C. (**A**) The olivine fractionation model fails to reproduce the rock compositions, resulting in a substantial magnitude of vectors in the left null space (vertical axis) of the model matrix (H_{model}, in the text). The failure of the model correlates with the magnitude of the plagioclase vector in the rock composition. (**B**) The olivine + plagioclase fractionation model fully captures the rock composition, leaving essentially no information in the left null vectors of the model matrix.

The objective is to convert the oxide components in *GCM* to the process vectors in H_{model}. Beginning with an $m \times m$ identity matrix *I*, we replace its column vectors with those in H_{model}, giving I_H. The columns in *I* we replace must be chosen such that I_H remains invertible, its rank being equal to *m*. The inverse of I_H gives the transformation matrix, *Tr*:

$$\underset{m \times m}{\text{Tr}} = \underset{m \times m}{I_H^{-1}}. \tag{3.8}$$

Multiplication of *Tr* and *GCM*,

$$\underset{m \times m}{Tr} \quad \underset{m \times n}{\text{GCM}} = \underset{m \times n}{\text{GCM}_{Tr}}, \tag{3.9}$$

gives GCM_{Tr}. This transformed *GCM* has, instead of oxides in its *m* rows, vector components corresponding to the columns in H_{model}. Rock compositions of this form represent the proportions of the process vectors necessary to reproduce the oxide basis composition. If the vectors in H_{model} represent real natural processes, this representation recovers their net contribution to each rock. The order of the components in GCM_{Tr} corresponds to the column position of model vectors in I_H.

3.6.1. An example from the synthetic Suite C

I transformed rock compositions in the synthetic Suite C according to the model vectors in $H_{model,Ol+Pl}$. Figure 3.9 compares the mole fractions of these vectors in the transformed rock compositions to their mole fractions in the synthesis of the data. The two quantities are essentially identical, all plotting on the 1:1 reference line. Thus, if geochemically accurate models of compositional variation are attainable, so too is precise quantification of their constituent processes.

3.7. Limitations

Geometric testing of geochemical hypotheses or models is subject to three main limitations. The first is that the methods test only the geometric viability of a hypothesis or model, but cannot distinguish between *geologically* reasonable or unreasonable ones. Other data sources deriving from field geology, petrography, mineralogy, and petrology are necessary to avoid misinterpretations of geometrically valid vectors.
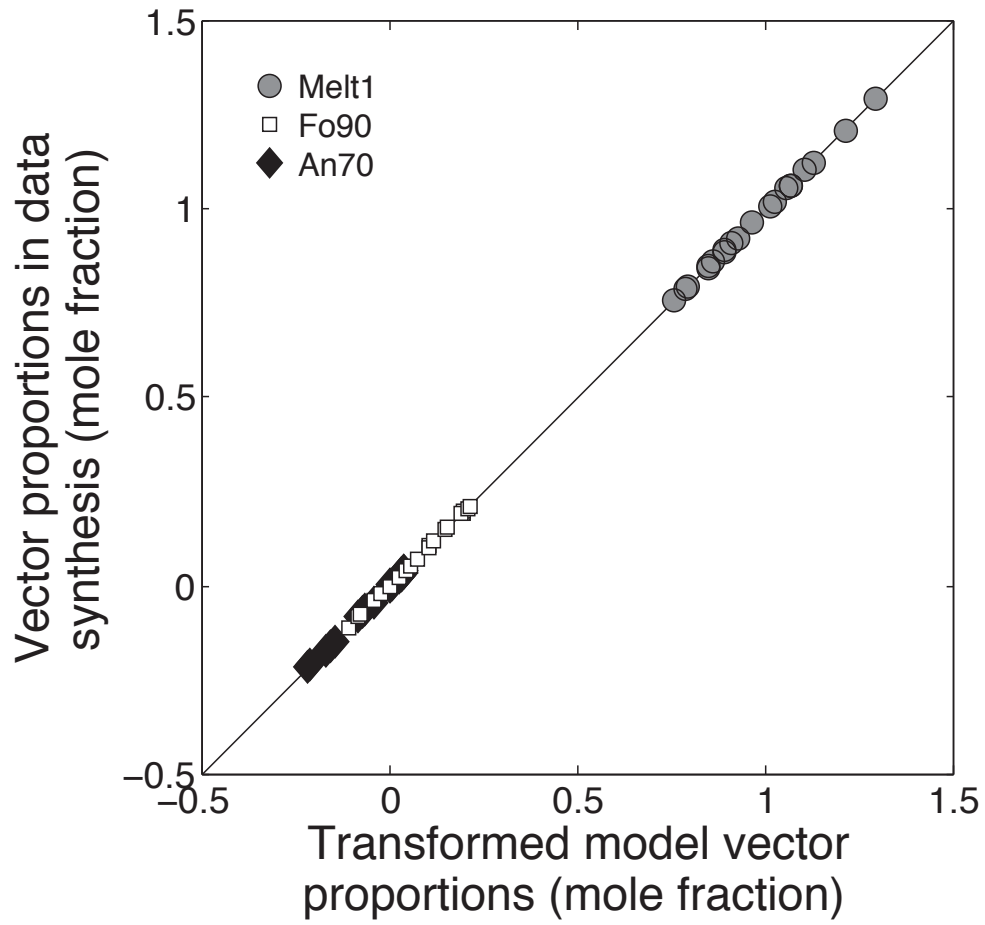
Figure 3.9. Recovered process proportions by transformation of rock compositions from Suite C into geochemical vectors, compared to process proportions known from computation of the dataset.

The second limitation concerns sample suites and models with as many linearly independent processes as components measured. If m oxide measurements are available and the rocks formed by m processes, all hypotheses are geometrically valid. Similarly, if a model has m processes, it will fully explain any rock composition with m components. No hypothesis or rock composition is testable against such full rank datasets or models, respectively; all will be geometrically acceptable.

The third limitation concerns independent geological processes that are linearly dependent in the numerical sense. For example, if pure forsterite and enstatite were variables in a suite of rocks, both of these geochemical vectors would be permissible. However, so too would MgO, as Mg_2SiO_4 (Fo) – $MgSiO_3$ (En) = MgO. Similarly, as $2MgSiO_3$ (En) – Mg_2SiO_4 (Fo) = SiO_2, the SiO_2 vector would also be valid. In this example, the geological processes produce a rock composition space that encompasses other potential geological processes (e.g., quartz or periclase fractionation), giving a geometrically valid result despite the process having not occurred in nature. This possibility further underscores the necessity of always pairing geochemical data analysis with other forms of geological information.

3.8. Conclusion

The methods in this chapter constitute novel approaches to testing the geochemical processes that produced compositional variation in rock suites, assessing the quality of models of such processes, and quantifying the contribution of geochemical vectors to each rock composition. They are straightforward to apply, computationally inexpensive, involve no invocation of element conservation, are immune to the effects of closure, and decisively reject invalid hypotheses. These methods are equally applicable to open or closed systems, and warrant application wherever geologists seek to explain geochemical diversity. Algorithms to facilitate implementation of the methods are available in Appendix A2.

CHAPTER 4: Magmatic compositional variability in komatiite lavas: Mg-Fe equilibria, olivine balance, and metasomatic disturbance

4.1. Introduction

Archean komatiitic magmas erupted with high fluxes and low viscosities that supported vast, laterally extensive lava fields (Hill, 2001; Prendergast, 2003; Arndt et al., 2008). The lava flows thickened throughout the course of eruption as continuous flow-through of liquid resulted in inflation of incipient flows (Arndt, 1982; Barnes et al., 1983; Lesher et al., 1984; Hill, 2001; Prendergast, 2003; Arndt et al., 2008; Houlé et al., 2009). Gravitational settling and in-situ growth of olivine within these lavas produced basal cumulates and spinifex textures, and drove chemical differentiation of the liquids (e.g., Smith et al., 1980; Arndt, 1986; Arndt et al., 2008). Large variations in overall thickness and the proportion of basal cumulus and upper spinifex-textured rocks in komatiites worldwide represent varying extents of flow-through and differentiation progress (e.g., Lesher et al., 1984; Barnes et al., 1988; Lesher, 1989; Arndt et al., 2008). The proportion of cumulate material commonly exceeds the amount that could arise from static fractional crystallization in stagnant liquid, thus implying rapid crystal accumulation within actively propagating flows. In the extreme (e.g., Perseverance Complex, Yilgarn craton, Western Australia), this mechanism produced thick (up to ~700 m) flows dominated by hundreds of metres of dunitic cumulates (e.g., Barnes et al., 1988; Arndt et al., 2008). In thinner flows (e.g., Pyke Hill), the presence of this excess olivine is less conspicuous and chemical metrics are necessary to evaluate whether the rocks represent stagnant, ponded differentiation or syn-propagation settling.

The amount of excess olivine has implications for the physical distribution of rocks within Archean volcanoes. Komatiite occurrences having excess olivine imply that their conjugate liquids continued to flow elsewhere (Lesher, 1989; Arndt et al., 2008). This lateral decoupling of cumulate material and evolved liquid may have produced lithological gradation within flows, with refractory rocks (cumulate dunite, peridotitic komatiite) proximal to the vent and evolved ones (komatiitic basalt) in the most distal regions (Lesher, 1989; Arndt et al., 2008). However, the commonly sporadic and isolated nature of komatiite exposures and regional deformation hamper field tests of this volcano-scale hypothesis, particularly against the competing (although not mutually

exclusive) idea of differentiation within magma chambers (Lesher, 1989; Shimizu et al., 2005). Nevertheless, quantification of excess olivine can yield insight into the relative position of an exposure with respect to its vent, and thus aide in volcanological reconstructions and interpretations of geological context of komatiites and their associated ore deposits (Lesher, 1989). Moreover, recovery of the compositions of the evolved liquids produced by within-flow fractionation can yield insights into the breadth of lithological diversity such a process might produce within Archean lavas and volcanoes.

The typical method (e.g., Arndt et al., 2008) to test for excess olivine in komatiite exposures involves comparing the MgO concentrations of a complete vertical section through the flow (MgO_{flow}), the average composition of cumulus olivine ($MgO_{olivine}$), and the composition of quench material (MgO_{chill}; e.g., chilled margins, clasts in flow-top breccia):

$$\% \text{ excess olivine} = 100 \times \frac{MgO_{flow} - MgO_{chill}}{MgO_{olivine} - MgO_{chill}}. \tag{4.1}$$

This metric gives the proportion of excess olivine in the flow, assuming that all variations in MgO concentration derive from fractionation of the average olivine composition from the liquid as approximated by chilled material (assuming negligible xenolithic olivine and no prior differentiation in a magma chamber). If those critical assumptions are valid, the method determines whether the rock compositions in the exposure could have differentiated from a stagnant parcel of the specified liquid composition. However, if any other processes modified the bulk compositions, the central assumption of a binary system is invalid and the strength of the conclusions diminishes. As closure ensures that mobilization of any element(s) disturbs the concentrations of others (Chapter 2 and references therein), alternative approaches are desirable.

Nevertheless, olivine fractionation is widely recognized to be the dominant or sole source of primary magmatic compositional variability in komatiites. This geochemically simple model is the basis for interpretation of komatiite compositions, in terms of: (i) assessing the extent of metasomatic alteration (LaHaye and Arndt, 1996; Arndt et al., 2008; Sossi et al., 2016); (ii) evaluating the composition of fractionating olivine (Arndt et al., 2008); and (iii) relating bulk compositions to primary liquid compositions and melting conditions (Walter, 1998; Sossi et al., 2016). As prior investigations confidently

identified the main magmatic differentiation process, komatiites are an excellent target for validation of the geometric methods of Chapter 3. Moreover, the pervasive alteration of these rocks provides an opportunity to quantify metasomatic disturbance and discover metasomatic reactions (Chapter 5).

Here I apply the geometric methods of Chapter 3 to komatiite lavas to determine the composition of olivine responsible for whole rock compositional diversity in several komatiite flows. I combine that information with Mg-Fe^{2+} partitioning constraints to estimate the composition and temperature of the evolved liquid, test for Mg-Fe equilibrium, and determine the extent of olivine enrichment in the classic Pyke Hill locality in the Abitibi greenstone belt. Finally, I test the ability of magmatic processes to explain rock compositions and develop a Metasomatic Index to represent deviation therefrom.

4.2. The komatiite lavas: Localities, lithofacies, petrography, and data sources

I examine the major element whole rock compositions (Table 4.1) reported in prior studies of six komatiite flows, including one from the Reliance Formation (Shimizu et al., 2005), one from the Komati Formation (Stuart's Flow; Smith et al., 1980; LaHaye et al., 1995), one from Alexo (LaHaye and Arndt, 1996), and three from Pyke Hill (Shore, 1997). Figure 1.1 shows their locations within their respective greenstone belts. Each locality has featured prominently in komatiite research. The Komati Formation and Pyke Hill flows were the subjects of seminal works (Viljoen and Viljoen, 1969a; Viljoen and Viljoen, 1969b; Pyke et al., 1973) that marked the onset of substantial interest in ultramafic lavas (Arndt et al., 2008). Many studies have investigated the geology, petrography, mineralogy, volcanology, and geochemistry of these rocks (e.g., Arndt et al., 1977; Smith et al., 1980; Parman et al., 1997; Shore, 1997; Dann, 2000; Dann, 2001). The Alexo flow has also been repeatedly studied for its magmatic and complex metasomatic geochemical variation (Barnes et al., 1983; Barnes, 1985; Arndt, 1986; LaHaye et al., 1995; LaHaye and Arndt, 1996, Houlé et al., 2012). The Reliance Formation rocks are the least altered Archean komatiites known, generally featuring minimal replacement of olivine and low volatile contents (Nisbet et al., 1987; Renner et

Table 4.1. Major element whole rock compositions (wt. % oxide), facies, and vertical positions of komatiite samples (where available).
Uncertainties are in 1σ. abs. = absolute; rel. = relative, as fraction; rnd. = rounding error.

Reliance Formation, Belingwe Greenstone Belt

Reference	Uncertainty*	*Shimizu et al., 2005*									
Sample	(rel.)	*BW116*	*BW130*	*BW135*	*BW272*	*BW460*	*BW478*	*BW483*	*BX001*	*BX003*	*BX004*
Facies		Spinifex	Cumulate	Cumulate	Cumulate	Cumulate	Cumulate	Cumulate	Spinifex	Cumulate	Cumulate
SiO_2	0.01	48.10	45.35	44.86	45.51	44.11	44.60	45.06	46.00	47.80	47.70
TiO_2	0.01	0.45	0.30	0.31	0.32	0.25	0.29	0.32	0.34	0.43	0.43
Al_2O_3	0.01	8.98	6.08	6.22	6.48	5.06	5.90	6.37	6.88	8.72	8.73
FeO^T	0.01	11.44	10.38	10.42	10.48	10.25	10.19	10.38	10.70	11.31	11.25
MgO	0.01	16.46	27.02	25.42	25.42	30.16	26.99	25.29	24.02	17.07	16.90
CaO	0.01	9.02	6.20	6.32	6.60	5.15	6.11	6.57	6.94	8.94	8.89
Na_2O	0.03	1.25	0.76	0.60	0.83	0.52	1.01	1.04	0.80	1.22	1.24
K_2O	0.03	0.072	0.042	0.061	0.100	0.047	0.078	0.100	0.058	0.078	0.085
P_2O_5	0.03	0.033	0.022	0.019	0.022	0.019	0.021	0.023	0.025	0.030	0.030

Stuart's Flow, Komati Formation, Barberton Greenstone Belt

Reference	Uncertainty	*Smith et al., 1980*						*LaHaye et al., 1995*				
Sample	(abs., rnd.)	*HSS-531*	*HSS-532*	*HSS-533*	*HSS-534*	*HSS-535*	*HSS-536*	*BI2*	*BI4*	*BI5*	*B20*	*B13*
Facies		Spinifex	Spinifex	Spinifex	Cumulate	Cumulate	Cumulate	Spinifex	Spinifex	Cumulate	Spinifex	Spinifex
SiO_2	0.01	47.77	47.72	47.98	47.38	47.38	46.74	46.95	47.69	46.11	47.74	48.13
TiO_2	0.01	0.38	0.38	0.40	0.35	0.35	0.30	0.43	0.43	0.30	0.42	0.38
Al_2O_3	0.01	4.26	4.25	4.32	3.81	3.80	3.29	4.43	4.32	2.98	4.33	4.12
$Fe_2O_3^T$	0.01	12.80	12.35	13.05	11.41	11.52	12.08	13.21	12.86	11.78	12.96	12.61
MgO	0.01	27.62	28.14	25.65	30.87	30.78	31.68	26.79	26.13	33.92	26.82	26.33
CaO	0.01	7.29	7.21	8.72	6.24	6.26	6.06	7.89	8.24	4.70	7.35	8.14
Na_2O	0.01	0.19	0.20	0.21	0.10	0.08	0.07	0.05	0.10	0.00	0.10	0.05
K_2O	0.01	0.02	0.02	0.03	0.03	0.03	0.01	0.01	0.02	0.00	0.02	0.01
P_2O_5	0.01	0.02	0.02	0.02	0.02	0.02	0.01	0.03	0.03	0.02	0.04	0.03
Distance from base (m)		3.0	2.6	2.0	1.5	0.8	0.2					

64

Table 4.1., continued.

Alexo flow, Abitibi Greenstone Belt

Reference	Uncertainty	*LaHaye and Arndt, 1996*									
Sample	(rel.)	M667	M666	M662	M663	M664	M654	M665	M656	M668	M657
Facies		Spinifex (breccia)	Spinifex	Spinifex	Spinifex	Spinifex	Spinifex	Spinifex	Spinifex	Spinifex	Spinifex
SiO_2	0.02	45.1	45.4	45.0	45.3	45.0	43.8	44.7	44.7	45.8	43.2
TiO_2	0.02	0.33	0.35	0.32	0.34	0.34	0.26	0.37	0.41	0.44	0.50
Al_2O_3	0.02	6.6	7.0	6.3	6.8	6.7	5.0	6.7	7.9	8.6	9.4
$Fe_2O_3^T$	0.02	12.0	12.0	11.5	11.9	11.2	11.2	11.8	12.3	12.7	13.4
MgO	0.02	30.4	27.9	29.6	28.4	29.4	34.7	28.2	23.6	23.5	19.9
CaO	0.02	4.8	6.6	6.1	6.2	6.3	4.4	7.4	10.6	7.8	12.8
Na_2O	0.05	0.30	0.29	0.44	0.42	0.30	0.03	0.07	0.12	0.09	0.03
K_2O	0.1	0.30	0.10	0.10	0.11	0.09	0.01	0.40	0.40	0.04	0.01
P_2O_5	0.1	0.00	0.00	0.00	0.00	0.00	0.00	0.00	0.00	0.00	0.00
Distance from base (m)		15.0	14.0	13.8	12.8	11.7	9.7	8.2	7.8	7.3	6.5

Alexo, cont'd

Reference	*LaHaye and Arndt, 1996*								
Sample	M6E8	M675	M676	M716	M715	M661	M714	M713	M712
Facies	Spinifex	Cumulate	Cumulate	Cumulate	Cumulate	Cumulate	Cumulate	Cumulate	Cumulate
SiO_2	43.4	46.0	45.0	45.2	44.5	43.7	45.2	44.6	44.4
TiO_2	0.32	0.43	0.36	0.35	0.21	0.19	0.25	0.21	0.21
Al_2O_3	6.0	7.2	5.7	6.5	4.3	3.2	3.2	3.8	3.7
$Fe_2O_3^T$	11.8	11.6	11.1	11.0	10.0	9.1	9.4	7.9	8.8
MgO	29.8	28.2	32.7	29.8	37.1	42.1	38.1	42.9	39.6
CaO	7.9	6.1	4.7	6.3	3.5	1.0	3.2	0.2	2.8
Na_2O	0.04	0.30	0.05	0.23	0.00	0.01	0.00	0.00	0.00
K_2O	0.01	0.10	0.09	0.10	0.00	0.01	0.00	0.00	0.10
P_2O_5	0.00	0.04	0.03	0.03	0.02	0.00	0.02	0.01	0.02
Distance from base (m)	5.8	4.5	4.5	4.0	3.5	3.0	2.5	1.5	0.5

Table 4.1., continued.

Pyke Hill, Abitibi Greenstone Belt Flow A

Reference	Uncertainty (abs.)	Shore 1997									
Sample#		ms-44(ag)	ms-23(ag)	ms-08(ag)	ms-60(ag)	MS91-15	MS91-14	ms-15B(ag)	ms-15A(ag)	ms-16(ag)	ms-20(ag)
Texture		Cumulate	Spinifex	Cumulate	Cumulate	Cumulate	Cumulate	Cumulate	Spinifex	Spinifex	Spinifex
SiO_2	0.04	43.17	43.44	41.63	42.97	41.21	42.00	43.00	43.82	42.89	43.61
TiO_2	0.001	0.276	0.344	0.228	0.305	0.2	0.216	0.313	0.355	0.357	0.326
Al_2O_3	0.02	5.99	7.40	4.88	6.55	4.30	4.63	6.69	7.60	7.66	6.99
$Fe_2O_3^T$	0.01	10.93	11.64	10.06	11.44	9.52	9.64	10.97	11.52	11.69	11.60
MgO	0.04	29.37	23.99	32.15	26.52	34.07	33.23	25.74	23.36	23.21	25.59
CaO	0.02	5.56	7.13	4.49	5.75	3.42	4.07	6.65	7.77	8.02	6.59
Na_2O	0.01	0.47	0.49	0.37	0.40	0.34	0.41	0.57	0.65	0.41	0.51
K_2O	0.0006	0.114	0.094	0.077	0.058	0.063	0.081	0.089	0.140	0.070	0.205
P_2O_5	0.001	0.016	0.020	0.013	0.017	0.013	0.014	0.019	0.020	0.020	0.018
Distance from base (m)		0.12	0.13	0.32	0.35	0.40	0.48	0.68	0.72	0.84	1.38

Pyke Hill, cont'd	Flow B										
Reference	Shore 1997										
Sample#	ms-69(ag)	MS91-09	MS91-10	MS91-13	MS91-02	MS91-03	MS91-06	MS91-12	MS91-01	MS91-05	MS91-04	MS91-11
Texture	Cumulate	Cumulate	Cumulate	Cumulate	Cumulate	Cumulate	Cumulate	Cumulate	Spinifex	Cumulate	Spinifex	Spinifex
SiO_2	43.02	44.27	43.95	40.59	41.90	42.22	43.06	42.33	43.75	42.29	43.34	44.44
TiO_2	0.34	0.325	0.325	0.19	0.245	0.248	0.281	0.26	0.312	0.264	0.291	0.335
Al_2O_3	7.30	7.05	6.98	4.04	5.28	5.38	6.05	5.55	6.72	5.62	6.29	7.24
$Fe_2O_3^T$	10.03	11.51	11.43	9.29	10.48	10.86	10.88	10.19	10.59	11.00	10.93	11.60
MgO	24.55	26.06	25.98	34.00	29.88	30.46	28.28	29.92	26.72	29.57	27.71	25.48
CaO	7.27	6.69	6.69	2.83	4.56	4.85	5.27	4.76	6.28	4.87	5.86	7.11
Na_2O	0.28	0.85	0.78	0.32	0.46	0.56	0.58	0.51	0.55	0.51	0.58	0.95
K_2O	0.235	0.110	0.107	0.046	0.063	0.067	0.087	0.068	0.113	0.074	0.110	0.117
P_2O_5	0.020	0.018	0.019	0.015	0.015	0.015	0.018	0.016	0.018	0.016	0.018	0.020
Distance from base (m)	0.02	0.20	0.20	0.20	0.25	0.25	0.25	0.25	0.30	0.30	0.45	0.50

Table 4.1., continued.

Pyke Hill, cont'd	*Flow C*												
Reference	*Shore 1997*												
Sample#	*MS93-02*	*MS93-03(A)*	*MS93-04*	*MS93-05*	*MS93-06*	*MS93-06(A)*	*MS93-07(ag)*	*MS93-07(A)*	*MS93-07(B)*	*MS93-07(CF)*	*MS93-07(FF)*	*MS93-07(sv)*	*MS93-08*
Texture	Cumulate	Cumulate	Cumulate	Cumulate	Cumulate	Cumulate	Cumulate	Cumulate	Cumulate	Cumulate	Cumulate	Cumulate	Cumulate
SiO$_2$	40.87	40.79	42.41	41	40.87	39.23	41.28	41.73	40.97	41.29	40.93	40.36	41.72
TiO$_2$	0.235	0.204	0.21	0.198	0.18	0.175	0.193	0.193	0.189	0.212	0.155	0.191	0.215
Al$_2$O$_3$	4.98	4.35	4.49	4.25	3.90	3.72	4.19	4.23	4.07	4.51	3.43	4.14	4.7
Fe$_2$O$_3$^{T}	9.36	8.95	8.47	9.11	8.55	8.43	8.49	8.57	8.62	8.84	8.32	9.06	9.35
MgO	30.79	32.87	34.41	33.75	35.11	34.06	34.47	34.71	34.51	33.9	35.36	33.22	32.88
CaO	4.54	3.86	3.97	3.39	2.66	2.56	2.96	2.97	2.93	3.38	2.29	2.67	3.91
Na$_2$O	0.32	0.24	0.28	0.34	0.24	0.29	0.28	0.3	0.29	0.36	0.23	0.17	0.45
K$_2$O	0.082	0.043	0.036	0.05	0.036	0.039	0.064	0.068	0.066	0.077	0.051	0.047	0.063
P$_2$O$_5$	0.0123	0.0121	0.0115	0.0119	0.011	0.01	0.0116	0.0117	0.0106	0.0134	0.01	0.0113	0.0123
Distance from base (m)	0.23	0.45	0.70	1.00	1.60	1.60	1.86	1.86	1.86	1.86	1.86	1.86	2.15

Pyke Hill, cont'd	*Flow C, cont'd*												
Reference	*Shore 1997*												
Sample#	*MS93-09*	*MS93-09(ag)*	*MS93-11*	*MS93-10*	*MS93-12*	*MS93-13(A)*	*MS93-13(B)*	*MS93-13(ag)*	*MS93-14(A)*	*MS93-14(B)*	*MS93-15*	*MS93-17A(A)*	*MS93-17A(B)*
Texture	Cumulate	Cumulate	Cumulate	Spinifex	Spinifex	Spinifex	Spinifex	Spinifex	Spinifex	Spinifex	Spinifex	Spinifex	Spinifex
SiO$_2$	41.8	41.39	43.78	43.69	45.06	44.97	45.81	45.36	43.38	43.38	44.09	*43.16*	43.08
TiO$_2$	0.22	0.226	0.373	0.324	0.368	0.36	0.391	0.379	0.321	0.326	0.328	*0.301*	0.3
Al$_2$O$_3$	4.81	4.88	7.81	6.95	7.92	7.84	8.51	8.17	6.94	7.06	7.17	*6.56*	6.51
Fe$_2$O$_3$^{T}	9.49	9.93	9.71	11.22	11.87	12.02	12.19	12.34	11.36	11.46	11.53	*10.82*	10.84
MgO	31.29	31.55	23.81	25.43	23.37	23.52	21.9	22.42	25.32	24.89	25.3	*26.73*	27.12
CaO	4.24	4.19	8.3	7.12	7.63	7.63	8.14	8.2	6.59	6.81	6.82	*6.32*	6.2
Na$_2$O	0.39	0.38	0.35	0.72	0.93	1.1	1.23	1.2	0.78	0.78	0.77	*0.67*	0.69
K$_2$O	0.059	0.059	0.035	0.108	0.099	0.133	0.168	0.125	0.105	0.103	0.143	*0.1*	0.106
P$_2$O$_5$	0.0133	0.013	0.0183	0.0183	0.0208	0.021	0.024	0.0219	0.018	0.0196	0.0194	*0.0177*	0.0181
Distance from base (m)	2.40	2.40	2.58	2.92	3.37	3.66	3.66	3.66	3.96	3.96	4.26	4.55	4.97

Table 4.1., continued.

Pyke Hill, cont'd	*Flow C, cont'd*		
Reference	*Shore, 1997*		
Sample#	*MS93-17B*	*MS93-18(A)*	*MS93-18(B)*
Texture	Spinifex	Spinifex (breccia)	Spinifex (breccia)
SiO_2	43.98	44.4	42.65
TiO_2	0.315	0.276	0.331
Al_2O_3	6.87	6.1	7.12
$Fe_2O_3^T$	10.97	9.64	10.85
MgO	26.28	26.11	24.5
CaO	6.54	6.94	7.64
Na_2O	0.71	0.28	0.35
K_2O	0.152	0.023	0.041
P_2O_5	0.019	0.0178	0.0196
Distance from base (m)	5.17	5.39	5.39

al., 1994; Shimizu et al., 2005). The selection of localities thus includes occurrences critical to modern knowledge of komatiites and spans a range of alteration intensity.

In addition to examination of magmatic processes, this work aims to examine the extent of metasomatism associated with the hydration processes that universally affected even the freshest komatiites (Echeverría, 1980; Aitken and Echeverría, 1984; Nisbet et al., 1993; Renner et al., 1994; Shimizu et al., 2005). Thus, I did not include examples of strongly silicified or carbonated komatiites (Hynes, 1980; Duchač and Hanor, 1987; Hanor and Duchač, 1990; Tourpin et al., 1991).

The following descriptions of various properties of the six komatiites derive from the papers (and thesis) from which I compiled geochemical data, as well as other works on the same lavas, as indicated.

4.2.1. Lithofacies

Komatiite flows commonly display two first order textural subdivisions – an upper spinifex zone (A layer) and a lower cumulate zone (B layer; Pyke et al., 1973; Smith et al., 1980; Arndt, 1986; Arndt et al., 2008). Many workers describe various finer subdivisions corresponding to the nature of the spinifex texture and the appearance of the weathering of the cumulates (Pyke et al., 1973; Arndt et al., 1977; Echeverría, 1980; Smith et al., 1980; Shore, 1997; Dann, 2000; Arndt et al., 2008). Notable textural subdivisions include flow-top breccias in the upper A layer, a basal chill zone in the B layer that is poorer in accumulated phenocrysts than the overlying cumulates, and a thin, phenocryst-poor upper region in the B layer lacking spinifex texture. Readers interested in these and other subdivisions may refer to descriptive works for more information (e.g., Pyke et al., 1973; Smith et al., 1980; Arndt, 1986; Silva et al., 1997; Dann, 2000). Samples of the lava flows examined in this study all represent both spinifex and cumulate zones of each flow. I refer readers to the primary sources (Smith et al., 1980; LaHaye et al., 1995; LaHaye and Arndt, 1996; Shore, 1997; Shimizu et al., 2005) for more detailed textural classifications in the interest of concision.

4.2.2. Petrography and mineralogy

The flows are typical komatiites in that they feature olivine as the main liquidus phase

and the sole silicate phenocryst. Small amounts of chromian spinel phenocrysts occur with olivine phenocrysts in the cumulus zones. The other principal magmatic mineral, clinopyroxene, occurs in various quench-textured forms along with spinifex olivine and chromian spinel. Plagioclase occurs in the innermost regions of some flows (LaHaye and Arndt, 1996; Shore, 1997), forming fine intergrowths with clinopyroxene. Most of the lavas contain devitrified and hydrated glass enclosing the phenocrystic and spinifex-textured minerals. Table 4.2 lists the basic textural and mineralogical features in the lavas.

Alteration mineralogy is more variable, although the most abundant minerals are similar in each lava flow. Table 4.2 lists the alteration minerals in some detail. Serpentine and magnetite replace olivine to varying degrees in all flows, typically without observed brucite, and both minerals are commonly present in altered glass/groundmass. Amphibole (typically reported as tremolite, although measurements are mainly magnesian actinolite; LaHaye and Arndt, 1996; Shore, 1997) replaces clinopyroxene to varying degrees. Chlorite is common in devitrified glasses, and replaces all phases in the flow-top breccia of the Alexo flow and olivine in its rodingitized portions. The groundmass of Alexo contains secondary titanite. Hydrogarnet occurs in the Pyke Hill flows and replaces chlorite along with clinopyroxene in rodingitized parts of Alexo. Sulphides occur in the flow-top of Alexo and in the Pyke Hill flows. Talc and carbonates occur in some of these rocks in minor quantities, mainly in flow-top breccias.

The lavas differ substantially in modal degree of alteration (Table 4.2). The Reliance Formation rocks are the least altered Archean komatiites known, mainly featuring only incipient replacement of olivine by serpentine-dominant assemblages and devitrification of glass. The other lavas are more altered, resulting in greater volatile contents and a higher modal proportion of secondary minerals. Flows A and B from Pyke Hill in the Abitibi are variably altered, but less so than the thicker Flow C (Shore, 1997). The Alexo flow ranges from partially (~30% olivine replacement) to completely serpentinized and is locally rodingitized (LaHaye and Arndt, 1996). Stuart's Flow of the classic Komati Formation shows virtually complete serpentinization of olivine and replacement of clinopyroxene by amphibole (Smith et al., 1980).

Table 4.2. Mineralogical summary

Locality	*Reliance Formation*	*Stuart's Flow*
Reference	*Shimizu et al., 2005; Renner et al., 1994*	*Smith et al., 1980; LaHaye et al., 1995*
Primary phases and textures	**Ol** - sub-euhedral, glomerophyric in cumulates; various skeletal and platy forms in spinifex rocks; phenocrystic and microglomerophyric in upper chill; microlitic in basal chill. **Cr-Sp** - euhedral in cumulates; dendritic to euhedral in spinifex. **Cpx** (*augite with minor Opx and cores, pigeonite rims*) - acicular, plumose, dendritic chains in spinifex and cumulates. Core of pigeonite also occur in the cumulates. **Pl** - forms interstitial intergrowths in Cpx in holocrystalline portions of Cumulate zone. **Glass** (*devitrified*) - present in upper regions of spinifex rocks and interstitial in cumulates.	**Ol** - equant, sub-euhedral in cumulates, various skeletal and platy forms in spinifex rocks.
Secondary phases and textures	**Srp + Mt** - after Ol, along cracks and grain boundaries; mostly minor, locally up to 95% replacement in portions of spinifex rocks. **Chl** - present in devitrified glass.	**Srp + Mt** - complete pseudomorphs after Ol except locally in the cumulate zone, where fresh. **Srp + Mt + Amph** +/- **Chl** - replacement of primary groundmass assemblage in spinifex and cumulate zones. LaHaye et al. (1995) report **Trm** and secondary **Cpx** (*augite*).

Table 4.2, continued.

Locality	*Alexo*	*Pyke Hill flows*
Reference	*LaHaye and Arndt, 1996; LaHaye et al., 1995*	*Shore 1997*
Primary phases and textures	**Ol** - polyhedral-to-skeletal in cumulates, various skeletal and platy forms in spinifex. **Cpx** - acicular and interstitial to olivine in spinifex and cumulate rocks.	**Ol** - polyhedral, equant, sub-euhedral in cumulates; skeletal to platy in spinifex rocks. **Cr-Sp** - equant and sub-euhedral in cumulates; dentritic to equant in spinifex rocks. **Cpx**(*augite*) - variously acicular and dendritic forms, interstitial with respect to Ol in cumulates and spinifex rocks. **Cpx** (*pigeonite*) - Equant grains in groundmass of cumulates, mantled by augite, and as dendritic intergrowths with Pl. **Pl** - Forms only in the innermost regions of Flow C, where intergrown with interstitial pigeonite.
Secondary phases and textures	**Srp + Mt** - pseudomophs after Ol (30% to complete replacement). **Trm** - replacing clinopyroxene. **Chl + Ttn + Mt** - replacing glass. **Chl** - replacing Ol in rodingitized spinifex rocks, all phases in flow-top breccia. **Srp + Brc + Mt** - replacing Ol in rodingitized cumulates. **Cpx** (*Aug*) + **H-Gnt** - replacing chlorite in rodingitized rocks. **Sulphides** - added to flow-top breccias.	Srp, Mt, Chl, Tlc, Trm, sulphides, Cc, Adr (textural positions and relationships unclear from descriptions).

4.2.3. Compositions of phenocrystic olivine

The cumulate facies rocks contain the bulk of the olivine that crystallized as phenocrysts in these lavas. Most of these crystals are (micro-)phenocrysts. The mean compositions of cumulus olivine in each flow are similar (Mg# ≈ 91), except for Alexo, where microphenocrysts and phenocrysts alike have Mg# of ~94 (Arndt, 1986; Sobolev et al., 2016). Phenocrysts in the Reliance flow are more magnesian than the microphenocrysts, and appear principally in the upper portions of the flow (Renner et al., 1994). Zoning, where reported, is normal and varies by under ~8 mol.%. The compositions from the Pyke Hill flows correspond to unspecified textural varieties (Shore, 1997), presumably including both cumulus and spinifex grains. Their mean composition is similar to the microphenocrysts in Stuart's Flow and the Reliance Formation.

4.2.4. Whole rock geochemistry

The whole rock compositions I compiled from prior studies are predominantly X-ray fluorescence measurements (LaHaye et al., 1995; LaHaye and Arndt, 1996; Shore, 1997; Shimizu et al., 2005). The primary source for some of the Stuart's Flow compositions (Smith et al., 1980) did not report the analytical method. Reporting of FeO and Fe_2O_3 was inconsistent and so I treated iron as single component (FeO^T or $Fe_2O_3^T$, depending on the dataset).

I performed all analyses in this thesis on a volatile-free basis, except in plots explicitly showing H content in the Pyke Hill Flow C (in Chapter 5). I estimated H_2O* (and H*) from the loss on ignition (LOI) or [100 - analytical total]. In these cases, I assumed all volatiles were H_2O, owing to the negligible content of carbonate and sulphide minerals indicated in the petrographic descriptions. Volatiles contained in these phases would increase the LOI, thereby increasing H_2O*. Oxidation of Fe^{2+} can yield a gain on ignition of a maximum of ~11% of the FeO content of the rock (assuming complete oxidation of initially divalent Fe). This effect could yield artificially low LOI and thus H_2O* by a maximum of ~1.0-1.2 wt.%. As the initial Fe_2O_3/FeO of these rocks is uncharacterized, I did not correct for this effect, and treated the LOI as the result of removal of structural H_2O alone.

4.3. Geometric hypothesis testing

4.3.1. Rank determination

Determination of the rank of the natural datasets is essential to recovering the dimensionality and identity of the rock composition space (Section 3.3). The most difficult aspect of rank determination is the decision as to whether a rank-reduced approximation is similar enough to the data to regard as insignificantly different. Two approaches are to (1) compute the difference matrix (data – approximation) and compare the differences to uncertainties in the data, and (2) compare the variances in the approximation to those of the data. The first approach deals with adjudicating whether the individual concentrations of the chemical components are reproduced within uncertainty. The second approach considers recovery of the total variance of those components across all samples and/or the total variance of all components within each sample. Applied alone, the first approach is likely to result in determination of a higher rank than the latter, which examines broader inter-measurement and inter-sample variability rather than more restrictive estimates of uncertainty of individual components. In this thesis, I chose the first method as it is less likely to oversimplify the data and thereby remove dimensions of real geological processes from the data. However, this approach will invariably incorporate a greater degree of insignificant variability (uncertainty) into the approximation of the data. Thus, a small amount of this uncertainty will remain in the rock composition space, and the potential for false positives in geometric hypothesis testing exists. For this reason, I emphasize here and elsewhere that geometrically valid hypotheses *must* be compatible with independent geological observations to be acceptable.

Determining rank requires stipulation of the tolerable uncertainty limits. Analytical uncertainty (Table 4.1) derives from sample processing, counting statistics, and any other processing or machine error associated with collection of the raw data. The data sources reported these uncertainties either in absolute (Shore, 1997) or relative (LaHaye et al., 1995; LaHaye and Arndt, 1996; Shimizu et al., 2005) terms, or not at all (Smith et al., 1980). These analytical uncertainties cannot account for natural geological sampling uncertainties arising from fine-scale compositional heterogeneities or modal biases in the componentry of samples that bear no geological significance. As I have

sourced the chemical analyses from prior studies, quantifying these errors directly is not a possibility. Instead I adopted a consistent, if arbitrary, approach using analytical uncertainties or the last reported decimal place (whichever is greater), assuming the latter represents 1σ, with the hope of accounting for geological sampling uncertainty. I chose 4.5σ as the uncertainty cutoff and permitted one measurement to fall outside this range. A total uncertainty of 4.5σ implies a sampling uncertainty of 4.39σ, calculated from the variances, or 97.5% of total uncertainty. The 4.39σ values from Shore's (1997) dataset broadly correspond (i.e., well within an order of magnitude) to the total uncertainty of serpentinite whole rock compositions (Snyder, 1994), supporting the 4.5σ uncertainty cutoff. This approach permitted some amount of rank reduction without appreciably modifying the rock compositions and their mutual relationships. I made the comparison by comparing $|GCM_{dif}|$ (the difference matrix, as in Chapter 3) to the uncertainty limits.

Applying the rank determination procedures of Chapter 3 to the datasets in Table 4.1 returns ranks of seven for each flow, except for Stuart's Flow, whose rank is six.

4.3.2. Parental melt compositions

Each lava flow differentiated from a liquid with a composition presumably limited in its initial variation. A melt composition vector is thus an ideal composition to represent the bulk composition of the system from which the rock compositions originated. Appropriate estimates of the parental melt compositions are available for each of the localities, based on measurements of melt inclusions in olivine (Sobolev et al., 2016) or chromite (Shimizu et al., 2001), and manipulations of whole rock compositions under the assumption that olivine fractionation is the source of magmatic variability (Sossi et al., 2016). Sobolev et al. (2016) reasoned that the Pyke Hill and nearby Alexo komatiites from the Abitibi belt originated from indistinguishable liquids, differing only as a consequence of basal assimilation in Alexo. Thus, I treated the estimates for the Pyke Hill flows as appropriate candidates for the parental liquid to the Alexo flow. Similarly, Sossi et al. (2016) derived an estimate of the parental melt to the Al-depleted Barberton komatiites in general, rather than Stuart's Flow specifically. I tested that estimate as the parent to Stuart's Flow. In total, I tested three parental melt compositions for the Pyke Hill and Alexo flows, two for the Reliance Formation, and one for Stuart's Flow using

the geometric methods in Chapter 3 (Figure 4.1).

Figure 4.1 shows the angles of separation of each melt composition vector from the rock composition spaces of the flows. In each of the Pyke Hill and Alexo flows, one of Sobolev et al.'s (2016) estimates has the lowest angle of separation, and it is within the rock composition space of each flow. I thus adopted that composition as the parental melt vector for those four flows. The two estimates from the Reliance Formation both have similar angles of separation and lie within the rock composition space. I adopted Shimizu et al.'s (2001) estimate over Sossi et al.'s (2016) because it derives from measurements of melt inclusions (i.e., samples of quenched liquid) and is a closer match to the Ti/Al ratio of the whole rocks. The estimate for Stuart's Flow has angles of separation about 3-6 times greater than the other estimates. This misfit requires either that the parental melt composition is inaccurate, or that metasomatism has modified the rock composition space sufficiently to exclude the parental liquid. Given that Stuart's Flow bears virtually complete modal replacement of olivine and clinopyroxene, I cautiously invoke the former interpretation and adopted this melt composition estimate in the definition of the magmatic space. Table 4.3 gives the parental liquid compositions I adopted in analysis of the six flows.

4.3.3. Olivine compositions

I tested 1001 olivine compositions spanning fayalite to forsterite to test the composition(s) of fractionating olivine permitted by whole rock compositions, using the geometric methods from Chapter 3. The results (Figure 4.2) reveal that magnesian olivine vectors are permissible in each dataset, except for Flow B, where the optimal composition (pure forsterite) is essentially on the uncertainty limit (Figure 4.2 E). Pure forsterite is geologically dubious, and this vector lies further out of the magmatic space than do the olivine vectors in the other datasets (with respect to uncertainty; Figure 4.2). These two features imply either that alteration has obliterated the primary olivine vector, leaving no acceptable olivine vector in the anhydrous rock composition space, or that the sample suite is of insufficient size to accurately capture the olivine signal.

Expanding the geometric test to all vectors in the SiO_2-FeO-MgO ternary tests the possibility of fortuitous validity of vectors with olivine stoichiometry, because the

Table 4.3. Geological bases* for magmatic spaces.

Locality	Reliance Formation		Stuart's Flow			Alexo			Flow A		Flow B		Flow C	
Vector identity	Parental melt (Shimizu**)	Olivine	Parental melt (Sossi**)	Olivine	Clinopyroxene	Parental melt (Sobolev**)	Olivine	Sediments (LaHaye**)	Parental melt (Sobolev**)	Olivine	Parental melt (Sobolev**)	Olivine	Parental melt (Sobolev**)	Olivine
SiO_2	0.8125	0.4776	0.7939	0.4790	0.8583	0.7506	0.4638	0.9465	0.7506	0.4772	0.7506	0.4798	0.7506	0.4779
TiO_2	0.0046	0.0000	0.0053	0.0000	0.0000	0.0034	0.0000	0.0113	0.0034	0.0000	0.0034	0.0000	0.0034	0.0000
Al_2O_3	0.0750	0.0000	0.0442	0.0000	0.0000	0.0579	0.0000	0.1253	0.0579	0.0000	0.0579	0.0000	0.0579	0.0000
FeO^T	0.1487	0.0802	0.0713	0.0843	0.1792	0.1438	0.0427	0.0228	0.1438	0.0792	0.1438	0.0864	0.1438	0.0812
MgO	0.5816	0.8749	0.6466	0.8737	0.3583	0.7791	0.8849	0.0662	0.7791	0.8752	0.7791	0.8731	0.7791	0.8746
CaO	0.1220	0.0000	0.1307	0.0000	0.3208	0.0963	0.0000	0.0289	0.0963	0.0000	0.0963	0.0000	0.0963	0.0000
Na_2O	0.0095	0.0000	0.0100	0.0000	0.0000	0.0076	0.0000	0.0136	0.0076	0.0000	0.0076	0.0000	0.0076	0.0000
K_2O	0.0002	0.0000	0.0004	0.0000	0.0000	0.0001	0.0000	0.0676	0.0001	0.0000	0.0001	0.0000	0.0001	0.0000
P_2O_5	NA		0.0003	0.0000	0.0000	NA			0.0001	0.0000	0.0001	0.0000	0.0001	0.0000

*These basis vectors are unit vectors with geological meaning that define all whole rock compositional changes that arrise from magmatic processes.

Sources: **Shimizu = Shimizu et al., 2001; **Sossi** = Sossi et al., 2016; **Sobolev** = Sobolev et al. (2016); **LaHaye** = LaHaye et al. (2001).
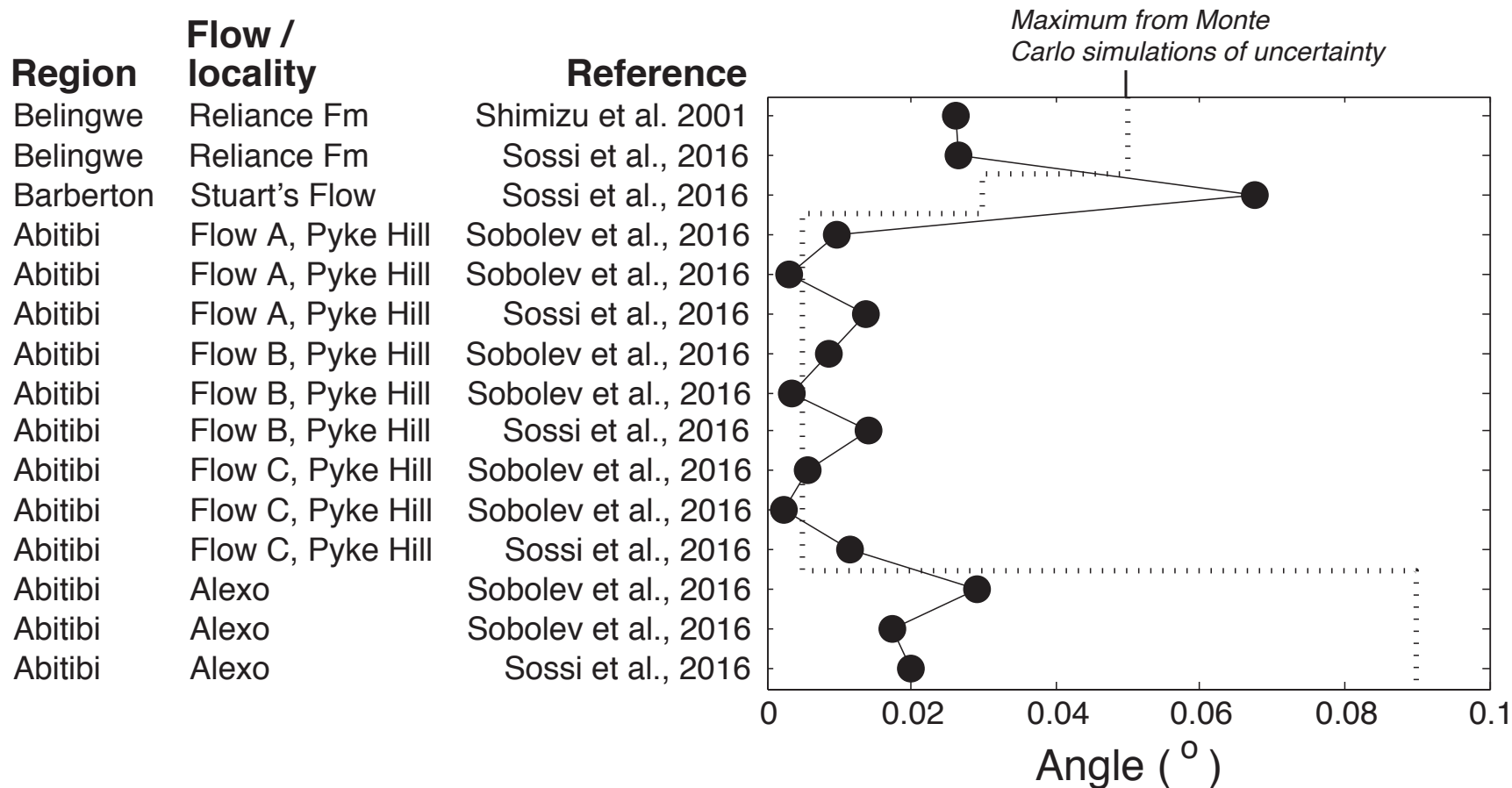
Figure 4.1. Angles of separation between the rock composition spaces and various estimates of parental melt compositions for komatiites from the Reliance Formation, Abitibi Greenstone Belt, and Barberton Greenstone Belt.
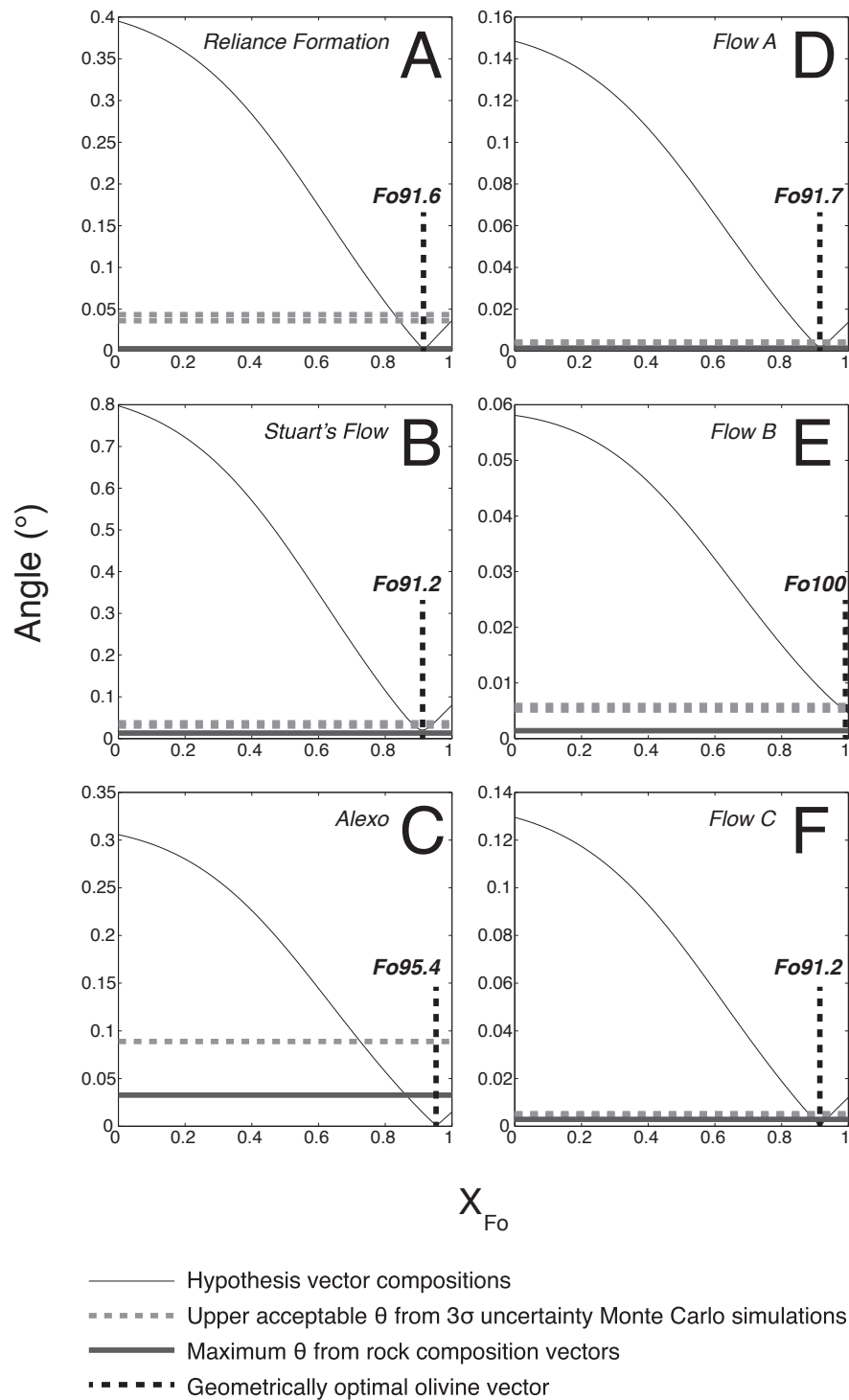
Figure 4.2. Angles of separation between all olivine compositions and the rock composition spaces of the six flows. The optimal olivine compositions (***dashed black lines***) lie well within uncertainty of the rock composition space of each lava, except in the case of Flow B (**Panel E**) where the optimal vector (forsterite) lies just within the uncertainty limit. The ***horizontal solid*** and ***dashed*** lines mark the maximum angles of the actual rock compositions and Monte Carlo simulations of 3σ uncertainty, respectively.

hypothesis vectors are no longer limited to a fixed SiO_2 content (Figure 4.3). The line with $SiO_2 = 33.33\%$ corresponds to the diagrams in Figure 4.2, which are sections at fixed silica content through the ternary. The rocks in each suite other than Flow B permit vectors with the stoichiometry of olivine that match the optimal vectors in Figure 4.2. In Flow B, the optimal SiO_2-FeO-MgO vector corresponds to a slightly silica-deficient and/or MgO-enriched (compared to olivine), iron-free composition (Figure 4.3 E). The optimal SiO_2-FeO-MgO vectors in some other flows (i.e., Stuart's Flow, Flow A) also lack the stoichiometry of olivine, but geologically reasonable olivine compositions are well within uncertainty of the rock composition space. Thus, whether the discrepancy is geologically meaningful or merely an artifact of uncertainty is unclear. Abitibi Flow C permits two full dimensions of vectors in SiO_2-FeO-MgO space, including olivine with Mg# ≈ 91.

Comparing the optimal olivine vectors to real olivine compositions from the lavas shows a good correspondence between the vector compositions and the mean composition of cumulus olivine cores (or olivines of unspecified texture in the case of Pyke Hill; Figure 4.4) in all lavas except Flow B and Alexo. In addition to the obviously aberrant case of Flow B, the Alexo vector also disagrees with the compositions of its olivines, it being more magnesian than any olivine composition measured therein. The mismatch between the optimal olivine compositions and measured compositions in these two flows may relate to the influence of metasomatism hindering recovery of the primary signals, uncertainties in the data, or some combination thereof. In the case of Alexo, uncertainties likely explain the disagreement (Figure 4.3 C), whereas in Flow B either metasomatism or insufficient sampling are more probable, as the measured olivine composition is outside the bounds of uncertainty (Figure 4.3 E).

I used the optimal olivine compositions of flows A and C, Stuart's Flow, and the Reliance Formation in Figure 4.2 to represent olivine fractionation. I stipulated a composition of Fo_{91} for Flow B, as this is a close match to its olivines and those of the related flows A and C. In the case of Alexo, I retained the apparently overly magnesian optimal vector instead of an arbitrary choice of another composition within uncertainty of the rock composition space.
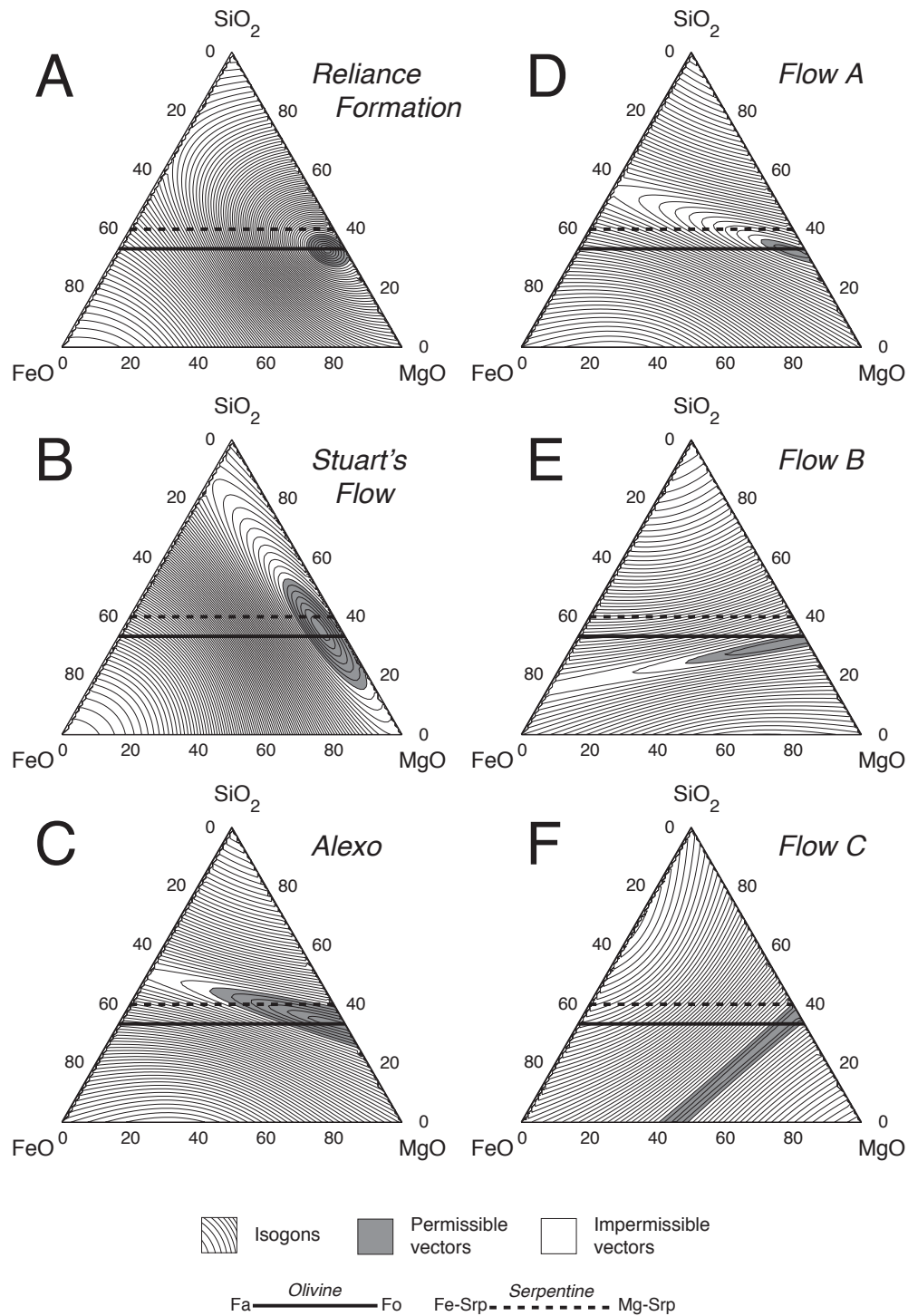
Figure 4.3. Ternary diagram of SiO_2, MgO, and FeO showing geometrically permissible vectors (***grey field***) in the rock composition spaces of the flows. The ***solid lines*** at 33.33% SiO_2 correspond to all olivine compositions, and correspond to the x-axes in Figure 4.2. The ***dashed lines*** at 40% SiO_2 correspond to stoichiometrically ideal serpentine compositions. Contours represent constant angles of separation.
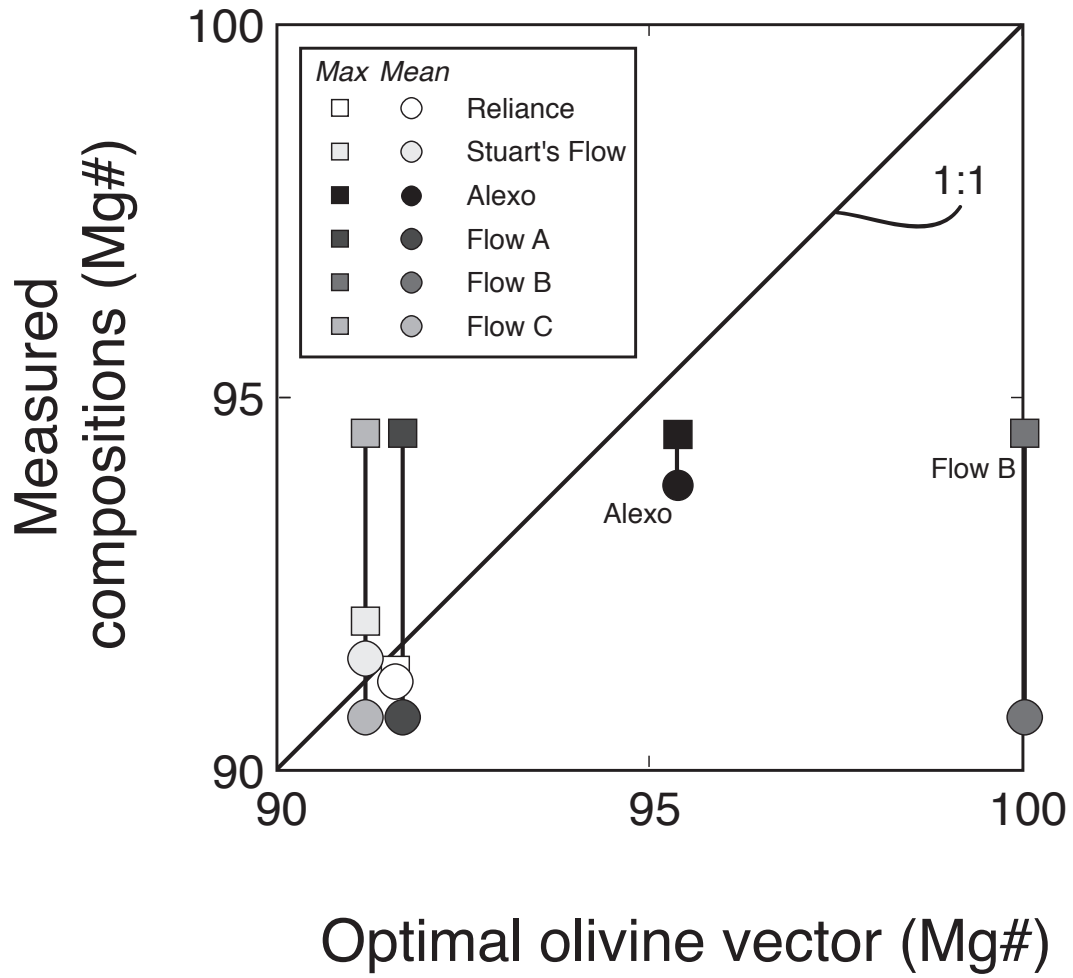
Figure 4.4. Comparison of the Mg#s of optimal olivine vectors to the mean and maximum values for olivines measured from the six flows.

4.3.4. Other sources of magmatic variability

In addition to olivine sorting, I tested for vectors corresponding to various other magmatic phases pertinent to komatiites, namely pyroxenes, spinels, and plagioclase. No dataset yielded any permissible spinel or plagioclase vectors. Stuart's Flow and the Reliance Formation rocks both permit compositions in the enstatite-ferrosilite-wollastonite ternary (Figure 4.5), corresponding to augite ($Mg_{0.84}Fe_{0.42}Ca_{0.75}Si_2O_6$) and ferroan augite verging on pigeonite ($Mg_{0.24}Fe_{1.34}Ca_{0.43}Si_2O_6$), respectively. Neither of these pyroxene vectors are plausible clinopyroxene fractionation vectors, as these rocks contain no pyroxene phenocrysts, nor is clinopyroxene present in the phase assemblage ~200 °C subliquidus in komatiite liquid (Arndt et al., 2008). However, the augite vector in the Stuart's Flow data corresponds well with the more evolved augites of the Barberton komatiites (Parman et al., 1997; Figure 4.6), and is thus a possible magmatic geochemical signal in the rock composition space of Stuart's Flow. The augite vector may represent late-stage reaction between evolved residual melt and earlier clinopyroxene, or formation of the secondary augite that LaHaye et al. (1995) reported. Alternatively, the vector may be a geologically meaningless linear combination of other process vectors.

The extreme Fe-enrichment of the pyroxene vector the Reliance rocks permit is well outside the typical limits of komatiitc clinopyroxenes, and bears no obvious relationship to clinopyroxene compositions in the Reliance komatiite specifically (Shimizu et al., 2005; Figure 4.6). Thus, this Fe-rich pyroxene vector does not appear to be a viable magmatic signal in the Reliance Formation composition space. This vector may merely be a linear combination of other thus far undetermined geological vectors, or represent some clinopyroxene-forming or modifying process that escaped notice (or measurement) of previous authors. Whatever the precise geological meaning of the vector (if any), it does not appear to belong in the magmatic space, and I thus exclude it therefrom.

LaHaye et al. (2001) concluded that the Alexo flow experienced contamination by the sulphidic sediments in the adjacent strata. Sobolev et al. (2016) invoked assimilation of this contaminant to explain compositional diversity in its olivine-hosted melt inclusions. I tested the average major element composition of these sediments (LaHaye et al., 2001) as a magmatic process vector in the rock composition space. That average
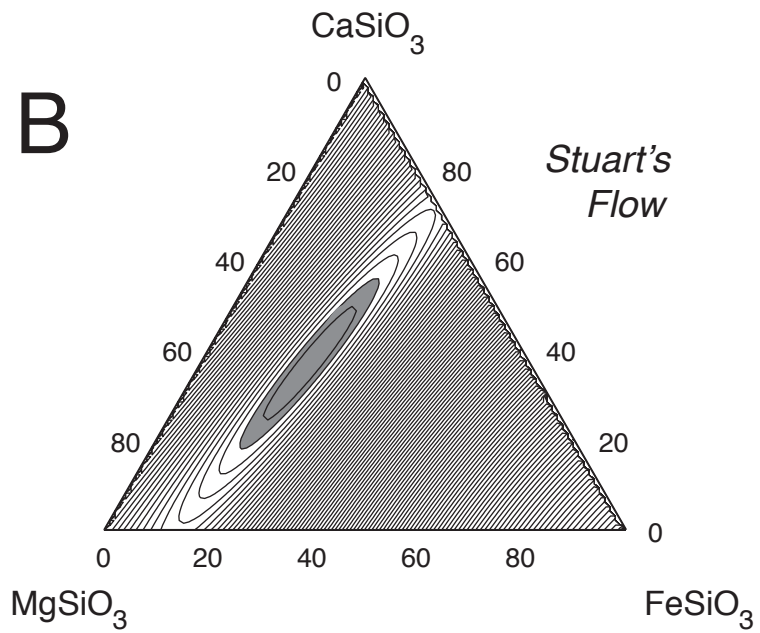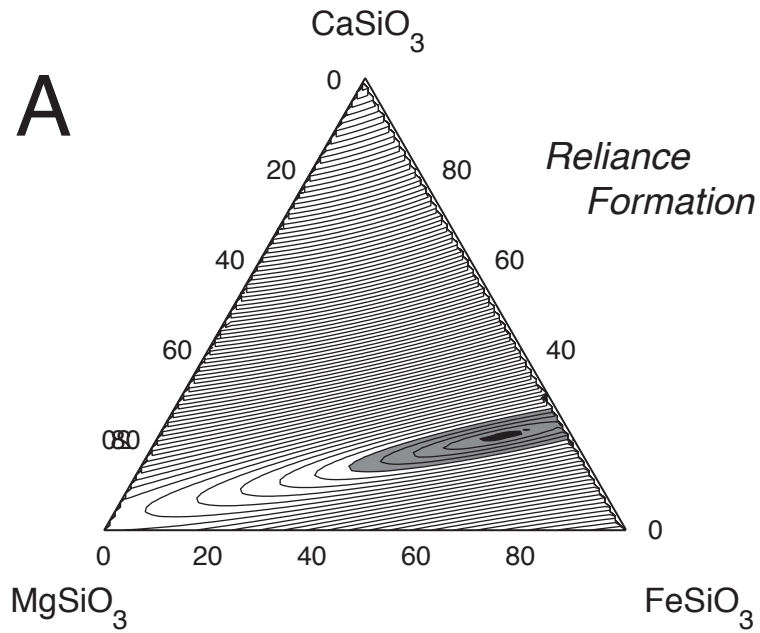
Figure 4.5. Ternary diagram of enstatitie, ferrosilite, and wollastonite showing geometrically permissible pyroxene vectors (***grey fields***) in the Reliance Formation (**A**) and Stuart's Flow (**B**). Contours represent constant angles of separation.
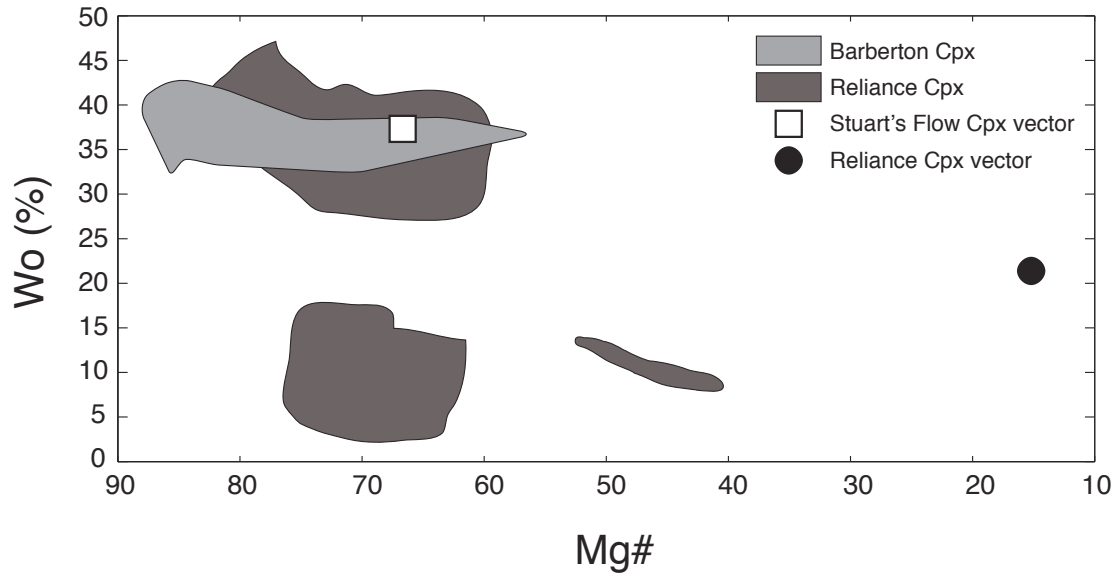
Figure 4.6. Comparison of the compositions of optimal pyroxene vectors in the Reliance Formation (***black circle***) and Stuart's Flow (***white square***) with clinopyroxenes from the Reliance (***dark grey fields***) and Barberton komatiites (***light grey field***). Data after Parman et al. (1997) and Shimizu et al. (2005).

composition is within uncertainty of the rock composition space (0.0514°), thus validating its inclusion in the magmatic space, and confirming the prior conclusions.

4.4. Olivine-liquid equilibria and the composition and temperature of komatiitic differentiates

4.4.1. Mg-Fe partitioning

Here I combine Mg-Fe^{2+} partitioning calculations with binary fractionation models and thermodynamically constrained recalculations of whole rock compositions to determine the composition of equilibrium liquid and the temperature of peak differentiation of komatiite lavas.

I applied Mg-Fe^{2+} partition coefficients between olivine and melt to determine Fe^{2+}:Mg of liquid in equilibrium with the optimal olivine compositions (Roeder and Emslie, 1970). Studies of the exchange of Mg and Fe^{2+} between liquids and olivine typically report distribution coefficients (K_d = [Fe^{2+}/Mg]$_{Ol}$ × [Mg/Fe^{2+}]$_{Liq}$) in the range of 0.3-0.35 for mafic-ultramafic bulk compositions (Roeder and Emslie, 1970; Kilinc et al., 1983; Putirka, 2005; Matzen et al., 2011). A literature review (Matzen et al., 2011) favoured a value of ~0.34 for basaltic compositions, whereas a new experimental study on komatiitic bulk compositions (Sossi and O'Neill, 2016) reports values ~0.3 at oxygen fugacities (fO$_2$) similar to determinations for natural komatiites. I thus used the value of 0.3 in all partitioning calculations (Sossi and O'Neill, 2016), and verified this choice using temperature and composition-dependent models (Putirka, 2005) following determination of liquid compositions and temperatures (sections 4.4.3 and 4.4.4).

Ratios of Fe^{2+} to Mg of liquids in equilibrium with optimal olivine compositions are higher than those of the parental melt estimates, with the sole exception of Alexo. This tendency towards higher Fe^{2+}/Mg indicates that these liquids are evolved differentiates of their parents. In the case of Alexo, the anomalously high forsterite content of the optimal olivine corresponds to a liquid more refractory than the parent. Given the uncertainty surrounding the optimal olivine for the Alexo rocks, and the absence of olivines of such extreme forsterite content therein, I regard the geometrically optimal olivine as either spurious or disturbed by metasomatism. I thus do not further consider its equilibrium liquid composition.

4.4.2. Binary fractionation models

I constructed model curves corresponding to linear combinations of optimal olivine and parental liquid to provide first-order estimates of evolved liquid compositions (Figure 4.7). The evolved equilibrium liquid is that with Fe^{2+}/Mg equal to that predicted from partitioning calculations. Assuming all Fe in the parental liquid was divalent, the optimal liquids range from ~27-31 mol.% MgO. This MgO content and the corresponding Fe^T/Mg are the most refractory equilibrium liquids permissible for the optimal olivine compositions, as the presence of trivalent Fe shifts the position of the equilibrium liquid along the fractionation curve to lower MgO and higher Fe^T/Mg (shown for the Abitibi Flow C model in Figure 4.8).

4.4.3. Whole rock equilibrium models

An alternative (and complementary) approach to modeling olivine-liquid equilibria is to recalculate whole rock compositions into the optimal olivine composition and the melt in equilibrium therewith (Russell and Snyder, 1997). Russell and Snyder (1997) used thermodynamic constraints relating temperature (T), Mg-Fe equilibria, Fe valence state, and fO_2 to perform such calculations (Roeder and Emslie, 1970; Sack et al., 1981; Kilinc et al., 1983; Kress and Carmichael, 1991). I applied that methodology (updated code courtesy of J.K. Russell, 2017) to the whole rock compositions from Abitibi Flow C – the best-characterized flow – and the parental melt composition for the Pyke Hill komatiites. The inputs are the optimal olivine composition, the bulk compositions, and a constant fO_2 value. The outputs include the bulk composition of the equilibrium liquid, the weight proportion of olivine required to produce it, its liquidus temperature (T_L), and its Fe^{3+}/Fe^{2+}.

 The specified fO_2, T_L, and liquid composition determine the Fe valance state (Kilinc et al., 1983). I chose the fO_2 value so that the calculation would return Fe^{3+}/Fe^{2+} that corresponds to known redox constraints on komatiitic liquids and the parental melt composition (Canil, 1997; Sobolev et al., 2016). The range of Fe^{3+}/Fe^{2+} expected for liquid compositions from the fractionation model of the Pyke Hill flows is ~0.07 to ~0.32 for the fO_2 of natural komatiites (-2 and +1 log units of the Ni-NiO buffer [NNO]; Canil, 1997). Estimates of the Pyke Hill parental melt composition have Fe^{3+}/Fe^{2+} of ~0.12-
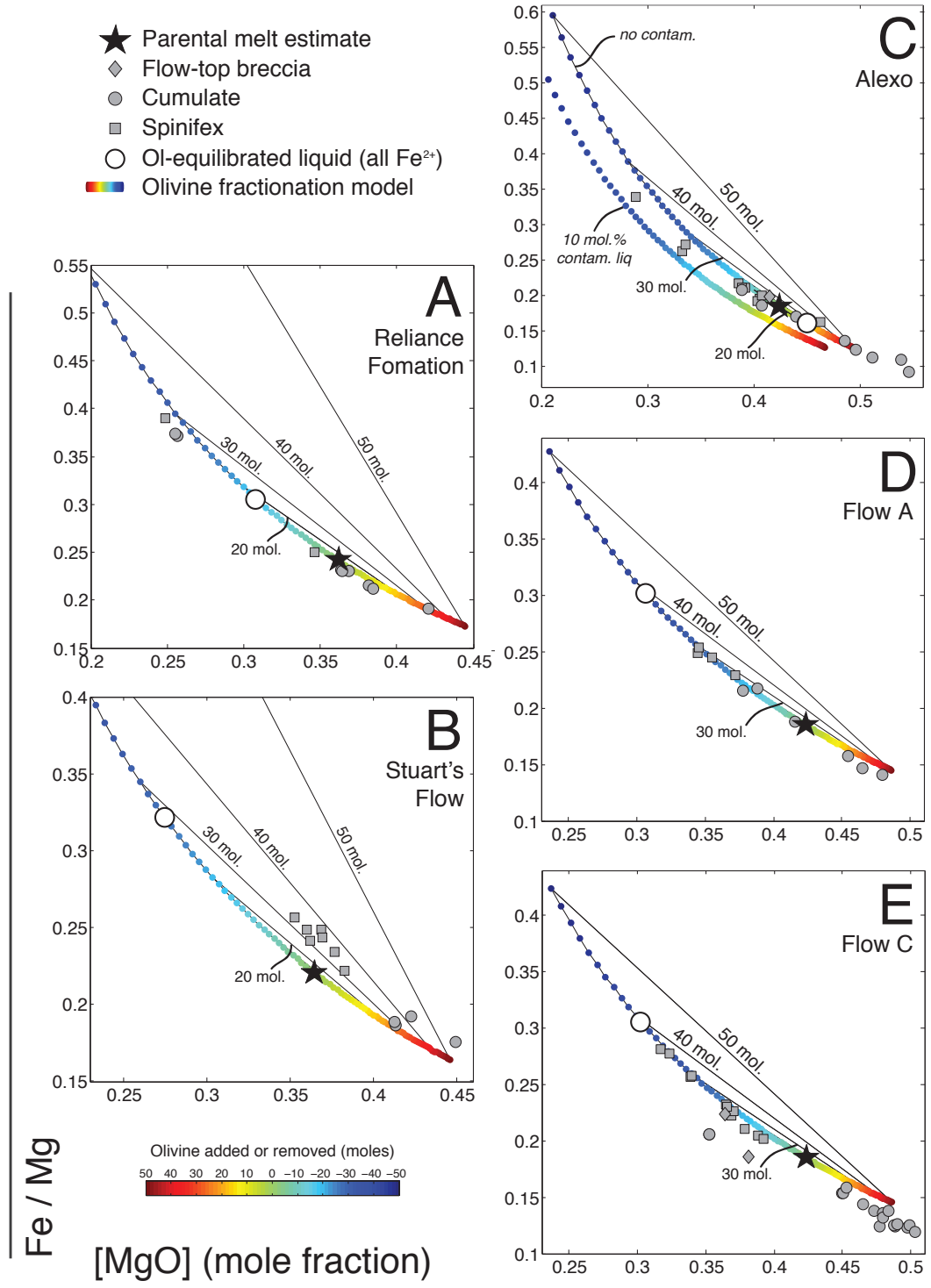
Figure 4.7. Systematics of MgO concentration and Fe^T/Mg in binary fractionation models comprising linear combinations of parental melt and optimal olivine compositions. The evolved liquids in equilibrium with optimal olivine are the most refractory liquids possible, owing to the assumption of only divalent Fe in the system. Each panel corresponds to a different flow, as annotated.
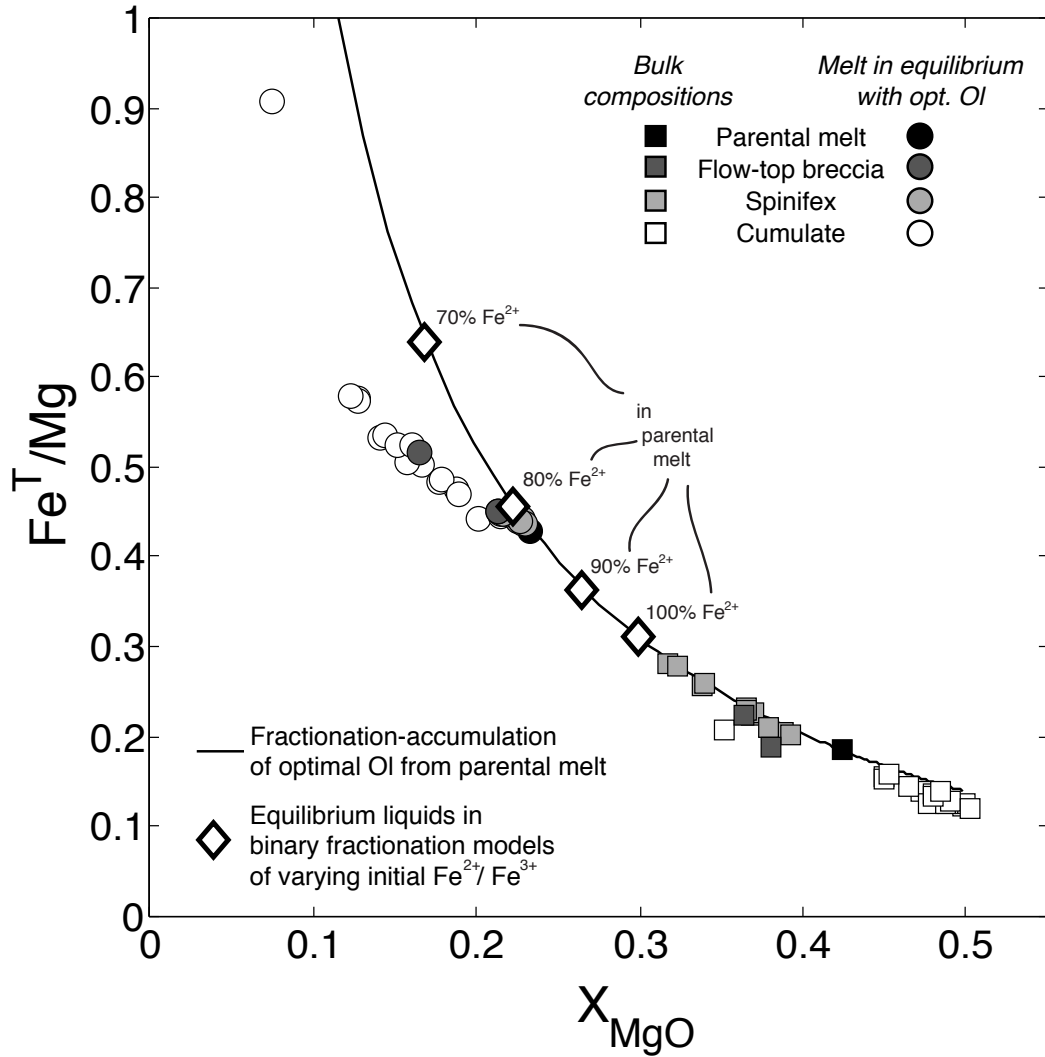
Figure 4.8. Bulk compositions (*squares*) and their calculated liquids in equilibrium with optimal olivine, Flow C. Calculated liquids (*circles*) from spinifex rocks converge with the fractionation curve, whereas cumulates and flow-top breccias diverge from it, likely resulting from metasomatism. Spinifex-textured thus retain primary Mg-Fe systematics. The position of equilibrium melts from binary fractionation models (*diamonds*) are shown for various assumed initial Fe^{2+}/Fe^{3+} of the parental melt.

0.17, nearly equal to NNO at T ≈ 1550 °C (Sobolev et al., 2016). If fO_2 remained near NNO during magmatic evolution, it would attain values of ~0.2 at T in the range of 1350 to 1450 °C. Thus, I iterated fO_2 in the calculation until parental bulk compositions equilibrated at Fe^{3+}/Fe^{2+} of ~0.2 (input value of $log(fO_2)$ = -4.6).

Liquids in equilibrium with whole rock compositions and optimal olivine from Abitibi Flow C range substantially in terms of MgO content and Fe^T/Mg (Figure 4.8). The highest Fe^T/Mg and lowest MgO content of the liquids correspond to cumulate-textured samples and a flow-top breccia. Calculated liquids from spinifex-textured rocks are less variable and nearly coincident with the model fractionation curve, and the parental melt composition ideally intersects it. Thus, spinifex bulk rock compositions are nominally consistent with Mg-Fe equilibrium between optimal olivine and this evolved liquid. This liquid has ~15.5 wt.% MgO, within the range of 18% down to ~6% for komatiitic basalts (by definition; Arndt et al., 2008). Bulk compositions of cumulates and flow-top breccias are inconsistent with Mg-Fe equilibrium between optimal olivine and this liquid – the cause of the deviation from the fractionation model is likely metasomatism, as other potential magmatic process vectors are not within the rock composition space.

4.4.4. Temperature of evolved komatiite liquid

The liquidus temperatures of mafic-ultramafic bulk compositions empirically correlate to their MgO content (Arndt et al., 2008). Another means to estimate T_L is to calculate the T of olivine saturation using $Mg-Fe^{2+}$ partitioning constraints (Roeder and Emslie, 1970; Russell and Snyder, 1997). I compared T_L determined by both methods for the liquids in equilibrium with whole rock compositions and optimal olivine in Abitibi Flow C (Figure 4.9). The two approaches yield similar, but not identical, results. The T_L for the liquid in equilibrium with the parental melt composition and optimal olivine (i.e., the preferred evolved liquid) is from 1345 to 1360 °C, depending on the thermometer. I verified the applicability of the partition coefficient using a temperature and composition-dependent model (Putirka, 2005) with both of these temperatures, returning values of 2.99 and 3.01, indistinguishable from the 3.00 value in equilibrium calculations. This range of T_L is well below that previously determined for the Pyke Hill and other komatiites (~1500-1650 °C;
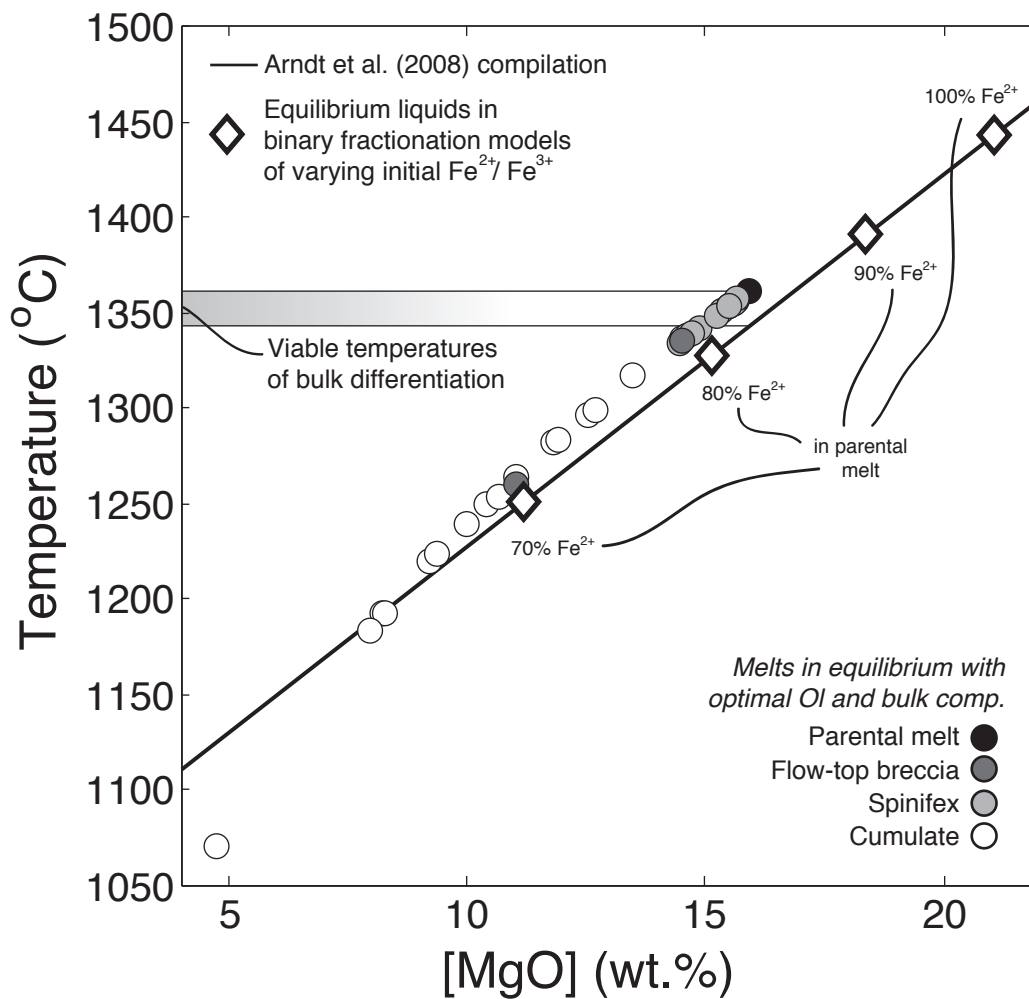
Figure 4.9. Comparison of olivine saturation temperatures of whole rock compositions of Flow C (*circles*) and the MgO content thermometer compiled by Arndt et al. (2008). The two methods broadly agree and return temperatures of ~1345 and ~1360 °C for the parental bulk composition at equilibrium with optimal olivine.

e.g., Green, 1975; Arndt, 1976), and likely corresponds to the T_L at which the bulk of olivine phenocryst crystallization and fractionation occurred, not the liquidus temperature of the parental liquid.

4.5. Assessment of bulk olivine accumulation

Identification of excess olivine is central to testing whether a given komatiite exposure differentiated synchronously with lava emplacement (Figure 4.10 A) or following ponding and stagnation (Figure 4.10 B). The detailed sampling through a vertical transect in Flow C from the Pyke Hill locality in the Abitibi, coupled with the preceding analyses, enables a rigorous assessment of the state of olivine enrichment or depletion therein.

Equilibrium calculations for bulk composition-optimal olivine pairs yielded ~10-28 wt.% olivine among the whole rock and parental liquid compositions. The proportion of equilibrium olivine in the parental liquid (19.76 wt.%) represents the proportion the entire vertical transect would retain if olivine settling occurred in a stagnant pond. To determine deviations from this olivine budget, I adopted the PER approach to restore extensive relationships; i.e., I divided the wt. % olivine (Ol_{wt}) by the wt.% Al_2O_3 ($Al_2O_{3\,wt}$, recalculated on a volatile-free basis, normalized to 100% total), the latter being a conserved component. The relative, extensive gain of olivine in a given sample (ΔOl_{Rock}) with respect to the parental bulk composition is

$$\Delta Ol_{Rock} = \frac{Ol_{wt}}{Al_2O_{3\,wt}}\,Rock - \frac{Ol_{wt}}{Al_2O_{3\,wt}}\,Parent. \tag{4.2}$$

Figure 4.11 shows variations in ΔOl_{Rock} with vertical position in Flow C. All spinifex-textured samples and flow-top breccias are olivine-deficient with respect to the parental liquid, whereas all cumulate facies rocks (except one, in the B1 layer) are olivine-enriched. Taking the integral of ΔOl_{Rock} over the thickness of the flow and dividing by the total thickness gives the overall gain or loss of olivine of the section, which translates to the +7.1% enrichment in olivine with respect to the parental liquid. Thus, this section of Flow C likely differentiated during active flow, with flow-through and departure of the evolved liquid ultimately yielding olivine enrichment.

Prior workers noted that the overabundance of olivine requires that the missing liquid flowed elsewhere (Lesher, 1989; Arndt et al., 2008), yielding more differentiated
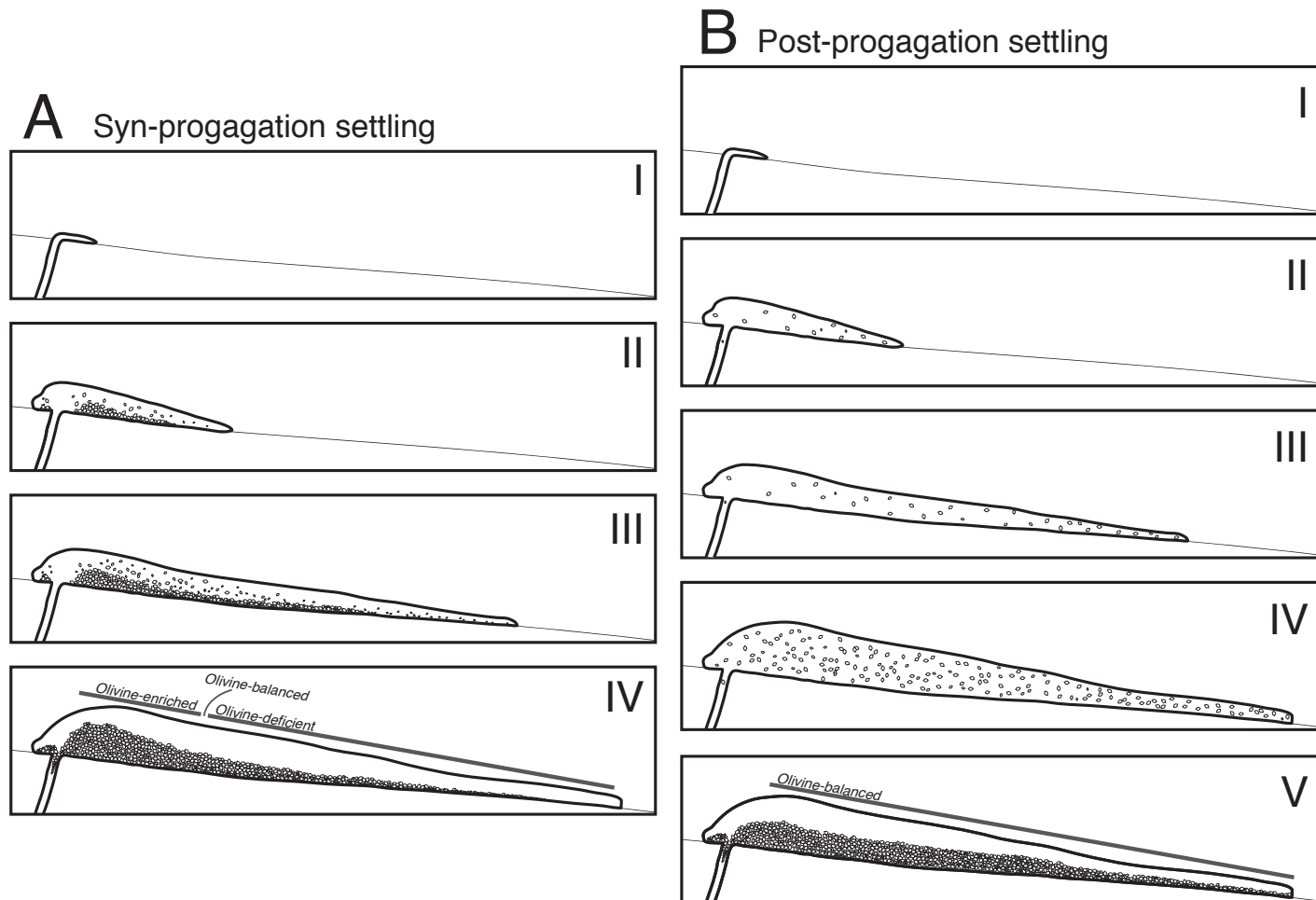
Figure 4.10. Schematic summary of two scenarios of lava propagation and olivine settling. (**A**) In the syn-propagation scenario, olivine phenocryst growth and settling occur as the flow propagates, leading to thicker cumulates near the vent and lateral variations in the degree of olivine enrichment or depletion. (**B**) In post-propagation settling olivine remains suspended during flow, settling after stagnation, thus yielding a net balance of olivine in vertical sections through the flow.
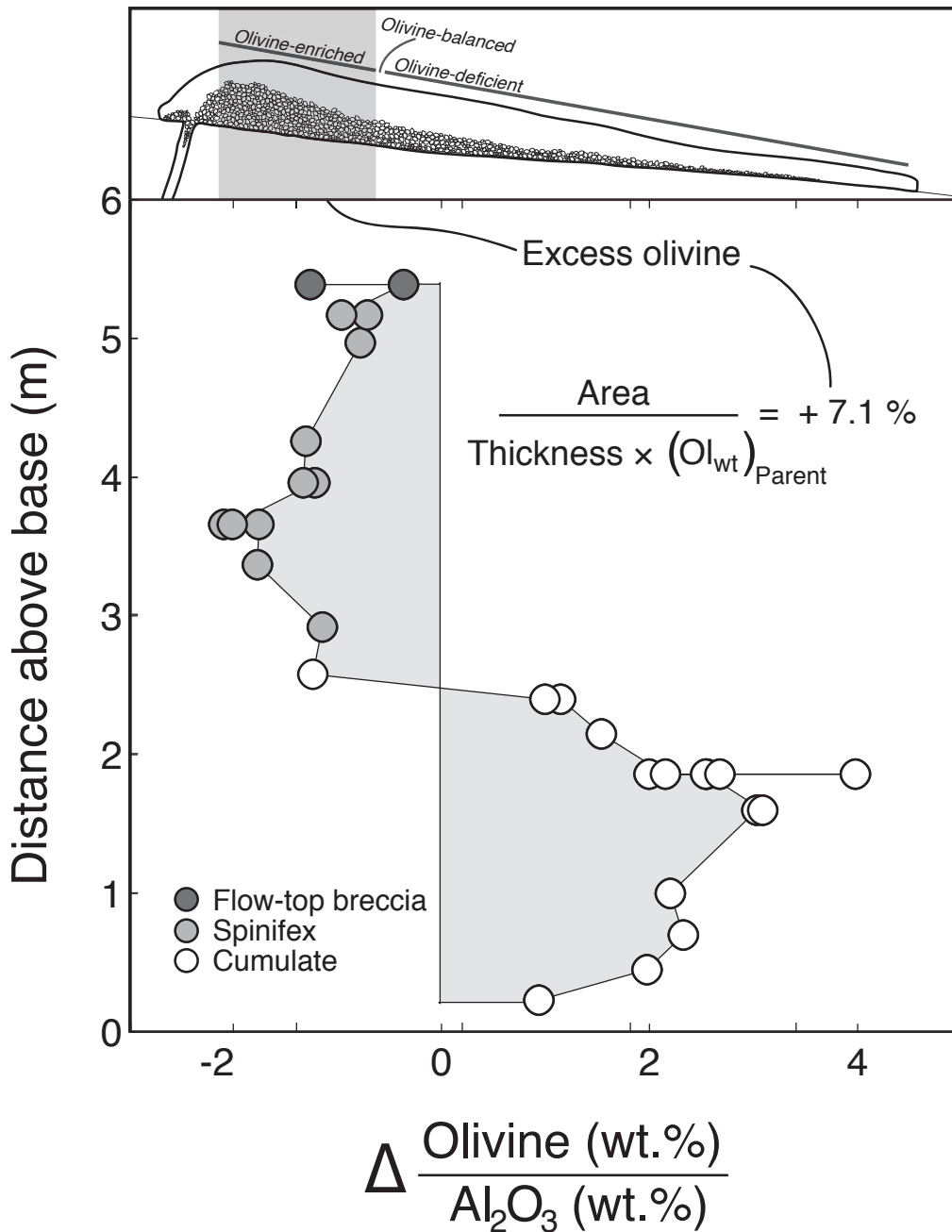
Figure 4.11. Gains and losses of olivine phenocrysts with respect to the parental melt, Flow C. This vertical section bears ~7% excess olivine over what would arise from static settling in a stagnant pond. This result thus implies syn-propagation settling, and places this exposure relatively close to the vent.

lavas downstream. Given that the equilibrium liquid composition here is chemically komatiitic basalt, I infer that complete lateral continuity between ultramafic komatiites and komatiitic basalts within individual lava flows is a geochemically viable hypothesis. The rigorous chemical deconstruction presented here concurs with independent prior conclusions from facies analysis, and can help explain the similarities of incompatible element systematics between some komatiite and komatiitic basalt co-occurrences, for example in Munro Township, Ontario (Arndt and Nesbitt, 1984). Moreover, the potential exists for within-flow differentiation of other low-viscosity magma types, if high-volume flow-through is persistent and subliquidus phase relationships are appropriate. Perhaps within-flow differentiation could be important in carbonatite or picrite lavas.

4.6. Magmatic space and metasomatic disturbance

The failure of the liquids in equilibrium with rock compositions of Abitibi Flow C and optimal olivine to follow the olivine fractionation model indicates the action of other chemical processes. Metasomatic modification likely explains this departure. Here I develop a new means to quantify the magnitude of metasomatic modification, the Metasomatic Index, which I apply to all of the six flows investigated here. The approach is to develop a magmatic model that should fully encompass magmatic compositional variability, and quantify deviation therefrom.

4.6.1. Magmatic space

The magmatic space is a model space (Chapter 3) that encompasses magmatic mass transfer processes. Thus, bases for the magmatic spaces of each dataset consist of the set of linearly independent mass transfer vectors that fully encompass the magmatic processes, as tested previously in this chapter. In each case, this space consists of the best available estimate of the parental melt and an olivine vector. In Stuart's Flow and Alexo, additional clinopyroxene and contaminant vectors (respectively) round out the magmatic space. The full sets of the specific magmatic space vectors are in Table 4.3. Testing rock compositions in a given dataset against this definition of the magmatic space determines how much a given sample's deviation from the parental melt cannot be explained by magmatic processes, as defined therein.

4.6.2. A metasomatic index for komatiites

If the magmatic space accounts for magmatic processes, the corollary is that it must fully contain rock compositions formed by those processes. Treating the magmatic basis as a model for the compositional variation allows application of the procedures in Chapter 3 (Section 3.5). The magmatic space becomes the model space, and we test the rock compositions against it to determine whether magmatic processes can fully explain the rocks. Figure 4.12 shows the results of projecting whole rock compositions onto U_H of the magmatic bases for the Reliance Formation and Abitibi Flow C. The diagrams show the orthogonal magnitude of processes other than olivine fractionation necessary to explain the whole rock compositions. Those processes are metasomatic, as magmatic variation lies in magmatic space only. The relationships in Figure 4.12 show differences between the datasets that mimic their petrographic and geochemical characteristics, namely the uniform extent of alteration of the Reliance sample suite (Shimizu et al., 2005), and the variable extent of alteration of Flow C (Shore, 1997).

Figure 4.13A visualizes the extent of deviation from the magmatic space in ternary diagrams, with two vertices containing the absolute magnitudes of the orthonormal vectors in the magmatic space, and one showing the absolute magnitude of vectors outside the magmatic space. The total magmatic fraction (Figure 4.13 B; i.e., the amount of a composition the magmatic space can explain), ranges from ~90% to >99% of any given composition.

If the magmatic spaces capture all meaningful magmatic variation (i.e., are sufficiently described by their basis vectors), the disagreement between real rock compositions and their projections onto the magmatic space must relate to the magnitude of additional processes. By the process of elimination, these processes must encompass the cumulative metasomatic effects resulting from hydrothermal alteration. Following the procedures in Chapter 3 (Section 3.5) for calculating the angle between a vector and a model space gives the angle by which each rock composition lies out of the magmatic space. The sine of this angle gives the Metasomatic Index (*MI*),

$$MI = \sin(\theta), \tag{4.3}$$

a quantity whose theoretical limits are zero and one that represents the magnitude of metasomatic processes operating *outside* the magmatic space. Any metasomatic
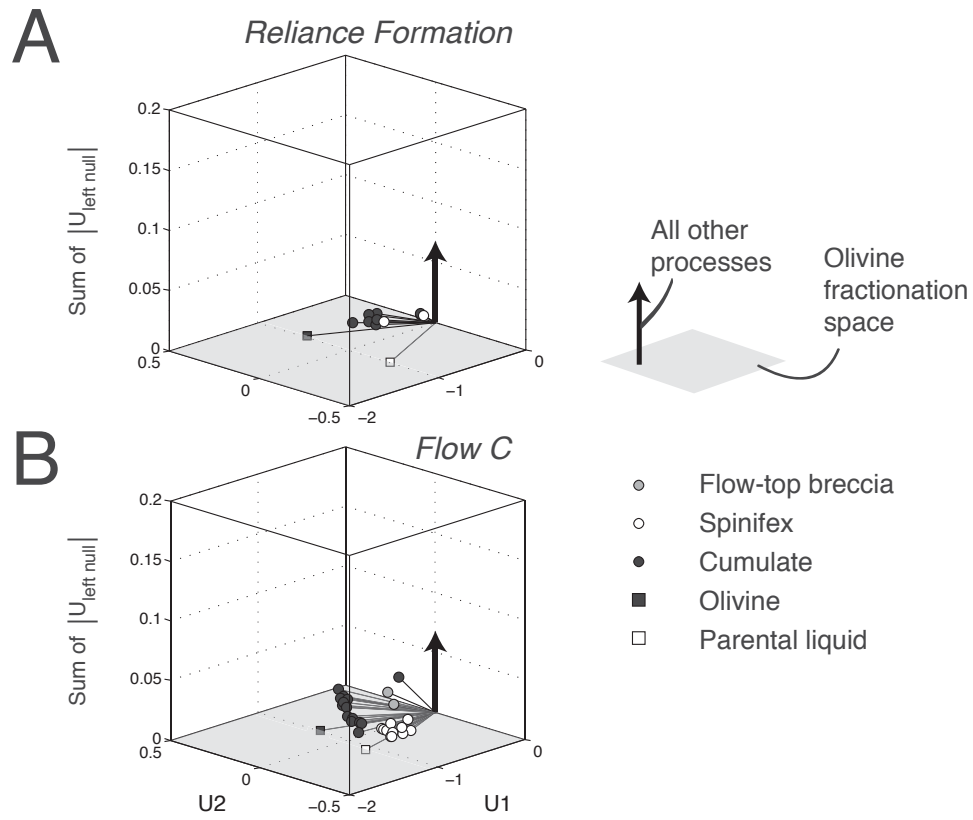
Figure 4.12. Projections of rock compositions from the Reliance Formation (weakly altered; **A)** and Flow C (variably altered; **B)** onto the magmatic space and its left null space. Processes other than olivine fractionation result in vertical displacement from the *grey plane*.
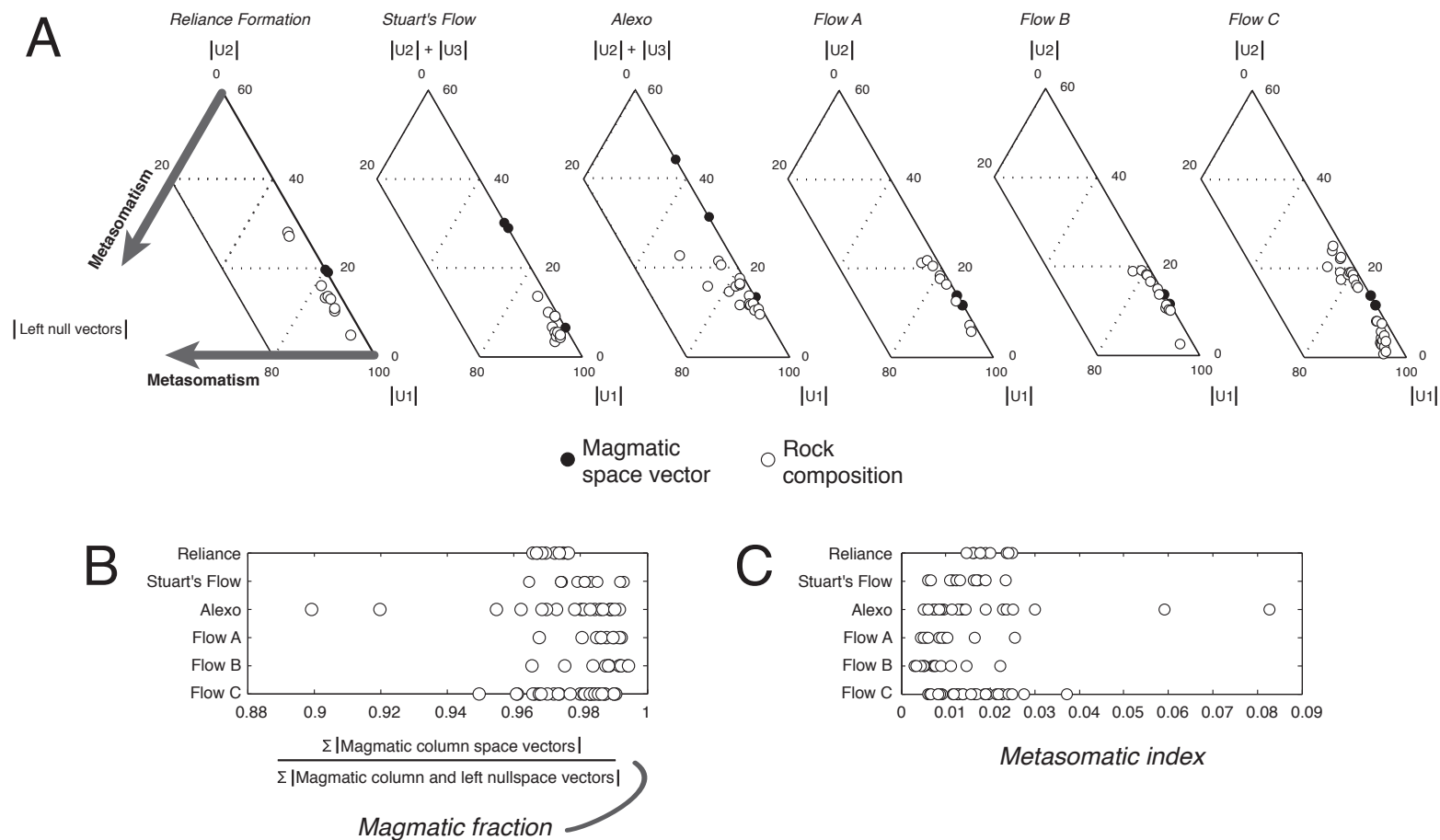
Figure 4.13. Diagrams illustrating the proportions of magmatic and non-magmatic components in rock compositions and their conversion into a metasomatic index. (**A**) Ternary diagrams of rock compositions projected onto magmatic space. The ternary vertices correspond to the orthonormal magmatic space and its left null space vectors. Deflection towards the left null space vertex (bottom left corner of the ternaries) corresponds to non-magmatic process (i.e., metasomatism). (**B**) The magmatic fraction of each rock composition in the komatiite flows. (**C**) The Metasomatic Index of the rock compositions from each komatiite flow.

processes operating *within* the magmatic space are geometrically indistinguishable from magmatic processes, and thus do not contribute to the *MI*, making it an estimate of the minimum influence of metasomatism upon rock compositions.

The *MI* of the komatiite lavas in this study range from <0.005 to ~0.08 (Figure 4.13C), with the lowest indices belonging to rocks from the Pyke Hill and Alexo flows, and the highest to Alexo. The variability of indices within each flow also differs, with the Reliance Formation showing the narrowest range of *MI*s and the variably and complexly altered Alexo showing the greatest. Although the Reliance Formation is the least altered of the lavas petrographically, it bears *MI*s similar to the Pyke Hill flows. This curious result could genuinely reflect an unexpected metasomatic signal, but would also arise if the parental melt estimate were slightly inaccurate. Inspection of the Reliance data on PER diagrams suggests that these chromite-hosted inclusion compositions require a minor correction beyond that already undertaken in the original study (Shimizu et al., 2001). Such an adjustment should decrease the *MI* of all samples.

4.6.3. Relation between Mg-Fe disequilibrium and metasomatism

Departures from the fractionation model for Abitibi Flow C (i.e., liquids in equilibrium with bulk compositions and optimal olivine; Figure 4.8) presumably result from metasomatism, as no other magmatic processes passed geometric testing. To demonstrate the use and effectiveness of the *MI*, I compared displacement of these liquids from the optimal evolved melt on the fractionation curve (Figure 4.8) to the *MI*s of their associated rocks (Figure 4.14). The comparison shows that, among most cumulus zone rocks, the Mg-Fe deviance correlates strongly with *MI*. However, the MI of spinifex-textured rocks bears no correlation with Mg-Fe deviance. Flow-top breccias and two outlying cumulates have unclear relationships between *MI* and Mg-Fe deviance, and one cumulate shows much higher deviance for its *MI* than any other rock in the suite. The main conclusion to draw from this diagram is that metasomatism of this komatiite expresses differently in cumulate zone and spinifex zone rocks, with the former recording a clear relation to Mg-Fe disequilibrium that is absent in the latter. Chapter 5 will deal in some detail with testing for viable metasomatic processes responsible for departures from magmatic space.
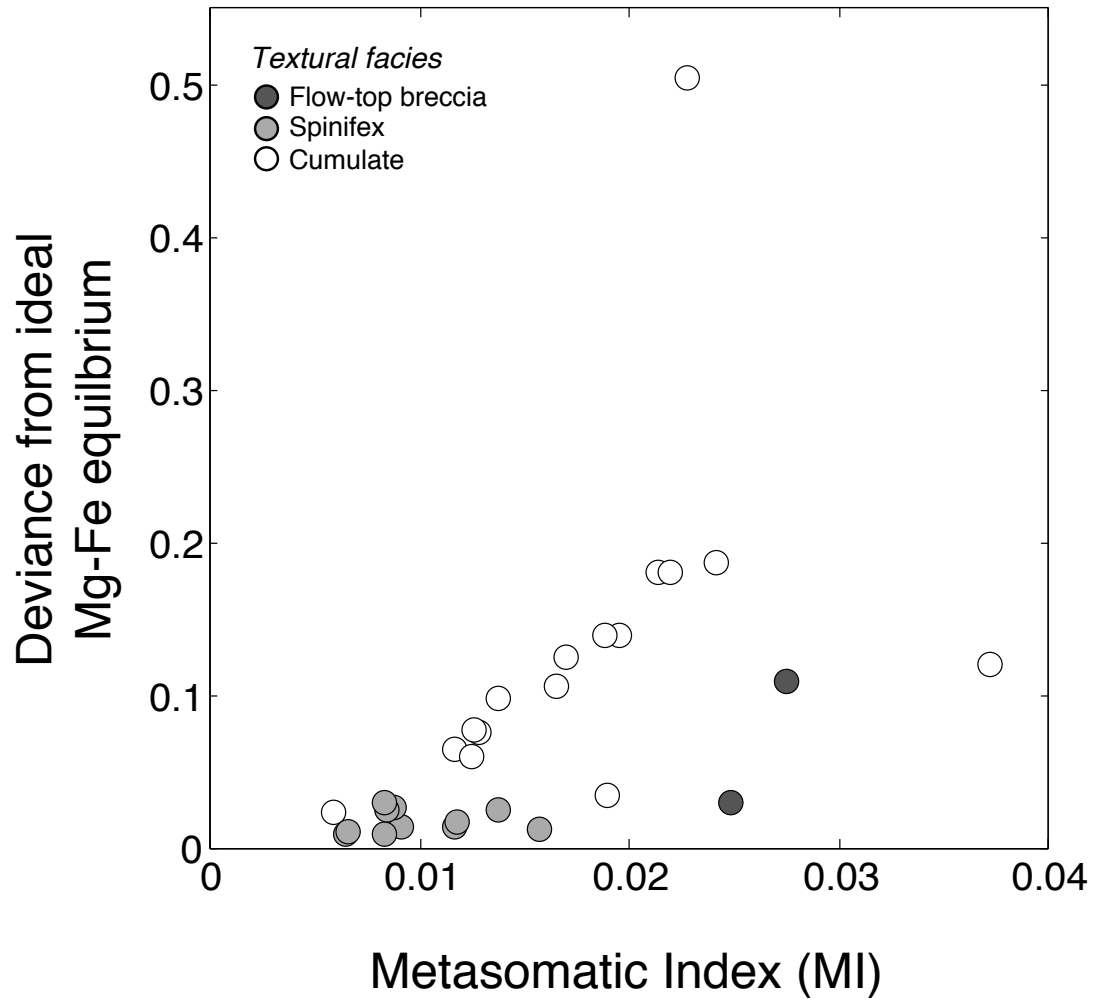
Figure 4.14. Influence of metasomatism on deviance from Mg-Fe equilibrium of whole rock compositions in Flow C. The Metasomatic Index correlates well with deviance in most cumulate facies compositions, but shows no correlation with the spinifex facies rocks. Thus, processes responsible for Mg-Fe deviance cannot account for all metasomatic disturbances.

4.7. Conclusion

Differentiation of komatiite magma within lava flows produces a komatiitic basaltic evolved liquid. Determination of the presence of a minor excess of olivine in vertical sections through a Pyke Hill lava flow supports the possibility that this liquid flowed downstream, consistent with within-flow, surficial differentiation of komatiite lavas. However, metasomatism of cumulates disturbs the Mg-Fe equilibria, reliance upon which enables calculation of excess olivine. Quantitative accounting of metasomatism is thus necessary to properly adjudicate the presence of excess olivine and fortify consequent conclusions.

CHAPTER 5: Quantitative dissection of metasomatism of a Pyke Hill komatiite flow

5.1. Introduction

Secondary mineral assemblages replace the primary mineralogy of komatiites, in whole or in part (e.g., Viljoen and Viljoen, 1969b; Pyke et al., 1973; Smith et al., 1980; Nisbet et al., 1993; LaHaye and Arndt, 1996; Arndt et al., 2008). This alteration hinders recognition of primary geochemical trends (e.g., Barnes et al., 1983; Beswick, 1983; Canil, 1987; LaHaye and Arndt, 1996; Shore, 1997; Walter, 1998; Arndt et al., 2008), and can elevate some otherwise sub-economic occurrences to mineable Ni-Cu deposits (Arndt et al., 2008). Primary geochemical features shape characterization of the Archean mantle and studies of Ni-Cu-PGE ore formation (Barnes et al., 2004; Le Vaillant et al., 2016), the latter of which commonly involves a magmatic assimilation component. Improvements in quantitative treatments of metasomatism can thus increase confidence in interpretation of petrogenesis, igneous differentiation, ore-forming processes (primary and secondary), and identification of metasomatic reactions, and provide quantitative estimates of the magnitude of each process. Such efforts may prove useful in exploration for and assessment of ore deposits.

The previous chapter developed a quantitative measure of the degree of metasomatism in komatiite lavas by exploiting knowledge of magmatic processes and parental melt compositions. This chapter aims to characterize the metasomatic reactions as a demonstration of the newfound capabilities geometric methods offer, particularly in the context of scientifically and economically significant altered rocks. In combining the Metasomatic Index, PER analysis, and geometric testing of hypothetical reactions, I quantified metasomatic modification of major elements, determined viable metasomatic processes, and related these quantities to one another and additional geological and geochemical features. The main conclusions of this chapter are:

- Samples of Pyke Hill Flow C in the Abitibi record variable gains and losses of Ca and Na, and variable losses of Fe, ranging from ca. -50 % to +80 % of their initial molar abundance;
- Either Mg or Si or both may have been mobile during metasomatism, but the amount of material gained or lost is small compared to their high concentrations in the protoliths and primary variability, and is similar to uncertainty estimates;

- The flows likely exchanged elements openly with infiltrating fluids and/or the surrounding environment;

- Three geometrically valid metasomatic reactions corresponding to formation of serpentine + chlorite, actinolite, and alkali feldspar are sufficient to explain all significant metasomatic changes in Fe, Ca, and Na in spinifex facies rocks, whereas other unidentified processes are responsible for some Na variability in the cumulate zone;

- Variability of Ca in Flow C results almost exclusively from breakdown of clinopyroxene to form actinolite, giving losses of Ca in the cumulate zone and gains in the spinifex zone;

- Serpentinization and chloritization can account for virtually all metasomatic losses of Fe and are responsible for disruption to whole rock Mg-Fe equilibria;

- The serpentinization and chloritization vector can only account for a portion of the volatile budget of the whole rocks, implying action of both metasomatic serpentinization and isochemical hydration end members;

- Serpentinization of Flow C was not an isochemical process.

5.2. Chemical effects of komatiite metasomatism

5.2.1. Components conserved during magmatic processes

The dominant magmatic differentiation process in komatiites is the sorting of olivine (e.g., Arndt et al., 2008). In principle, the major elements Ti, Al, P, Ca, Na, and K are conserved during this process. Molar element ratio trends from Abitibi Flow C show that Ti, Al, and P were all mutually conserved in the chemical differentiation of Flow C, whereas Ca, Na, and K were not (Shore, 1997). Magmatic processes cannot explain this non-conservation, suggesting metasomatic disturbance is responsible (Shore, 1997).

For a fixed and known parental melt composition, differences in the ratios of Ca, Na, and K to a conserved element (e.g., Al) between the rocks and the liquid correspond to their net gain or loss from the protolith. Figure 5.1 shows how these ratios vary with increasing metasomatic indices in Flow C. Both Na/Al and Ca/Al variations record gains and losses, spanning ca. -50 % to +80 %, and -30% to +25%, respectively. These two ratios broadly co-vary in spinifex and cumulus facies, but are diametrically opposed in
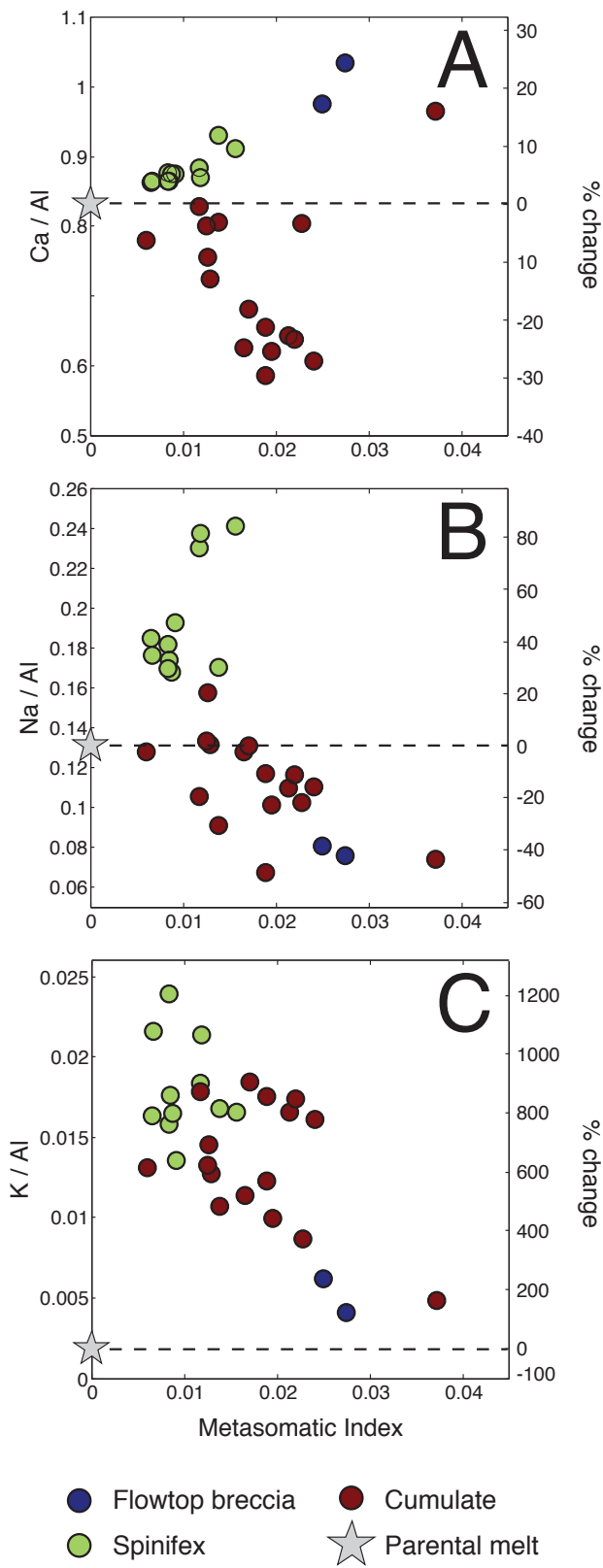
Figure 5.1. Changes in the molar ratios of Ca (**A**), Na (**B**), and K (**C**) to Al attending metasomatism of komatiite Flow C.

their behaviour in the most metasomatized cumulus rock and the flow-top breccias. The ratio K/Al varies largely with Na/Al, except that it decreases progressively from the least to most metasomatized samples without any defined increasing trend at low indices. The extent of its enrichment is nevertheless large compared to the parental melt, but its low concentration in these rocks renders the gain in mass trivial. Moreover, measurement of alkalis in glass inclusions is subject to analytical difficulties (Nielsen and Sigurdsson, 1981), thus making the comparison to whole rock XRF analyses particularly uncertain.

5.2.2. Components unconserved during magmatic processes

Fractionation of olivine involves removal or addition of Mg, Fe, and Si to or from a given komatiite sample with respect to the parental liquid. Any metasomatic modification of these elements attending hydrothermal alteration thus acts upon this preexisting source of variability.

The ideal way to assess whether metasomatism disturbed Si-Mg-Fe systematics is to subtract the olivine signal and examine the residual chemical variability. This idea is similar to the standard approach of examining olivine-control lines on variation diagrams (Smith et al., 1980; LaHaye et al., 1995; LaHaye and Arndt, 1996; Rollinson, 1999; Arndt et al., 2008; Sossi et al., 2016), and prior interpretations of molar element ratio diagrams (Beswick, 1983; Barnes, 1985; Canil, 1987; Shore, 1997; Walter, 1998), which I apply here. Figure 5.2 A plots whole rock compositions from Abitibi Flow C on the standard molar element ratio diagram that tests for olivine sorting (Beswick, 1983; Pearce, 1987; Russell and Nicholls, 1988; Russell and Stanley, 1990a; Russell and Stanley, 1990b), as well as the line corresponding to the magmatic space from Chapter 4. The data cluster tightly (with two exceptions) about the magmatic model, implying good preservation of the primary systematics. However, Figure 5.2 B shows a systematic deflection from the magmatic space towards high Mg# with increasing Si/Al, predominantly in cumulus samples. This pattern cannot merely result from cumulus olivine being more magnesian, as no vectors with the stoichiometry of olivine other than $Fo_{91.2}$ exist within the rock composition space (Figure 4.4 F). The deflection thus implies mobility of Mg, Fe, and/or Si during metasomatism. Figure 5.2 C shows close agreement between the Mg-Si systematics of the magmatic model and the whole rock compositions.
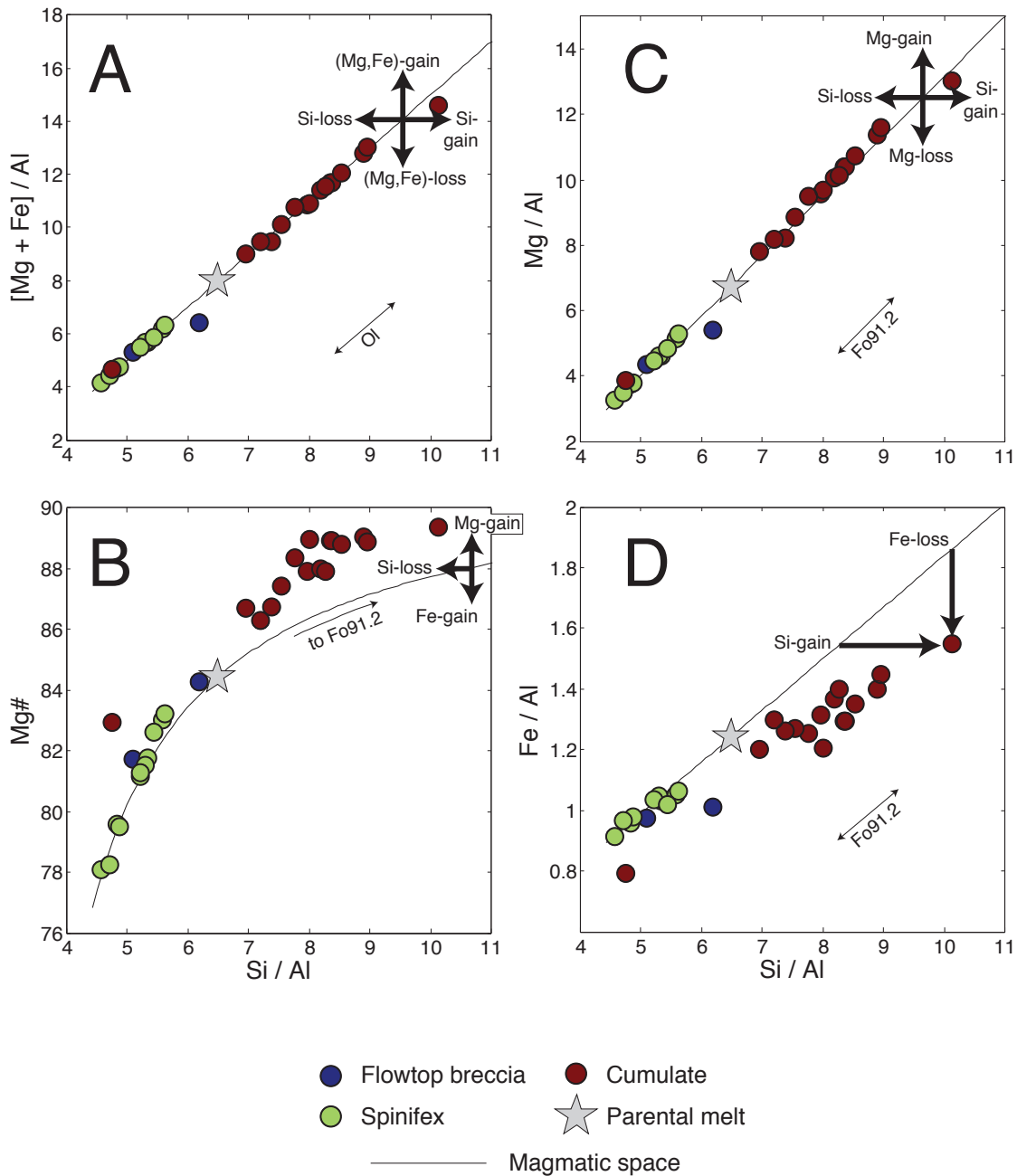
Figure 5.2. Comparison of Mg-Fe-Si systematics of Flow C rocks to the magmatic space. (**A**) The standard molar ratio diagram that tests for olivine sorting shows close agreement between the rock compositions and the magmatic space. (**B**) Cumulate samples deflect away from the magmatic space towards high Mg# with respect to the magmatic space. (**C**) The stoichiometric relationships between Si and Mg show little apparent deviation from the magmatic space, as originally noted by Shore (1997). (**D**) At a given Si/Al value, cumulate samples show a systematic depletion of Fe/Al, as originally noted by Shore (1997).

Any metasomatic process that affected these components failed to significantly decouple Mg from Si, inasmuch as this diagram can illustrate. In contrast, Fe-Si systematics show conspicuous disagreement between the magmatic model and the rocks (Figure 5.2 D). Shore (1997) inferred from diagrams like Figure 5.2 C and D that Fe was mobile during alteration, whereas Mg and Si were not.

A problem with subtracting the olivine signal from the whole rock data is that no unique solution exists. The essence of the problem is that to know the amount of olivine to subtract, we must know where upon the magmatic line in Figure 5.2 D (for example) the protolith originally plotted. As the system contained Si-Mg-Fe variability prior to alteration, returning to the original position requires knowledge of the mass transfer vector by which metasomatism occurred, which is the very phenomenon we seek to determine. Thus, subtraction of the olivine signal can be achieved by a number of pathways, and the numerical structure of the data alone does not permit selection of any one over another without using circular reasoning, as long as the candidate vectors are in the rock composition space. Moreover, the metasomatic vectors responsible for modifying Si-Mg-Fe systematics in Figure 5.2 need not exist in the Si-Mg-Fe ternary, as they could contain significant abundances of other elements (e.g., Ca, Na).

One means to examine the relative metasomatic disturbance of Si, Mg, and Fe is to assume that one of these components was immobile. For example, if Si were immobile during alteration, all of its variation must result from magmatic processes alone. If the assumption of Si immobility is valid, the difference between the magmatic model Mg/Al and Fe/Al and that in the whole rocks, at a given Si/Al value, would represent metasomatic disturbance. This approach gives the gains or losses of Fe and Mg necessary to explain their deviations from the magmatic space, under the condition that Si remained immobile.

I applied this approach under three hypothetical conditions of elemental immobility during metasomatism: Si, Mg, or Fe (Figure 5.3). Under the assumptions of immobile Si or Mg, similar differences (Δ) in Fe/Al are necessary to explain deviations from magmatic space (Figure 5.3 A, B). If Fe were immobile, gains in Mg and Si are necessary (Figure 5.3 C). Recasting these changes in terms of percent gains or losses (Figure 5.3 D-F) shows that the Fe loss, assuming immobile Si or Mg, is up to ~20%,
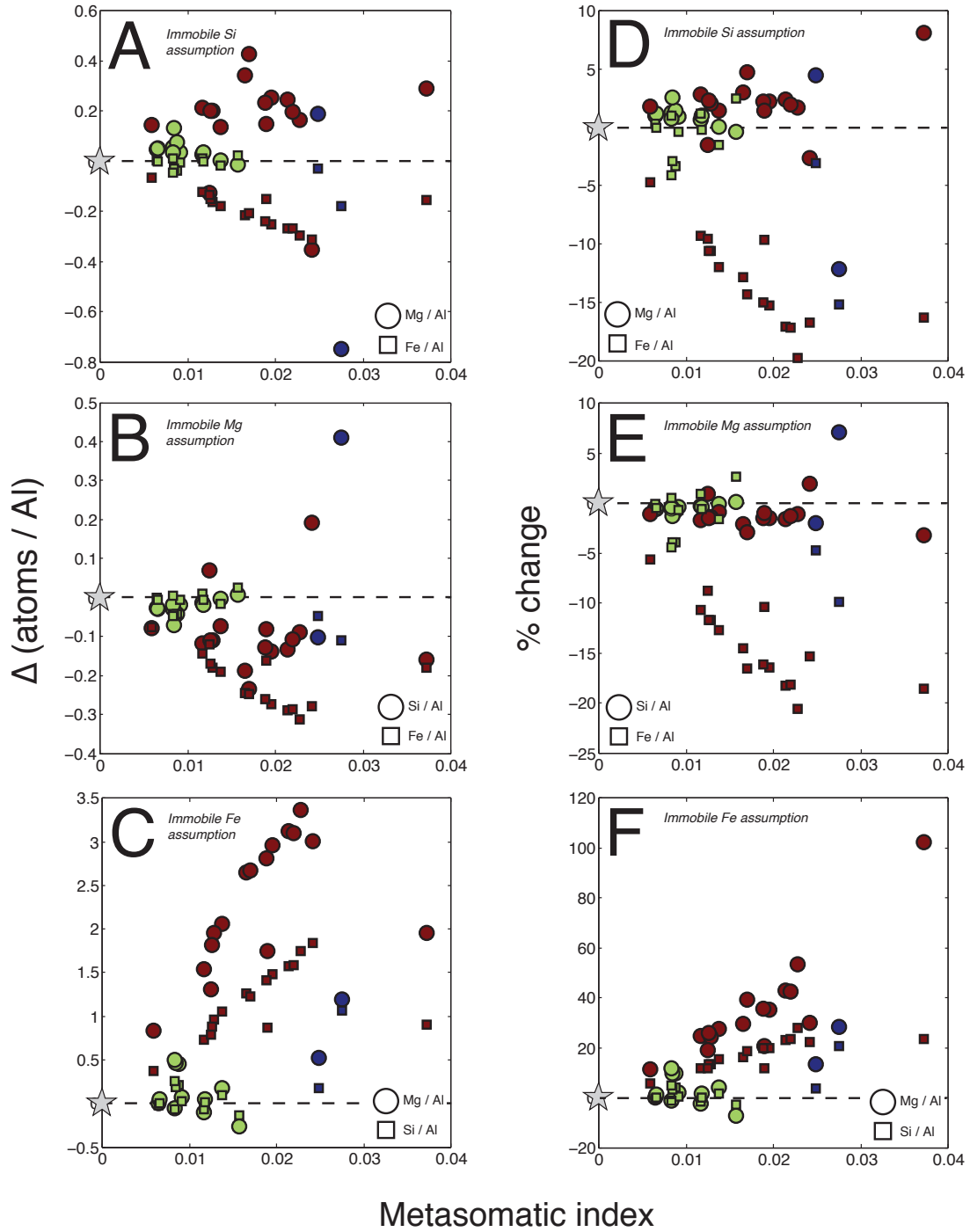
Figure 5.3. Deviations (Δ) in (Si,Mg,Fe)/Al systematics between the magmatic space and rock compositions of Flow C, as calculated assuming immobile Si (**A**), Mg (**B**), or Fe (**C**). Panels **D-F** show percent changes relative to the protolith.

whereas the gains in Mg and Si required if Fe was immobile are up to ~100% and ~28%, respectively. For changes in Mg or Si, assuming immobility of the other, the percent changes are comparatively small (all < 15%, most < 5%).

The above analysis of the data is equivocal. However, observations suggest that the metasomatic processes removed significant amounts of Fe. First, nominal preservation of magmatic Si-Mg systematics (equivalent to sorting of ~$Fo_{91.2}$; Figure 5.2 C) requires that the relationship between Si and Mg remained essentially undisturbed (Shore, 1997) relative to the magnitude of their primary variation. Weak mobility of Si and Mg during metasomatism satisfies this requirement, as does the unlikely case of mobility at a fixed Mg-Si ratio similar to $Fo_{91.2}$. Second, the molar amount of Fe loss (up to ~0.32 Fe/Al) under the condition of immobile Mg or Si is small compared to the amount of Mg and Si that must be added if Fe were immobile (~6 [Si + Mg]/Al). This relatively small loss of matter is easier to reconcile with the cryptic evidence for volumetric expansion attending serpentinization (Hostetler et al.,1966; Thayer, 1966; Coleman and Keith, 1971; Moody, 1976; Wicks and Whittaker, 1977; O'Hanley, 1992; O'Hanley, 1996). Such expansion would necessarily be more extreme than that attending simple isochemical serpentinization (cf. Hostetler et al., 1966; Thayer 1966; Wicks and Whittaker, 1977; O'Hanley, 1992; O'Hanley, 1996) if Mg and Si content increased by up to 100% and 25%, respectively. Finally, hydrothermal fluids issuing from serpentinizing peridotites and gabbros at the Rainbow vent fields along the Mid-Atlantic Ridge contain approximately 3.5 and 20 times more Fe than Si and Mg, respectively, and higher Fe content than other Mid-Atlantic Ridge hydrothermal fluids (Douville et al., 2002). These lines of evidence collectively and individually support the notion that metasomatism of Abitibi Flow C involved loss of Fe perhaps with some addition of Mg or loss of Si (Figure 5.3). In either case, the removal of Fe is far greater as a proportion of initial Fe content than the addition of removal of Mg or Si (Figure 5.3 D-F).

5.2.3. Within flow redistribution of elements

Quantification of metasomatic disturbances permits an assessment of whether chemical exchange occurs within komatiite lavas (closed system) or with their surrounding environments (open system). I consider the relationship between the depth in Flow C and

its metasomatic gains and losses of components. I also examine whether the predominant textural facies (cumulus and spinifex) in this lava and other flows from Pyke Hill and the Reliance formation record complementary metasomatic gains that could support within-flow confinement of elemental redistribution.

Flow C exhibits changes in the extent and nature of metasomatism at various depths in the flow (Figure 5.4 A). The upper half of the flow records little modification of Fe, and gains in Ca, Na, and K. The net result is a gain of ~0.1 atoms per Al in the protoliths of this spinifex-dominated region, excluding volatiles (Figure 5.4 A). The lower portion of the flow, although similarly enriched in K, records losses of Fe, Ca, and Na, resulting in a net loss of up to ~0.5 atoms per Al (Figure 5.4 A). Gains in H^*/Al (100 $- \Sigma$ wt. oxides $= H_2O^*$) dwarf any other changes by 1-2 orders of magnitude (Figure 5.4 B).

The changes in Na and Ca are broadly complementary between the spinifex and cumulus zones of Flow C; i.e., both components are enriched in the spinifex rocks and depleted in the cumulate zones. As these two textural subgroups commonly represent the major proportion of komatiite flows, whether spinifex rocks might balance elemental losses from cumulates is worth considering. Figure 5.5 compares the effects of metasomatism on the spinifex and cumulus-textured rocks of the three Pyke Hill flows (A, B, and C) and the Reliance Formation. Changes in Fe are consistently negative or nearly zero in both the spinifex and cumulus rocks of these lavas, implying no complementarity and thus low potential for within-flow balance. In contrast, gains in Ca in spinifex rocks could counterbalance losses in cumulates (with the exception of the weakly altered Reliance Formation). Changes in Na may be positive or negative in both textural varieties, and K appears to have broadly similar behaviour in the two facies in each flow (mutual gain or loss). Thus, potential for within-flow balance of Ca redistribution exists, whereas Fe, Na, and K appear more likely to have exchanged openly with their surrounding environment in most cases.

5.3. Characterization of metasomatic reactions

Here I test metasomatic reactions responsible for non-magmatic variability in Abitibi Flow C rocks. As the magmatic space accounts for two out of seven dimensions of rock
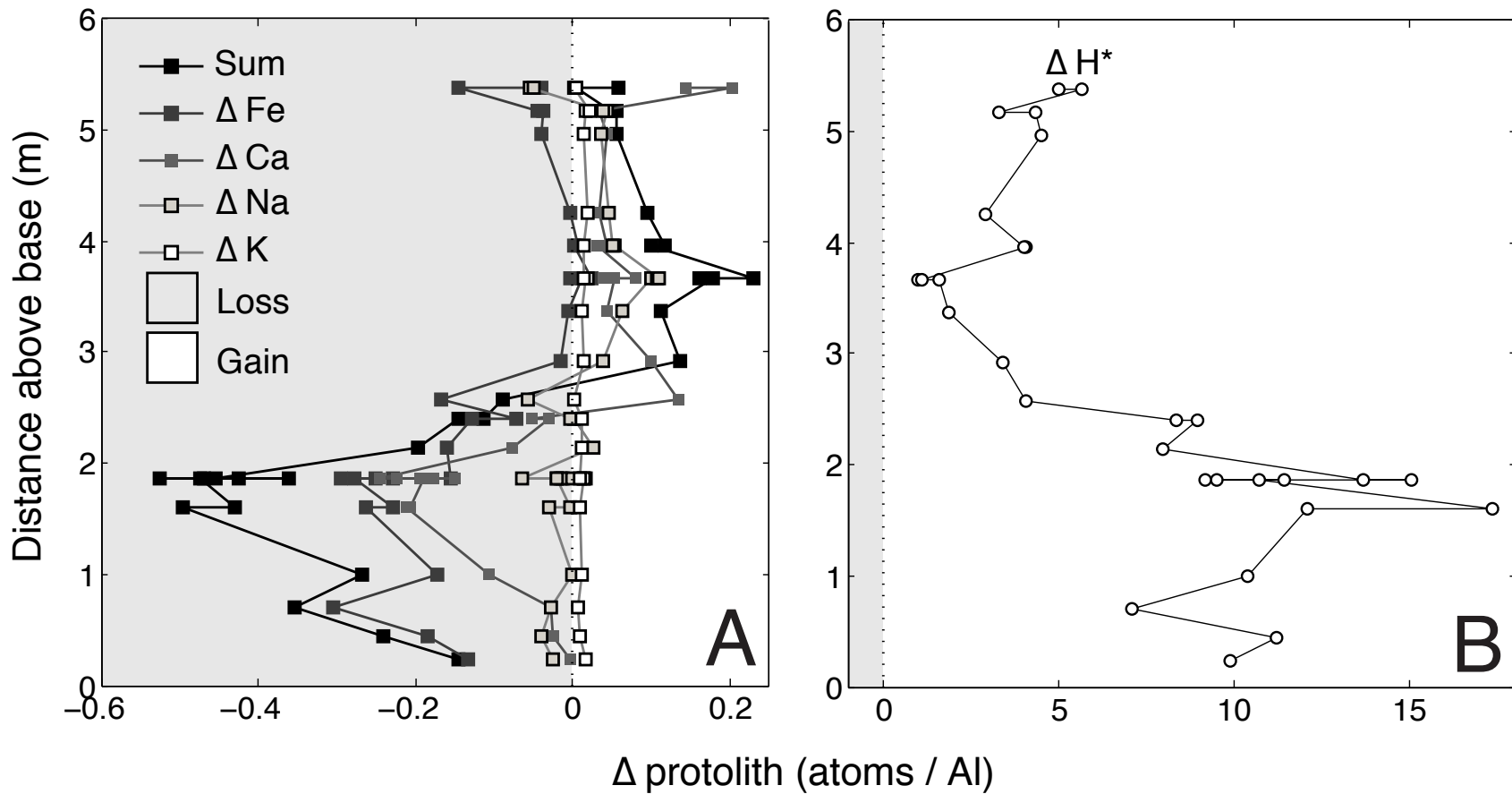
Figure 5.4. Changes attending metasomatism of Flow C as a function of position in the flow. **Panel A** shows changes in elements other than H, whereas **panel B** shows only the latter. Changes in Fe/Al are those calculated assuming Si immobility during metasomatism.
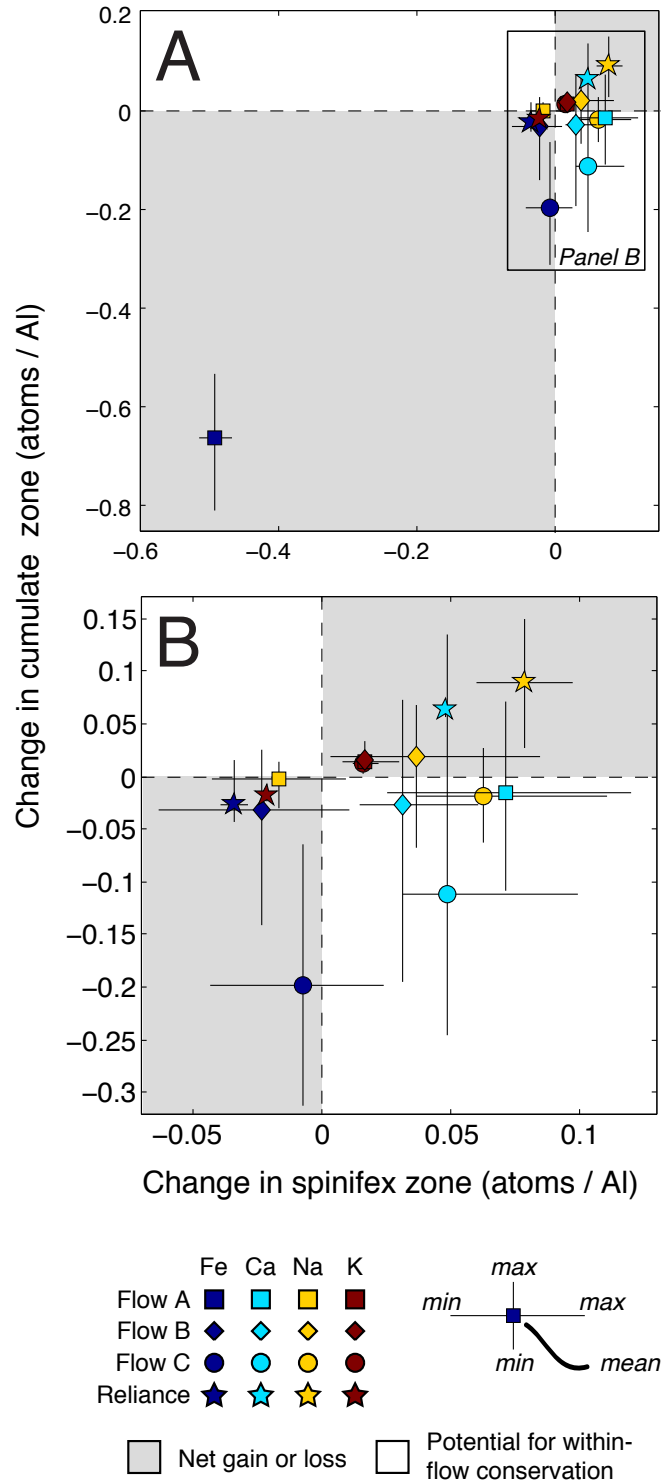
Figure 5.5. Comparison of metasomatic changes to Fe, Ca, Na, and K in spinifex and cumulate facies of the Pyke Hill flows A, B, and C, and the Reliance Formation. **Panel B** is a magnification of **Panel A**. Complementary changes plot in the ***white fields***, whereas changes in the same direction plot in the ***grey fields***.

composition space, as many as five metasomatic reactions are necessary to satisfactorily model all chemical variability. These reactions may involve any of the demonstrably unconserved elements, namely Si, Fe, Mg, Ca, Na, and K.

5.3.1. Serpentinization and chloritization

Formation of serpentine and chlorite after olivine and groundmass is pervasive in komatiites (e.g., Arndt et al., 2008), including the Pyke Hill flows (Pyke et al., 1973). A general reaction that encompasses both of these replacements is

x Olivine + y Groundmass + z Water + w Aqueous component(s)
$\rightarrow a$ Serpentine + b Chlorite + c Aqueous component(s)   (5.1)
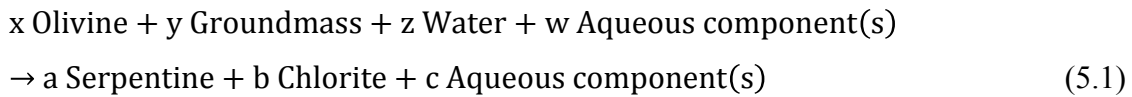
Adjustment of the coefficients, the compositions of the ferromagnesian solid solutions, and/or the compositions of the aqueous components permits many means to balance the reaction. To reduce the number of possibilities to those more relevant to komatiites, I imposed the following restrictions:

- Al is conserved in the reaction (Shore, 1997), thus fixing the ratio of chlorite to groundmass;
- The ferromagnesian phases have fixed Mg# that correspond to measurements from komatiites (LaHaye and Arndt, 1996).

Given these restrictions, three end-member reactions encompass all the remaining possibilities: constant Si, constant Fe, and constant Mg. As I have argued for mobility of Fe earlier in this chapter, I consider the constant Si and Mg reactions as possibilities.

   The cumulate facies of komatiite lavas and the modal variability of olivine requires that we consider the coefficient x a variable, thus I considered the fixed Si and Mg reactions for $x=0$ and up (to 50 units of olivine), and tested them as possible metasomatic reactions. In defining the reaction vectors, I used the evolved melt composition from Chapter 4 as an approximation of the groundmass, and the optimal olivine composition ($Fo_{91.2}$). I fixed the Mg# of serpentine and chlorite to match average values from the Alexo flow (LaHaye and Arndt, 1996), which experienced a similar metamorphic history to the Pyke Hill flows (Jolly, 1982; Shore, 1997). The constant Mg and constant Si end-member reactions are valid with ~19.5 or ~21 units of olivine per unit groundmass, respectively (Figure 5.6; Table 5.1):
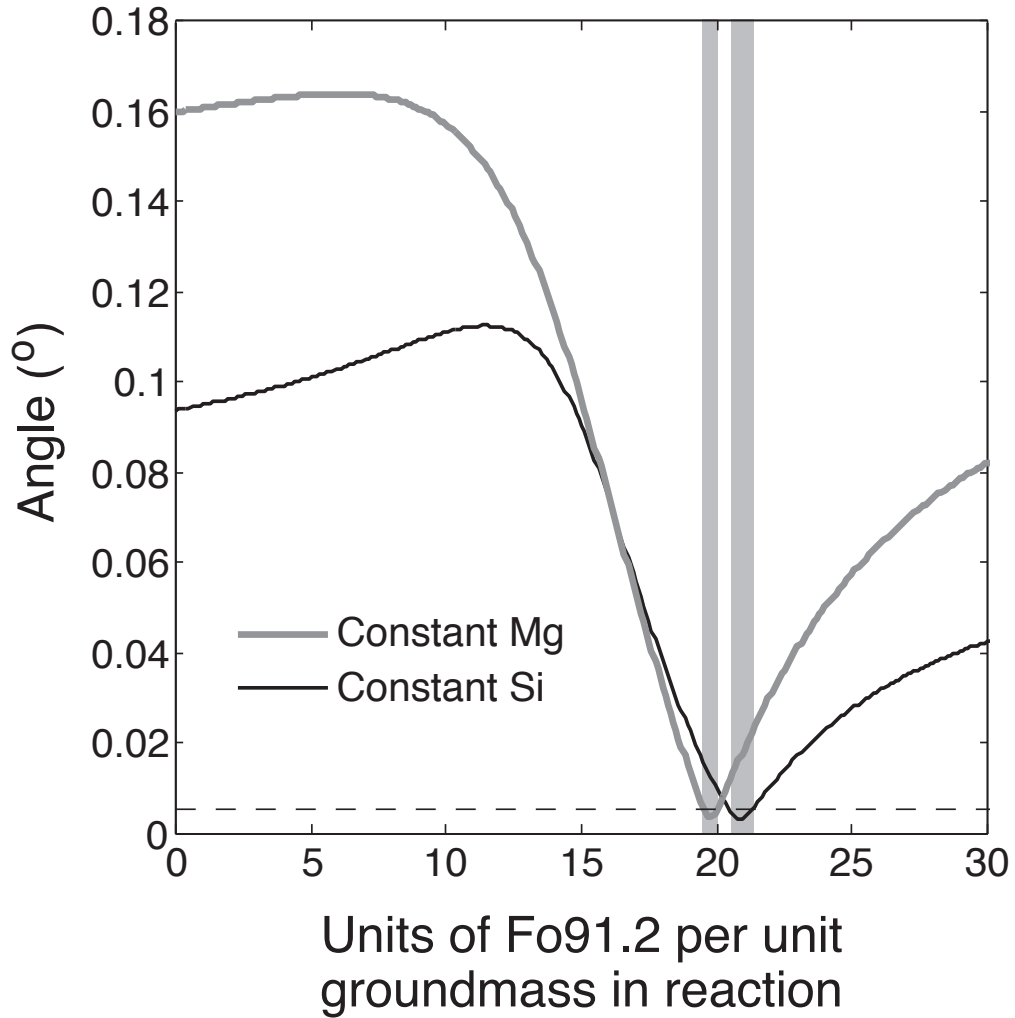
Figure 5.6. Angles separating net transfer vectors from Flow C rock composition space for reaction of olivine and groundmass to form serpentine and chlorite. The x-axis shows the number of olivine units per unit groundmass in the net transfer reaction (Section 5.3.1). The two curves show constant Si (***black curve***) and constant Mg (***grey curve***) end member reactions. The ***grey fields*** highlight the viable reaction vectors.

Table 5.1. Optimal serpentine + chlorite-forming reactions, Flow C, Pyke Hill.

	Constant Si	Constant Mg
Net transfer reactions		
SiO$_2$	0	1.07
TiO$_2$	0	0
Al$_2$O$_3$	0	0
FeO	-2.40	-2.21
MgO	-1.96	0
CaO	0	0
Na$_2$O	0	0
K$_2$O	0	0
P$_2$O$_5$	0	0
Units per reaction		
Groundmass	10.74	10.74
Olivine	20.9	19.8
Serpentine	13.23	13.21
Chlorite	1.00	1.00

$$20.9Mg_{1.824}Fe_{0.176}SiO_2 + 10.7Mg_{0.501}Fe_{0.174}Al_{0.186}Si_{0.797}O_{1.61} + 30.4H_2O$$
        Olivine   **Groundmass**   **Fluid**

$$\rightarrow 13.2Mg_{2.827}Fe_{0.183}Si_2O_5(OH)_4 + Mg_{4.290}Fe_{0.710}Al_2Si_3O_{10}(OH)_8 + 2.40FeO$$
        Serpentine   **Chlorite**   **Aq.**

    $+ 1.96MgO,$ (5.2)
    Aq.

and

$$19.8Mg_{1.824}Fe_{0.176}SiO_2 + 10.7Mg_{0.501}Fe_{0.174}Al_{0.186}Si_{0.797}O_{1.61} + 1.07SiO_2 + 30.4H_2O$$
        Olivine   **Groundmass**   **Aq.**   **Fluid**

$$\rightarrow 13.2Mg_{2.827}Fe_{0.183}Si_2O_5(OH)_4 + Mg_{4.290}Fe_{0.710}Al_2Si_3O_{10}(OH)_8$$
        Serpentine   **Chlorite**

    $+ 2.21FeO.$ (5.3)
    Aq.

These reactions are two possibilities within two dimensions of permissible vectors in Mg-Fe-Si space (Figure 4.3 F). Olivine ($Fo_{91.2}$) accounts for one dimension, and a metasomatic reaction accounts for the other. I arbitrarily adopt the constant Si reaction as a model metasomatic reaction, although the constant Mg alternative is an equally valid choice geometrically.

5.3.2. Reaction of clinopyroxene to actinolite

Amphibole replaces clinopyroxene in the Pyke Hill flows (Pyke et al., 1973; Shore, 1997). This transformation could occur by four main reactions involving the end-members diopside, hedenbergite, tremolite, and Fe-actinolite: constant Si, constant Mg, constant Fe, and constant Ca. At Mg# corresponding to komatiite-derived clinopyroxene and actinolite (LaHaye and Arndt, 1996), a matrix of these net transfer reactions (Table 5.2) has a rank of two, indicating linear redundancy. Thus, linear combinations of two of these end-member reactions encompass all the possible outcomes that satisfy the naturally occurring mineral compositions. Figure 5.7 shows the angular separation of all combinations of the constant Fe and constant Ca reactions from the rock composition space, giving an optimal solution of ~ 25% of the constant Fe reaction (Table 5.2):

$$5.37Mg_{0.866}Fe_{0.134}CaSi_2O_6 + 0.036FeO + H_2O$$
        Clinpyroxene   **Aq.**   **Fluid**

$$\rightarrow Mg_{0.824}Fe_{0.176}Ca_2Si_8O_{22}(OH)_2 + 0.627SiO_2 + 0.121MgO + 0.769CaO.$$
        Actinolite   **Aq.**   **Aq.**   **Aq.**   (5.4)
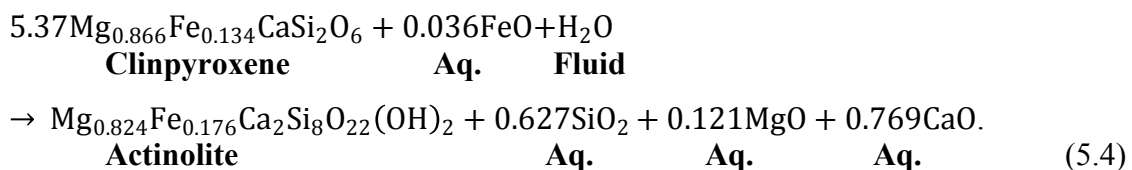
Table 5.2. End-member and optimal clinopyroxene-to-actinolite reactions.

	Constant Si	Constant Mg	Constant Ca	Constant Fe	Optimal
Net transfer reactions					
SiO$_2$	0	-1.52	4	-5.09	-2.75
TiO$_2$	0	0	0	0	0
Al$_2$O$_3$	0	0	0	0	0
FeO	0.34	0.24	0.61	0	0.16
MgO	0.66	0	2.39	-1.54	-0.53
CaO	-2	-2.76	0	-4.54	-3.38
Na$_2$O	0	0	0	0	0
K$_2$O	0	0	0	0	0
P$_2$O$_5$	0	0	0	0	0
			25.6% constant Ca, 74.3% constant Fe		
Units per reaction					
Clinopyroxene	4	4.76	2	6.54	
Actinolite	1	1	1	1	
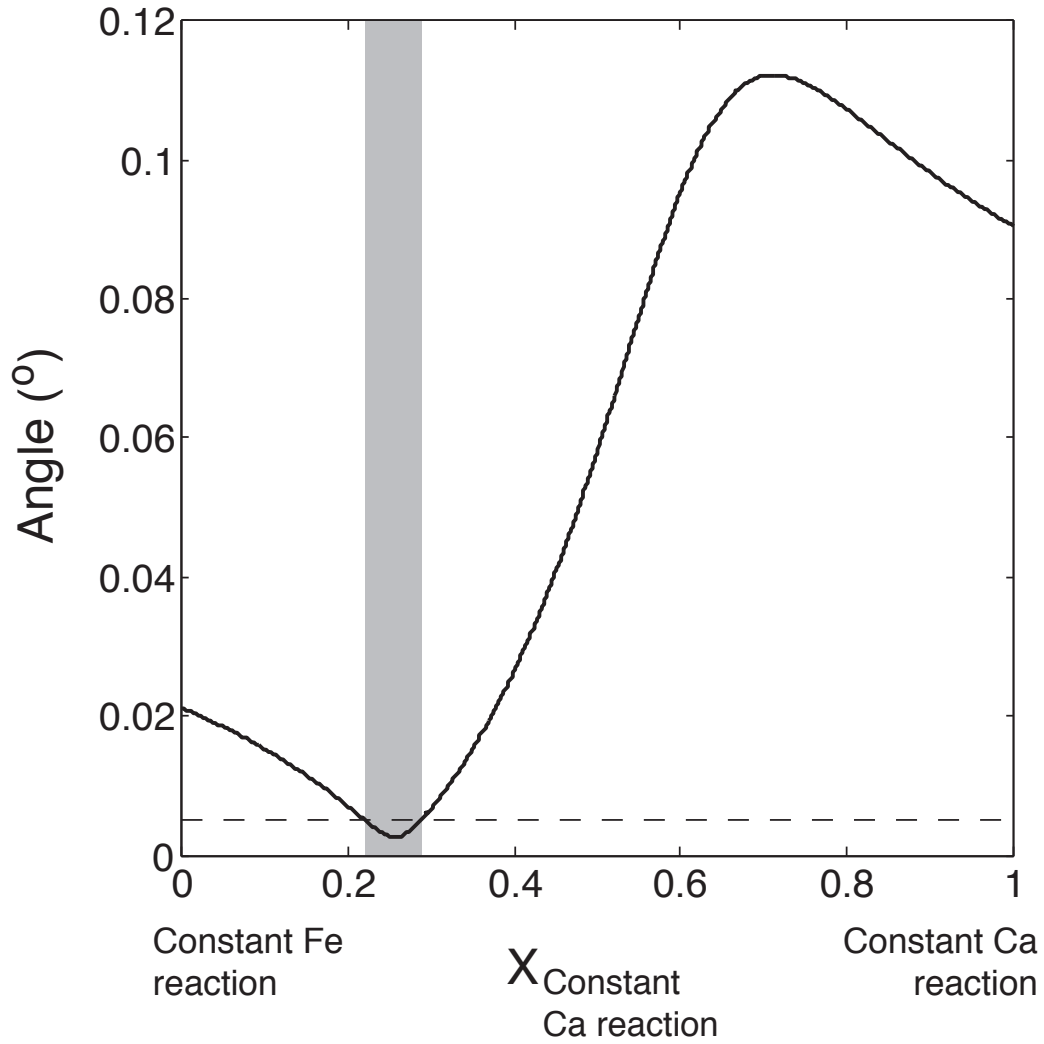
Figure 5.7. Angles separating net transfer vectors from Flow C rock composition space for reaction of clinopyroxene to actinolite. The x-axis shows the proportions of the constant Ca and constant Fe reactions (Table 5.2). The **grey field** highlights the viable reaction vectors.

This vector represents the best estimate of the actinolite-forming reaction, as it is the sole permissible vector in the two dimensions of possibilities.

5.3.3. Alkali variability

The groundmass of Archean komatiites, including the Pyke Hill flows, is always recrystallized, generally forming an aggregate of optically irresolvable low-temperature minerals that formed during initial cooling and/or later prograde and/or retrograde metamorphism (Pyke et al., 1973; Nisbet et al., 1987; Arndt et al., 2008). This alteration assemblage must contain one or more alkali-bearing phases, as alkalis may be enriched in altered komatiites and none of the major secondary phases contains appreciable alkalis. The most important alkali-bearing mineral in prehnite-pumpelleyite facies mafic bulk compositions is albite. Hence I determined net transfer reactions for the formation of all Na-K feldspars after groundmass, and tested these against the rock composition space. I restricted these tests to reactions conserving Al (Table 5.3). The net transfer reaction corresponding to formation of $Ab_{82.5}Or_{17.5}$ lies within the rock composition space (Figure 5.8; Table 5.3):

$$10.74Na_{0.024}K_{0.00034}Al_{0.186}Si_{0.797}O_{1.61} + 0.87Na_2O + 1.00K_2O$$
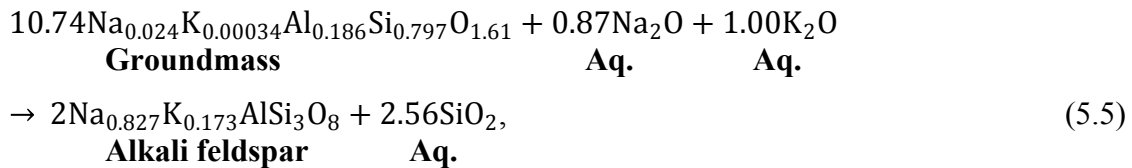**Groundmass** Aq. Aq.

$$\rightarrow 2Na_{0.827}K_{0.173}AlSi_3O_8 + 2.56SiO_2, \tag{5.5}$$
Alkali feldspar Aq.

Thus formation of alkali feldspars by ingress of Na-K-bearing fluids is a viable process, geometrically. However, phase equilibria under water-saturated conditions show that feldspar of this composition would form at temperatures around or above 600 °C (Bowen and Tuttle, 1950). The Pyke Hill flows experienced peak metamorphism in the prehnite-pumpelleyite facies (Jolly, 1982) and therefore much cooler conditions. Thus, if formation of such feldspar occurred, it would represent subsolidus alteration associated with the primary cooling of the lava.

5.3.4. Other processes

At this stage, I have identified five geometrically valid and geologically reasonable chemical vectors within rock composition space: two magmatic vectors and three

Table 5.3. Constant Al end-member and optimal groundmass-to-alkali feldspar reactions.

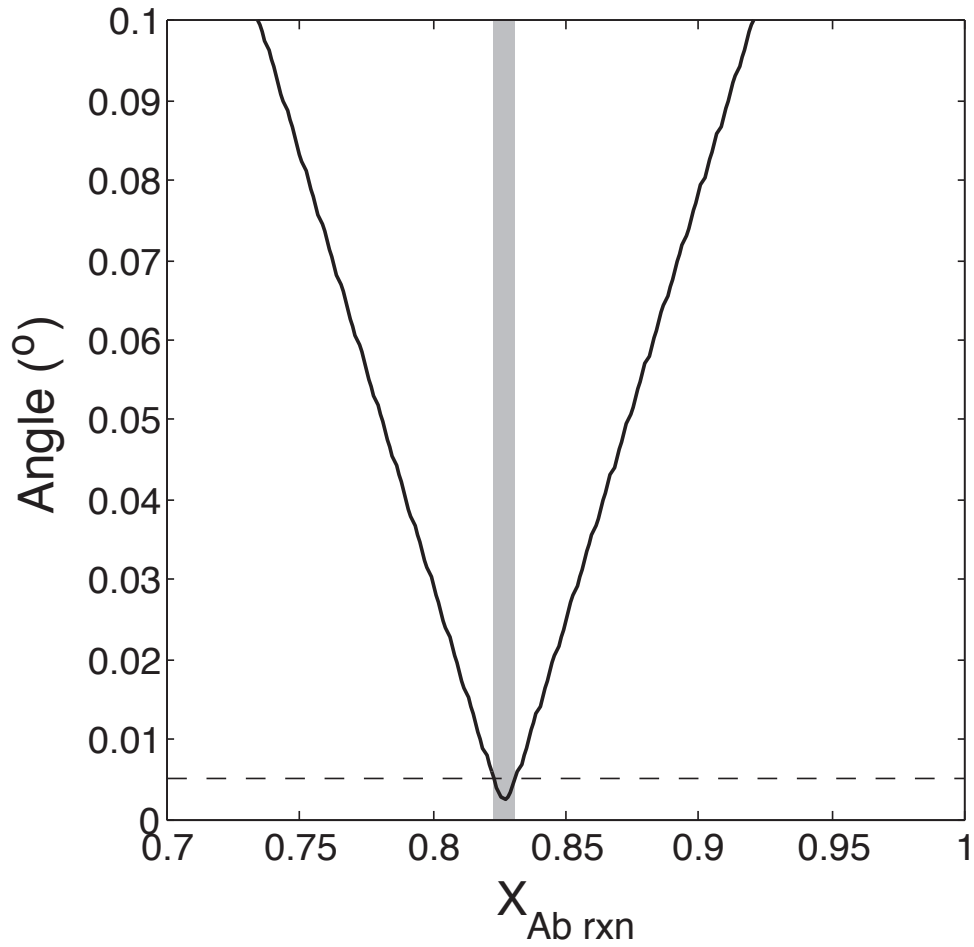|	K-feldspar	Albite	Optimal
Net transfer reactions			
SiO_2	-2.56	-2.56	-2.56
TiO_2	0	0	0
Al_2O_3	0	0	0
FeO	0	0	0
MgO	0	0	0
CaO	0	0	0
Na_2O	0	0.87	0.72
K_2O	1.00	0	0.17
P_2O_5	0	0	0

17.3% K-feldspar, 82.7% albite

Figure 5.8. Angles separating net transfer vectors from Flow C rock composition space for reaction of groundmass to alkali feldspars. The x-axis shows the proportions of the constant Al reactions of albite through K-feldspar (Table 5.3). The **grey field** highlights the viable reaction vectors.

metasomatic reaction vectors. Two additional dimensions of this space exist within analytical uncertainty of the geochemical data (Section 4.3.1), so two further geochemical processes could remain uncharacterized. As the valid vectors encompass the primary magmatic signals, involve all important alteration phases, and involve every unconserved element, testing of additional vectors becomes increasingly speculative and tenuous. The remaining dimensions of rock composition space likely encompass minute variations heavily influenced by both sampling and analytical uncertainties. I refrained from further hypothesis testing to avoid overcomplicating the forthcoming geochemical model, which will account for most geochemical variability within the dataset (Section 5.4.2).

5.4. Recovering the magnitude of geochemical processes

5.4.1. Model basis

A geochemical model for a suite of altered komatiite rocks includes two main portions: magmatic processes and metasomatic processes (Table 5.4). The magmatic space of Abitibi Flow C includes a liquid composition and an olivine vector (Chapter 4). For the present purpose, I use the composition of the evolved rather than parental liquid in the magmatic portion of the model (Table 5.4) so that both magmatic vectors will have positive values in every rock, which simplifies scrutiny of forthcoming reconstructions of rock compositions. The metasomatic portion of the model includes the three reaction vectors for formation of serpentine + chlorite, actinolite, and alkali feldspar (Table 5.4).

5.4.2. Model approximation of rock compositions

The set of model vectors constitutes a model space (per Chapter 3) whose purpose is to capture the important geochemical variability in the lava. Figure 5.9 shows the angular separation of the modeled rock compositions from rock composition space with stepwise addition of vectors to the model. The model space captures rock compositions increasingly well with addition of reaction vectors, with the magnitude of improvement depending on the textural facies of the sample. Addition of the serpentine-chlorite reaction vector best improves approximation of the cumulus samples, whereas the alkali feldspar-forming reaction is most important to approximation of the spinifex rocks. Addition of the actinolite-forming reaction improves approximation of all rock types.

Table 5.4. Model vectors (unit length).

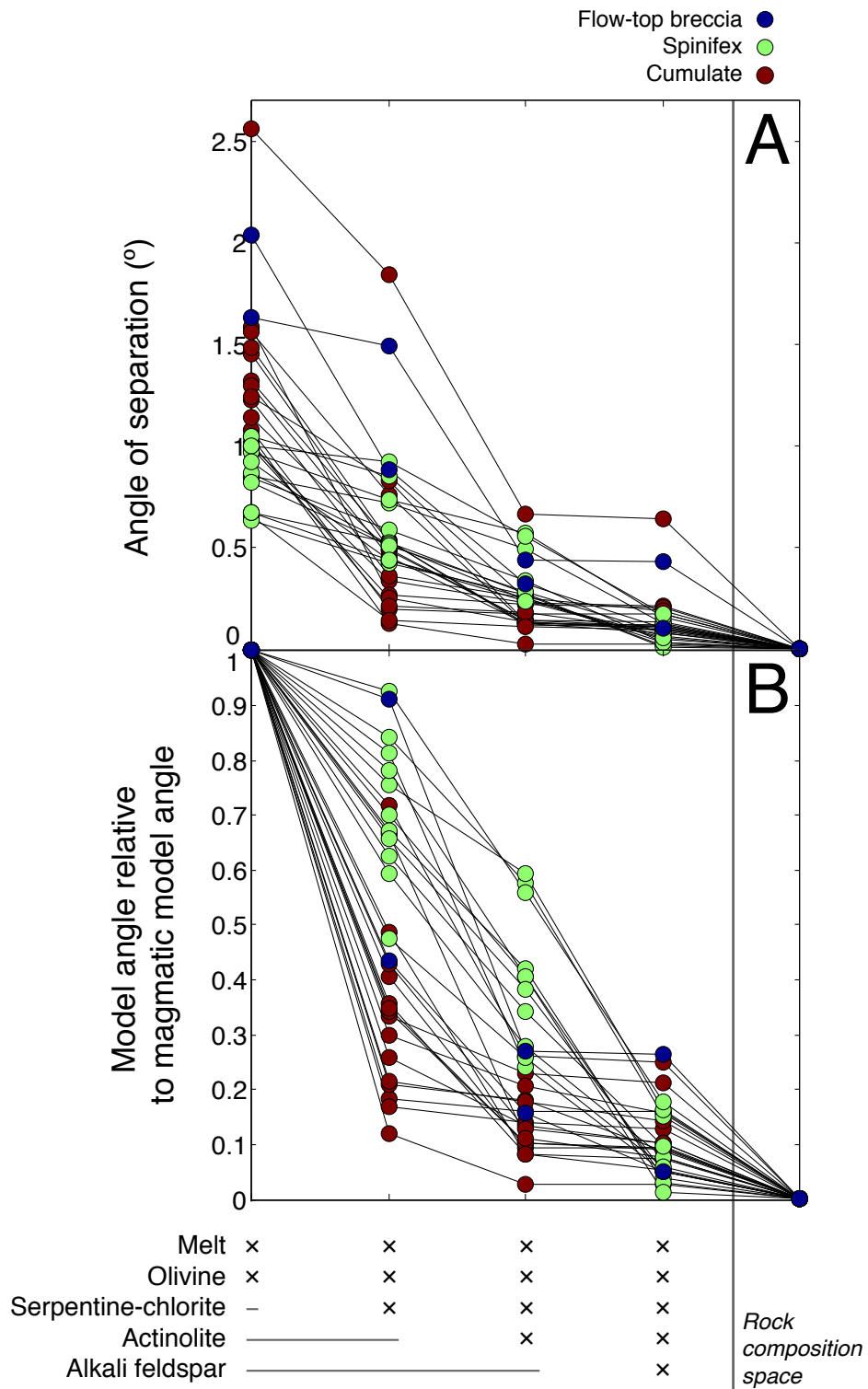|	Magmatic vectors		Metasomatic vectors		
	Evolved melt	*Fo91.2*	*Serpentine +* *chlorite formation*	*Actinolite* *formation*	*Alkali feldspar* *formation*
SiO$_2$	0.8178	0.4779	0	-0.6266	-0.9607
TiO$_2$	0.0056	0	0	0	0
Al$_2$O$_3$	0.0956	0	0	0	0
FeO	0.1789	0.0812	-0.7743	0.0357	0
MgO	0.5144	0.8746	-0.6328	-0.1212	0
CaO	0.1590	0	0	-0.7690	0
Na$_2$O	0.0125	0	0	0	0.2699
K$_2$O	0.0002	0	0	0	0.0649
P$_2$O$_5$	0.0002	0	0	0	0

Figure 5.9. Progressive changes in the angles of separation of Flow C rock compositions from model spaces with successive addition of model vectors. **Panel A** shows the angles of separation. **Panel B** shows the angles of separation of the model divided by those of the magmatic model.

Overall, the angles separating rock compositions from the magmatic-metasomatic model space is $\sim< 5\text{-}30\%$ of the separation from magmatic space (Figure 5.9 B). Although most rock compositions achieve angles of $< 0.25°$ out of the magmatic-metasomatic space (Figure 5.9 A), these angles are still larger than those out of the rock composition space ($\sim< 0.005°$). This difference reflects geochemical variability the metasomatic model space fails to capture, which includes a combination of uncertainty and small-magnitude processes absent in the model.

The model rocks (Table 5.5) match the original measurements well, with the poorest reconstructions being of conserved components (Al_2O_3, TiO_2, P_2O_5; Figure 5.10), and the least abundant mobile components (Na_2O, K_2O; Figure 5.10). The relatively poor reconstruction of conserved components may seem counterintuitive. However, this result is predictable – that the model treats these components as conserved requires that they are only present in one model vector (the melt), and thus there is just one adjustable variable that affects their concentrations in model reconstructions. This scenario is the least forgiving possible in the reconstruction of their abundances. Moreover, although the differences of these components are commonly outside of analytical uncertainty (here shown as 3σ), they represent mismatch of a *maximum* of about 12 and 15% for Al_2O_3 and TiO_2, respectively, indicating that the missing variable is of little geological consequence.

In contrast, the respective relative differences in Na_2O and K_2O reach ~100 and $\sim450\%$, as well as being beyond the bounds of uncertainty. Some model approximations have negative amounts of K_2O (Table 5.5). The model is therefore an unsatisfactory explanation for total alkali variability. I thus infer that the mismatch between the rock and model compositions owes to minor (geologically insignificant) variations in the conserved elements and alkali-mobilizing processes the model does not encompass. Moreover, the low abundances of alkalis (especially K) in these rocks likely result in a significant uncertainty overprint, obfuscating the natural variability and contributing to the mismatch between the real and modeled compositions. Nevertheless, modeled and original rock compositions are close matches overall, with a maximum of $\sim0.6°$ separating any such pair in the nine dimensions of the oxide space.

Table 5.5. Modeled rock compositions, Flow C, Pyke Hill.

Sample#	MS93-02	MS93-03(A)	MS93-04	MS93-05	MS93-06	MS93-06(A)	MS93-07(ag)	MS93-07(A)	MS93-07(B)	MS93-07(CF)	MS93-07(FF)	MS93-07(sv)	MS93-08
Texture	Cumulate	Cumulate	Cumulate	Cumulate	Cumulate	Cumulate	Cumulate	Cumulate	Cumulate	Cumulate	Cumulate	Cumulate	Cumulate
SiO_2	40.90	40.82	42.45	41.02	40.89	39.25	41.30	41.75	40.99	41.32	40.92	40.37	41.74
TiO_2	0.214	0.187	0.190	0.187	0.169	0.162	0.182	0.186	0.178	0.192	0.163	0.184	0.208
Al_2O_3	4.67	4.08	4.16	4.09	3.70	3.54	3.98	4.06	3.89	4.20	3.56	4.01	4.56
$Fe_2O_3^T$	9.38	8.97	8.49	9.12	8.56	8.44	8.50	8.58	8.63	8.86	8.31	9.07	9.36
MgO	30.78	32.86	34.40	33.74	35.10	34.05	34.46	34.70	34.50	33.89	35.37	33.21	32.87
CaO	4.52	3.84	3.95	3.38	2.65	2.55	2.95	2.96	2.92	3.36	2.30	2.66	3.90
Na_2O	0.45	0.35	0.41	0.40	0.32	0.36	0.37	0.37	0.37	0.48	0.19	0.23	0.51
K_2O	0.036	0.015	0.036	0.036	0.015	0.035	0.026	0.025	0.027	0.061	-0.027	-0.026	0.060
P_2O_5	0.0127	0.0111	0.0113	0.0111	0.0100	0.0096	0.0108	0.0110	0.0105	0.0114	0.0096	0.0109	0.0124

Sample#	MS93-09	MS93-09(ag)	MS93-11	MS93-10	MS93-12	MS93-13(A)	MS93-13(B)	MS93-13(ag)	MS93-14(A)	MS93-14(B)	MS93-15	MS93-16	MS93-17A(A)
Texture	Cumulate	Cumulate	Cumulate	Spinifex	Spinifex	Spinifex	Spinifex	Spinifex	Spinifex	Spinifex	Spinifex	Spinifex	Spinifex
SiO_2	41.80	41.40	43.88	43.70	45.06	44.95	45.79	45.33	43.38	43.38	44.09	43.17	43.09
TiO_2	0.220	0.217	0.316	0.315	0.364	0.367	0.400	0.385	0.319	0.323	0.328	0.296	0.293
Al_2O_3	4.82	4.74	6.90	6.88	7.96	8.02	8.73	8.41	6.97	7.06	7.16	6.46	6.40
$Fe_2O_3^T$	9.49	9.94	9.77	11.22	11.87	12.01	12.17	12.32	11.36	11.46	11.53	10.83	10.85
MgO	31.29	31.54	23.77	25.43	23.37	23.53	21.91	22.43	25.32	24.89	25.30	26.73	27.12
CaO	4.24	4.18	8.24	7.12	7.63	7.64	8.16	8.22	6.59	6.81	6.82	6.31	6.19
Na_2O	0.39	0.44	0.70	0.75	0.91	1.03	1.14	1.10	0.77	0.78	0.78	0.71	0.74
K_2O	0.012	0.030	0.066	0.086	0.115	0.155	0.178	0.171	0.091	0.093	0.089	0.082	0.094
P_2O_5	0.0131	0.0129	0.0187	0.0187	0.0216	0.0218	0.0237	0.0228	0.0189	0.0191	0.0194	0.0175	0.0173

Table 5.5., continued.

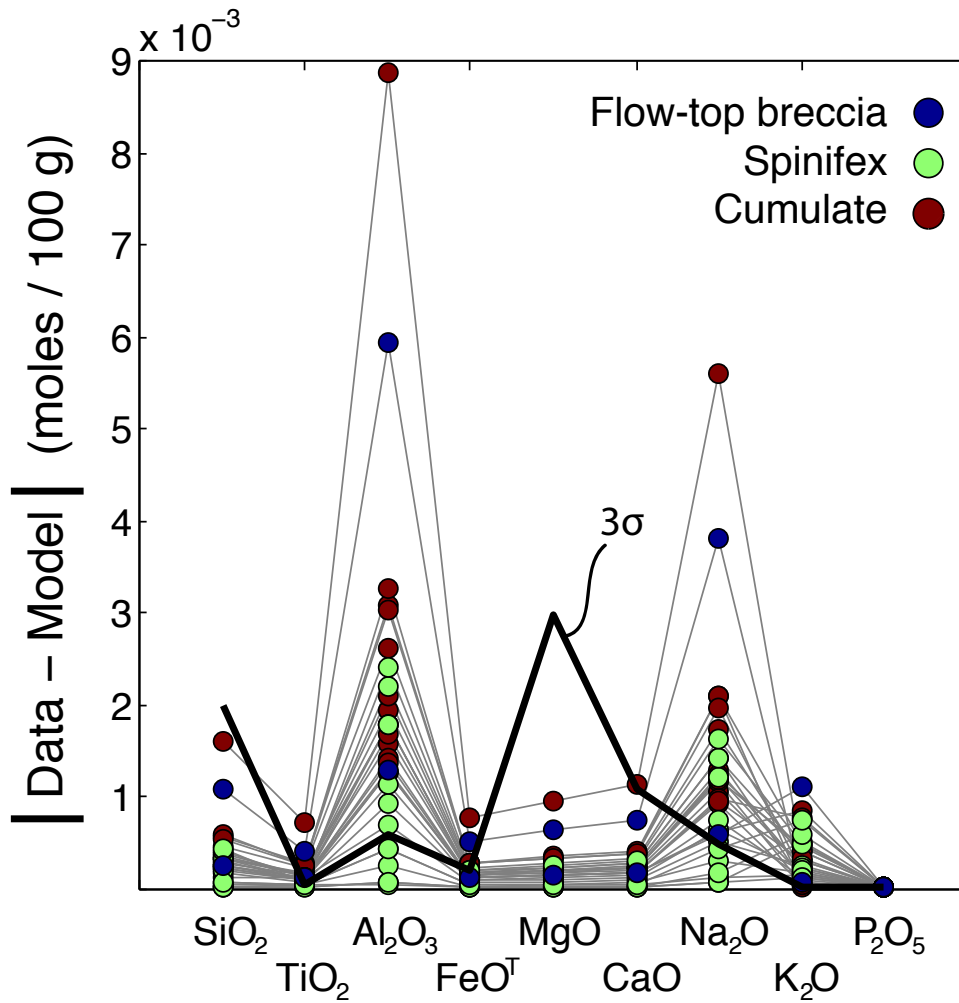| Sample#	MS93-17A(B)	MS93-18(A)	MS93-18(B)
Texture	Spinifex	Spinifex (breccia)	Spinifex (breccia)
SiO$_2$	43.98	44.39	42.71
TiO$_2$	0.312	0.285	0.298
Al$_2$O$_3$	6.83	6.23	6.51
Fe$_2$O$_3$^{T}	10.97	9.63	10.89
MgO	26.28	26.12	24.47
CaO	6.54	6.95	7.60
Na$_2$O	0.74	0.24	0.59
K$_2$O	0.082	-0.082	0.036
P$_2$O$_5$	0.0185	0.0169	0.0177

Figure 5.10. Differences of all major element oxides between modeled and real rock compositions from Flow C.

Rock compositions transformed into model vectors (Table 5.6) are principally mixtures of the evolved liquid and olivine (Fo$_{91.2}$). These two vectors account for >~95% of most rock compositions (Figure 5.11). However, the nature of the metasomatic process depends upon the lithofacies and position in the flow (Figure 5.12).

The serpentine and chlorite-forming reaction is most significant in cumulate-textured rocks, mirroring petrographic observations of the extent of serpentinization therein (Pyke et al., 1973; Shore, 1997). This reaction explains virtually all metasomatic movement of Fe (Figure 5.13), and is likely responsible for the disruptions to whole rock Mg-Fe equilibria (Figure 5.14; Section 4.6.2), as the other metasomatic reactions do not correlate with this deviation. Thus, despite the small magnitude of the metasomatic serpentinization-chloritization process, it bears significant consequences for the compositional relationships within this komatiite flow and perhaps others.

The actinolite-forming vector explains most losses and gains of Ca, with flow-top breccias and select cumulate samples deviating most significantly (Figure 5.15). Its variation in the flow indicates actinolite-formation and removal of Ca in the cumulus zone, whereas the spinifex zone absorbed a portion of those losses. Amphibole occurs after clinopyroxene in the cumulate zone of the Pyke Hill flows, whereas most clinopyroxene in the spinifex zone is unaltered (Pyke et al., 1973; Shore, 1997). Late clinopyroxene overgrowths and/or re-equilibration rims occur in the spinifex zones of some komatiite flows (LaHaye and Arndt, 1996; Arndt et al., 2008). Such secondary clinopyroxene could host these elemental gains, if phase equilibria permit stability of actinolite and late clinopyroxene contemporaneously in the cumulate and spinifex bulk compositions, respectively.

5.5. The nature of serpentinization in the Abitibi Flow C komatiite

The recovery and quantification of metasomatic serpentinization reactions has relevance to all ultramafic systems. The process of serpentinization is a vibrant area of research including topics such as volatile cycling within and on Earth (Hattori and Guillot, 2007; Deschamps et al., 2013) and Mars (Ehlmann et al., 2011), the origins of life (Sleep et al., 2004; Sleep et al., 2011; McCollom and Seewald, 2013; Holm et al., 2015), and

Table 5.6. Transformed rock compositions, Flow C, Pyke Hill.

Sample#	MS93-02	MS93-03(A)	MS93-04	MS93-05	MS93-06	MS93-06(A)	MS93-07(ag)	MS93-07(A)	MS93-07(B)	MS93-07(CF)	MS93-07(FF)	MS93-07(sv)	MS93-08
Texture	Cumulate	Cumulate	Cumulate	Cumulate	Cumulate	Cumulate	Cumulate	Cumulate	Cumulate	Cumulate	Cumulate	Cumulate	Cumulate
Evolved melt	0.4326	0.3653	0.3493	0.3527	0.3085	0.3054	0.3311	0.3341	0.3265	0.3538	0.2950	0.3497	0.3931
Fo91.2	0.5482	0.6134	0.6170	0.6140	0.6487	0.6525	0.6224	0.6179	0.6305	0.6020	0.6611	0.6130	0.5708
Serpentine + chlorite formation	0.0202	0.0222	0.0328	0.0223	0.0276	0.0248	0.0308	0.0313	0.0279	0.0277	0.0297	0.0214	0.0237
Actinolite formation	-0.0052	-0.0021	-0.0027	0.0071	0.0140	0.0135	0.0131	0.0141	0.0122	0.0093	0.0179	0.0199	0.0053
Alkali feldspar formation	0.0042	0.0012	0.0039	0.0040	0.0012	0.0040	0.0025	0.0024	0.0028	0.0072	-0.0044	-0.0045	0.0072
Sum	1.0000	1.0000	1.0002	1.0000	1.0000	1.0001	0.9999	0.9998	0.9999	1.0001	0.9994	0.9996	1.0001

Sample#	MS93-09	MS93-09(ag)	MS93-11	MS93-10	MS93-12	MS93-13(A)	MS93-13(B)	MS93-13(ag)	MS93-14(A)	MS93-14(B)	MS93-15	MS93-16	MS93-17A(A)
Texture	Cumulate	Cumulate	Cumulate	Spinifex	Spinifex	Spinifex	Spinifex	Spinifex	Spinifex	Spinifex	Spinifex	Spinifex	Spinifex
Evolved melt	0.4335	0.4296	0.7236	0.6881	0.7891	0.7847	0.8536	0.8403	0.6853	0.7041	0.6998	0.6242	0.6112
Fo91.2	0.5398	0.5488	0.2807	0.3053	0.1867	0.1847	0.1041	0.1332	0.2941	0.2796	0.2803	0.3569	0.3674
Serpentine + chlorite formation	0.0224	0.0150	0.0331	0.0132	0.0162	0.0153	0.0205	0.0136	0.0129	0.0114	0.0133	0.0165	0.0160
Actinolite formation	0.0034	0.0032	-0.0454	-0.0185	-0.0077	-0.0066	-0.0036	-0.0116	-0.0048	-0.0079	-0.0058	-0.0086	-0.0073
Alkali feldspar formation	0.0005	0.0032	0.0090	0.0118	0.0160	0.0220	0.0254	0.0249	0.0124	0.0129	0.0119	0.0109	0.0126
Sum	0.9997	0.9999	1.0011	1.0000	1.0002	1.0001	1.0000	1.0003	0.9999	1.0000	0.9996	0.9999	1.0000

Table 5.6., continued.

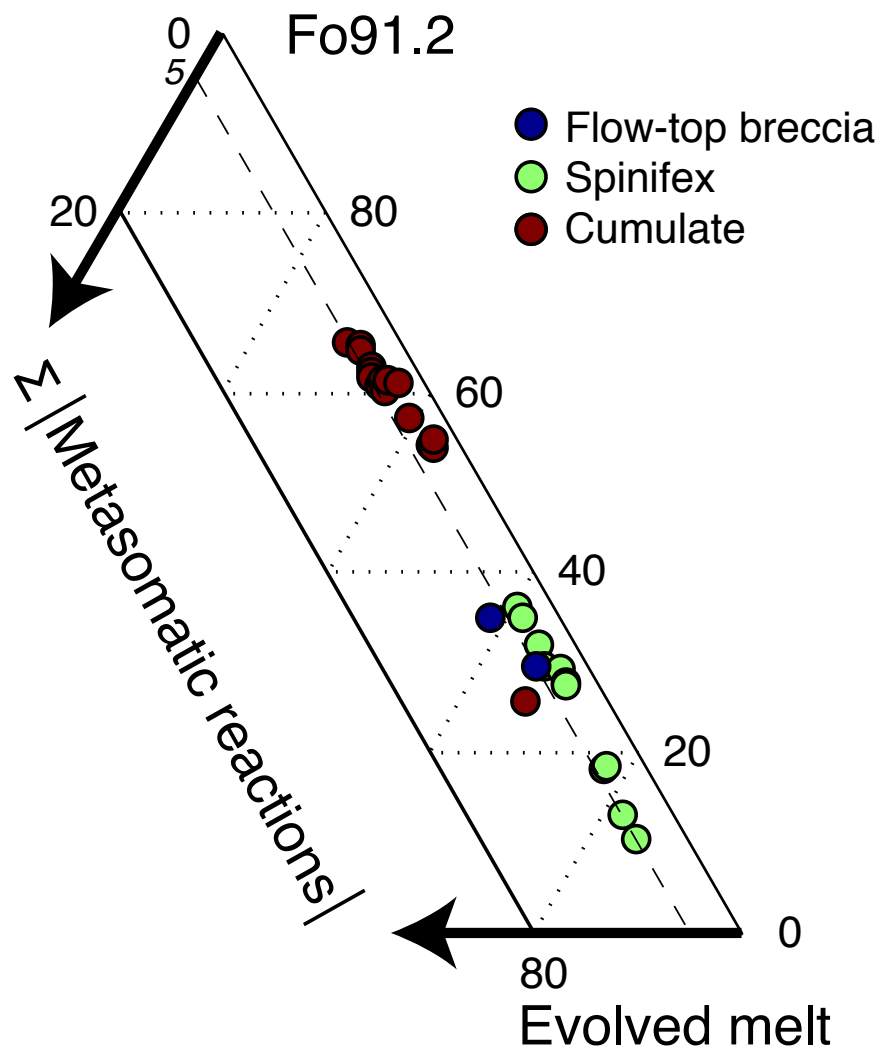| Sample#	MS93-17A(B)	MS93-18(A)	MS93-18(B)
Texture	Spinifex	Spinifex (breccia)	Spinifex (breccia)
Evolved melt	0.6525	0.6330	0.7081
Fo91.2	0.3234	0.3790	0.3195
Serpentine + **chlorite formation**	0.0191	0.0305	0.0087
Actinolite formation	-0.0062	-0.0286	-0.0402
Alkali feldspar **formation**	0.0108	-0.0150	0.0043
Sum	0.9995	0.9990	1.0004

Figure 5.11. Ternary diagram plotting transformed rock compositions from Flow C. The magmatic vectors (***Evolved melt*** and ***Fo91.2***) define two apices and the sum of the absolute values of the metasomatic vectors (Σ | ***Metasomatic reactions*** |) defines the third.
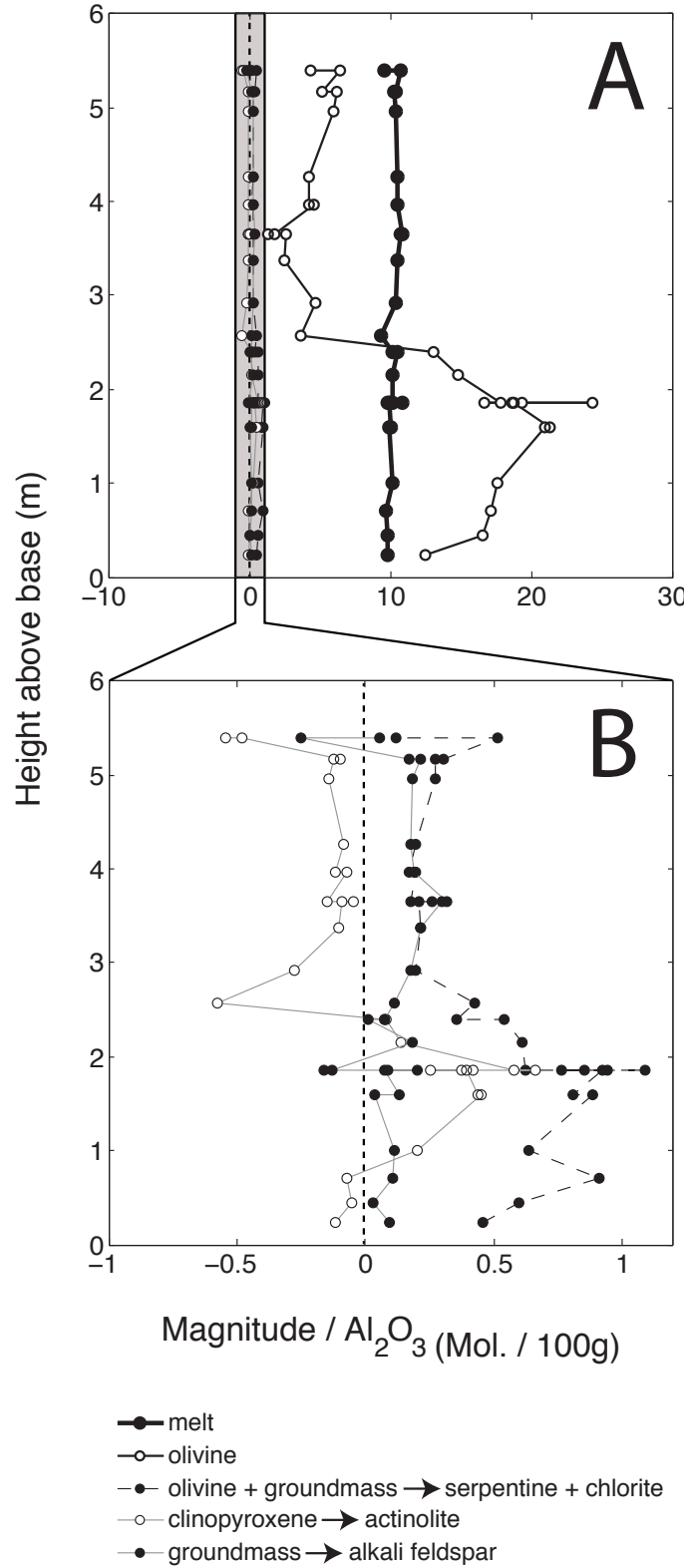
Figure 5.12. Relationship of model vector components to distance above the base of Flow C, normalized to Al_2O_3. **Panel A** shows all model vectors and **Panel B** focuses on the small magnitude metasomatic vectors.

Figure 5.13. Relationship between Fe contained within metasomatic vectors to metasomatic changes recorded by measured rock compositions from Flow C, normalized to Al.

Figure 5.14. Relationship between the value of the serpentine and chlorite-forming vector and Mg-Fe disequilibrium shift in Flow C.
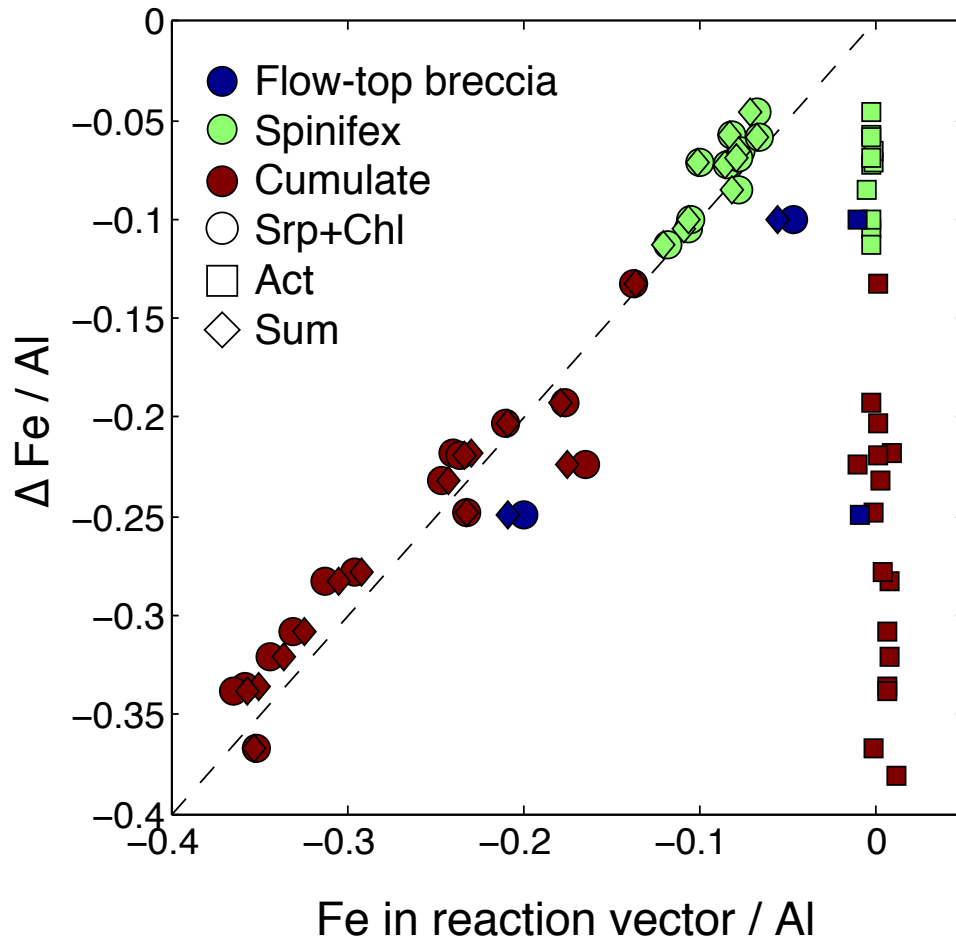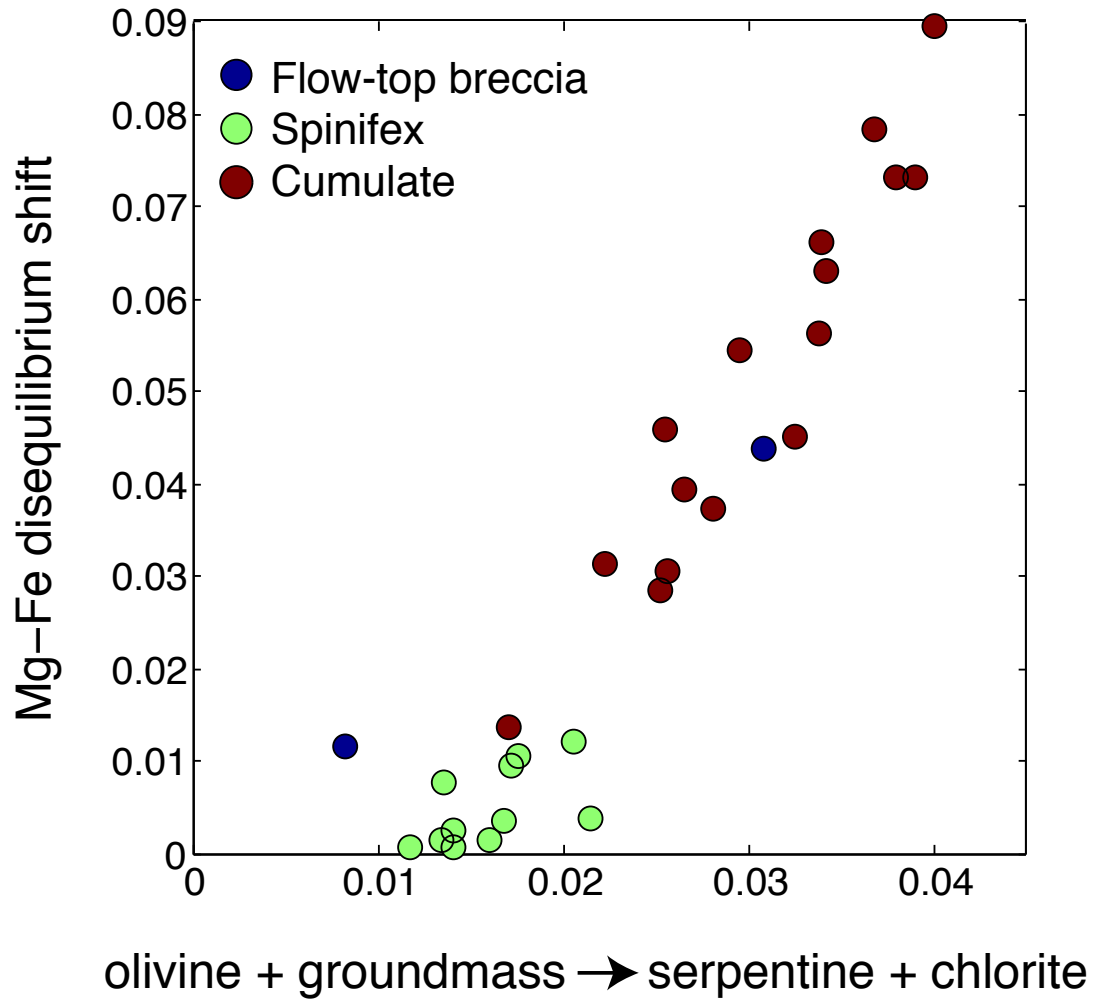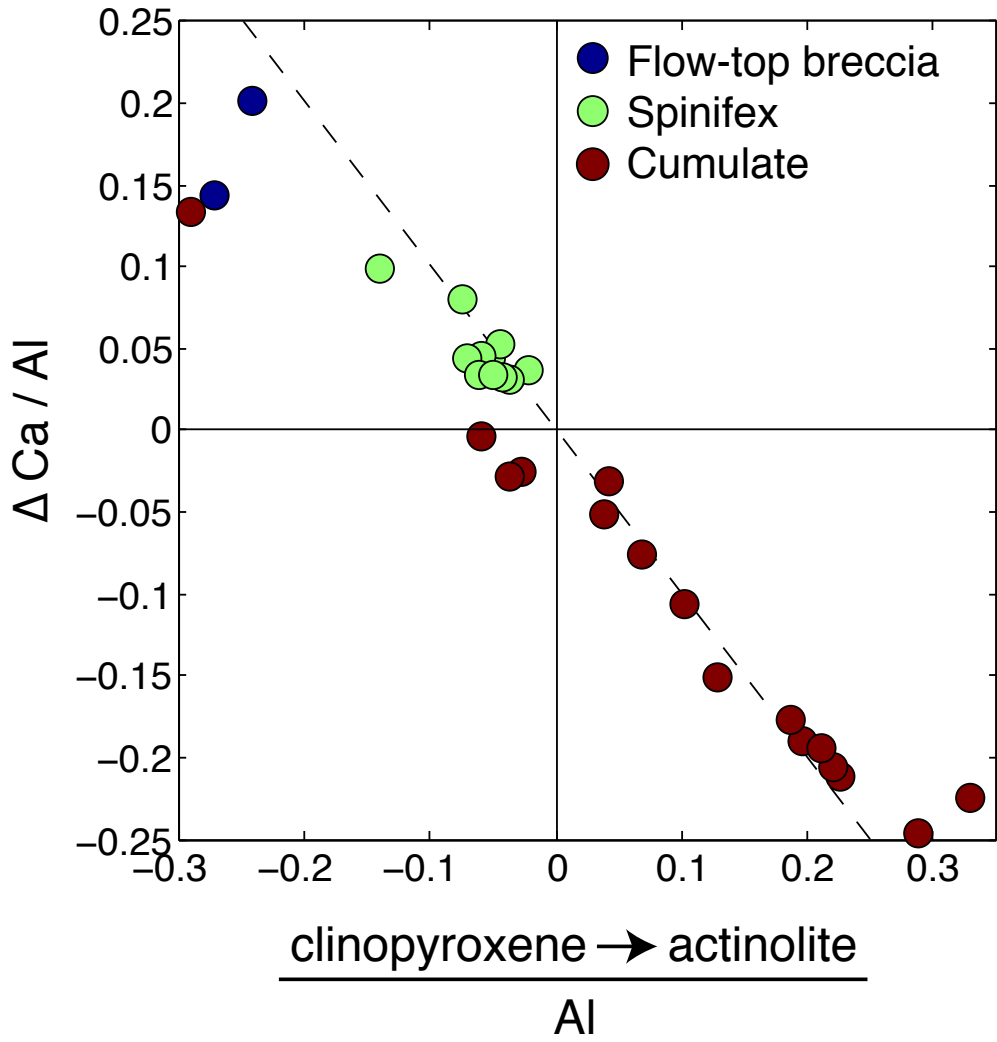
Figure 5.15. Relationship between Ca contained within the actinolite-forming vector to metasomatic changes recorded by measured rock compositions from Flow C, normalized to Al.

production of magmas parental to volcanic arcs (Hattori and Guillot, 2003). The nature of the serpentine-forming reactions is directly or indirectly intertwined with all research in serpentinization and serpentinites; the key question of whether serpentinization is a nominally isochemical hydration process (i.e., all components conserved apart from H_2O) or metasomatic remains open, and likely may depend on the geological environment (cf. Hostetler et al., 1966; Thayer, 1966; Coleman and Keith, 1971; Moody, 1976; Komor et al., 1985; Peacock, 1987; O'Hanley, 1992; Shervais et al., 2005; Sparks et al., 2009; Frost et al., 2013; Schwarzenbach et al., 2015).

Recovery of a viable metasomatic serpentinization reaction enables an assessment of the relative importance of metasomatic and isochemical end member reactions in the Flow C komatiite. Figure 5.16 A shows the relationship between the magnitude of the serpentinization reaction and the amount of H* in the rocks, expressed as molar ratios of Al. The trend corresponding to reaction stoichiometry defines a lower bound to the data, with most samples having excess H. The slope on this diagram relates to the contributions of metasomatic and isochemical end member reactions, the latter defining a vertical line. A binary diagram illustrates this relationship and enables estimation of the proportions of isochemical and metasomatic end members (Figure 5.16 B). The slope of the line of best fit corresponds to a metasomatic fraction (X_{meta}) of ~0.67. The range of X_{meta} for most samples is from 0.4 to 1, indicating a tendency toward greater contribution of metasomatic serpentinization than isochemical hydration. This result provides a solution to the nature and geochemical expression of serpentinization reactions on the outcrop and hand sample scales within a komatiite flow. Application of the methods employed here to other ultramafic rocks would reveal geological controls on the isochemical-metasomatic ratio, and provide definitive resolution to this longstanding debate.

5.6. Conclusion

Combining PERs with geometric testing methods and linear transformations unlocks new potential to characterize the effects of magmatic and metasomatic processes upon whole rock compositions. Application to the Abitibi Flow C komatiite reveals modifications to Ca, Na, K, Fe, and perhaps Si and/or Mg during metasomatism. Reactions producing
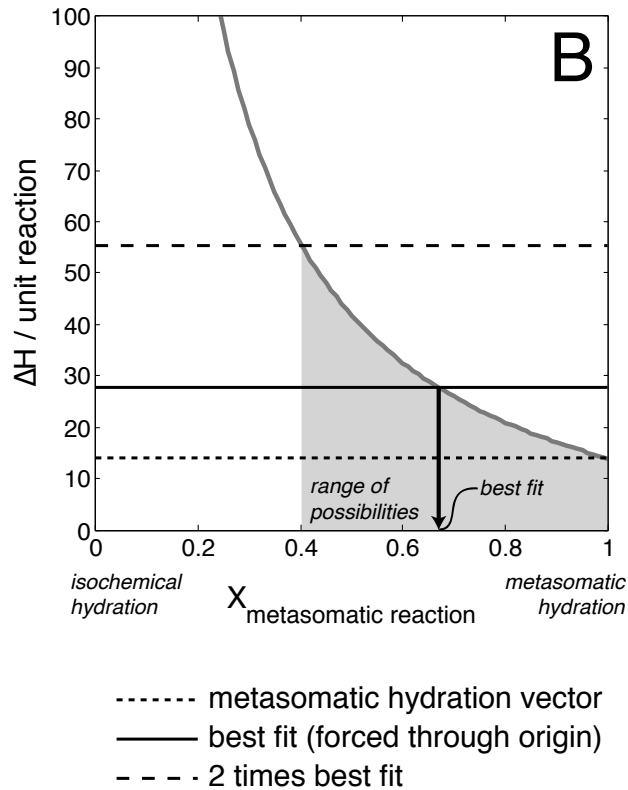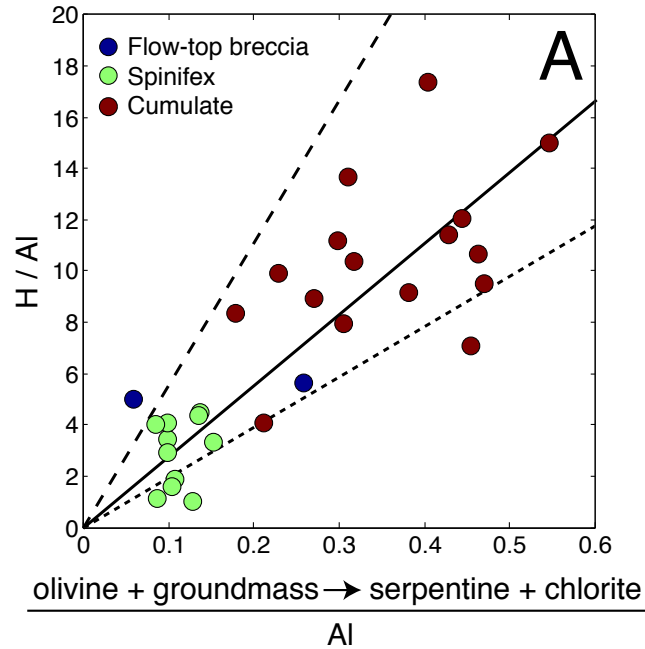
Figure 5.16. Diagrams estimating the relative proportions of isochemical and metasomatic end members of serpentinization in Flow C. (**A**) Relationship between the serpentine and chlorite-forming vector and H* in whole rocks, normalized to Al. (**B**) Dependence of slope in panel A on the proportion of metasomatic and isochemical hydration end members ($X_{metasomatic\ reaction}$).

serpentine + chlorite, actinolite, and alkali feldspar pass geometric testing and explain most geochemical variability in the rocks, in combination with primary magmatic processes. Replacement of clinopyroxene in the cumulate zone liberates Ca that spinifex rocks partially absorb. All significant losses of Fe occur by the serpentinization reaction. Formation of autometamorphic alkali feldspar in the spinifex zone could explain much of the variability of Na. However, other unidentified processes are necessary to fully capture alkali variability, and lack of independent geological information on the identity of alkali-bearing phases reduces confidence in the meaningfulness of this conclusion. Serpentinization of the Flow C komatiite involved both metasomatic and isochemical end-member reactions, with the former being the dominant process. Application of these methods to other komatiite occurrences and their surrounding rocks could elevate traditional lithogeochemical exploration techniques from reliance on empirical bivariate diagrams (Barnes et al., 2004; Le Vaillant et al., 2016) to a process-driven approach. Extending the applications of these methods to testing serpentinization in ultramafic rocks more generally could resolve the longstanding debate about the nature of serpentinization reactions (Hostetler et al., 1966; Thayer, 1966; Coleman and Keith, 1971; Moody, 1976; Komor et al., 1985; Peacock, 1987; O'Hanley, 1992; Shervais et al., 2005; Frost et al., 2013; Schwarzenbach et al., 2015).

CHAPTER 6: Conclusions

6.1. Brief summary

The first goal of this work was to devise lithogeochemical methods that test geochemical processes at any stage of rock formation or modification, without assumptions (Figure 6.1 A). I overcame key limitations in existing methods using linear algebraic techniques (Fisher, 1989; Strang, 2009) that recognize rock compositions as vectors in high-dimension spaces (Gordon, 2000; Gordon and Russell, 2006). This approach enabled stringent tests of magmatic and metasomatic processes in komatiites (Figure 6.1 B), aiding realization of the other major goals. Among these was to test the nature and magnitude of magmatic processes in komatiites, particularly with respect to the hypothesis of within-flow differentiation and continuity between komatiites and associated komatiitic basalts (Lesher, 1989; Figure 6.1 C). The final goal was to quantify metasomatism and determine viable metasomatic reactions in komatiites, especially with regard to whether serpentinization reactions are metasomatic or purely isochemical (Hostetler et al., 1966; Thayer, 1966; Coleman, 1971; Moody, 1976; O'Hanley, 1992; Figure 6.1 D).

I tested proposed parental liquid compositions (Shimizu et al., 2001; Sobolev et al., 2016; Sossi et al., 2016) and determined the composition of olivine responsible for differentiation of komatiite flows. Partitioning calculations (Roeder and Reynolds, 1991; Russell and Snyder, 1997; Putirka, 2005; Sossi and O'Neill, 2016) and phase equilibria (Russell and Snyder, 1997) estimated the evolved liquid composition and its temperature, and enabled determination of the relative distance of an exposure from its vent. This analysis constrained an exposure from the Pyke Hill region to the proximal regions of the volcanic system. Excess olivine in these rocks implies that a portion of the evolved, komatiitic basaltic liquid flowed downstream, confirming the possibility of continuity between komatiite and komatiitic basalt within individual flows (Figure 6.1 C).

Determination of magmatic differentiation processes enabled construction of a model space (magmatic space) that contains all thus derived compositional diversity. Deviation from this space corresponds to the magnitude of metasomatic disturbance, thereby yielding a quantitative Metasomatic Index for komatiites. The Metasomatic Index
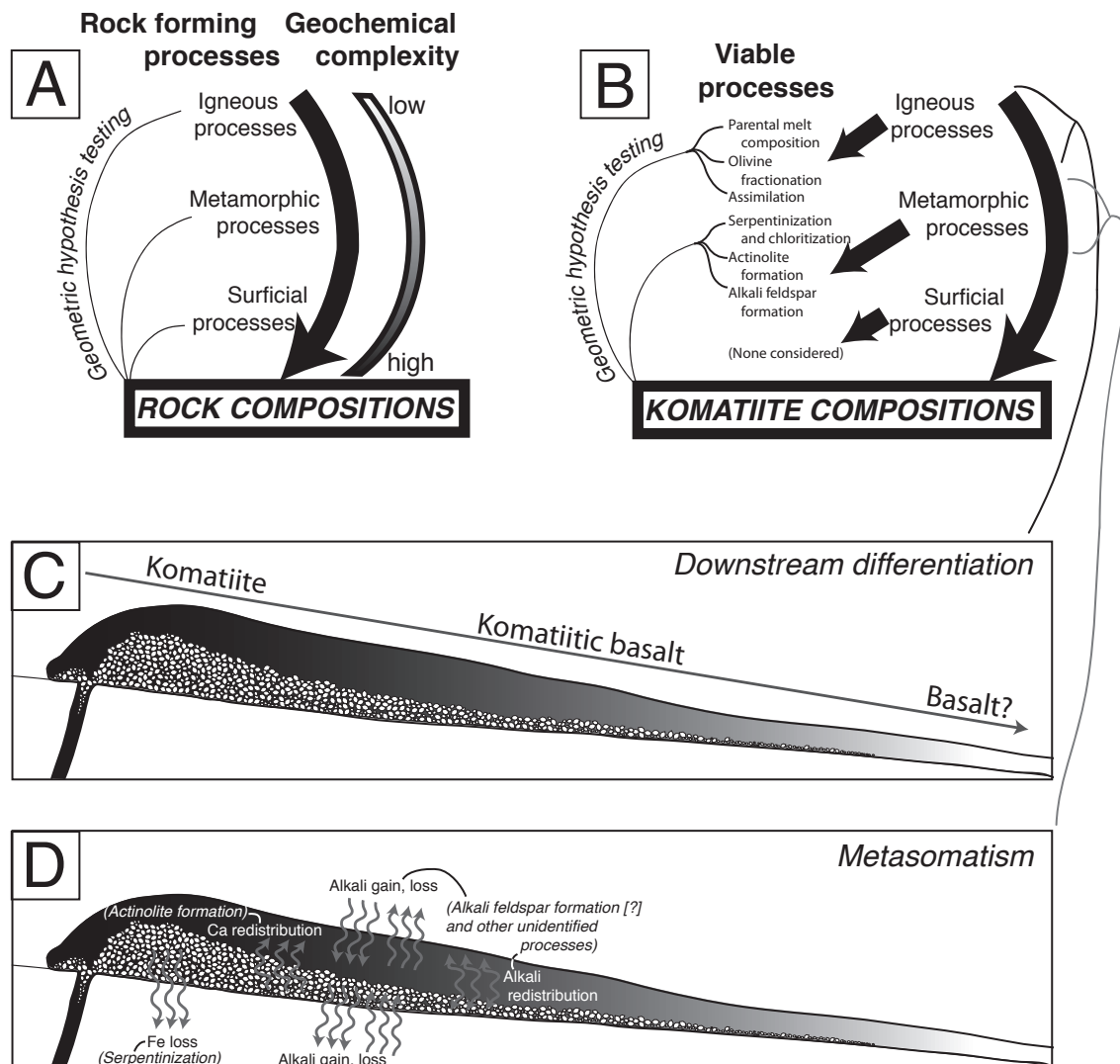
Figure 6.1. Graphic summary of the main contributions of this work. (**A**) The geometric methods from Chapter 3 enable robust testing of any geochemical mass transfer hypothesis ranging from the highest to lowest temperature rock-forming and -modifying processes, in geochemically simple or complex systems. (**B**) Applications to komatiites enabled recovery of igneous and metamorphic processes, including olivine fractionation, assimilation of sedimentary substrate, serpentinization + chloritization, and actinolite-formation. (**C**) Application of classic petrological tools to the optimal olivine compositions revealed strong geochemical support for within-flow differentiation and lateral continuity of komatiites and komatiitic basalts. (**D**) Analysis of Pearce element ratios and geometric modeling of metasomatism identified significant losses of Fe attending serpentinization, redistribution of Ca attending actinolite formation, and redistribution, gains, and losses of alkalis attending undetermined processes (possibly including alkali feldspar formation). Serpentinization was neither isovolumetric nor isochemical, but was a combination of an isochemical and metasomatic end-member.

correlates well with the extent of whole rock Mg-Fe disequilibrium of cumulus facies samples, whereas metasomatism of spinifex rocks is independent thereof.

Combining the Metasomatic Index with PER analysis (Pearce, 1968) and geometric hypothesis testing revealed metasomatic changes and viable chemical reactions in the Abitibi Flow C (Figure 6.1 D). Metasomatism mainly affected Fe, Ca, Na, and K among the major elements. Expanding the magmatic model to include reaction vectors for formation of serpentine + chlorite, actinolite, and alkali feldspar enabled good recovery of whole rock compositions, with alkalis and conserved elements being the most poorly reconstructed. Release of Ca associated with actinolite formation in the cumulus zone tended to be absorbed within the spinifex zone (Figure 6.1 D). This process explains virtually all metasomatic disturbance of Ca. Formation of serpentine and chlorite explains losses of Fe in the cumulus zone. Serpentinization included both this metasomatic and an isochemical hydration end member, with the former contribution exceeding the latter. Serpentinization of komatiites thus cannot be assumed to be purely isochemical.

6.2. The significance of this thesis

The main contributions of this thesis are fourfold. First, the adoption of linear algebraic analysis to test mass transfer hypotheses and models represents a significant advancement. This approach recognizes rock compositions as vectors in high dimension rock composition spaces (Gordon, 2000; Gordon and Russell, 2006), which encompass bulk compositions and their PER equivalents. Geometric testing circumvents the weaknesses and points of contention in variation diagram analysis (Harker, 1909; Chayes, 1962) and the PER/isocon approach (Pearce, 1968; Grant, 1986; Pearce, 1987; Rollinson and Roberts, 1987; Nicholls, 1988; Russell and Nicholls, 1988; Stanley, 1993; Grant, 2005; Guo et al., 2009); in particular, the new method avoids both the problem of closure (Chayes, 1962) and the necessity of closed-system behaviour of at least one element (Pearce, 1968; Stanley, 1993). Mass transfer processes spanning the entire rock cycle present opportunities for applications (Figure 6.2). Topics such as magma generation and differentiation (e.g., fractionation, assimilation, magma mixing), sedimentary mixing and sorting, hydrothermal alteration/metasomatism, ore-formation and concentration, and chemical weathering are all ready opportunities for study.
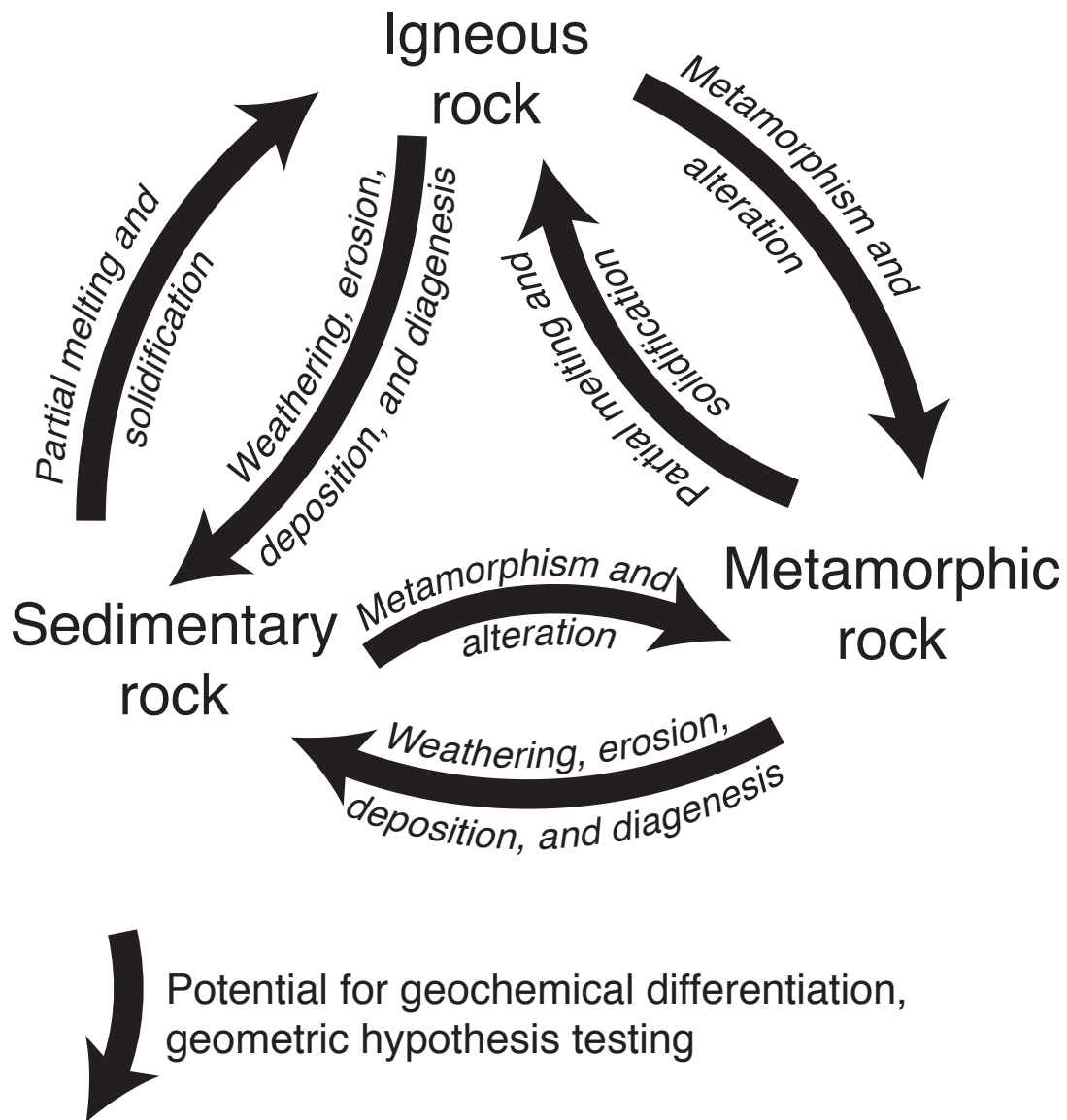
Figure 6.2. Schematic of the rock cycle and rock forming processes highlighting the opportunities for geometric testing (***black arrows***) of geochemical hypotheses.

The second principal contribution stems from applications to magmatic differentiation of komatiites. Strong geochemical support for the notion of within-flow differentiation extensive enough to produce komatiitic basalt (Lesher, 1989) has potential significance to Archean field geology (Figure 6.3) and the structure of komatiite volcanoes. For example, outcrops of komatiite and komatiitic basalt in the Abitibi greenstone belt (Arndt et al., 1977) need not represent separate lava flows on the basis of bulk compositional differences, but may in some cases be vent-proximal and distal exposures of the same flow, respectively (Lesher, 1989). A fictive example in Figure 6.3 demonstrates how within-flow lithological gradients could lead to incorrect interpretation of field relations. This possibility is important to interpretations of field relations between komatiites and komatiitic basalts. For example, geochemically alike occurrences in the Reliance Formation were proposed to represent parcels of an evolving magma chamber (Shimizu et al., 2005). The alternative explanation – that the basalts represent within-flow differentiates – requires no magma chamber whatsoever. Indeed, crustal residence of a ~1600 °C magma chamber without appreciable xenolith assimilation, as occurred in other associated komatiitic basalts (Shimizu et al., 2005), seems implausible. Distinguishing these differing possibilities in the Reliance Formation and other komatiite-basalt associations has significant implications for the distribution of heat within the Archean crust in the vicinity of komatiite and komatiitic basalt occurrences. If komatiitic magma chambers were abundant, their thermal contribution could have added significant heat to the Archean crust, promoting its anatexis and formation of continental crust. Hence, interpretation of these geochemical relationships informs broader questions about Archean geology.

The third significant finding concerns serpentinization and metasomatism. A central and outstanding issue concerning serpentinization is whether it occurs by simple isochemical hydration (addition of H_2O without other modification) or by a metasomatic reaction, one extreme of which is isovolumetric serpentinization (Figure 6.4). Since the inconclusive debate in the late 1960s and early 1970s (Hostetler et al., 1966; Thayer, 1966; Coleman and Keith, 1971; Moody, 1976), the question has been addressed in case studies (Komor et al., 1985; Peacock, 1987; Shervais et al., 2005; Stripp et al., 2006; Frost et al., 2013; Schwarzenbach et al., 2015). However, as these analyses suffered the
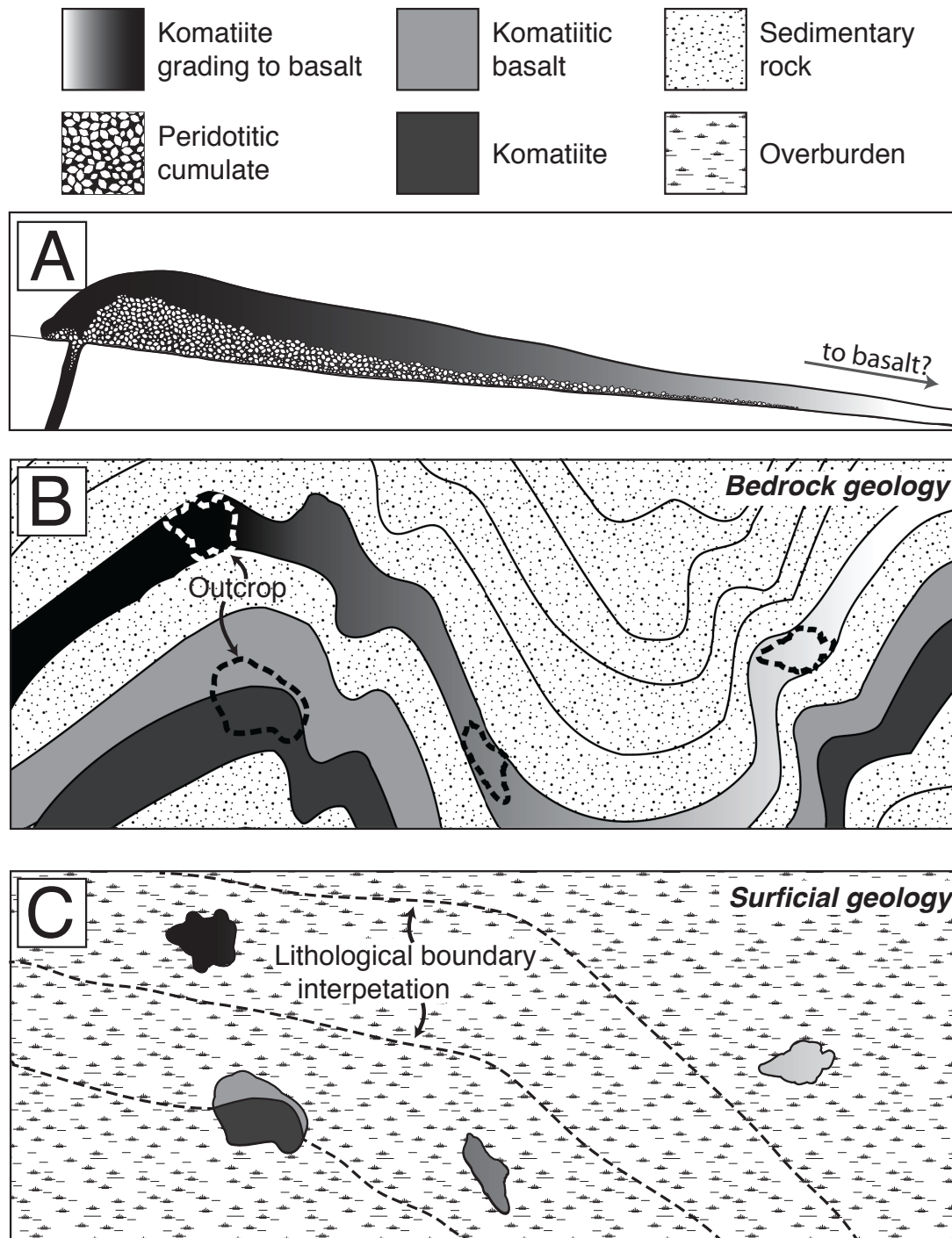
Figure 6.3. Schematics illustrating potential significance of lateral differentiation (**A**) in komatiite lavas to interpretation of field relations. (**B**) Hypothetical bedrock geology showing folded and interlayered volcanic and sedimentary rocks, and locations of outcrops (***dashed lines***). Volcanic strata include homogeneous komatiitic basalt, homogeneous komatiite, and komatiite grading to basalt. (**C**) Hypothetical outcrop exposures through overburden with inferred lithology-based contacts. The inferred contacts are erroneous in this rhetorical example.
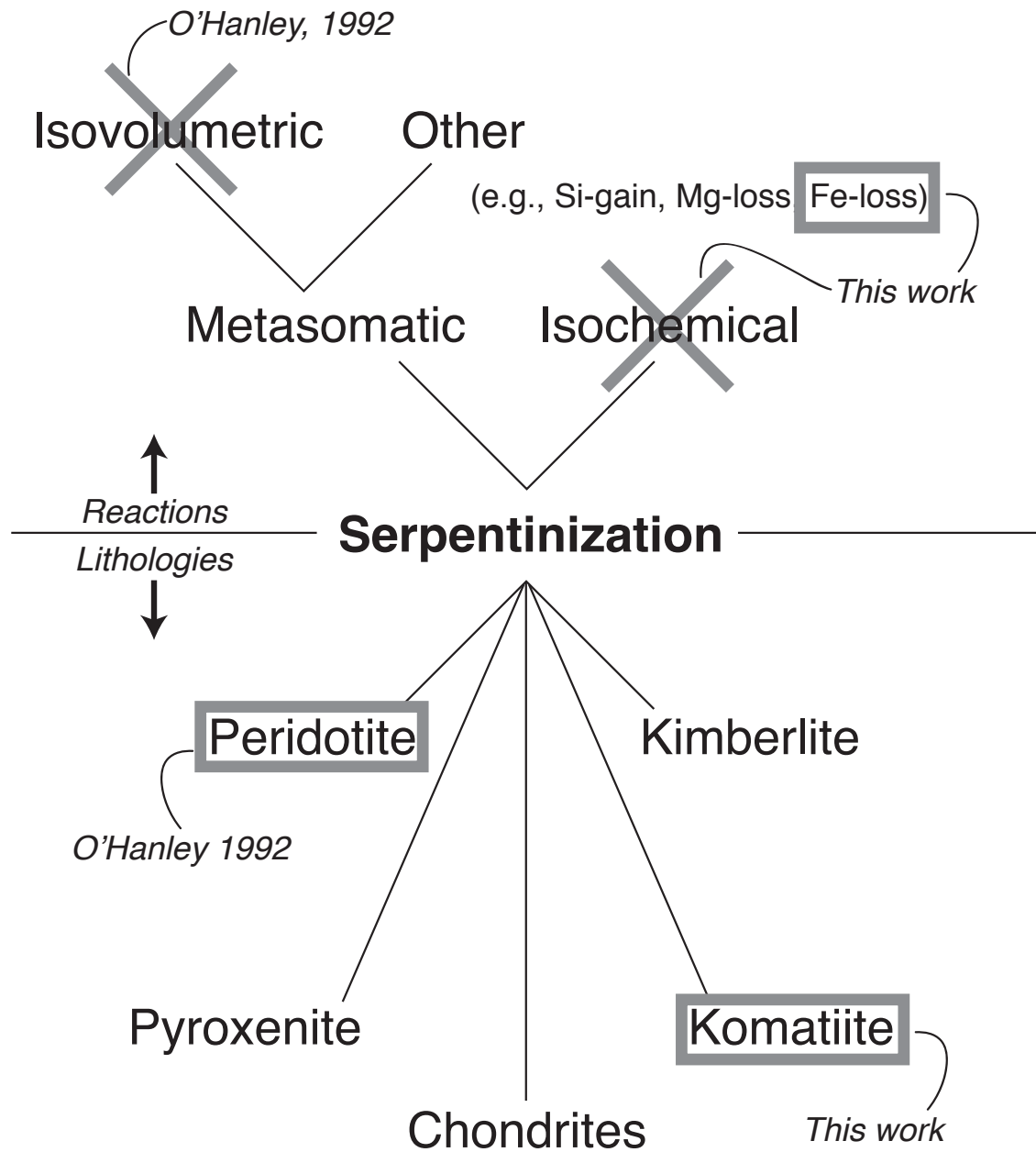
Figure 6.4. Variety of serpentinization reactions (***upper half***) and the lithologies (***lower half***) they affect. O'Hanley's textural observations precluded isovolumetric serpentinization of peridotites, whereas this work identified serpentinization by Fe-loss in komatiite. Definitive tests of serpentinization reactions in other lithologies and the different geological settings in which they occur would expand knowledge of their effects on both the host rock, its surrounding environment, and the global geochemical system.

intrinsic problems of binary variation and isocon diagrams, and/or correct interpretation of textures, little definitive geochemical evidence for or against metasomatism has been presented. Moreover, although recognition of cryptic expansion textures discounts isovolumetric serpentinization (O'Hanley, 1992), it does not quantitatively address other metasomatic reactions (Figure 6.4). Determination of viable metasomatic reactions and the relative proportions of the metasomatic and isochemical end members is a significant contribution to knowledge of whole-rock scale metasomatism attending serpentinization. The reactions I uncovered are inconsistent with either isochemical or isovolumetric serpentinization of komatiite cumulates. If these methods enable robust testing of chemical reactions upon future applications to other ultramafic systems (e.g., Alpine peridotites, oceanic mantle, layered mafic intrusions, kimberlites, mantle xenoliths), the approach I applied will be central to resolving this longstanding problem (Figure 6.4).

Finally, a significant result of this work is that, despite significant modal replacement of primary mineralogy in komatiites, the metasomatic portion of rock compositions is small (~5%). Nevertheless, metasomatism was sufficient to destroy primary Mg-Fe equilibria in cumulates, and disturb Ca/Al systematics in all komatiite facies. These disruptions provide a lesson in the interpretation of primary processes using modestly metasomatized rock compositions – little total modification of whole rocks is sufficient to eradicate meaningful information regarding the protolith. The ratios of Ca to Al were once considered an important component in the geochemical classification of komatiites, until workers discovered their sensitivity to metasomatism (history summarized in Arndt et al., 2008). The results of this work show that a small magnitude of the actinolite-forming reaction was sufficient to cause changes in Ca/Al that would once have led to misinterpretation of petrogenesis. These findings highlight that neglect of even small metasomatic contributions to whole rock compositions could compromise the conclusions of petrogenetic or petrological studies of altered igneous rocks.

6.3. Future directions

Geochemical diversity arises from differentiation processes. Constraints on the possible chemical processes by which differentiation occurs are central to geological research. The new approach to geochemical testing (Chapter 3) elevates whole rock geochemistry to a

new level of capability, spanning magmatic, metasomatic, sedimentary, diagenetic, and meteoric processes (Figure 6.2). Liberation from the constraint of element conservation (Pearce, 1968; Grant, 1986; Russell and Nicholls, 1988; Stanley, 1993; Grant, 2005; Guo et al., 2009) opens new opportunities wherever geoscientists measure bulk compositions from thoughtfully sampled rock suites. These opportunities include any appropriate existing datasets, published or otherwise, as well as current and future research.

An intriguing line of komatiite research would expand upon the hypothesis that within-flow lateral differentiation physically and genetically links some komatiite and komatiitic basalt occurrences (Lesher, 1989; Chapter 4 of this thesis). The main motivation would be to determine which komatiitic basalt flows differentiated in magma chambers, and which differentiated from komatiite melt in lava flows (Figure 6.5). Two geochemical classes of komatiitic basalt in the Reliance Formation, one contaminated and the other not (Shimizu et al., 2005), may provide an indication. Perhaps magma chamber-derived komatiitic basalt would be contaminated owing to the assimilation potential of extremely hot parental liquids (Figure 6.5 D-G), whereas those differentiated in surficial flows may lack significant contamination (Figure 6.5 A-C), in cases where basal assimilation beneath flows was negligible. Combinations of field observation, major and trace element compositions, isotopic compositions, and perhaps geophysical imaging would aid testing whether komatiitic basalt lavas are lateral continuations of komatiite flows. Theoretical constraints from physical modeling of the flow of liquid and liquid-crystal mixtures, crystal settling rates, heat exchange, and solidification would also help to test the viability of the hypothesis by placing constraints on the permissive conditions (e.g., subaerial or subaquatic, slope angles, flow velocity, crystal content, substrate type).

Serpentinization is a pressing area for future research. Motivations to study serpentinization span the origins of life on Earth (Sleep et al., 2004; Sleep et al., 2011; Guillot and Hattori, 2013; McCollom and Seewald, 2013; Holm et al., 2015) and beyond (Nna-Mvondo and Martinez-Frias, 2007; Holm et al., 2015), the water budget of Mars (Ehlmann et al., 2011), cycling of volatiles within the Earth (Hattori and Guillot, 2007; Deschamps et al., 2013), thermal modeling of igneous and hydrothermal systems (Allen and Seyfried, 2004; Afanasyev et al., 2014), and recovery of primary compositions of igneous protoliths (Sparks et al., 2009; Brooker et al., 2011). This thesis demonstrates
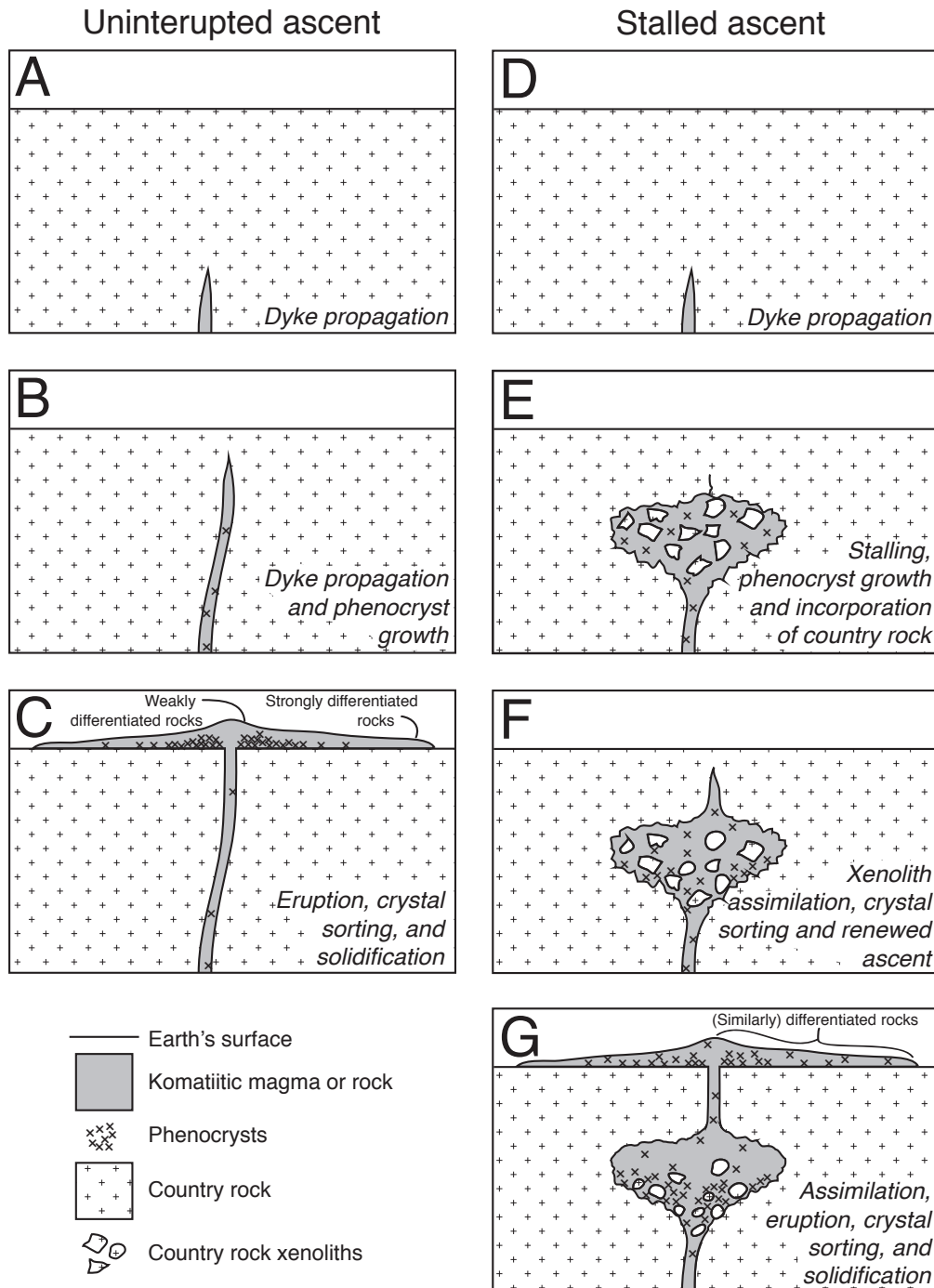
Figure 6.5. Schematics of uninterrupted and stalled ascent of komatiite magma. (**A-C**) Uninterrupted ascent implies little time for cooling, crystallization, fractionation, and contamination/assimilation, leading to extrusion of nominally undifferentiated komatiite lava. Fractionation within the propagating flow may give rise to lateral compositional and lithological gradients. (**D-G**) Interruption of magma ascent in the crust affords time for cooling, crystallization, fractionation, and xenolith assimilation. Renewed ascent delivers contaminated, evolved, and comparatively cool magma that extrudes to form lava flows with minimal lateral differentiation.

that viable serpentinization reactions are identifiable. Reduction of H^+ in water to H_2 by oxidative magnetite formation during serpentinization is particularly critical; such processes are important to methanogenic microbial communities and drive speculation about a link to life's origins and the chemical evolution of the Archean atmosphere (Sleep et al., 2004; Sleep et al., 2011; Lazar et al., 2012; Guillot and Hattori, 2013; McCollom and Seewald, 2013; Holm et al., 2015). Future studies quantifying the oxidation state of Fe could test serpentinization reactions through time and provide evidence of the H_2-production potential of the Archean ultramafic crust. Perhaps H_2-producing reactions were prevalent in the early Earth (Figure 6.6), owing to the availability of surficial ultramafic rocks (komatiites) and the lack of oxygen in its fluid envelopes (Holland, 2006). Studies combining reaction tests (e.g., this work) with geochronology of serpentinization (Cooperdock and Stockli, 2016) are thus a tantalizing prospect.
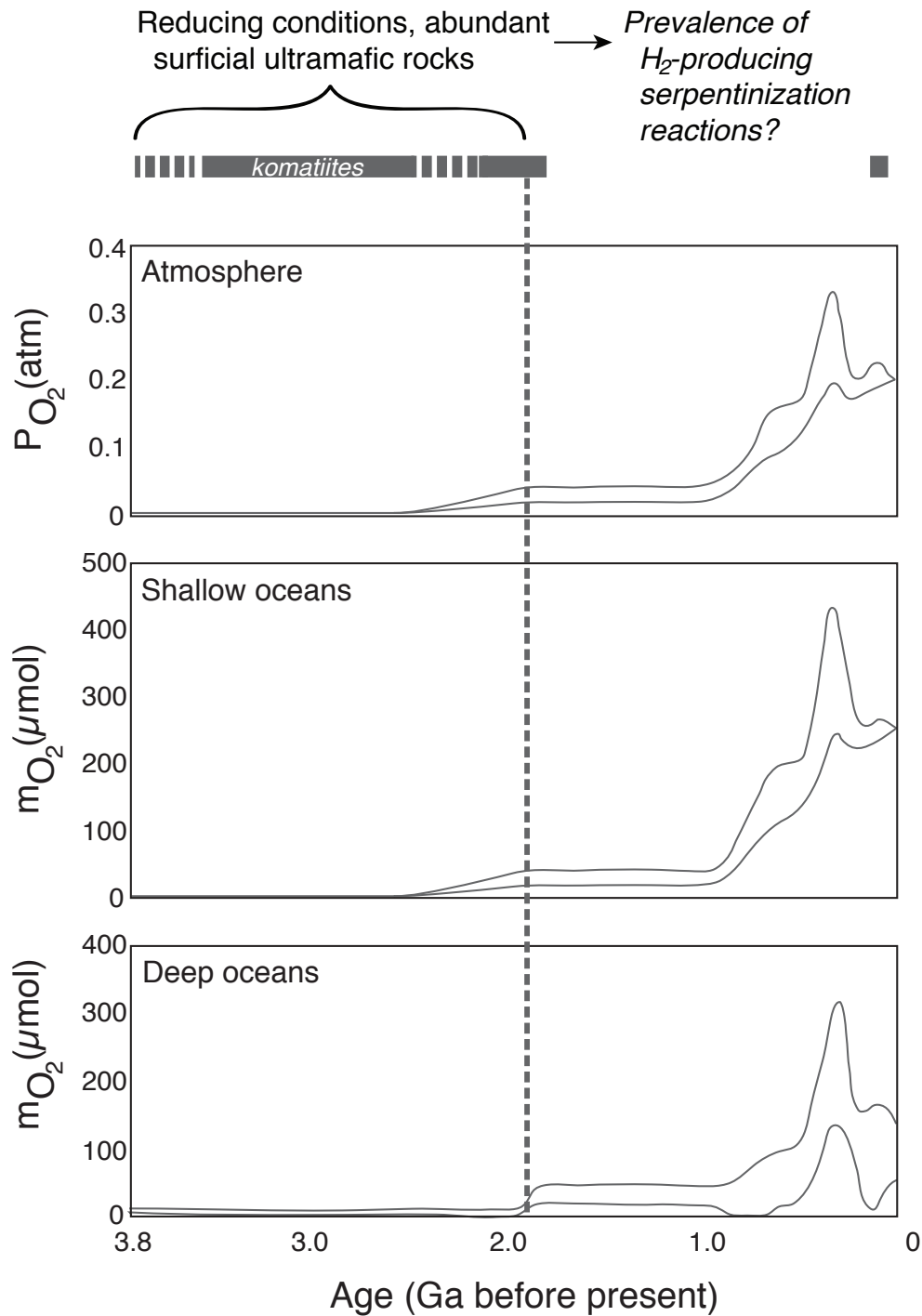
Figure 6.6. Comparison of the timing of komatiite emplacement to changes in oxygen content (as partial pressure, *P*, or molality, *m*) of Earth's fluid envelopes through time. Komatiites mainly extruded prior to ~2 Ga, at which time the oceans and atmosphere were anoxic. Abundant komatiite exposures at the surface under these reducing conditions may have fostered conditions ideal for H_2 gas production attending serpentinization. Komatiite age ranges after Arndt et al. (2008). Oxygen content models after Holland (2006).

References

Afanasyev, A.A., Melnik, O., Porritt, L., Schumacher, J.C., and Sparks, R.S.J., 2014, Hydrothermal alteration of kimberlite by convective flows of external water: Contributions to Mineralogy and Petrology, v. 168, no. 1, p. 1038, doi: 10.1007/s00410-014-1038-y.

Aitken, B.G., and Echeverría, L.M., 1984, Petrology and geochemistry of komatiites and tholeiites from Gorgona Island, Colombia: Contributions to Mineralogy and Petrology, v. 86, p. 94–105.

Allen, D.E., and Seyfried, W.E., Jr, 2004, Serpentinization and heat generation: constraints from Lost City and Rainbow hydrothermal systems: Geochimica et Cosmochimica Acta, v. 68, no. 6, p. 1347–1354, doi: 10.1016/j.gca.2003.09.003.

Arndt, N.T., 1986, Differentiation of komatiite flows: Journal of Petrology, v. 27, p. 279–301.

Arndt, N.T., 1976, Melting relations of ultramafic lavas (komatiites) at 1 atm and high pressure: Carnegie Institute of Washington Yearbook, v. 75, p. 555–562.

Arndt, N.T., 1982, Proterozoic spinifex-textured basalts of Gilmour Island, Hudson Bay: Geological Survey of Canada: Current Research, Paper 82-1A, 137–142 p.

Arndt, N.T., and Nesbitt, R.W., 1984, Magma mixing in komatiitic lavas from Munro Township, Ontario, *in* Springer Berlin Heidelberg, Berlin, Heidelberg, p. 99–114.

Arndt, N.T., Ginibre, C., Chauvel, C., Albarède, F., Cheadle, M., Herzberg, C., Jenner, G., and LaHaye, Y., 1998, Were komatiites wet?: Geology, v. 26, no. 8, p. 739, doi: 10.1130/0091-7613(1998)026<0739:WKW>2.3.CO;2.

Arndt, N.T., Lesher, C.M., and Barnes, S.J., 2008, Komatiite: Cambridge University Press.

Arndt, N.T., Naldrett, A.J., and Pyke, D.R., 1977, Komatiitic and iron-rich tholeiitic lavas of Munro Township, northeast Ontario: Journal of Petrology, v. 18, no. 2, p. 319–369, doi: 10.1093/petrology/18.2.319.

Barnes, S.J., 1985, The petrography and geochemistry of komatiite flows from the Abitibi Greenstone Belt and a model for their formation: Lithos, v. 18, p. 241–270, doi: 10.1016/0024-4937(85)90030-1.

Barnes, S.J., Gorton, M.P., and Naldrett, A.J., 1983, A comparative study of olivine and clinopyroxene spinifex flows from Alexo, Abitibi greenstone belt, Ontario, Canada: Contributions to Mineralogy and Petrology, v. 83, p. 293–308.

Barnes, S.J., Hill, R.E.T., and Gole, M.J., 1988, The Perseverance Ultramafic Complex, Western Australia: The product of a komatiite lava river: Journal of Petrology, v. 29, no. 2, p. 305–331, doi: 10.1093/petrology/29.2.305.

Barnes, S.J., Hill, R.E.T., Perring, C.S., and Dowling, S.E., 2004, Lithogeochemical exploration for komatiite-associated Ni-sulfide deposits: strategies and limitations: Mineralogy and Petrology, v. 82, no. 3-4, p. 259–293, doi: 10.1007/s00710-004-0051-7.

Barnes, S.J., Lesher, C.M., and Sproule, R.A., 2007, Geochemistry of komatiites in the Eastern Goldfields Superterrane, Western Australia and the Abitibi Greenstone Belt, Canada, and implications for the distribution of associated Ni–Cu–PGE deposits: Applied Earth Science, v. 116, no. 4, p. 167–187, doi: 10.1179/174327507X271996.

Berry, A.J., Danyushevsky, L.V., St C O'Neill, H., Newville, M., and Sutton, S.R., 2008, Oxidation state of iron in komatiitic melt inclusions indicates hot Archaean mantle: Nature, v. 455, no. 7215, p. 960–963, doi: 10.1038/nature07377.

Beswick, A.E., 1983, Primary fractionation and secondary alteration within an Archean ultramafic lava flow: Contributions to Mineralogy and Petrology, v. 82, p. 221–231.

Blichert-Toft, J., and Arndt, N.T., 1999, Hf isotope compositions of komatiites: Earth and Planetary Science Letters, v. 171, no. 3, p. 439–451, doi: 10.1016/S0012-821X(99)00151-X.

Bowen, N.L., and Tuttle, O.F., 1950, The system $NaAlSi_3O_8$-$KAlSi_3O_8$-H_2O: The Journal of Geology, v. 58, no. 5, p. 489–511, doi: 10.1086/625758.

Brooker, R.A., Sparks, R.S.J., Kavanagh, J.L., and Field, M., 2011, The volatile content of hypabyssal kimberlite magmas: Some constraints from experiments on natural rock compositions: Bulletin of Volcanology, v. 73, no. 8, p. 959–981, doi: 10.1007/s00445-011-0523-7.

Canil, D., 1987, The geochemistry of komatiites and basalts from the Deadman Hill area, Munro Township, Ontario, Canada: Canadian Journal of Earth Sciences, v. 24, p. 998–1008.

Canil, D., 1997, Vanadium partitioning and the oxidation state of Archaean komatiite magmas: Nature, v. 389, no. 6653, p. 842–845, doi: 10.1038/39860.

Carlson, R.W., Garnero, E., Harrison, T.M., Li, J., Manga, M., McDonough, W.F., Mukhopadhyay, S., Romanowicz, B., Rubie, D., Williams, Q., and Zhong, S., 2014, How did early Earth become our modern world?: Annual Review of Earth and Planetary Sciences, v. 42, no. 1, p. 151–178, doi: 10.1146/annurev-earth-060313-055016.

Carten, R.B., 1986, Sodium-calcium metasomatism; chemical, temporal, and spatial relationships at the Yerington, Nevada, porphyry copper deposit: Economic Geology, v. 81, no. 6, p. 1495–1519, doi: 10.2113/gsecongeo.81.6.1495.

Chayes, F., 1962, Numerical correlation and petrographic variation: The Journal of Geology, v. 70, p. 440–452.

Coleman, R.G., 1971, Plate tectonic emplacement of upper mantle peridotites along continental edges: Journal of Geophysical Research, v. 76, no. 5, p. 1212–1222, doi: 10.1126/science.154.3755.1405.

Coleman, R.G., and Keith, T.E., 1971, A chemical study of serpentinization – Burro Mountain, California: Journal of Petrology, v. 12, no. 2, p. 311–328, doi: 10.1093/petrology/12.2.311.

Condie, K.C., Aster, R.C., and van Hunen, J., 2016, A great thermal divergence in the mantle beginning 2.5 Ga: Geochemical constraints from greenstone basalts and komatiites: Geoscience Frontiers, v. 7, no. 4, p. 543–553.

Cooperdock, E.H.G., and Stockli, D.F., 2016, Unraveling alteration histories in serpentinites and associated ultramafic rocks with magnetite (U-Th)/He geochronology: Geology, v. 44, no. 11, p. 967–970, doi: 10.1130/G38587.1.

Dalton, J.A., and Presnall, D.C., 1998, The continuum of primary carbonatitic-kimberlitic melt compositions in equilibrium with lherzolite: Data from the system CaO-MgO-Al_2O_3-SiO_2-CO_2 at 6 GPa: Journal of Petrology, v. 39, no. 11-12, p. 1953–1964, doi: 10.1093/petroj/39.11-12.1953.

Dann, J., 2001, Vesicular komatiites, 3.5-Ga Komati Formation, Barberton Greenstone Belt, South Africa: inflation of submarine lavas and origin of spinifex zones: Bulletin of Volcanology, v. 63, no. 7, p. 462–481, doi: 10.1007/s004450100164.

Dann, J.C., 2000, The 3.5 Ga Komati Formation, Barberton Greenstone Belt, South Africa, Part I: New maps and magmatic architecture: South African Journal of Geology, v. 103, no. 1, p. 47–68, doi: 10.2113/103.1.47.

Deschamps, F., Godard, M., Guillot, S., and Hattori, K., 2013, Geochemistry of subduction zone serpentinites: A review: Lithos, v. 178, p. 96–127, doi: 10.1016/j.lithos.2013.05.019.

Dilles, J.H., and Einaudi, M.T., 1992, Wall-rock alteration and hydrothermal flow paths about the Ann-Mason porphyry copper deposit, Nevada; a 6-km vertical reconstruction: Canadian Society of Economic Geologists Conference: The Future of Petrology, v. 87, no. 8, p. 1963–2001.

Douville, E., Charlou, J.L., Oelkers, E.H., Bienvenu, P., Jove Colon, C.F., Donval, J.P., Fouquet, Y., Prieur, D., and Appriou, P., 2002, The Rainbow vent fluids (36°14′N, MAR): the influence of ultramafic rocks and phase separation on trace metal content in Mid-Atlantic Ridge hydrothermal fluids: Chemical Geology, v. 184, no. 1-2, p. 37–48, doi: 10.1016/S0009-2541(01)00351-5.

Duchač, K.C., and Hanor, J.S., 1987, Origin and timing of the metasomatic silicification of an early Archean komatiite sequence, Barberton Mountain Land, South Africa: Precambrian Research, v. 37, no. 2, p. 125–146, doi: 10.1016/0301-9268(87)90075-1.

Echeverría, L.M., 1980, Tertiary or Mesozoic komatiites from Gorgona Island, Colombia: Field relations and geochemistry: Contributions to Mineralogy and Petrology, v. 73, no. 3, p. 253–266, doi: 10.1007/BF00381444.

Eckart, C., and Young, G., 1936, The approximation of one matrix by another of lower rank: Psychometrika, v. 1, no. 3, p. 211–218, doi: 10.1007/BF02288367.

Ehlmann, B.L., Mustard, J.F., Murchie, S.L., Bibring, J.-P., Meunier, A., Fraeman, A.A., and Langevin, Y., 2011, Subsurface water and clay mineral formation during the early history of Mars: Nature, v. 479, no. 7371, p. 53–60, doi: 10.1038/nature10582.

Einaudi, M.T., and Burt, D.M., 1982, Introduction; terminology, classification, and composition of skarn deposits: Economic Geology, v. 77, no. 4.

Ernst, R.E., Fowler, A.D., and Pearce, T.H., 1988, Modelling of igneous fractionation and other processes using Pearce diagrams: Contributions to Mineralogy and Petrology, v. 100, no. 1, p. 12–18, doi: 10.1007/BF00399436.

Escartín, J., Hirth, G., and Evans, B., 2001, Strength of slightly serpentinized peridotites: Implications for the tectonics of oceanic lithosphere: Geology, v. 29, no. 11, p. 1023, doi: 10.1130/0091-7613(2001)029<1023:SOSSPI>2.0.CO;2.

Evans, B.W., Hattori, K., and Baronnet, A., 2013, Serpentinite: What, why, where?: Elements, v. 9, no. 2, p. 99–106, doi: 10.2113/gselements.9.2.99.

Fiorentini, M.L., Barnes, S.J., Lesher, C.M., Heggie, G.J., Keays, R.R., and Burnham, O.M., 2010, Platinum group element geochemistry of mineralized and nonmineralized komatiites and basalts: Economic Geology, v. 105, no. 4, p. 795–823, doi: 10.2113/gsecongeo.105.4.795.

Fisher, G.W., 1993, An improved method for algebraic analysis of metamorphic mineral assemblages: American Mineralogist, v. 78, p. 1257–1261.

Fisher, G.W., 1989, Matrix analysis of metamorphic mineral assemblages and reactions: Contributions to Mineralogy and Petrology, v. 1989, p. 69–77.

Frost, B.R., Evans, K.A., Swapp, S.M., Beard, J.S., and Mothersole, F.E., 2013, The process of serpentinization in dunite from New Caledonia: Lithos, v. 178, p. 24–39, doi: 10.1016/j.lithos.2013.02.002.

Gordon, T.M., 2000, Vector subspace analysis applied to inverse geochemical mass transfer problems: a generalization of the element-ratio method: Canadian Society of Economic Geologists Conference: The Future of Petrology.

Gordon, T.M., and Russell, J.K., 2006, Wide open spaces: The linear algebra of geochemical mass transfer problems: Geological Association of Canada - Mineralogical Association of Canada Annual Meeting: Abstracts, v. 31, p. 58.

Grant, J.A., 2005, Isocon analysis: a brief review of the method and applications: Physics and Chemistry of the Earth, v. 30, p. 997–1004.

Grant, J.A., 1986, The isocon diagram; a simple solution to Gresens' equation for metasomatic alteration: Economic Geology, v. 81, no. 8, p. 1976–1982, doi: 10.2113/gsecongeo.81.8.1976.

Green, D.H., 1975, Genesis of Archean peridotitic magmas and constraints on Archean geothermal gradients and tectonics: Geology, v. 3, no. 1, p. 15, doi: 10.1130/0091-7613(1975)3<15:GOAPMA>2.0.CO;2.

Green, D.H., Nicholls, I.A., Viljoen, M., and Viljoen, R., 1975, Experimental demonstration of the existence of peridotitic liquids in earliest Archean magmatism: Geology, v. 3, p. 11–14.

Greenwood, H.J., 1967, The N-dimensional tie-line problem: Geochimica et Cosmochimica Acta, v. 31, p. 465–490.

Gresens, R.L., 1967, Composition-volume relationships of metasomatism: Chemical Geology, v. 2, p. 47–65.

Groat, L.A., Giuliani, G., Marshall, D.D., and Turner, D., 2008, Emerald deposits and occurrences: A review: Ore Geology Reviews, v. 34, p. 87–112.

Grove, T.L., and Parman, S.W., 2004, Thermal evolution of the Earth as recorded by komatiites: Earth and Planetary Science Letters, v. 219, no. 3-4, p. 173–187, doi: 10.1016/S0012-821X(04)00002-0.

Gruau, G., Chauvel, C., Arndt, N.T., and Cornichet, J., 1990, Aluminum depletion in komatiites and garnet fractionation in the early Archean mantle: Hafnium isotopic constraints: Geochimica et Cosmochimica Acta, v. 54, no. 11, p. 3095–3101, doi: 10.1016/0016-7037(90)90125-5.

Gudfinnsson, G.H., and Presnall, D.C., 2005, Continuous gradations among primary carbonatitic, kimberlitic, melilititic, basaltic, picritic, and komatiitic melts in equilibrium with garnet lherzolite at 3-8 GPa: Journal of Petrology, v. 46, no. 8, p. 1645–1659, doi: 10.1093/petrology/egi029.

Guillot, S., and Hattori, K., 2013, Serpentinites: Essential roles in geodynamics, arc volcanism, sustainable development, and the origin of life: Elements, v. 9, no. 2, p. 95–98, doi: 10.2113/gselements.9.2.95.

Guo, S., Ye, K., Chen, Y., and Liu, J.B., 2009, A normalization solution to mass transfer illustration of multiple progressively altered samples using the isocon diagram: Economic Geology, v. 104, no. 6, p. 881–886, doi: 10.2113/gsecongeo.104.6.881.

Gustafson, L.B., and Hunt, J.P., 1975, The porphyry copper deposit at El Salvador, Chile: Economic Geology, v. 70, p. 857–912.

Hanor, J.S., and Duchač, K.C., 1990, Isovolumetric silicification of early Archean komatiites: geochemical mass balances and constraints on origin: The Journal of Geology, v. 98, no. 6, p. 863–877.

Hansen, L.D., Dipple, G.M., Gordon, T.M., and Kellett, D.A., 2005, Carbonated serpentinite (listwanite) at Atlin, British Columbia: A geological analogue to carbon dioxide sequestration: The Canadian Mineralogist, v. 43, no. 1, p. 225–239, doi: 10.2113/gscanmin.43.1.225.

Harker, A., 1909, The natural history of igneous rocks: London 344p.

Hattori, K.H., and Guillot, S., 2007, Geochemical character of serpentinites associated with high-to ultrahigh-pressure metamorphic rocks in the Alps, Cuba, and the Himalayas: Recycling of elements in subduction zones: Geochemistry, Geophysics, Geosystems, v. 8, no. 9.

Hattori, K.H., and Guillot, S., 2003, Volcanic fronts form as a consequence of serpentinite dehydration in the forearc mantle wedge: Geology, v. 31, no. 6, p. 525, doi: 10.1130/0091-7613(2003)031<0525:VFFAAC>2.0.CO;2.

Heald, P., Foley, N.K., and Hayba, D.O., 1987, Comparative anatomy of volcanic-hosted epithermal deposits; acid-sulfate and adularia-sericite types: Economic Geology, v. 82, no. 1, p. 1–26.

Hemley, J.J., and Jones, W.R., 1964, Chemical aspects of hydrothermal alteration with emphasis on hydrogen metasomatism: Economic Geology, v. 59, no. 4, p. 538–569.

Herzberg, C., 1992, Depth and degree of melting of komatiites: Journal of Geophysical Research: Solid Earth, v. 97, no. B4, p. 4521–4540, doi: 10.1029/91JB03066.

Herzberg, C., 2004, Geodynamic information in peridotite petrology: Journal of Petrology, v. 45, no. 12, p. 2507–2530, doi: 10.1093/petrology/egh039.

Herzberg, C., and O'Hara, M.J., 1998, Phase equilibrium constraints on the origin of basalts, picrites, and komatiites: Earth-Science Reviews, v. 44, no. 1-2, p. 39–79, doi: 10.1016/S0012-8252(98)00021-X.

Herzberg, C., and Zhang, J., 1996, Melting experiments on anhydrous peridotite KLB-1: Compositions of magmas in the upper mantle and transition zone: Journal of Geophysical Research: Solid Earth, v. 101, no. B4, p. 8271–8295, doi: 10.1029/96JB00170.

Hill, R.E.T., 2001, Komatiite volcanology, volcanological setting and primary geochemical properties of komatiite-associated nickel deposits: Geochemistry: Exploration, Environment, Analysis, v. 1, p. 365–381.

Hirth, G., and Guillot, S., 2013, Rheology and tectonic significance of serpentinite: Elements, v. 9, p. 107–113.

Holland, H.D., 2006, The oxygenation of the atmosphere and oceans: Philosophical Transactions of the Royal Society B: Biological Sciences, v. 361, no. 1470, p. 903–915, doi: 10.1098/rstb.2006.1838.

Holm, N.G., Oze, C., Mousis, O., Waite, J.H., and Guilbert-Lepoutre, A., 2015, Serpentinization and the formation of H_2 and CH_4 on celestial bodies (planets, moons, comets): Astrobiology, v. 15, no. 7, p. 587–600, doi: 10.1089/ast.2014.1188.

Hostetler, P.B., Coleman, R.G., and Evans, B.W., 1966, Brucite in alpine serpentinites: America Mineralogist, v. 51, p. 75–98.

Houlé, M.G., Lesher, C.M., and Davis, P.C., 2012, Thermomechanical erosion at the Alexo Mine, Abitibi greenstone belt, Ontario: implications for the genesis of komatiite-associated Ni–Cu–(PGE) mineralization: Mineralium Deposita, v. 47, no. 1-2, p. 105–128, doi: 10.1007/s00445-003-0301-2.

Houlé, M.G., Préfontaine, S., Fowler, A.D., and Gibson, H.L., 2009, Endogenous growth in channelized komatiite lava flows: evidence from spinifex-textured sills at Pyke Hill and Serpentine Mountain, Western Abitibi Greenstone Belt, Northeastern Ontario, Canada: Bulletin of Volcanology, v. 71, p. 881–901.

Huppert, H.E., and Sparks, R., 1985, Komatiites I: Eruption and flow: v. 26, p. 694–725.

Huppert, H.E., Sparks, R., Turner, J.S., and Arndt, N.T., 1984, Emplacement and cooling of komatiite lavas: Nature, v. 309, no. 3, p. 19–22.

Hynes, A., 1980, Carbonatization and mobility of Ti, Y, and Zr in Ascot Formation metabasalts, SE Quebec: Contributions to Mineralogy and Petrology, v. 75, no. 1, p. 79–87, doi: 10.1007/BF00371891.

Jolly, W.T., 1982, Progressive metamorphism of komatiites and related Archaean lavas of the Abitibi area, Canada, *in* Arndt, N.T. and Nisbet, E.G. eds., Komatiites, London: George Allen and Unwin.

Kamenetsky, V.S., Gurenko, A.A., and Kerr, A.C., 2010, Composition and temperature of komatiite melts from Gorgona Island, Colombia, constrained from olivine-hosted melt inclusions: Geology, v. 38, no. 11, p. 1003–1006, doi: 10.1130/G31143.1.

Kerrick, D.M., 1977, The genesis of zoned skarns in the Sierra Nevada, California: Journal of Petrology, v. 18, no. 1, p. 144–181, doi: 10.1093/petrology/18.1.144.

Kilinc, A., Carmichael, I., and Rivers, M.L., 1983, The ferric-ferrous ratio of natural silicate liquids equilibrated in air: Contributions to Mineralogy and Petrology, v. 83, p. 136–140.

Komor, S.C., Elthon, D., and Casey, J.F., 1985, Serpentinization of cumulate ultramafic rocks from the North Arm Mountain massif of the Bay of Islands ophiolite: Geochimica et Cosmochimica Acta, v. 49, p. 2331–2338.

Kress, V.C., and Carmichael, I., 1991, The compressibility of silicate liquids containing Fe_2O_3 and the effect of composition, temperature, oxygen fugacity and pressure on their redox states: Contributions to Mineralogy and Petrology, v. 108, p. 82–92.

Kyser, T.K., O'Hanley, D.S., and Wicks, F.J., 1999, The origin of fluids associated with serpentinization processes: evidence from stable-isotope compositions: The Canadian Mineralogist, v. 37, p. 223–237.

LaHaye, Y., and Arndt, N.T., 1996, Alteration of a komatiite flow from Alexo, Ontario, Canada: Journal of Petrology, v. 37, no. 6, p. 1261–1284, doi: 10.1093/petrology/37.6.1261.

LaHaye, Y., Arndt, N.T., Byerly, G., Chauvel, C., Fourcade, S., and Gruau, G., 1995, The influence of alteration on the trace-element and Nd isotopic compositions of komatiites: Chemical Geology, v. 126, no. 1, p. 43–64, doi: 10.1016/0009-2541(95)00102-1.

LaHaye, Y., Barnes, S.J., Frick, L.R., and Lambert, D.D., 2001, Re-Os isotopic study of komatiitic volcanism and magmatic sulfide formation in the southern Abitibi greenstone belt, Ontario, Canada: The Canadian Mineralogist, v. 39, no. 2, p. 473–490, doi: 10.2113/gscanmin.39.2.473.

Lazar, C., McCollom, T.M., and Manning, C.E., 2012, Abiogenic methanogenesis during experimental komatiite serpentinization: implications for the evolution of the early Precambrian atmosphere: Chemical Geology, v. 326-327, p. 102–112.

Le Vaillant, M., Fiorentini, M.L., and Barnes, S.J., 2016, Review of lithogeochemical exploration tools for komatiite-hosted Ni-Cu-(PGE) deposits: Journal of Geochemical Exploration, v. 168, p. 1–19.

Lesher, C.M., 1989, Komatiite-associated nickel sulfide deposits, *in* Whitney, J.A. and Naldrett, A. eds., Reviews in Economic Geology, Society of Economic Geology, p. 45–101.

Lesher, C.M., and Arndt, N.T., 1995, REE and Nd isotope geochemistry, petrogenesis and volcanic evolution of contaminated komatiites at Kambalda, Western Australia: Lithos, v. 34, p. 127–157.

Lesher, C.M., Arndt, N.T., and Groves, D.I., 1984, Genesis of komatiite-associated nickel sulphide deposits at Kambalda, Western Australia: A distal volcanic model *in* Sulphide deposits in mafic and ultramafic rocks (D. L. Buchanan & M. J. Jones, Eds.): London: Institution for Mining and Metallurgy.

Lowe, D.R., and Byerly, G.R., 1986, Archaean flow-top alteration zones formed initially in a low-temperature sulphate-rich environment: Nature, v. 324, p. 245–248.

Matzen, A.K., Baker, M.B., Beckett, J.R., and Stolper, E.M., 2011, Fe-Mg partitioning between olivine and high-magnesian melts and the nature of Hawaiian parental

liquids: Journal of Petrology, v. 52, no. 7-8, p. 1243–1263, doi: 10.1093/petrology/egq089.

McCollom, T.M., and Seewald, J.S., 2013, Serpentinites, hydrogen, and life: Elements, v. 9, no. 2, p. 129–134, doi: 10.2113/gselements.9.2.129.

Meinert, L.D., 1992, Skarns and skarn deposits: Geoscience Canada, v. 19, no. 4, p. 145–161.

Mitchell, R.H., 1986, Kimberlites: Geochemistry, mineralogy, and petrology: Springer.

Moody, J.B., 1976, Serpentinization: a review: Lithos, v. 9, no. 2, p. 125–138, doi: 10.1016/0024-4937(76)90030-X.

Nicholls, J., 1988, The statistics of Pearce element diagrams and the Chayes closure problem: Contributions to Mineralogy and Petrology, v. 99, no. 1, p. 11–24, doi: 10.1007/BF00399361.

Nicholls, J., and Gordon, T.M., 1994, Procedures for the calculation of axial ratios on Pearce element-ratio diagrams: The Canadian Mineralogist, v. 32, p. 969–977.

Nielsen, C.H., and Sigurdsson, H., 1981, Quantitative methods for electron microprobe analysis of sodium in natural and synthetic glasses: American Mineralogist, v. 66, p. 547–552.

Nisbet, E.G., Arndt, N.T., Bickle, M.J., Cameron, W.E., Chauvel, C., Cheadle, M., Hegner, E., Kyser, T.K., Martin, A., Renner, R., and Roedder, E., 1987, Uniquely fresh 2.7 Ga komatiites from the Belingwe greenstone belt, Zimbabwe: Geology, v. 15, no. 12, p. 1147, doi: 10.1130/0091-7613(1987)15<1147:UFGKFT>2.0.CO;2.

Nisbet, E.G., Cheadle, M.J., Arndt, N.T., and Bickle, M.J., 1993, Constraining the potential temperature of the Archaean mantle: A review of the evidence from komatiites: Lithos, v. 30, no. 3-4, p. 291–307, doi: 10.1016/0024-4937(93)90042-B.

Nixon, P.H., 1987, Mantle xenoliths: John Wiley & Sons Ltd.

Nna-Mvondo, D., and Martinez-Frias, J., 2007, Review komatiites: from Earth's geological settings to planetary and astrobiological contexts: Earth, Moon, and Planets, v. 100, no. 3-4, p. 157–179, doi: 10.1007/s11038-007-9135-9.

O'Hanley, D.S., 1996, Serpentinites: Records of tectonic and petrological history: Oxford University Press.

O'Hanley, D.S., 1992, Solution to the volume problem in serpentinization: Geology, v. 20, no. 8, p. 705, doi: 10.1130/0091-7613(1992)020<0705:STTVPI>2.3.CO;2.

Parman, S.W., 2004, A subduction origin for komatiites and cratonic lithospheric mantle: South African Journal of Geology, v. 107, no. 1-2, p. 107–118, doi: 10.2113/107.1-

2.107.

Parman, S.W., and Grove, T.L., 2004, Harzburgite melting with and without H_2O: Experimental data and predictive modeling: Journal of Geophysical Research: Solid Earth, v. 109, no. B2, doi: 10.1029/2003JB002566.

Parman, S.W., Dann, J.C., Grove, T.L., and De Wit, M.J., 1997, Emplacement conditions of komatiite magmas from the 3.49 Ga Komati Formation, Barberton greenstone belt, South Africa: Earth and Planetary Science Letters, v. 150, p. 303–323.

Peacock, S.M., 1987, Serpentinization and infiltration metasomatism in the Trinity peridotite, Klamath province, northern California: implications for subduction zones: Contributions to Mineralogy and Petrology, v. 95, no. 1, p. 55–70, doi: 10.1007/BF00518030.

Pearce, T.H., 1968, A contribution to the theory of variation diagrams: Contributions to Mineralogy and Petrology, v. 19, no. 2, p. 142–157, doi: 10.1007/BF00635485.

Pearce, T.H., 1987, The identification and assessment of spurious trends in Pearce-type ratio variation diagrams: a discussion of some statistical arguments: Contributions to Mineralogy and Petrology, v. 97, no. 4, p. 529–534, doi: 10.1007/BF00375331.

Polito, P.A., Kyser, T.K., and Stanley, C., 2007, The Proterozoic, albitite-hosted, Valhalla uranium deposit, Queensland, Australia: a description of the alteration assemblage associated with uranium mineralisation in diamond drill hole V39: Mineralium Deposita, v. 44, no. 1, p. 11–40, doi: 10.2343/geochemj.33.109.

Prendergast, M.D., 2003, The nickelifeous Late Archean Reliance komatiitic event in the Zimbabwe Craton -- Magmatic architecture, physical volcanology, and ore genesis : Economic Geology, v. 98, no. 5, p. 865–891.

Putirka, K.D., 2005, Mantle potential temperatures at Hawaii, Iceland, and the mid-ocean ridge system, as inferred from olivine phenocrysts: Evidence for thermally driven mantle plumes: Geochemistry, Geophysics, Geosystems, v. 6, no. 5, p. n/a–n/a, doi: 10.1146/annurev.ea.14.050186.002425.

Putnis, A., and Austrheim, H., 2010, Fluid-induced processes: metasomatism and metamorphism: Geofluids, v. 10, no. 1-2, p. 254–269, doi: 10.1111/j.1468-8123.2010.00285.x.

Pyke, D.R., Naldrett, A.J., and Eckstrand, O.R., 1973, Archean ultramafic flows in Munro Township, Ontario: Geological Society of America Bulletin, v. 84, no. 3, p. 955, doi: 10.1130/0016-7606(1973)84<955:AUFIMT>2.0.CO;2.

Rakotondrazafy, A., Giuliani, G., and Ohnenstetter, D., 2008, Gem corundum deposits of Madagascar: A review: Ore Geology Reviews, v. 34, p. 134–154.

Renner, R., Nisbet, E.G., Cheadle, M.J., Arndt, N.T., Bickle, M.J., and Cameron, W.E.,

1994, Komatiite flows from the Reliance Formation, Belingwe Belt, Zimbabwe: I. Petrography and Mineralogy: Journal of Petrology, v. 35, no. 2, p. 361–400, doi: 10.1093/petrology/35.2.361.

Roeder, P.L., and Emslie, R.F., 1970, Olivine-liquid equilibrium: Contributions to Mineralogy and Petrology, v. 29, no. 4, p. 275–289, doi: 10.1007/BF00371276.

Roeder, P.L., and Reynolds, I., 1991, Crystallization of Chromite and Chromium Solubility in Basaltic Melts: Journal of Petrology, v. 32, no. 5, p. 909–934, doi: 10.1093/petrology/32.5.909.

Rollinson, H., 1999, Petrology and geochemistry of metamorphosed komatiites and basalts from the Sula Mountains greenstone belt, Sierra Leone: Contributions to Mineralogy and Petrology, v. 134, p. 86–101.

Rollinson, H.R., and Roberts, C.R., 1987, Ratio correlations and major element mobility in altered basalts and komatiites - reply to K.J. Vines: Contributions to Mineralogy and Petrology, v. 97, no. 4, p. 527–528, doi: 10.1007/BF00375330.

Russell, J.K., and Nicholls, J., 1988, Analysis of petrologic hypotheses with Pearce element ratios: Contributions to Mineralogy and Petrology, v. 99, no. 1, p. 25–35, doi: 10.1007/BF00399362.

Russell, J.K., and Snyder, L.D., 1997, Petrology of picritic basalts from Kamloops, British Columbia: Primary liquids from a Triassic-Jurassic arc: The Canadian Mineralogist, v. 35, p. 521–541.

Russell, J.K., and Stanley, C.R., 1990a, A theoretical basis for the development and use of chemical variation diagrams: Geochimica et Cosmochimica Acta, v. 54, p. 2419–2431.

Russell, J.K., and Stanley, C.R., 1990b, Origins of the 1954–1960 Lavas, Kilauea Volcano, Hawaii: Major element constraints on shallow reservoir magmatic processes: Journal of Geophysical Research: Solid Earth, v. 95, no. B4, p. 5021–5047, doi: 10.1029/JB095iB04p05021.

Russell, J.K., Dipple, G.M., Lang, J.R., and Lueck, B., 1999, Major-element discrimination of titanium andradite from magmatic and hydrothermal environments: An example from the Canadian Cordillera: European Journal of Mineralogy, v. 11, p. 919–935.

Russell, J.K., Nicholls, J., Stanley, C.R., and Pearce, T.H., 1990, Pearce element ratios: A paradigm for testing hypotheses: Eos, v. 71, p. 234–6– 246–7.

Sack, R.O., Carmichael, I.S.E., Rivers, M., and Ghiorso, M.S., 1981, Ferric-ferrous equilibria in natural silicate liquids at 1 bar: Contributions to Mineralogy and Petrology, v. 75, no. 4, p. 369–376, doi: 10.1007/BF00374720.

Scarfe, C.M., and Takahashi, E., 1986, Melting of garnet peridotite to 13 GPa and the early history of the upper mantle: Nature, v. 322, no. 6077, p. 354–356, doi: 10.1038/322354a0.

Schwartz, G.M., 1939, Hydrothermal alteration of igneous rocks: Geological Society of America Bulletin, v. 50, no. 2, p. 181–238, doi: 10.1130/GSAB-50-181.

Schwarzenbach, E.M., Caddick, M.J., Beard, J.S., and Bodnar, R.J., 2015, Serpentinization, element transfer, and the progressive development of zoning in veins: evidence from a partially serpentinized harzburgite: Contributions to Mineralogy and Petrology, v. 171, no. 1, p. 5, doi: 10.1007/s00410-015-1219-3.

Shervais, J.W., Kolesar, P., and Andreasen, K., 2005, A field and chemical study of serpentinization—Stonyford, California: Chemical flux and mass balance: International Geology Review, v. 47, no. 1, p. 1–23, doi: 10.2747/0020-6814.47.1.1.

Shimizu, K., Komiya, T., Hirose, K., Shimizu, N., and Maruyama, S., 2001, Cr-spinel, an excellent micro-container for retaining primitive melts – implications for a hydrous plume origin for komatiites: Earth and Planetary Science Letters, v. 189, no. 3-4, p. 177–188, doi: 10.1016/S0012-821X(01)00359-4.

Shimizu, K., Nakamura, E., and Maruyama, S., 2005, The geochemistry of ultramafic to mafic volcanics from the Belingwe greenstone belt, Zimbabwe: Magmatism in an Archean continental large igneous province: Journal of Petrology, v. 46, no. 11, p. 2367–2394.

Shirey, S.B., Cartigny, P., Frost, D.J., and Keshav, S., 2013, Diamonds and the geology of mantle carbon, *in* Reviews in Mineralogy and Geochemistry, Mineralogical Society of America, v. 75, p. v. 75: 355–421.

Shore, M., 1997, Cooling and crystallization of komatiite flows: PhD thesis, University of Ottawa.

Sillitoe, R.H., 2010, Porphyry Copper Systems: Economic Geology, v. 105, no. 1, p. 3–41, doi: 10.2113/gsecongeo.105.1.3.

Silva, K.E., Cheadle, M.J., and Nisbet, E.G., 1997, The origin of B1 zones in komatiite flows: Journal of Petrology, v. 38, no. 11, p. 1565–1584, doi: 10.1093/petroj/38.11.1565.

Sleep, N.H., Bird, D.K., and Pope, E.C., 2011, Serpentinite and the dawn of life: Philosophical Transactions of the Royal Society B: Biological Sciences, v. 366, no. 1580, p. 2857–2869, doi: 10.1098/rstb.2011.0129.

Sleep, N.H., Meibom, A., Fridriksson, T., Coleman, R.G., and Bird, D.K., 2004, H_2-rich fluids from serpentinization: Geochemical and biotic implications: Proceedings of the National Academy of Sciences, v. 101, no. 35, p. 12818–12823, doi: 10.1073/pnas.0405289101.

Smith, H.S., Erlank, A.J., and Duncan, A.R., 1980, Geochemistry of some ultramafic komatiite lava flows from the Barberton Mountain Land, South Africa: Precambrian Research, v. 11, p. 399–415.

Snyder, L., 1994, Petrological studies within the Iron Mask Batholith, south central British Columbia: MSc thesis, University of British Columbia.

Sobolev, A.V., Asafov, E.V., Gurenko, A.A., Arndt, N.T., Batanova, V.G., Portnyagin, M.V., Garbe-Schönberg, D., and Krasheninnikov, S.P., 2016, Komatiites reveal a hydrous Archaean deep-mantle reservoir: Nature, v. 531, no. 7596, p. 628–632, doi: 10.1038/nature17152.

Sossi, P.A., and O'Neill, H.S.C., 2016, Liquidus temperatures of komatiites and the effect of cooling rate on element partitioning between olivine and komatiitic melt: Contributions to Mineralogy and Petrology, v. 171, no. 5, p. 49, doi: 10.1007/s00410-016-1260-x.

Sossi, P.A., Eggins, S.M., Nesbitt, R.W., Nebel, O., Hergt, J.M., Campbell, I.H., O'Neill, H.S.C., Van Kranendonk, M., and Davies, D.R., 2016, Petrogenesis and geochemistry of Archean komatiites: Journal of Petrology, v. 57, no. 1, p. 147–184.

Sparks, R.S.J., Brooker, R.A., Field, M., Kavanagh, J., Schumacher, J.C., Walter, M.J., and White, J., 2009, The nature of erupting kimberlite melts: Lithos, v. 112, p. 429–438, doi: 10.1016/j.lithos.2009.05.032.

Stanley, C.R., 1993, Effects of non-conserved denominators on Pearce element ratio diagrams: Mathematical Geology, v. 25, no. 8, p. 1049–1070, doi: 10.1007/BF00911549.

Strang, G., 2009, Introduction to Linear Algebra: Wellesley-Cambridge Press, Wellesley.

Stripp, G.R., Field, M., Schumacher, J.C., Sparks, R.S.J., and Cressey, G., 2006, Post-emplacement serpentinization and related hydrothermal metamorphism in a kimberlite from Venetia, South Africa: Journal of Metamorphic Geology, v. 24, no. 6, p. 515–534, doi: 10.1111/j.1525-1314.2006.00652.x.

Sun, S.-S., 1987, Chemical composition of Archaean komatiites: Implications for early history of the earth and mantle evolution: Journal of Volcanology and Geothermal Research, v. 32, no. 1-3, p. 67–82, doi: 10.1016/0377-0273(87)90037-0.

Takahashi, E., 1986, Melting of a dry peridotite KLB-1 up to 14 GPa: Implications on the Origin of peridotitic upper mantle: Journal of Geophysical Research: Solid Earth, v. 91, no. B9, p. 9367–9382, doi: 10.1029/JB091iB09p09367.

Takahashi, E., and Scarfe, C.M., 1985, Melting of peridotite to 14 GPa and the genesis of komatiite: Nature, v. 315, no. 6020, p. 566–568, doi: 10.1038/315566a0.

Taylor, B.E., and O'Neil, J.R., 1977, Stable isotope studies of metasomatic Ca-Fe-Al-Si

skarns and associated metamorphic and igneous rocks, Osgood Mountains, Nevada: Contributions to Mineralogy and Petrology, v. 63, no. 1, p. 1–49, doi: 10.1093/petrology/10.2.307.

Thayer, T.P., 1966, Serpentinization considered as a constant-volume process: American Mineralogist, v. 51, p. 685–710.

Thompson, J.B., 1982a, Composition space: An algebraic and geometric approach, *in* Reviews in Mineralogy and Geochemistry, Mineralogical Society of America, v. 10, p. 1–32.

Thompson, J.B., 1982b, Reaction space: An algebraic and geometric approach, *in* Reviews in Mineralogy and Geochemistry, Mineralogical Society of America, v. 10, p. v. 10: 33–52.

Tourpin, S., Gruau, G., Blais, S., and Fourcade, S., 1991, Resetting of REE, and Nd and Sr isotopes during carbonitization of a komatiite flow from Finland: Chemical Geology, v. 90, p. 15–29.

Turner, F.J., and Verhoogen, J., 1960, Igneous and metamorphic petrology: McGraw-Hill Companies.

Urqueta, E., Kyser, T.K., Clark, A.H., Stanley, C.R., and Oates, C.J., 2009, Lithogeochemistry of the Collahuasi porphyry Cu-Mo and epithermal Cu-Ag (-Au) cluster, northern Chile: Pearce element ratio vectors to ore: Geochemistry: Exploration, Environment, Analysis, v. 9, no. 1, p. 9–17, doi: 10.1144/1467-7873/07-169.

Velbel, M.A., 2014, Stoichiometric reactions describing serpentinization of anhydrous primary silicates: A critical appraisal, with application to aqueous alteration of chondrule silicates in CM carbonaceous chondrites: Clays and Clay Minerals, v. 62, no. 2, p. 126–136.

Viljoen, M.J., and Viljoen, R.P., 1969a, Evidence for the existence of a mobile extrusive peridotitic magma from the Komati Formation of the Onverwacht Group: Geological Society of South Africa, v. 21, p. 87–112.

Viljoen, M.J., and Viljoen, R.P., 1969b, The geology and geochemistry of the lower ultramafic unit of the Onverwacht Group and a proposed new class of igneous rocks: Geological Society of South Africa, v. 21, no. 55-85.

Walter, M.J., 1998, Melting of garnet peridotite and the origin of komatiite and depleted lithosphere: Journal of Petrology, v. 39, no. 1, p. 29–60, doi: 10.1093/petroj/39.1.29.

Wicks, F.J., and Whittaker, E., 1977, Serpentine textures and serpentinization: The Canadian Mineralogist, v. 15, p. 459–488.

Zhang, J., and Herzberg, C., 1994, Melting experiments on anhydrous peridotite KLB-1

from 5.0 to 22.5 GPa: Journal of Geophysical Research, v. 99, no. B9, p. 17729–17742.

Zhu, Y., An, F., and Tan, J., 2011, Geochemistry of hydrothermal gold deposits: a review: Geoscience Frontiers, v. 2, no. 3, p. 367–374.

Appendix

A1. Supplementary figure

The last page of this appendix shows Figure A1, the isocon plots (and related modifications) omitted from the main text for synthetic suites B-D.

A2. Algorithms

This section contains algorithms that indicate the necessary steps to execute the methods of Chapter 3. The aim is to provide a guide to implementing the theory. However, statistical considerations important to decision making in steps 6-10 in the *Testing hypotheses* algorithm are omitted, as are error propagation techniques that aid in determining the significance of angles of separation.

The algorithms assume that your bulk compositional dataset has more samples (n) than measured components (e.g., oxides; m).

A2.1. Testing hypotheses

1. Ensure dataset is an appropriate selection of samples/compositions to test geological hypotheses of interest.

2. Ensure data are converted to molar proportions, not weight percent.

3. Place all rock compositions in a single geochemical matrix (**GCM**), with m rows of components and n columns of samples.

4. Design hypotheses to test and place them in a hypothesis matrix (**H**). Hypotheses should be in molar proportions. Hypotheses must be $m \times 1$ vectors of the same m components as the rock compositions. That is, if rock compositions contain components c_1 to c_m as oxides or elements, so too must hypotheses. Include zeros as appropriate.

5. Compute the singular value decomposition (SVD) of the data matrix, giving matrices **U**, **S**, and **V**.

6. Replace the lowest value in the S matrix from the SVD with zero.

7. Reconstruct the data matrix by USV^T using the modified S matrix from step 6.

8. Observe the reconstructed data matrix (**GCM$_{rec}$**) from step 7 and decide whether it is

significantly different from original matrix. *The approach to this decision will ultimately determine the rank of the rock composition space and its defining axes. Carefully devise your method of determining what is a significant difference.*

9. If the reconstruction GCM_{rec} reproduces the original GCM to within acceptable statistical limits return to step 6. Otherwise proceed to step 10.

10. (At this step you should have produced a reconstructed data matrix that is significantly different from the data.) Determine the rank of the dataset. The rank (r) is the number of m components minus the number of acceptable rank reduction steps (i.e., number of times you did step 6).

11. Identify the rock composition space ($\mathbf{u_r}$); it is the first r columns of the U matrix from the SVD.

12. Project the hypotheses (i.e., the hypothesis matrix H) onto the rock composition space $\mathbf{u}$, giving $\mathbf{H_{proj}}$.

13. Recalculate the hypotheses from $\mathbf{H_{proj}}$ using their $\mathbf{u_r}$ coordinates, giving $\mathbf{H_{rec}}$.

14. Determine the angles separating hypotheses ($\mathbf{H}$) from their reconstructions ($\mathbf{H_{rec}}$).

15. Compare angles to the maximum angle your statistical treatment of rank reduction and uncertainties permits to be within uncertainty of zero.

16. Hypotheses with angles that are within uncertainty of zero are geometrically valid. Now crosscheck your results with independent information to assess their geological validity.

A2.2. Testing models

1. Ensure dataset is an appropriate selection of samples/compositions to test geochemical model of interest.

2. Ensure model and data are converted to molar proportions, not weight percent.

3. Place all rock compositions in a single data matrix (**GCM**), with m rows of components and n columns of samples.

4. Place all model vectors in a single matrix (**M**). Each model vector must be $m \times 1$ of the same m components as the rock compositions. That is, if rock compositions contain components c_1 to c_m as oxides, so too must model vectors. Include zeros as appropriate.

5. Compute the singular value decomposition (SVD) of the **model** matrix, giving
   matrices **U**, **S**, and **V**.

6. Identify the model space (**u_m**); it is the first η columns of the U matrix from the SVD,
   where η is the number of columns in the model matrix.

7. Project the rock compositions (GCM) onto the model space (u_m).

8. Recalculate the rock compositions from their model space coordinates, giving **GCM_m**.

9. Determine the angles separating modeled rocks GCM_m from original rocks GCM.

10. Compare the modeled rock compositions (GCM_m, from step 8) to the original
    compositions, both by their angles and the concentrations of their components.
    *The assessment of angles and concentrations will require a consistent approach
    that is up to the user to devise or choose*.

11. Satisfactory reproduction of rock compositions validates the model. The converse is
    also true.

A2.3. Transforming to model components

Note: More than one approach to performing these transformations is possible. The
approach here, particularly steps 3-5 that involve projections onto orthonormal bases,
gives model vector contributions that best recover the whole rock compositions.

1. Ensure the model vectors are valid inasmuch as they are geologically feasible, pass
   geometric testing (unless a strong rationale permits an exception), and
   satisfactorily reproduce rock compositions.

2. Ensure model and data are converted to molar proportions, not weight percent, and
   place them the model matrix **M** and geochemical matrix **GCM**, respectively.

3. Follow steps 4-6 from ***Testing models*** algorithm, above.

4. Project the model matrix onto the orthonormal model space (**u_m**) from the U matrix of t
   he SVD, giving **M_proj**.

5. Project the rock compositions onto the orthonormal model space **u_m** from the U matrix
   of the SVD, giving **GCM_proj**.

6. Create an $m \times m$ identity matrix **I**.

7. From left to right, replace the columns of the identity matrix (I) with the *projected*

model vectors, M_{proj}. Assuming the η model vectors are fewer than *m* (they cannot be greater than and should usually not be equal to *m*), leave the remaining columns of the identity matrix unchanged once all projected model vectors are included.

8. Invert the modified identity matrix from step 7, giving the transformation matrix, **T**.

9. Transform the projected rock compositions by matrix multiplication, giving **GCM$_{model}$**:

$$GCM_{model} = T\ GCM_{proj.}$$

10. The data are now in model vector proportions, with the rows corresponding to each model vector. The values remaining in untransformed rows correspond to the amount of these components the model cannot explain.
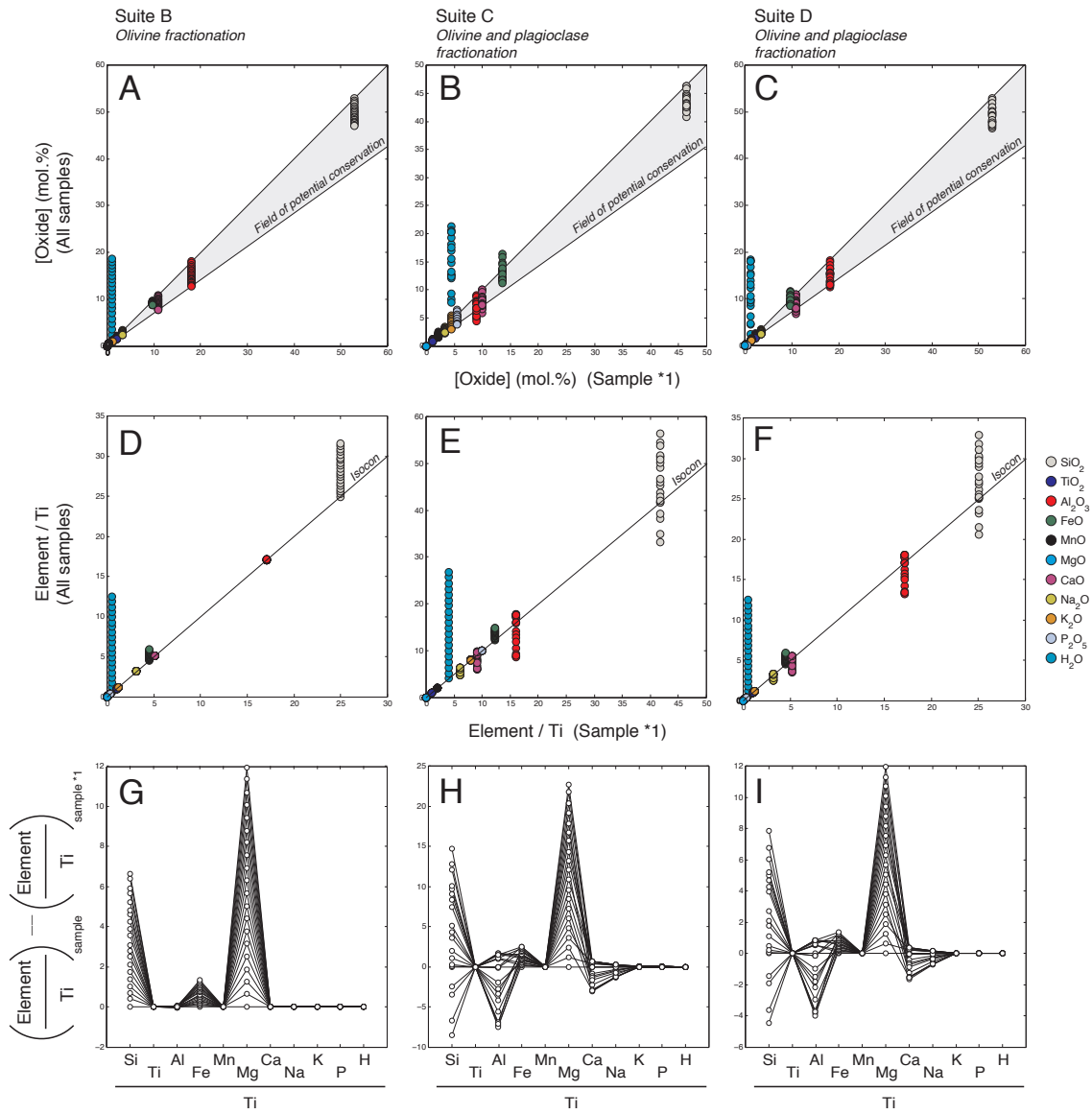
Figure A1. Isocon diagrams and their modifications for synthetic data suites B-D. **A-C**. Standard isocon diagrams comparing all samples to sample *1 (i.e., B1, C1, D1). **D-F**. Pearce element ratio-style isocon diagrams all samples to sample *1. **G-I**. Translated element ratio diagrams showing deviations from sample *1.